Shear and thermal induced aggregation of amyloidogenic and non-amyloidogenic proteins and the effect of a neuroprotective plant, *Centella asiatica* on protein aggregation

A thesis submitted

In Fulfilments of the Requirements

for the degree of

DOCTOR OF PHILOSOPHY

by

Laipubam Gayatri Sharma

176106013

Under the supervision of

Prof. Lalit Mohan Pandey

Department of Biosciences and Bioengineering

Indian Institute of Technology Guwahati

Guwahati 781039, Assam, India

18th November 2024

Dedicated

to

My Family

DECLARATION

I, hereby declare that the research carried out in the thesis entitled " ***Shear and thermal induced aggregation of amyloidogenic and non-amyloidogenic proteins and the effect of a neuroprotective plant, Centella asiatica on protein aggregation,*** " submitted by me to the *Indian Institute of Technology Guwahati*, for the award of the Doctor of Philosophy, is a bonafide work carried out by me under the supervision of Prof. Lalit Mohan Pandey. The content of this thesis, in whole or in parts, has not been submitted to any other University or Institute for the award of any degree or diploma. I also wish to state that nothing in this report amounts to plagiarism to the best of my knowledge and understanding.

Laipubam Gayatri Sharma
Department of Biosciences and Bioengineering,
Indian Institute of Technology Guwahati,
Guwahati - 781039, Assam, India

Date: 18th November 2024

CERTIFICATE

This is to certify that the thesis entitled " ***Shear and thermal induced aggregation of amyloidogenic and non-amyloidogenic proteins and the effect of a neuroprotective plant, Centella asiatica on protein aggregation,*** " submitted by **LAIPUBAM GAYATRI SHARMA (176106013)**, a Ph.D. student in the *Department of Biosciences and Bioengineering, Indian Institute of Technology Guwahati*, for the award of the degree of Doctor of Philosophy, is a record of an original research work carried out by her under my supervision and guidance. The thesis has fulfilled all requirements as per the Institute's regulations and, in my opinion, has reached the standard needed for submission. The results embodied in this thesis have not been submitted to any other University or Institute to award any degree or diploma.

Supervisor
Prof. Lalit Mohan Pandey
Department of Biosciences and Bioengineering,
Indian Institute of Technology Guwahati,
Guwahati - 781039, Assam, India

Date: 18th November 2024

ACKNOWLEDGEMENTS

First and foremost, I would like to thank my supervisor, **Prof. Lalit Mohan Pandey**, for believing in me and allowing me to work on such an intriguing topic. His mentorship refined my analytical abilities and shaped the outcome with his invaluable guidance, ideas, and suggestions. I will always be grateful and indebted for his priceless support.

I also wish to express my heartfelt appreciation to my committee members, **Prof. Soumen Kumar Maiti, Prof. Pankaj Tiwari, and Prof. Latha Rangan** (my DC Chairperson), for their insightful feedback, valuable suggestions, constructive criticisms, and instrumental role in guiding me to achieve this significant milestone.

I sincerely thank the Department of Biosciences and Bioengineering (BSBE) at the Indian Institute of Technology Guwahati for allowing me to be part of this esteemed institution. I am grateful to the faculty members and staff of BSBE for their assistance and support. Additionally, I thank the Central Instrument Facility (CIF) at IIT Guwahati for allowing me to conduct my experiments using their advanced instruments.

I am also thankful to the Centre for the Environment, Indian Institute of Technology Guwahati, for providing me with the facility to analyse the size of samples through Dynamic light scattering (DLS).

I want to express my gratitude to my seniors, **Dr Abshar Hasan, Dr Varun Saxena, Dr Poulomi Datta, and Dr Rahul Verma and my dear labmates, Dr. Aquib Jawed, Aman Bhardwaj, Rushikesh Fopase, Vivek Yadav, Anurag Mishra, Mehak, Chinmaya Panda, Shalini Prajapati, Shilpa Nandi, Smriti Sonbhadra, Jayprabhakaran, Debasmita Seal, Akshay Kumar, Deepak and Shalini S.**

Their invaluable support during challenging times helped me persevere, and our engagement in thought-provoking discussions kept me on edge. Their presence brought joy and courage, reminding me of the power of unity. Simple moments, like tea breaks, became cherished memories that rejuvenated us and fuelled our determination.

I am indeed grateful to have the company of my dear junior **Dr Maibam** and members of integrated bioprocessing lab including **Yashwant, Suraj, Sahil, Meenakshi, Bhumika and Pragati**.

I am also indebted to **Dr Sanjana** for helping me in the plant extraction process and am very thankful to her.

I am also grateful to **my friends** and **acquaintances**, whom I have not mentioned, for their tremendous help and support, directly or indirectly, in my PhD journey.

I also want to thank my dear friend **Dr Swati Sharma** for always supporting and standing with me in tough times.

I would also like to thank my partner for life, **Dr Ratan Kumar**, for always being there in every circumstances.

Additionally, I extend my greatest appreciation to my beloved **family members** for their unflinching support and faith in me.

Lastly, I thank my **almighty God** for being the beacon of light in every breadth of my life.

With heartfelt appreciation,
Laipubam Gayatri Sharma

ABSTRACT

Shear-induced aggregation of protein is one of the important factors leading to aberrant protein folding and aggregation. Shear impact on protein is accompanied physiologically in the narrow periarterial region as a result of the flow of the cerebrospinal fluid and also in other body parts with stenotic and aneurytic condition in blood vessels. These conditions play a crucial role in the early phase of the devastating Alzheimer’s disease and in thrombosis, which leads to myocardial infarction and transient ischemic attack, respectively. Another important shear implication is in the therapeutic industry where protein formulations, cytokines, enzymes, etc., have to endure processing conditions like stirring, shaking, pumping, freeze-thawing, filling, and so on, which generates various kinds of shear. In fact, thermomechanical energy is accompanied by such processing conditions. Therefore, it is imperative to study shear and thermomechanical induced aggregation both from a physiological and pharmaceutical perspective. With this account, two amyloidogenic proteins (Amyloid beta 1-40 and Hen egg white lysozyme) and two non-amyloidogenic proteins (Bovine serum albumin and Bovine fibrinogen) were selected for study pertaining to the thermomechanical induced aggregation in this doctoral work. To address the aggregation issue, crude extract of neuroprotective plant *Centella asiatica* was checked for its impact on the aggregation of protein from one of each type studied. The entire thesis has been divided into four main sections. In the first section, shear and thermally induced aggregation of the above two amyloidogenic proteins, Aβ (1-40) and HEWL, were studied. The impact of varying shear as well as constant shearing on Aβ (1-40) was performed, and the impact of pre-shearing on HEWL was determined. In the second part, the impact of the thermomechanical treatment on two non-amyloidogenic proteins, BSA and BFG, were performed. In the first study, the energetics of the thermomechanical treatment BSA, along with its related impact on the unfolding and aggregation behaviour, have been explored to decipher the roles of the thermal as well as the dissipation energy. Similarly, thermomechanical and thermal induced aggregation were compared and studied in BFG. In the next section, a neuroprotective, memory-enhancing plant, *Centella asiatica* was extracted and characterised. In the last and fourth sections, the extracts of *Centella asiatica* were checked for their inhibitory properties against the shear and thermally induced aggregation of BSA, a non-amyloidogenic protein and on the thermally induced aggregation of HEWL, an amyloidogenic protein. The binding energetics of the extract with these two proteins were also determined through various fluorescence as well as calorimetric techniques. Further, the impact of the aggregates in the presence and absence of the extract was also determined on a neuroblast cell line IMR32 as ultimately, the impact of the extract as well as the aggregates needs to be comprehended on a cellular level. To sum up, the various macro and microanalysis of thermomechanical impact on amyloidogenic as well as non-amyloidogenic proteins was determined and could reveal crucial elements mainly in terms of their secondary structure. The *Centella asiatica* extract, through interaction with the monomeric protein, significantly inhibits thermomechanical as well as thermal induced aggregation. The toxicity of aggregates, mainly the amyloidogenic HEWL, could be protected to an extent by the presence of *Centella asiatica* extract. Hence, the study could provide a basic understanding in the future for research in the field of protein aggregation studies, more profoundly in thermomechanical related studies and also the protein aggregation inhibition potential through the small molecule phytochemical can be encouraged.

CONTENTS

LIST OF FIGURES

LIST OF TABLES

ABBREVIATIONS

Acronyms and nomenclature

AD	Alzheimer's disease
Aβ	Amyloid beta
AFM	Atomic force microscopy
ANS	8-anilino-1-naphthalenesulfonic acid
apoC-II	Apo lipoprotein C-II
APP	Amyloid precursor protein
BSA	Bovine serum albumin
BFG	Bovine fibrinogen
BBB	Blood-brain barrier
CA	*Centella asiatica*
CD	Circular dichroism
CSF	Cerebrospinal fluid
CNS	Central nervous system
DMSO	Dimethyl sulfoxide
DPPH	1-diphenyl-2 picrylhydrazyl
DLS	Dynamic light scattering
DMEM	Dulbecco's Modified Eagle Medium
EGCG	Epigallocatechin-3-gallate
FTIR	Fourier transform infrared spectroscopy
FDA	Food and Drug Administration
FC	Folin-ciocalteu
GIT	Gastrointestinal tract

hIAPP	Human islet amyloid polypeptide
HEWL	Hen egg white lysozyme
HRLCMS	High-resolution liquid chromatography and mass spectrometry
HPLC	High pressure liquid chromatography
IAPP	Islet amyloid polypeptide
ITC	Isothermal titration calorimetry
IDPs	Intrinsically disordered proteins
IF	Interstitial fluid
MRE	Mean residue ellipticity
MTT	3-(4,5-dimethylthiazol-2-yl)-2,5-diphenyltetrazolium bromide
mAbs	Monoclonal antibodies
PBS	Phosphate buffer saline
PP50	Parallel plate geometry (50 mm diameter).
PD	Parkinson's disease
PNS	Peripheral nervous system
ROS	Reactive oxygen species
SEC	Size Exclusion Chromatography
SV	Stern-Volmer
SbVP	Sub-visible particle
SAA	Serum amyloid A amyloidosis
SOD1	Superoxide dismutase 1
Th-T	Thioflavin T
TRX	Thioredoxin A
TEM	Transmission electron microscopy

Symbols

T	Temperature (K)
ΔC_p	Heat capacity change (kJ $mol^{-1}K^{-1}$)
ΔH	Enthalpy (J)
$\Delta G°$	Gibbs free energy (J)
K	Kelvin
k	Equilibrium constant
T_m	Melting temperature (K)
R	Gas constant (J $mol^{-1}K^{-1}$)
E_a	Activation energy (kJ mol^{-1})
A	Pre exponential factor
K	Consistency coefficient
η	Viscosity (Pa s)
C	Concentration factor
M	Molecular weight factor
d_H	Hydrodynamic diameter (nm)
D	Diffusion coefficient
K	Boltzmann constant
θ	Machine CD signal value in millidegree (mdeg)
α	Folded fraction
θ_t	MRE value at the desired state of the sample
θ_u	MRE values of the unfolded
θ_f	MRE values of the folded state
I_t	Fluorescence intensity at time t

I_{max}	Maximum fluorescence intensity
τ	Shear stress (Pa)
γ	Shear rate (s^{-1})
MRW	Mean residue weight
P	Pathlength (cm)
C	Concentration (mg/ml)

CHAPTER-1

Introduction

Proteins are among the crucial biomolecules of the living world, which perform many functions. It involves the building of the structural network of the cells, in transportation, and as enzymes controlling the catalytic activity of the whole system of the living world [1]. Proteins can perform numerous biological functions accurately. Both globular proteins, with their stable 3D folded structures, and intrinsically disordered proteins (IDPs), with their flexible and unstructured conformations, are highly functional. Their folded or unfolded states enable each to play unique, critical roles in cellular processes [2].

This specific native conformation may sometimes deform or denature by various intrinsic and extrinsic factors. Intrinsic factors comprise the protein's primary, secondary, tertiary, and quaternary structure. The extrinsic factors include environmental factors, such as pH, temperature, pressure, mechanical shear, processing conditions for biopharmaceutical products, etc. Protein denaturation or aggregation happen at the cellular level when the misfolded proteins cannot be degraded by the cell's proteasome or the autophagy system [3, 4]. The protein aggregation process is thought to proceed with polymerisation growth, starting with the nucleation of the aggregates [5]. The monomeric form of the protein dimerises initially and gradually forms different oligomeric species, which finally give rise to the highly structured mature amyloid fibrils. The initial aggregation process where the monomer starts to form the pre-aggregates is somewhat thought to be thermodynamically unfavourable. However, after a specific concentration, the nucleus is formed, from where the fibrillation begins to form the more considerable aggregate structure like the protofibrils, which is also considered to be thermodynamically stable. The newly formed aggregates can dissociate and associate and can also initiate polymerisation. It is surprising that more than 20 different diseases related to amyloidogenesis, which are formed due to totally unrelated proteins and peptides, share the same features of the amyloid fibrils [6]. It is still unclear whether amyloid assembly is a symptom or a cause of neurodegenerative disease [7, 8].

The spontaneous assembly of the misfolded and or unfolded proteins has led to life-threatening diseases, both neurodegenerative and pathological diseases, which include Alzheimer's, Parkinson's, prion and type II diabetes. Many amyloidogenic proteins, including amyloid beta peptide, human islet amyloid polypeptide (hIAPP), tau proteins, insulin, transerythrin, immunoglobulin light chain, α-synuclein, lysozyme etc., have been reported to form amyloid aggregate and of different morphologies [9]. These peptides /proteins are responsible for causing the Alzheimer's disease, type 2 diabetes, Parkinson's disease, lysozyme amyloidosis respectively.

Among various causes of protein aggregation, the study of shear-induced aggregation of protein is an essential field, considering its prevalence in both physiological and biopharmaceutical industries. In the biopharma company, protein products and formulations are subjected to numerous processing techniques, e.g. stirring, pumping, filling, freeze-thawing, transportation of the products (drugs), etc., [10] which generates various kinds of shear. Both thermal and shear are accompanied by many of the processing techniques involved. These conditions may denature or alter the native protein conformation, which can initiate protein aggregation. These protein products can lose their function and enzymatic activity and even initiate immunogenic responses. Physiologically, it has been hypothesised that Aβ peptide and α synuclein protein are subjected to extensional as well as laminar shear flow as a result of the flow of the cerebrospinal fluid in the perivascular region of the brain [11]. The shear flow, therefore, could be one of the reasons that initiate the unfolding and denaturation of these proteins, leading to Alzheimer's and Parkinson's diseases, respectively.

Another important implication of shear is abnormal thrombosis, which may lead to devastating diseases like myocardial infarction and transient ischemic attack [12]. The shear rate generated from the normal haemodynamic blood flow is required to activate essential proteins, like the von Willebrand factor, in the early stages of thrombosis. In abnormal thrombotic conditions, aneurytic and stenotic lesions are formed, creating differential shear in the region. So, in such situations, proteins involved in thrombosis and other plasma proteins are exposed to these shear forces, which could alter protein structure. Another physiological situation under which proteins are denatured is the case of matricryptic proteins. Matricryptic sites, or "cryptic sites" within proteins of the extracellular matrix (ECM), become exposed when mechanical forces, such as stretching or injury, disrupt the protein's folded structure. This process reveals previously hidden amino acid sequences that can serve as binding sites for cells, signalling molecules, or enzymes involved in repair [13, 14].

Therefore, studying and understanding protein behaviour by creating similar shear and thermal conditions on a laboratory scale is imperative. To contribute to research in this field, both amyloidogenic and non-amyloidogenic proteins were subjected to shear and thermal conditions to check and induce aggregation. For amyloidogenic proteins, Aβ (1-40) with an intrinsically disordered structure and HEWL with a compact globular structure were chosen as both are amyloidogenic yet their physiological features are totally different. For non-amyloidogenic proteins, BSA and BFG which are both important serum proteins one which is a globular and the other fibrous in nature are chosen. These proteins were studied in different experimental conditions as each protein is structurally as well as physiologically different from each other. The key physical properties of these proteins are given in **Table 2.2**.

After the aggregation is induced, the corresponding changes in their structure, rheology, morphology, etc., were then analysed and discussed. The aggregate toxicity was also checked with a neuroblast cell line IMR32. Moreover, to address the protein aggregation issue, an extract of *Centella asiatica*, a nootropic plant, was checked for its anti-aggregation ability, and its binding with the protein was also studied.

1.1. Objective

To bridge the knowledge lacuna as reviewed in Chapter 2 and to provide deeper insight into the study of shear and thermal-induced aggregation of protein, the four thesis objectives are as follows:

1. Shear and thermally induced aggregation of two amyloidogenic proteins [Aβ (1-40) and (HEWL)]
2. Shear and thermally induced aggregation of two non-amyloidogenic proteins [BSA and BFG]
3. Extraction and characterisation of *Centella asiatica*, a neuroprotective plant extract
4. Interactions of proteins with natural extracts towards their stability and in-vitro study of the cytotoxicity of the aggregates formed due to shearing of amyloidogenic protein (HEWL) and non-amyloidogenic protein (BSA) on neuroblast cells (IMR32)

1.2. Thesis outline

The following seven thesis chapters were formed based on the above four objectives. A chapter-wise thesis outline is as follows:

1.2.1. Chapter 2

This chapter reviews the different aspects of protein aggregation, focussing on shear-induced aggregation and the other mechanisms of how protein aggregates. Various small molecule ligands employed for protein aggregation prevention were also reviewed.

1.2.2. Chapter 3

In this chapter, two amyloidogenic proteins, Aβ (1-40) (Amyloid beta 1-40) and HEWL (Hen Egg White Lysozyme), were subjected to shear and thermal induced aggregation. The aggregates' aggregation kinetics, change in secondary structure, and morphology were then analysed. Aβ (1-40) peptide, a derivative of Amyloid precursor protein, was subjected to constant (300 s^{-1}, 500 s^{-1}, 700 s^{-1}) and varying (ramp) shear in a parallel plate geometry to explore the implications of shear in terms of macro (viscosity) and micro (secondary structure, morphology) characteristics. Next, another amyloidogenic protein, HEWL, was subjected to 65°C thermal induced aggregation at pH2 to induced aggregation. Samples pre-sheared at 300 s^{-1} for an hour at 65°C were used as seeds and incubated at 65°C to compare with the un-sheared, non-seeded sample.

1.2.3. Chapter 4

This chapter studied the shear and thermal-induced aggregation of two non-amyloidogenic proteins, BSA and BFG. In the first study, the energetics of the thermomechanical treatment of bovine serum albumin (BSA) and its related impact on the unfolding and aggregation behaviour have been explored to decipher the roles of the thermal and dissipation energy. Shear-induced aggregation of the BSA at a constant shear rate of 300 s^{-1} was performed at the three temperatures (55, 60 and 65 °C) using a Rheometer and the aggregation behaviour was experimentally analysed. Next, thermal and shear-induced aggregation of another non-amyloidogenic protein, BFG (Bovine fibrinogen), was performed. The thermal aggregation was carried out at 45°C, 60°C, and 90°C. The thermal and shear-induced aggregation was carried out at 300 s^{-1} and 60°C using an Anton Paar rheometer with a parallel plate geometry.

1.2.4. Chapter 5

In this chapter, *Centella asiatica*, a neuroprotective herbaceous plant, was extracted through the soxhlet method using three solvents with increasing polarity. These crude extracts were then checked for their antioxidant property, phenolic content, and flavonoid content. The crude extracts were then analysed through HPLC, and two of the crude extracts, which show maximum inhibition of protein aggregation, were additionally analysed through HRLCMS to identify the bioactive components present in the extract.

1.2.5. Chapter 6

In this chapter, the effect of *Centella asiatica* extracts on the aggregation of a non-amyloidogenic protein (BSA) and an amyloidogenic protein (HEWL) was studied. The aggregation kinetics was monitored through the Th-T fluorescence assay, the secondary structure was determined through CD spectroscopy, and the aggregate size was determined through DLS and AFM analysis. Binding studies were performed through fluorescence quenching and docking analysis for both proteins. In addition, an ITC study was conducted for BSA to determine the best fraction of crude water extract from *Centella asiatica*. In addition, the in-vitro study of the cytotoxicity of the aggregates formed due to the shearing of amyloidogenic protein (HEWL) and non-amyloidogenic protein (BSA) on neuroblast cells (IMR32) was performed.

1.2.6. Chapter 7

In this chapter, the overall research contribution is conferred, and future research ideas related to shear and thermal-induced protein aggregation are also discussed.

CHAPTER-2

REVIEW OF LITERATURE

This chapter reviews the various aspects of protein aggregation-related topics, including the factors influencing it and its mechanism and, most importantly, the significance of studying shear and thermal-induced aggregation. Further, the strategy for approaching aggregation inhibition and the different types of small molecule inhibitors employed are discussed. The advantages of using plant-derived inhibitors and the impact of *Centella asiatica* plant on protein aggregation and cognitive enhancement are also emphasised.

2.1. Protein aggregation

It is the formation of amorphous or highly structured β-sheet-rich fibrils by misfolding/unfolding of proteins and peptides under conditions that can be intrinsic and extrinsic. The study of protein aggregation is a very important field of research, considering its ill impact pathophysiologically and industrially **(Figure 2.1)**. A protein aggregation study was carried out using different proteins and peptides by different means, both chemically and physically. Proteins that are aggregation-prone and readily form amyloid are generally related to various proteinopathy diseases, which is an umbrella term for many types of neurodegenerative diseases like Alzheimer's disease and Parkinson's' disease [15]. But again, some proteins do not readily aggregate to form amyloids. Structure-function relationships of biological macromolecules, such as proteins, provide crucial insights for fundamental biochemistry, medical research, and early drug discovery. However, the issue arises during the production of recombinant proteins, which have different uses, either for structure determination or for use as biopharmaceutical products. They are generally unstable and have a propensity to aggregate in solution in vitro. Poor-quality protein samples are often associated with reduced reproducibility and high research and production expenses [16].

Liquid biopharmaceuticals, like monoclonal antibodies (mAbs), have been known to undergo various stresses during shipping/handling and even during storage. Mechanical stresses, like shaking during shipping, have been widely known to cause protein aggregation and sub-visible particle (SbVP) formation, mostly in liquid biopharmaceutical formulations [17]. Knowledge of protein behaviour/stability during freeze/thaw (FT) operations is essential for storage and production processes in the biopharmaceutical industry. FT stress involves freeze concentration, cold denaturation, and ice crystal formation, which can result in protein aggregation [18]. In the burgeoning biopharmaceutical industry, protein misfolding and aggregation pose significant challenges to economically manufacturing safe and effective protein products.

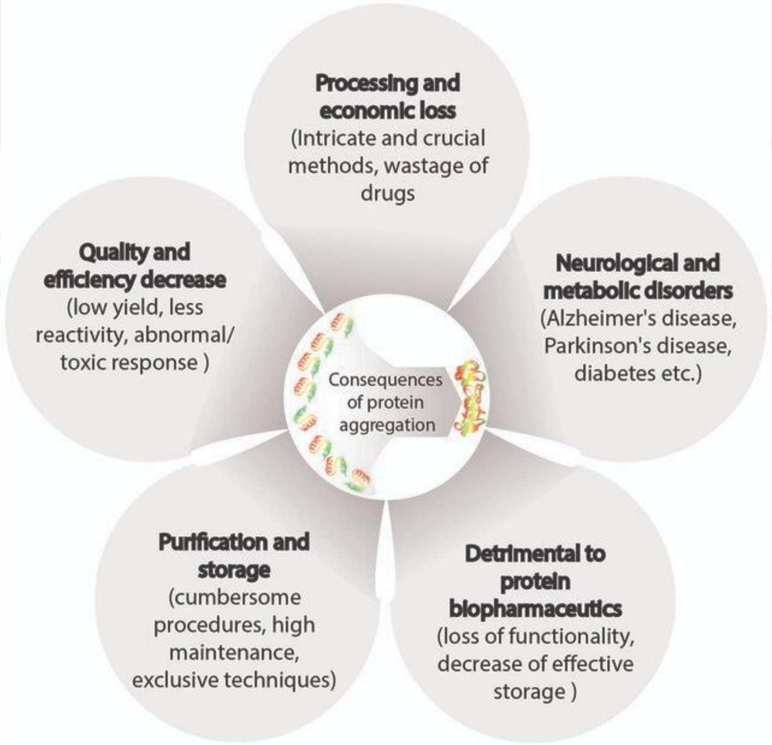

Figure 2.1. Protein aggregation and its disadvantages [19].

2.2. Amyloidogenic proteins

Amyloidogenic proteins are a group of proteins that can misfold and aggregate into insoluble fibrillar structures known as amyloid fibrils which is made up of highly structured β-sheet-rich motif. This structured region, also referred as the "β-core" defined by the densely packed beta-sheet regions supports the mature fibril's rigidity and stability. This core is created by certain intermolecular interactions between misfolded protein areas that are prone to aggregation, like the Aβ peptide in Alzheimer's disease. The β-core plays a key role in the development of amyloid plaques and is generally resistant to proteolysis, which helps explain why these aggregates remain in afflicted tissues[20]. Key hydrophobic amino acid residues are involved in the development of the β-core in amyloid fibrils. These include isoleucine (Ile), valine (Val), leucine (Leu), and phenylalanine (Phe), which through intermolecular interactions help to stabilise beta-sheet structures[21].

These amyloids can bind specific dyes like Thioflavin T, congo red, ANS, etc. Though their specific contacts and binding processes vary, Thioflavin T (ThT) and Congo Red (CR) both attach to protein aggregates by targeting the beta-sheet structures found in amyloid fibrils. ThT inserts into the grooves of these stacked beta-sheets and binds perpendicularly to the beta-strands within the amyloid cross-beta structure. ThT's fluorescence is significantly increased as a result of this binding, which makes it a valuable dye for amyloid development monitoring in real time. Along the beta-sheets of amyloid fibrils, Congo Red binds in a parallel, planar pattern. Its flat, elongated shape intercalates between the strands in alignment with the beta-sheet stacks. In contrast to ThT, this binding causes a noticeable shift in the absorbance spectrum of CR and also shows distinctive birefringence under polarised light [22, 23].

Proteinopathy, or the abnormal folding of proteins, has led to the pathogenesis of more than 20 human diseases, which include neurodegenerative diseases like Alzheimer's disease and Parkinson's disease; Nonneuropathic systemic amyloidosis, like Lysozyme amyloidosis and serum amyloid A amyloidosis (SAA amyloidosis); Nonneuropathic localised diseases such as type 2 diabetes, and so on [24, 25]. Amyloid β peptide, α synuclein, and amylin, which cause the above-mentioned proteinopathy diseases, are usually present in a disordered state in their native conformation, which, if abnormally aggregated, forms an insoluble proteinaceous substance called amyloid, which is proven to be toxic to the cells [25].

Not only do proteins present disorderly in their native state from amyloid, but some globular proteins also tend to be amyloidogenic, like in the case of non-neuropathic systemic amyloidosis or familial amyotrophic lateral sclerosis [26]. Some diseases related to abnormal protein folding are listed in **Table 2.1**. Natively compact proteins such as β-2-microglobulin, immunoglobulins, superoxide dismutase 1, transthyretin and lysozyme, under physiological conditions, are generally soluble unless due to certain situations in in-vitro, got unfolded or partially denatured, which exposes the hydrophobic region leading to the self-assembly and finally forming amyloid aggregates [27]. These hydrophobic regions are supposedly associated with aggregation-prone regions, which, when exposed, initiate the aggregation reaction leading to the formation of β sheet-rich fibrils. These amyloidogenic regions coincide with the interface area, where self-assembly and fibrillation occur.

These amyloidogenic regions have been associated with various polypeptides, which are responsible for multiple neurodegenerative as well as systemic amyloidogenic diseases.

The polypeptides responsible for neurodegenerative diseases like Alzheimer's and Parkinson's are devoid of regular structure, whereas the proteins causing familial amyotrophic lateral sclerosis or non-neuropathic systemic amyloidosis are proper globular proteins. The mechanism by which globular proteins, under physiological conditions, aggregate from their initially folded and soluble conformations is not properly understood.

The polypeptides that form insoluble amyloid protein deposits in tissues are unrelated in sequence or conformation. Examples include amylin, amyloid-β-protein, α-synuclein and so on. In contrast, many other amyloidogenic proteins are globular in their native state, implying an adequately packed and cooperatively sustained structure under physiological conditions. This includes β-2-microglobulin, transthyretin, lysozyme, superoxide dismutase 1 and immunoglobulins [26]. However, it has been shown that, in vitro, under conditions where they become totally or partially unfolded, both these pathogenic proteins and many globular polypeptides not related to disease readily convert into aggregates and ultimately into highly structured amyloid fibrils. This self-association is triggered by the deterioration and opening of the native structure. This led to the exposure of previously protected aggregation-prone regions that can nucleate the aggregation reaction and thereby participate in forming the β-core of the mature fibril through specific intermolecular interactions [16] [18]. Such amyloidogenic sequence stretches have been described in most polypeptides underlying neurodegenerative and systemic amyloidogenic disorders.

In our study, two of such amyloidogenic proteins which will be studied to check the impact of shear and thermally induced aggregation are Aβ (1-40) and Hen egg white lysozyme (HEWL).

2.2.1. Aβ (1-40)

Amyloid-β (Aβ) peptide accumulation is one of the essential hallmarks of the neurodegenerative Alzheimer's disease. It is a highly amyloidogenic aggregation-prone peptide with residue ranging from 39 to 43. The 40 residue Aβ (1-40) isoform is among the most crucial peptide marker next to Aβ (1-42). Studies have shown that the Aβ (1-40) concentration increases in the brain in the pathology of AD [28, 29]. The structure of Aβ (1-40) changes with the environment. Typically, it has a helix-coil conformational switch that depends on the pH, a hydrophobic C-terminus, N-terminus, β-strand, helical domains and a type 1 beta-turn [30, 31]. **Figure 2.2** shows the 3D solution structure of Aβ (1−40), in aqueous sodium dodecyl sulfate (SDS) micelles, determined through NMR spectroscopy at pH 5.1. The peptide is unstructured between residues 1 and 14, which are primarily polar and probably solvated by water, in this environment, which somewhat mimics a water-membrane medium. The remainder of the protein, however, takes on an α-helical shape between residues 15 and 36, with a hinge or kink at 25–27. SDS probably solvates this mostly hydrophobic area.

Research reveals a pH-dependent helix-coil conformational transition between pH 4.2 and 7.9. The helix is uncharged, unbroken, and lipid-soluble at lower pH levels where the carboxylate residues are protonated. A portion of the helical area (15–24) loses structure as the pH rises beyond 6.0, especially in the vicinity of residues E22 and D23, where deprotonation seems to aid in the helix's unwinding. Any inclination of this peptide to cluster to a β-sheet when the pH rises is preceded by this pH-dependent unfolding to a random coil shape [31].

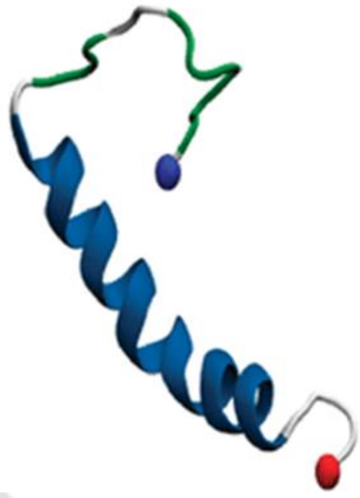

Figure 2.2. Structure of amyloid beta (1-40) (*adapted with permission from Olubiyi et.al, 2012*)[32].

2.2.2. HEWL

Another amyloidogenic protein is the Chicken egg white lysozyme/hen egg white lysozyme, a globular protein with a molecular weight of around 14305 kDa **(Figure 2.3)**. It has 129 amino acid residues, of which 17 are positively charged and 9 are negatively charged residues. The most crucial active site residues are Glu_{35}, Asp_{52}, Trp_{62}, Trp_{63}, Asp_{101} and Trp_{108}. Among these, Glu at 35 position and Asp at 52, which are positioned oppositely, are the most critical residues for substrate binding. The active sites are distributed on the two domains of HEWL: the α domain and the β domain. Antiparallel β sheets are the principal constituent of the β domain, whereas the α domain is mainly constituted by 3_{10} helix and α-helices [33].

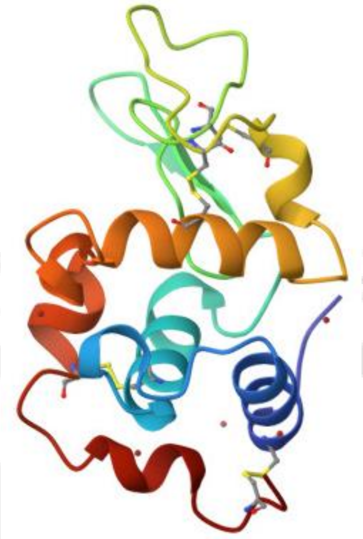

Figure 2.3. Structure of hen egg white lysozyme (PDB ID 6LYZ)

Table 2.1: Diseases related to amyloid aggregation or depositions

Disease name	**Protein/peptide involved**	**Location**	**Symptoms**	**Native conformation**	**Refs.**
Alzheimer's disease	Amyloid beta (Aβ) peptide	Brain	Cognitive impairment, agitation, anxiety, depression	Mostly unfolded or random coil	[10, 11]
Huntington's disease	Huntingtin	Brain	Cognitive impairment	Natively unfolded	[12]
Parkinson's disease	α- synuclein	Brain	bradykinesia, hypomimia, difficulty walking, freezing, postural instability and rigidity,	Intrinsically disordered	[13]
Spongiform encephalopathies	Prion protein	Brain, peripheral nervous system (PNS)	locomotion problem, memory change	α-helical	[14]
Amyotrophic lateral sclerosis	Superoxide dismutase	Brain	Distorted speech, difficulty in swallowing, weakness, stiff muscle	All β form	[15]
Senile systemic amyloidosis	Transthyretin wild type	Microvasculature	Dizziness, irregular heartbeat, fatigue	All β forms	[15]
Lysozyme amyloidosis	Lysozyme mutants	Salivary gland, vasculature and gastrointestinal tract (GIT)	Gastrointestinal, hepatic and renal symptoms, sicca syndrome, diarrhoea etc.	α + β forms	[16][34]
AL amyloidosis	Immunoglobulin light chain	Most tissues	Weakness, poor appetite, shortness of breath, swelling, etc.	β forms	[17]
Type II diabetes	Amylin / (IAPP) islet amyloid polypeptide	Pancreas / Islet	Tiredness, excessive thirst, breathlessness, etc.	natively unfolded	[18]
Cataract	γ- crystallin	Eye	Clouding of the eye leading to blindness	all β forms	[19]
Medullary carcinoma of the thyroid	Calcitonin	Thyroid tissues	Hoarseness, neck pain, difficulty in swallowing	unfolded state	[20]
Injection localized amyloidosis	Insulin	Skin, muscles	Severe hypoglycaemia	All α forms	[21]

2.3. Non-amyloidogenic proteins

Non-amyloidogenic proteins are non-pathogenic proteins which are generally soluble and are not aggregation-prone under normal physiological conditions unless induced by external forces. Many enzymes, transport proteins, antibodies, and hormones are generally non-amyloidogenic. Some examples are myoglobin, ubiquitin, thioredoxin, maltose binding protein [26], bovine serum albumin and fibrinogen. However, the mutated light chain Aα gene (FGA) of fibrinogen leads to the formation of hereditary renal amyloidosis [35]. The aggregation-prone region in such proteins does not coincide with the interface region, where self-assembly occurs if it forms aggregate or amyloid fibrils. For example, human myoglobin, a compact non-pathogenic protein, is present mostly in its α helical native form in solution. It possesses around four aggregations-prone regions from residue 8 to 15, 28 to 33, 67 to 76 and 110 to 117. The aggregation prone region was populated with hydrophobic amino acid residues such as Val, Leu, Ile, Phe and Met. However, only the last segment partially coincides with the segment which is found to engage in amyloid formation, which is the region 100 to 114 [27]. Even if the aggregation-prone region is exposed, for example, in the case of Thioredoxin A (TRX), it was found to be involved in forming its complex with its target peptide but not in aggregate formation. As opposed to amyloidogenic proteins, why, in these cases, no amyloid aggregation occurs, perhaps because evolution has designed a counteracting system to avoid amyloid aggregation. Aggregation-prone regions are flanked by aggregation keeper sequences, mainly sequences made up of charged amino acid residues like arginine, lysine, glutamate and aspartate, which repel self-assembly formation [36]. Two of the non-amyloidogenic proteins that will be studied in this thesis are Bovine serum albumin (BSA) and Bovine fibrinogen (BFG).

2.3.1. BSA

It comprises three domains with two subdomains and is intricately stabilised by 17 intramolecular disulphide bonds, excluding one free thiol residue Cys34 [37]. BSA has a molecular weight of around~66 kDa and is majorly constituted by a helical secondary structure [38]. These features make BSA a model protein for various biophysical and biochemical studies [39]. Apart from its physiological importance, it is one of the main components of whey proteins, and it is used as a gelling agent, emulsifier, or foaming agent to provide desirable tastes and texture to the food. Therefore, the quality of these proteins wholly depends on the processing conditions [40] [41]. For instance, the extrusion process in the biotechnology process, pasteurisation and ultra-high temperature processing of milk involves thermal and mechanical treatments [42]. Therefore, knowing how this protein behaves under a certain external force or stimuli is essential in deciding the processing parameters and the desired product [43]. In another study by Arakawa *et al.*, BSA was exposed to thermal stress at 50, 60 and 70°C, and the aggregation was checked through native gel electrophoresis and circular dichroism (CD). It was found that no aggregates were formed at 50°C as there were only monomer and dimer bands, and in the other cases, the monomer band was reduced, and few new aggregate bands were observed [44].

In the case of the whey proteins, it is majorly constituted by β- lacto globulin, α- lactalbumin, BSA, immunoglobulins, and the minor lactoferrin, lysozyme, lacto peroxidase and growth factors. Whey proteins have more secondary and tertiary structures than the casein from which it has been manufactured. This makes the whey proteins more susceptible to denaturation from heat processing. The globular proteins undergo unfolding, which interacts within each other and also with other milk proteins to form aggregates. The aggregation process due to heat generation was caused by the exposure of the free SH group and the hydrophobic moiety present at the core of the protein structure. BSA, among the major components, begins denaturation at around 62°C, where it is found to be in a reversible state between its native and the molten globule state. When the heating process is enhanced, it undergoes irreversible aggregation to form a hydrophobic conformation, finally leading to intermolecular hydrophobic aggregation [45] [46].

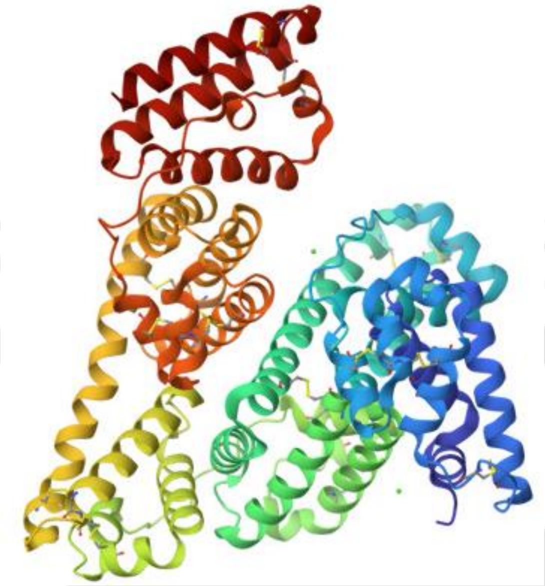

Figure 2.4. Structure of BSA (PDB ID 3V03)

2.3.2. Bovine fibrinogen (BFG)

BFG is a glycoprotein found in the blood plasma of cows (bovines) **(Figure 2.5)**. It plays a crucial role in the blood clotting process, coagulation. It has a molecular weight of 340 kDa [47], about 45 nm long, and a diameter of about 5 nm. The whole globular structure is a dimer of three pairs of different polypeptide chains Aα, Bβ and ϒ and has 29 disulphide bonds without any free sulfhydryl groups. It has three domains: two distal D domains, which are formed by the C terminal end of Bβ and ϒ, and the central E domains formed by the N terminal ends of Aα, Bβ and ϒ. The D domain is centrally connected to the E domain, a compact structure through a coil-coiled triple helix [48, 49]. The NH_2 terminal portions of the six chains are linked together to the central region of the molecule by 11 disulphide bonds, forming a small globular domain called the disulphide knot [32] in the centre. The C terminal region of Aα extends through the D domain and forms the highly mobile αC region. It interacts intramolecularly with the central compact E domain in fibrinogen monomer form. However, their interaction is intermolecular when two fibrinogen monomers form the fibrin monomer. This process is initiated when thrombin cleaves fibrinopeptides A and B from fibrinogen to form fibrin monomers. The cleavage exposes the A and B knobs and leads to fibrin polymer extension. Fibrinogen has significant implications both in physiological conditions and in biomaterial adsorption. Blood clotting is an essential procedure for quitting blood overflow in vascular injury. However, clots in specific areas like the heart, lungs and brain lead to thromboembolic diseases and can lead to heart attack, pulmonary embolism and stroke.

Renal hereditary amyloidosis, a group of rare autosomal dominant disorders, is caused by a mutation in the gene coding the αC domain. These mutations lead to the improper folding of the protein, which then leads to the formation of amyloid depositions, mostly in the kidney [50]. Over time, these amyloid deposits pose a severe threat to kidney functions as well as impair its structure and are associated with other physiological breakdowns such as hypertension. Though the deposits of renal amyloidosis are prominent in the kidney, the fibrinogen amyloidosis pathology is not restricted to the kidney. It has been found in other regions, including vascular walls and atheromatous plaques, leading to cardiovascular atheromatous diseases [51, 52].

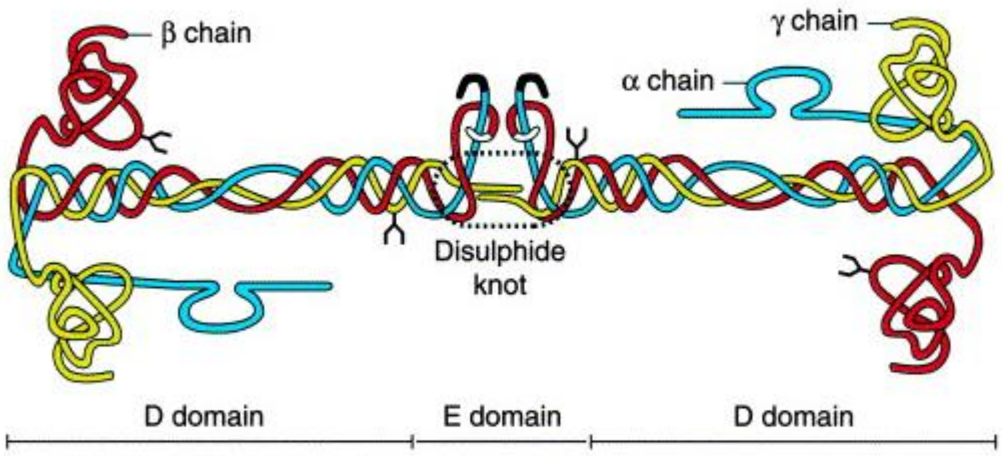

Figure 2.5. Schematic structure of bovine fibrinogen (*adapted with permission from Herrick et.al, 1999*) [53].

Table 2.2: Key physical properties of the different protein studied

Protein	Nature	Molecular Weight (kDa)	Secondary structure	pI (Isoelectric Point)	Function
Bovine Serum Albumin (BSA)	Globular	~66	Mostly alpha-helical	~4.7	Transport protein
Bovine Fibrinogen (BFG)	Globular and fibrous	~340	Fibrous, three-chain structure	~5.8	Blood clotting and hemostasis
Amyloid Beta 40 (Aβ40)	Intrinsically disordered	~4.3	Lacks stable native structure	~5.5	Neuronal function, implication in Alzheimer's disease
Hen Egg-White Lysozyme (HEWL)	Globular	~14.3	Alpha and beta, compact	~11	Bacteriolytic enzyme, immune defense

2.4. Classification and characteristics of protein aggregates

Researchers have classified the aggregates in several ways, but no definite term exists. However, protein aggregates can generally be in vivo, in vitro, amorphous, or fibrillary aggregates. One example is the ordered amyloid fibrils, a fibrillary aggregate experimentally observed in vitro and in vivo. The amorphous aggregates are those of the inclusion bodies, which are also not structurally defined and, therefore, are disordered **(Figure 2.6)**. Some more types of aggregates used and defined by various research groups are chemical (covalent) and non-covalent physical aggregates. Others include reversible and irreversible aggregates, soluble oligomers (small aggregates), and insoluble aggregates [1, 54]. Several research groups have proposed that oligomers and protofilaments formed in the earlier stage of protein fibrillation are more toxic than ordered mature amyloid fibrils [55]. Many experiments related to both disease-causing and non-disease-causing protein aggregates have been studied, and also the early Aβ (1-42) oligomeric species studied through in vivo cell culture have proven the above and are found to be neurotoxic [56-58]. The oligomeric forms like the dimers and trimers of Aβ are found to have adverse effects on the cognitive abilities of rats. Experiments with polyclonal antibodies had shown that they suppress the toxic properties of the soluble oligomers, while no antibody response was seen in the case of the mature amyloid fibrils. Studies on different protein species like α-synuclein, transerythrin and Aβ proposed that cytotoxicity is unrelated to specific protein sequences. Also, the prefibrillar or early aggregate forms of different proteins have been proven to be toxic to cells. It is still unclear how Aβ induces toxicity to the neuronal cells. Still, some significant hypotheses include generating reactive oxygen species, membrane perturbation, GTP hydrolysis, and cell membrane components-induced toxicity [59]. Moreover, the cytotoxicity may have arisen from the fact that numerous amyloidogenic proteins are capable of forming pores on the cell membrane, which might be because of the hydrophobic region of aggregates coming in proximity to the cell surface. Additionally, since the early soluble aggregates are small, they can easily cross cell membranes [60-62]. Typically, the fibril's diameter ranges from about 60-120 Å and is very robust. This robustness can be attributed to the rich β-sheet structure, which forms hydrogen bonds parallel to the fibrillar axis and between the polypeptide chains [63].

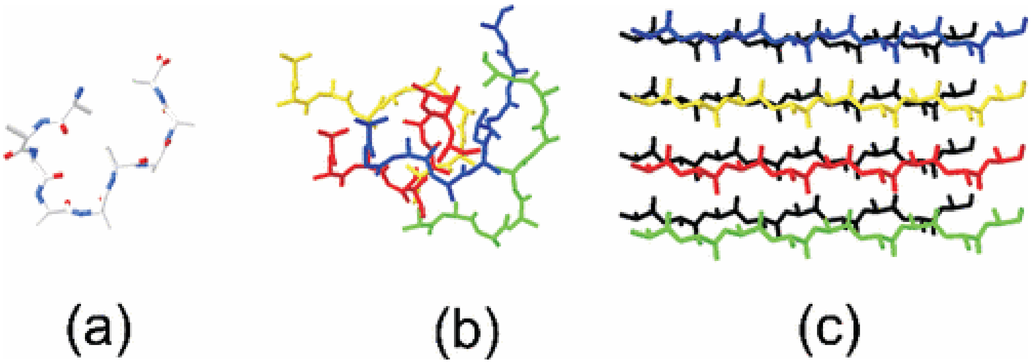

Figure 2.6. Image showing a) native, b) amorphous, and c) amyloid fibril structure (*adapted with permission from Lee, 2009*) [54].

2.5. Physical forces determining protein stability

The spatial arrangement of the constituting atoms determines protein conformation. The conformation a protein obtains in a specific situation or condition is the one with the lowest Gibbs free energy. The spatial fold or arrangement of the atoms in which a protein is functional is the native conformation. It has been discovered that the stability of a protein's conformation was determined mainly by weak interacting forces. Even though the native conformation is functional, the stability is relatively marginal, as seen from the $\Delta G°$ difference of folding and unfolding, i.e. about 20 to 65 kJ mol^{-1} [64]. Therefore, a polypeptide has a high degree to be in several conformations, leading it to be in the unfolded state. This property and the hydrogen bonding interaction from the solvent, i.e., water, dominate the unfolded conformation. But there are forces which counteract these forces. These forces that try to maintain the native state of the protein are the covalent and non-covalent interactions. The covalent force is contributed by the disulphide bonds, whereas the non-covalent or weak interaction includes the hydrogen bond, hydrophobic bonds and ionic interactions. Most proteins do not have disulphide bonds, and extracellularly secreted proteins have them. In the case of intracellular proteins, weak interactions are important as they help fold the primary structure to the secondary and tertiary structures. For a covalent bond to break, about 200 to 460 kJ mol^{-1} of energy is required, whereas only about 4 to 30 kJ mol^{-1} is required to break the weak interaction forces. However, despite this, these weak interaction forces stabilised the protein, as the number of these interactions is much higher than the number of strong covalent forces [65].

2.6. Mechanism of protein aggregation

Protein aggregation can occur in several ways and mechanisms, the most common of which are aggregation through unfolded intermediates, protein-protein self-association or chemical linkage, and chemical degradation **(Figure 2.7)**. The chemical degradation process generally occurs in the non-physiological settings. Protein structures can become unstable and aggregate as a result of chemical deterioration caused by processes including oxidation, deamidation, or non-enzymatic glycation. Extreme pH, high temperatures, or harsh chemical exposure can cause protein degradation in lab or industrial environments, which encourages aggregation through changed or unfolded protein structures. In the physiological condition few process like oxidative stress due to ROS, enzymatic glycation and deamidation can lead to protein denaturation.

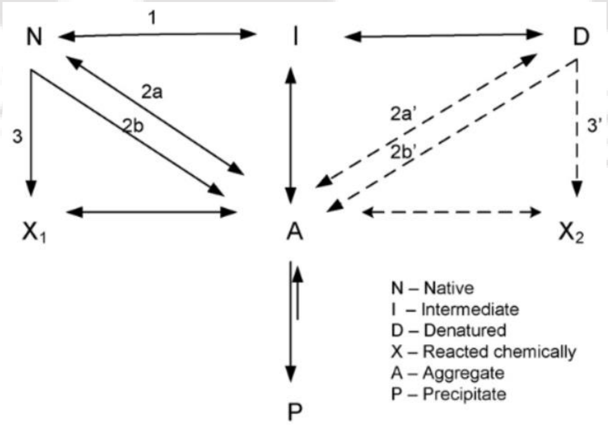

Figure 2.7. Possible protein aggregation pathways (*adapted with permission from Wang et.al, 2010*) [10].

In the case of the unfolded intermediate pathway, there are two probable intermediates, i.e. the native-like and the unfolded-like intermediate. Proteins fully unfolded are not prone to aggregation, whereas the unfolded intermediates are more prone to aggregation because the hydrophobic patches are close. In the case of total unfolded protein, the hydrophobic regions are far apart [66]. In the second type of aggregation pathway, protein monomers self-assemble with one another without forming any intermediates. The driving forces for such pathways are electrostatic, van der Waals and hydrophobic interactions. The aggregate arising from such a route does not have a definite conformation, and the aggregates are sometimes reversible [67]. In the third pathway, chemical linkage results in the aggregation of proteins. For example, disulphide bonds are formed by the free cysteine residues present at the surface. This leads to the further physical aggregation of proteins [68]. The fourth pathway is the most common, i.e. protein aggregation through chemical degradation. This includes oxidation, glycation, amidation, etc. Such a process entirely changed the physical properties of the proteins, such as hydrophobicity, structural conformations, secondary and tertiary structure, thermodynamics of unfolding, etc. [69].

2.7. A simple two-step protein unfolding kinetics

The process of protein folding and unfolding process accompanies the heat change. The heat change or effects can be determined by the enthalpy of the whole process. The enthalpic changes arising from the temperature change are significant in a protein folding and unfolding system. To know the thermodynamic properties of the protein folding and unfolding system, knowing the relationship between the enthalpy and temperature is crucial and can be derived from the equilibrium thermodynamics. For a simple two-step protein unfolding system, the conversion of native (N) to the unfolded state (U),

$$N \xrightarrow{K_U} U \qquad [2.1]$$

The equilibrium constant at a given temperature is given by equation (2.2), and the Gibbs free energy ($\Delta G°$) as a function of temperature T is given by equation (2.3) where k is the equilibrium constant, T_m is the transition temperature, $\Delta H°$ is the enthalpy, ΔC_p is the heat capacity change upon unfolding. The significance of equation number (2.3) is that if we know the parameters, T_m, ΔC_p, $\Delta H(T_m)$, the main thermodynamics parameter could be found easily [70].

$$K(T) = \frac{[U]}{[N]} \qquad [2.2]$$

$$\Delta G°(T) = \frac{T_m - T}{T_m}\Delta H(T_m) + \Delta C_p(T - T_m) + T.\Delta C_p.\ln\left(\frac{T_m}{T}\right) \qquad [2.3]$$

2.8. Different factors inducing protein aggregation

There are several factors which influence the aggregation of a protein or peptide. Some of the main factors are discussed below. Among these factors, effect of protein structure, Ionic charge and pH are physiologically relevant whereas the effect of temperature, chemical agents and process conditions have relevance in in vitro conditions like biopharmaceutical industry, plants etc.

2.8.1. Effect of protein structure

The chemistry of protein structure is one of the main factors that helps identify to what extent or how vulnerable it is to aggregation. The primary structure, the amino acid sequence of a particular protein, could be used to predict the aggregation propensity [71, 72]. Mostly, it is believed and has been shown by various studies that the hydrophobic regions in a protein sequence are the main culprits for forming an aggregate [73]. These amyloidogenic or aggregation-prone regions are mainly buried inside the core of a protein three-dimensional structure. But if it opens up or unfolds by any external criteria, then an aggregation process might proceed. The three-dimensional structure and the secondary structure also influence the aggregation propensity. It is believed that α-helix generally leads to the formation of β-sheet structure, resulting in the aggregation of a protein or a peptide [74].

2.8.2. Effect of temperature

Temperature is among the critical factors that affect the aggregation of a protein or peptide in various ways. It influences several protein properties like its solution condition, rate of diffusion, protein-protein collision, interactions with one another, etc. Temperature also accelerates the rate of protein interaction and aggregation by initiating the unfolding of the native structure [75]. The rate of protein aggregation as a result of thermal degradation can be determined by using the famous Arrhenius relationship ($k = Ae^{\frac{E_a}{RT}}$), where k is the rate constant, T is the temperature in °K, R is the gas constant, E_a is the activation energy, and A is the pre-exponential factor. However, it has been shown that not all types of protein aggregation follow the Arrhenius equation, which is limited to a narrow temperature window [76]. The non-Arrhenius nature of the aggregation process may be because of the changes which arise due to alteration in the stability of the protein conformation, its solubility condition, the effects of change in reversibility and most importantly, the rate of aggregation kinetics [76-78]. Not only does the increase in temperature, but the cold condition also affects the protein by inducing its unfolding and denaturation. Ribosomal protein L9 has been shown to aggregate in cold conditions. The population of cold-enveloped ribosomal proteins increased from 36% to 76% at 25°C and 4°C respectively [79]. Certain monoclonal antibodies have also undergone cold denaturation and precipitation. Cold temperature has been shown to irreversibly oligomerise peptides and proteins and lead to the formation of opalescence in the solution, which is a gel-like opaque substance and also leads to liquid-liquid separation of phase [74, 80-82].

2.8.3. Chemical agents

Proteins sometimes follow numerous chemical denaturation and degradation methods, which affects their secondary structure conformation and stability [83]. This often induces the native conformation to initiate aggregation. Oxidation is one such process that induces the aggregation propensity of proteins and peptides by increasing the hydrophobicity of the surface, enhancing interaction, and destabilising conformation as a whole [84]. Oxidising agents like metals, hydrogen peroxide, etc., are mostly shown to affect the proteins [85]. Other processes, like glycation, glycosylation, deamidation and so on, affect the hydrophobicity, charge, conformation, etc., of a protein and may accelerate or decelerate aggregation depending on the property of the protein and the attacking group [86, 87].

2.8.4. Ionic charge and pH

The colloidal and conformational stability of a protein solution also greatly correlates with the propensity of a protein to undergo aggregation [88]. Now, these factors are directly related to the properties of the solution, like pH, ionic strength, additives or excipients, etc. The isoelectric point and the pka values of the amino acids are given below in **Table 2.3.** In a study with IgG1, a little exposure of the solution (pH 6) to (pH 1) initiates the formation of an unstable unfolded intermediate, which forms aggregates later [89]. The pH of the solution affects the nature of protein interaction among its monomers, the degree of crosslinking with one another, and the nucleation and further growth of the aggregation process [90, 91]. The same goes for the ionic strength, which is highly dependent on the pH of the solution [92]. The effect of ionic strength interfering with the protein-protein interaction and stability of monomer conformation, leading to a fibrillation process, has been shown by researchers in the case of aggregation kinetics [93]. Excipients and additives in pharmaceutical formulations generally inhibit or decelerate the aggregation rate. Still, some sugars like trehalose and sucrose have been found to enhance the aggregation of several proteins like ovalbumin keratinocyte growth factor, etc., [94, 95]. Another substance that impacts the aggregation process of proteins is the surfactant molecule, which, when it undergoes degradation, gives simpler compounds that directly interfere in the aggregation process by inducing the same. Insoluble fatty acids, aldehydes, esters of fatty acids, etc., are some of the smaller products that form as a result of the degradation of the surfactant molecule [96]. In addition, polymers, amino acids like arginine, antimicrobial agents, etc., are also responsible for inducing aggregates [97, 98].

Table 2.3. Isoelectric points and the pKa values of the 20 amino acids [65].

			pKa values					
Amino acid	**Abbreviation/ symbol**	**M_r**	**pK_1 (-COOH)**	**pK_2 ($-NH_3^+$)**	**pK_R (-R group)**	**pI**	**Hydropathy index**	**Occurrence in protein (%)**
Nonpolar, aliphatic R groups								
Glycine	Gly, G	75	2.34	9.60		5.97	-0.4	7.2
Alanine	Ala, A	89	2.34	9.69		6.01	1.8	7.8
Proline	Pro, P	115	1.99	10.96		6.48	1.6	5.2
Valine	Val, V	117	2.32	9.62		5.97	4.2	6.6
Leucine	Leu, L	131	2.36	9.60		5.98	3.8	9.1
Isoleucine	Ile, I	131	2.36	9.68		6.02	4.5	5.3
Methionine	Met, M	149	2.28	9.21		5.74	1.9	2.3
Aromatic R groups								
Phenylalanine	Phe, F	165	1.83	9.13		5.48	2.8	3.9
Tyrosine	Tyr, Y	181	2.20	9.11	10.07	5.66	-1.3	3.2
Tryptophan	Trp, W	204	2.38	9.39		5.89	-0.9	1.4
Polar, uncharged R groups								
Serine	Ser, S	105	2.21	9.15		5.68	-0.8	6.8
Threonine	Thr, T	119	2.11	9.62		5.87	-0.7	5.9

Cysteine	Cys, C	121	1.96	10.28	8.18	5.07	2.5	1.9
Asparagine	Asn, N	132	2.02	8.80		5.41	-3.5	4.3
Glutamine	Gln, Q	146	2.17	9.13		5.65	-3.5	4.2
Positively charged R groups								
Lysine	Lys, K	146	2.18	8.95	10.53	9.74	-3.9	5.9
Histidine	His, H	155	1.82	9.17	6.00	7.59	-3.2	2.3
Arginine	Arg, R	174	2.17	9.04	12.48	10.76	-4.5	5.1
Negatively charged R groups								
Aspartate	Asp, D	133	1.88	9.60	3.65	2.77	-3.5	5.3
Glutamate	Glu, E	147	2.19	9.67	4.25	3.22	-3.5	6.3

2.8.5. Process conditions

Process conditions involve the various steps a protein formulation must go through in the downstream processing steps. This includes mechanical agitation/ shearing, freeze-thawing, drying, pumping, light exposure, etc. [99]. Agitation includes shaking, vortexing, stirring, etc., which gives rise to shearing stress, induces the unfolding of protein monomers and exposes it more towards a more hydrophobic environment, which finally leads to aggregation [100-102]. Other processes like spray drying, pumping the products for capillary filling, freezing and thawing repeatedly, etc., contribute to protein aggregation.

2.9. Significance of shear-induced aggregation study

Shear force or mechanical shearing is one of the factors which is inevitable in the biopharmaceutics industry, and somehow, therapeutic drugs based on proteins and other protein and peptide formulations are bound to be exposed to the shear developed as a result of the bioprocessing techniques done at the refining steps [103]. Moreover, the overexpression of protein on the industrial scale leads to the production of protein in higher concentrations, which enhances the probability of aggregation [104]. Compared to the effects of other external factors on protein, such as pH, temperature, ionic strength, etc., shear-related effects/ causes related to misfolding and protein aggregation are rarely studied in detail [105, 106]. In addition to the above issue, proteins and peptides are exposed to shear inside the physiological body system. Many studies and evidence of amyloid solution experiencing both extensional and laminar flows inside the brain have been published. So, it has been hypothesised that these shear forces could possibly initiate the oligomerisation process of amyloid beta (Aβ) [11]. Also, the aggregates' morphology and kinetics of sheared and unsheared proteins differ. Therefore, such shear forces may be responsible for initiating or inducing the etiology of various neurodegenerative diseases like Alzheimer’s disease, tauopathies, alpha-synucleinopathies etc., [107]. So broadly, the related study of proteins and peptides has two major implications: the bioprocessing industry and the physiological implication, which we have discussed further.

2.9.1. Biopharmaceutical implications

Since the development of the recombinant insulin proteins and approval by the FDA in 1982, there has been a sudden surge in the production of protein-based therapeutic drugs by the pharmaceutical industries. There are over 250 protein drug therapeutics manufactured through bioprocessing industries [108, 109]. Many diseases need the requirement of various therapeutic protein-based drugs to be treated, among which diabetes and cancers of various forms are at the forefront. Protein-based drugs, owing to their small size, greater specificity towards their target and lower toxicity, are more advantageous to other small molecule drugs.

The problem here is the vulnerability of protein to aggregate by various conditions in the upstream as well as in the downstream processing. Factors like pH, temperature, ionic strength and the presence of surfactant molecules can cause aggregation of the therapeutic protein, and apart from this, processing conditions, which involve shaking, stirring, filling and so on, are related to mechanical forces, which involve shearing and tearing. In addition, shear forces can also be experienced in the end processing steps, which are storing, shifting, and delivery, as well as while administering the products to the patients.

Liquid biopharmaceutical products, such as monoclonal antibodies (mAbs), have been found to undergo several stresses associated with handling, delivery and even storage.

Monoclonal antibody production is growing fast as it is highly specific towards its target, so its specificity can be engineered according to the targets of different kinds and for its potency. It is one of the best therapeutic agents for treating cancers and autoimmune diseases. Monoclonal antibodies generally undergo non-native protein aggregation because of the various processing conditions.

These mechanical stresses generally lead to the formation of sub-visible particles in such liquid biopharmaceutical formulations. The freeze-thaw process, which is a part of storing, is also one of the important causes of protein denaturation and aggregation. The aspects of freeze-thaw that need to be monitored are freeze concentrations, ice crystal formation and cold denaturation [110]. Stirring and shaking involved in the processing of mainly liquid pharma products can also lead to a larger particulate formation if an air-water headspace is present [17, 111, 112]. Therefore, protein aggregation of biopharmaceutical products poses serious threats as it can lead to loss of activity and function and induce immunogenicity, rendering drug resistance [113].

2.9.2. Physiological implications

The physiological implications can be discussed in two subsections, one of which concerns the shear arising in the cerebrospinal fluid (CSF) and the other about abnormal thrombosis.

2.9.2.1. CSF and shear

Recent studies revealed that the amyloid beta (Aβ), containing cerebrospinal fluid (CSF) and interstitial fluid, flows through the narrow parenchyma and the perivascular region of the brain. It has been hypothesised that this flow can distort Aβ, which can result in its conformational change. This event may perhaps be one of the initiating events of the devastating disease AD [11]. Brain angiopathy and related conditions can result from the deposition of the peptides on the walls of the arterioles. Both laminar and extensional shear flow have been predicted to be present in these narrow perivascular regions of the brain. Moreover, studies have shown that very moderate shear force is present in the brain's veins and arteriole system, which probably could not break the weakest hydrogen bonds. But, since we are talking about intrinsically disordered proteins such as the Aβ and α-synuclein, these weak forces can easily distort these peptides, exposing the hydrophobic regions [105, 107, 114, 115].

2.9.2.2. Abnormal thrombosis

Many serious deaths in modern developed regions are caused by cardiovascular diseases, which generally result from the aberrant hemodynamic situations in the arteries. The blood flow in the arteries is multiphasic and non-Newtonian pulsatile flow, a combination of a time-dependent varying flow and a mean. Both biochemical and biomechanical factors have a synergistic crucial role in the events of platelets and other thrombogenic factors at a vascular injury site. Adhesive molecules, soluble agonists and extracellular proteins are components of the biochemical factors, and blood shear elements or haemodynamic shear constitutes the biomechanical factors.

The biochemical cascade, which plays a vital role in blood clots and thrombosis, has been vastly studied and investigated compared to the impact of biomechanical shear forces generated in the arteries and veins, which also play a vital role in platelet activation and clotting. The plasma protein, von Willebrand factor, is a crucial protein sensitive to the shear microenvironment and plays a significant role in the process of haemostasis after binding to the glycoprotein receptor of platelet, the GPIbα [116]. This interaction between the protein and ligand plays a key role in thrombosis. In normal haemostasis, the clot formation is confined only to the injury site. In the case of stenotic and aneurysm or diseased site, the thrombogenic cascade spreads and can block the veins or artery. So here, haemodynamic shear plays a critical role in disrupting normal thrombosis by increasing and disrupting the shear rate in and around the vascular lesion, mainly because of the geometry of the stenosis [117].

2.10. Shear-induced aggregation study on proteins

The effects of shear on the induction of aggregation of various proteins involved in numerous physiological processes and drugs are studied using different shearing means and protocols. For example, the shear-induced aggregation leading to the formation of amyloid fibril of human Apo lipoprotein C-II (apoC-II) was studied at different shear rates of 150, 300 and 500 s^{-1} using a custom-built couette cell. It was found that shear increases fibrillation rates up to 5 to 10 fold. The fibrils formed at the lower shear were like twisted ribbons, whereas, at the higher shear rate, the morphology changed to tangled rope-like, as analysed through transmission electron microscopy (TEM). Also, various other techniques like circular dichroism, intrinsic tryptophan fluorescence, and Thioflavin T assay were used to analyse the aggregation, showing that the aggregates were irreversible [118]. In another study by Dave E. Dunstan et al., the amyloid beta solution was sheared or agitated in two different ways, i.e. by normal magnetic stirrer and shearing using a Couette cell. The aggregation rate, monitored through Thioflavin T assay, accelerated in the case of Couette shearing compared to the stirring using magnetic beads.

Atomic force microscopy (AFM) analysis indicates the growth and entwining of fibril morphology with time. From circular dichroism spectroscopy, the peptide conformation was changed from random coil to α helix to a β-sheet-rich structure [114]. Elisabeth K. Hill et al. study the in vitro fibrillation of β lactoglobulin using a novel couette cell with varying shear rates. The fibrillation process monitored through real-time fluorescence shows the formation of spheroidal seed-like species, which enhances the further aggregation process. Also, it was implicated that the preformed fibrils disintegrated when exposed to higher shear rates [119]. Vivek Sharma et al. studied the bulk and interfacial viscoelastic properties of the globular protein BSA by employing a stress-controlled torsional rheometer and a microfluidic rheometer and interfacial measurements. The protein solution has been reported to have a solid-like behaviour, even at very low concentrations of 0.03% by weight. Because of this, the solutions show a yielding effect and a shear-thinning response. This property may have arisen from the formation of thin films by the adsorbed protein at the solution and air interface [120]. In another study, the adsorption and aggregation of protein molecules were correlated with the rise in viscosity and shear yielding. This study used a highly sensitive rotational and surface rheometer with a double-walled ring to test the rheological properties of BSA and IgG1 monoclonal antibodies, which have considerably high molecular weights. It was shown that there was an interfacial viscosity contribution in addition to the bulk viscosity in the case of the surfactant-free BSA.

Bulk viscosity of a fluid is the viscosity in the bulk phase, away from any interfaces. It is the internal resistance to flow inside the entire volume of a solution or suspension. Whereas, interfacial viscosity is the viscosity at the interface between two phases, like the liquid-solid boundary or the air-water contact. In systems where proteins or other molecules build up at surfaces to form a separate layer, interfacial viscosity is very important. Increased interfacial viscosity from protein adsorption at an interface may aid in the stabilisation and development of ordered structures like thin films or fibrils [121].

For the surfactant-rich IgG1 protein solution, the interfacial viscosity contribution was found to be negligible. Here, the formation of films in the solution air interface contributes to the apparent increase in the bulk viscosity. Also, steady shear viscosity was analysed at around $1s^{-1}$, which contributes much information regarding the protein solution's stability and was seldom reported in much literature [122].

Most studies on shear-induced aggregation of proteins were conducted using either a stirrer, which generates uncontrolled shear, or the Couette cell. Recently, the synergistic effects of shear on the aggregation of proteins were explored. A recent study by Grigolato *et al.* revealed the synergistic effect of solid-liquid interfaces and hydrodynamic flow in the flow-induced aggregation of immunoglobulin IgG1 [123]. Similarly, a combination of thermal and mechanical treatment in a closed cavity rheometer resulted in increased reaction rates and, therefore, a higher degree of aggregation of β-Lactoglobulin [42].

2.11. General types of flow for studying protein aggregation

The general shear fields employed in shear experiments are the extensional and the simple shear flows **(Figure 2.8).** The extensional flow is also a stretching flow described by a linear velocity gradient. Here, the strain rate remains constant. In the case of simple shear flow, it is characterised by a velocity gradient which is perpendicular to the flow. It can be thought of as a combination of a rotational and an elongational flow. When subjected to the rotational flow, protein solution experiences total body rotation but no hydrodynamic shear strain, whereas proteins are stretched when exposed to an extensional flow. The hydrodynamic stress from the shear field is believed to denature the protein conformation, leading to its aggregation. For a fluid following Newtonian behaviour, the relationship between the stress and the shear rate (velocity gradient) mathematically is given as:

$$\tau = \eta \dot{\gamma} \qquad [2.4]$$

Where τ denotes the shear stress, η denotes the viscosity, and $\dot{\gamma}$ denotes the shear rate. A tangential stress of the above type is termed shearing, in which very small, thin layers of fluids slide over one another in a laminar fashion. The unit of stress is force per unit area (N m^{-2}), and the unit of the viscosity and shear rate are Pa. s and s^{-1}, respectively. The stress here is the hydrodynamic drag force, which acts on the solution of the protein under study. Also, the dissipation energy produced from the shearing of a protein solution can be calculated from the product of the square of the shear rate and the viscosity of the sheared solution ($\dot{\gamma}^2 \times \eta$). This dissipation energy relates to the Gibbs-free energy of unfolding the protein.

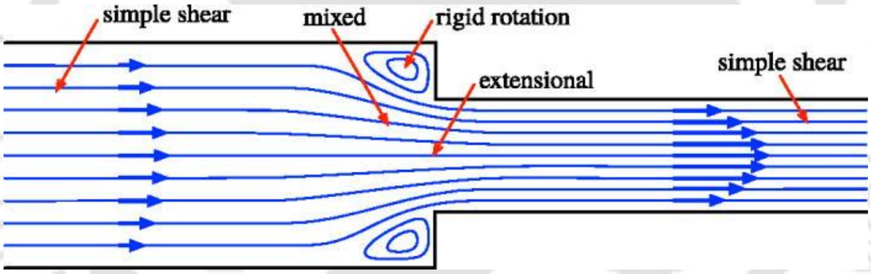

Figure 2.8: A classic illustration of nonviscometric flow is the channel flow through a contraction. A stiff rotation at the centre of the vortices, shear flows distant from the contracting zone, extensional flows near the centerline of the contracting region, and mixed flows in the intermediate regions are all comparable to the gradient of the velocity field in such a steady flow [124].

2.11.1. Instruments/ machines for generating shear flow

Generally, protein shear experiments use devices that create uniform flow or heterogeneous flow patterns (by stirring, shaking, vortexing, etc.). Experiments under uniform shear flow or velocity gradients are much more favourable and quantifiable, providing accurate stress for interpreting various flow properties. The most commonly used experimental devices for protein shear study are capillary and rotational. In the case of a capillary flow device, the sample solution is passed through a channel or tube of known dimensions by generating a pressure difference between the ends. In rotational devices, shear stress is applied to the protein solution in a narrow gap. Some commonly used rotational devices or geometries are shown in (**Figure 2.9.**). All these devices have two parts: the upper movable and the lower fixed portion. These devices are parts of a machine known as the rheometer, a very useful instrument for measuring a material's rheology, i.e., how a material or fluid deforms as a function of force, time and spatial orientation. Some techniques that can be measured using a rheometer are discussed as follows.

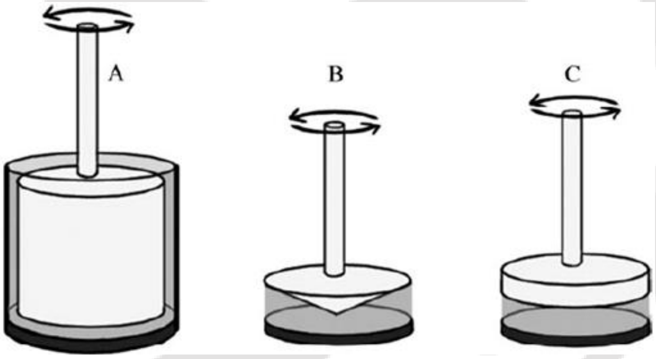

Figure 2.9. Commonly used rotational flow geometries or devices. (A) concentric cylinder (B) cone and plate (C) parallel plate [105]

2.11.1.1. Single point measurements

Viscosity is measured in constant settings in a single-point measurement.

2.11.1.2. Flow curve and viscosity measurement

Here, the sample is subjected to a shear ramp, and correspondingly, the viscosity is recorded. The plot of shear stress vs the shear rate is termed the flow curve, whereas the plot of the viscosity vs the shear rate is called the viscosity curve.

2.11.1.3. Temperature ramp test

In the temperature ramp test, the viscosity of protein solution as a function of increasing temperature can be determined by keeping the shear stress or the shear rate constant.

2.11.1.4. Oscillatory test

This test examines viscoelastic materials of all types, from very low-viscosity liquids to rigid solid materials. The LVR is the Linear Viscoelastic Region. It denotes the range of applied stress or strain when the response of a material stays linearly proportionate to the stress or strain. In this area, the material exhibits predictable behaviour: doubling the stress or strain results in a corresponding doubling of the reaction.

The first step for determining the linear viscoelastic region is the amplitude sweep test, where the frequency of rotation is held constant. In contrast, the amplitude or the strain percent is varied. In a region where the amplitude is not too high, the sample or the material being tested remains unchanged or not deformed, as can be seen from the rheological material value function, i.e. G′ (the storage modulus) and the G″ (the loss modulus) remains independent of the amplitude. Then, to further examine the properties of the substance, a frequency sweep test is conducted within the linear viscoelastic region determined earlier. In this test, the frequency is varied by keeping the LVE strain constant. This test can be applied to protein solutions when being aggregated. Because it specifies the circumstances under which a material's rheological characteristics can be precisely described without changing its structure, the LVR is essential. Larger strains could harm or disturb the internal networks of soft materials like gels, polymers, and biological samples, therefore this is especially crucial. It can be used for determining material stability, for comparing materials, characterizing viscoelastic properties, predicting processing behaviour etc.

2.12. Protein aggregation inhibition strategies

Several methods have been employed to inhibit protein aggregation, including protein mutation to stabilise the native structure and the widely studied addition of excipients or small molecules (**Table 2.4.**) to the protein solution. The protein aggregation inhibitors can inhibit the aggregation in various ways, including reducing the toxicity of aggregate species, inhibiting or arresting the aggregate species to prevent further fibrillation, disintegration or clearing of the aggregates, etc. Some of the different strategies in which the inhibitors work is attenuating protein production, which can misfold by acting at post-translational modification steps, which include phosphorylation of proteins, proteolysis, etc. The second is blocking the pre-conformational changes of monomer by binding and stabilising and also blocking at another critical step, such as the nucleation phase or by binding at already formed fibril to attenuate further process. Third is by disaggregating the already formed aggregates. The fourth is targeting the ill consequences of protein aggregation. This is possible by converting the aggregate species to nontoxic forms by attenuating signalling pathways triggered by aggregate moieties, which can lead to inflammation. Some of the small molecule excipients, such as metal ions, plant polyphenols, vitamins, nanoparticles, and so on, have been studied profusely, and here, some of the widely accepted types were discussed.

2.12.1. Amino acids

Amino acids such as Glycine, Proline, and Arginine have been used to prevent the aggregation of proteins in various conditions. Arginine has been frequently used for studies in protein aggregation inhibition and protein surface interactions, generally during the protein refolding and purification process. The mechanism of action has been explained in terms of its effects on the water, its interaction with peptide bonds and the side chain of amino acids and the preferential binding with protein [125]. In another instance, arginine was shown to inhibit the aggregation of a chaperone protein β-casein, which was also found to be involved in breast amyloidosis [126]. Amydated amino acids are used to inhibit protein aggregation. In one such study, amydated glycine inhibited lysozyme protein aggregation. X-ray crystallographic studies found that the amydated glycine binds near the aromatic amino acid residues on the surface, leading to decreased bound water, thereby increasing protein mobility. It was proposed that shielding the hydrophobic patches may be the reason for preventing the aggregation [127].

2.12.2. Polyphenols

Many protein aggregation inhibition studies have profusely experimented with polyphenols as small molecule inhibitors. Since Resveratrol and epigallocatechin-3-gallate (EGCG) have been known to inhibit Aβ (1-42) fibrillation, a molecular dynamics simulation study was performed with both of these compounds and Aβ (1-42) dimers and the protofibrils. Their results show that both these molecules can bind the monomer of Aβ (1-42) and thus inhibit the dimerisation process. The major binding forces involved between EGCG and Aβ (1-42) were π-π stacking, hydrophobic and hydrogen bonding and between resveratrol and Aβ (1-42), π-π stacking was the major force. Both molecules could disrupt the β-sheet-rich fibrillar structure and the salt bridges [128]. Another compound, hesperidin, a bioflavonoid, was tested for its anti-aggregation property against insulin aggregation. Hesperidin was found to inhibit insulin aggregation at 20 and 50 µM concentrations. In the presence of the compound, the transition of the α- helix secondary structure to the β- sheet structure decreased, and the hydrophobicity decreased; both were reversed in the control sample without hesperidin. The aggregates also showed dose-dependent toxicity towards neuronal cell line SH-SY5Y, wherein hesperidin could prevent the toxicity [129]. In another study, luteolin, a flavonoid, inhibited the aggregation of human lysozyme. The inhibition mechanism was explained through three points. The first was the presence of numerous aromatic groups, which can hinder fibrillation; the second was the antioxidant property delivered by the presence of consecutive hydroxyl groups; and the third was the antiglycation property [130]. Focusing on the inhibition of α-synuclein aggregation, hybrids of Quinone acids were designed and synthesised in a study. α-synuclein aggregates, as we know, form the main components of the Lewy bodies, which are responsible for the deterioration of dopaminergic neurons leading to Parkinson's disease. The synthesised compound could inhibit the aggregation at a low IC_{50} value of 1.6 µM. It was found to stabilise the monomeric α-synuclein proteostasis and block the aggregation at the lag phase [131].

Various amide derivatives of ferulic acid were synthesised and checked for their anti-aggregation (anti-oligomeric and anti-fibrillar) properties on AD pathologies. The most potent was the azetidine attached and triphenyl derivatives with an IC_{50} value of 1.8 uM for inhibiting oligomer, and about 21% fibrillation inhibition was obtained [132].

Additionally, ellagic acid, another polyphenolic compound, inhibited α-synuclein aggregation and could reduce α-synuclein oligomers and fibrils-induced cytotoxicity [133].

Another study studied the EGCG effect on the co-fibrillation of Aβ (1-40) and Aβ (1-42) through a molecular dynamics approach. EGCG could attenuate the dimerisation of the above peptide by obstructing interchain formation between the two. The prominent binding forces involved between the polyphenol and the peptides were hydrogen bonding, π-π stacking and cation-π interaction, and the residues involved were mostly polar and aromatic. Additionally, EGCG could impede the co-fibrillation of the peptides [134].

2.12.3. Nanoparticles

There has been growing research on nanoparticle-based protein aggregation inhibitors, as nanoparticles provide enhanced efficiency compared to inhibitors used alone. On such note, many researchers have studied nanoparticle-based anti-aggregation compounds. One example is a study where osmolytes such as Proline, Glycine and Hydroxyproline were coated on thermos and thermostable gold nanoparticles. These nanoformulations were observed to inhibit both seed-induced and spontaneous aggregation of insulin. Unlike the indirect solvent-mediated protection of the osmolytes alone, these nanoformulations directly interacted with aggregation-prone, exposed regions [118].

In another study, copolymeric nanoparticle N-isopropyl acrylamide: N-test-butyl acrylamide (NiPAM: BAM) of different hydrophobicity were tested for the aggregation inhibition capability on the Aβ aggregation. The surface properties of these nanoparticles hindered the Aβ aggregation in the nucleation phase. The lag phase was found to increase, which was found to correlate with the amount and surface property of the nanoparticles. These nanoparticles interact with the monomer and the oligomer of Aβ and, to a certain limit, can also halt and reverse the further formation of fibrils [135].

Another nanoparticle inhibitor was synthesised, and the protein was used to cap it. Two formulations that showed tau aggregation inhibition in vivo were protein-capped iron oxide nanoparticles (PC-Fe_3O_4) and protein-capped cadmium sulphide nanoparticles (PC-CdS). The iron oxide-based nanoparticle could inhibit aggregation, but it does not hinder the viability of the neuroblastoma cells. The CdS-based protein capped, on the other hand, could inhibit and disintegrate the aggregates [136].

Another Nano formulation uses green tea polyphenols to cap silver nanoparticles, which showed enhanced aggregation inhibition and reduced cytotoxicity of two proteins, α synuclein and human insulin aggregates. Here, an enhanced property is also observed when capped on nanoparticles compared to when free polyphenol was used. The enhanced property of the GTP-AGNPs was attributed to the surface-by-volume ratio, which increased the binding probability towards the aggregates and the antioxidant property. With different proteins, the inhibition mechanism was also reported to be different. For instance, in the case of fully structured insulin aggregation, it inhibits the process by binding and stabilising the native protein, whereas, in the case of intrinsically disordered proteins, like α-synuclein, it redirects the aggregation towards off-pathway nontoxic species [137].

Another study synthesised a metal phenolic network using EGCG and Zn II (MPN). This was then conjugated with a gold nanoparticle MPN@AuNp construct. When coated over the nanoparticle, it was reported that its efficiency to inhibit Aβ aggregation and toxicity was enhanced in vitro. This property was better than when EGCG was used without the metal network. This was attributed to the enhanced porosity and larger surface area of MPN compared to using EGCG alone on AuNp [138].

Next, a polymer polyvinyl pyrrolidone**,** in conjugation with polyphenol, curcumin and this conjugate in conjugation with gold nanoparticle, was checked for its inhibitory action against hen egg white lysozyme (HEWL) protein. These conjugates showed anti-aggregation properties at 31 µg/ml for C-PVP and 30 µg/ml for C-PVP-Au [139].

Another polymer-based Nano formulation used polyvinyl pyrrolidone conjugated with quercetin, a polyphenol. This formulation (Q-PVP) was then tested in an Aβ (1-42) mutant of

Drosophila melanogaster. Through the crawling and climbing test, an improvement in motor activity was reported. This mutant has typically dark-pigmented, narrow and small eyes. A change in the phenotype was reported to be observed, correlated to the disintegration and clearance of the amyloid plaque [140].

Curcumin, a known amyloidogenic bioactive molecule, was used to prepare Nano formulations to increase its bioavailability. A water-stable and polar polymeric nanoparticle was prepared using PVP, and curcumin was encapsulated inside. This Nano-formulation (PVP-C-AuNp) was then used against Aβ (1-16) peptide aggregation, as it is known for aggregation through seeding in healthy brains. The formulation was reported to inhibit aggregation and disintegrate them, as observed from NMR spectroscopy and TEM analysis [139].

An already-known amyloidogenic sugar, trehalose, was used to prepare Nano formulations with gold nanoparticles. This trehalose functionalised gold nanoparticle inhibited a mutant protein containing polyglutamine inside the neuronal cells. This conjugate enhanced cell viability by inhibiting protein aggregation [141].

2.12.4. Peptides

For inhibiting the aggregation of the core sequence of amyloid beta or the aggregating peptide (AP) as they have been named, peptide inhibitors were synthesised, focussing on the recognition and β breaking element in the inhibitor sequence. The inhibitor peptide (IP) was reported to inhibit the AP fibrillation by binding the corresponding region of AP by the recognition unit present in the IP through intermolecular hydrophobic bonding.

For this PI was created having both recognition and β-breaking sequence. A bent unit was attached in situ, to function as the disruption moiety. This bent unit was created by forming cyclic peptide, using the "O → N acyl migration" approach. For the recognition unit, phenylalanine residue (FF) was used as recognition unit. The presence of residue in the IP, which can form cyclic dipeptide in situ, which probably can break the β-sheet region, helps in the inhibition process. The mechanism of cyclic dipeptide formation was based on the concept of the O to N acyl migration and then the nucleophilic attack of serine to the succinamide carbonyl group to form the cyclic peptide [142]. Next, a serum-stable, nontoxic heptapeptide (*KR7 (KPWWPRR*-NH2)) was synthesised against insulin aggregation. Through various biochemical and spectrometry techniques, the peptide was reported to target the elongation step of fibril with a minimum impact at the lag phase [143]. Another peptide-based inhibitor for Aβ fibrillation was synthesised using the C terminal sequences of the peptide Aβ (38-40) and Aβ (40-42). These peptide inhibitors were reported to inhibit the Aβ (1-42) fibrillation and its toxicity towards neuronal cells. One of the inhibitors showed the highest per cent viability of 94.3 % at just a concentration of 2 μM. The absence of β-sheet-rich secondary structure formation was also reported to be halted, as observed from CD and TEM analysis [144]. In another study, 38 tetra-peptides derived from the Aβ (39-42) C terminus region were synthesised to inhibit the Aβ aggregation. These peptide inhibitors could attenuate Aβ (1-42) aggregation as demonstrated by various techniques, including CD, ANS, TEM, etc. Properties like enhanced activity, proteolytic stability and enhanced blood-brain barrier permeability were attributed to using unnatural amino acids on the peptide inhibitor sequences [145]. Peptide designs based on the aggregation-prone sequence are one of the frequently used techniques. A peptide inhibitor was reported and rationally synthesised based on the aggregation-prone region of an amyloidogenic protein, hen egg white lysozyme (HEWL). The hexa-peptide (Y-P-Q-I-P-N) was reported to inhibit HEWL with 70 % aggregation at acidic (pH 2.2) and about 50% inhibition at nearly neutral (pH 7.5). The mechanism was based on monomeric protein stabilisation where the inhibitor peptide binds the aggregation-prone region, including the residues W_{62} and W_{63}, halting conformation change towards the fibrillar structure [146].

2.12.5. Molecular tweezers

Researchers have shown that the aggregation of α-synuclein can be controlled kinetically through the reconfiguration rate of the unstructured protein chain. So, if the reconfiguration occurs fast, the aggregation rate will automatically be delayed. Therefore, to control the kinetics towards slowing the aggregation rate, molecular tweezer CLR01 could bind selectively to the side chain of the lysine residue. Through fluorescence and mass spectrometry analysis, an increase in the reconfiguration rate was observed with the increase in the molecular tweezer concentration. Also, the inhibitor is mainly bound at the N terminal region, with residues L10 and L12 [147].

CLR01 molecular targets the Lysine and Arginine residues, and many studies have employed these molecular tweezers for fibril inhibition. In one such work, CLR01, the mechanism of how this molecular tweezer binds to various proteoforms of α-synuclein have been studied. Through native mass spectrometry analysis, CLR01 was found to bind with the α-synuclein bound with copper and manganese ions, and α-synuclein phosphorylated at serine 129 residue. Through Electron capture dissociation (ECD) with Fourier transform-ion cyclotron resonance (FT-ICR) top-down (TD) mass spectrometry of the molecular tweezer –α-synuclein complex, the exact location was reported to be at the N terminal region. The binding of CLR01 leads to the compactness of the monomer structure of α-synuclein, which explains the attenuation of aggregation of α-synuclein to form oligomers and fibrils [148]. Another work on CLR01 reported its aggregation inhibition capability on islet amyloid polypeptide (IAPP), the causative peptide for type two diabetes. Despite having only one lysine residue at position one of IAPP, it was reported to inhibit the aggregation at sub-stoichiometric concentrations. For efficiently attenuating the aggregation, excess of the molecular tweezer is required. Various biochemical, spectroscopic and computational analyses showed that, at low CLR01 concentration, it binds to the Lysine at residue one, nucleating the non-amyloidogenic, toxic structures and at an excess concentration of CLR01, it binds the Arginine at position 11, halting the formation of non-toxic structures [149]. Based on the ground knowledge that phosphate-substituted molecular tweezer 1a (having lithium methane-phosphonate moiety) binds primarily to the lysine residues of α-synuclein and Aβ (1-42) aggregation, four modified, water-soluble molecular tweezer 1a were synthesised by substituting different groups. The groups added were phosphate, methane phosphate, sulphate and O-methylene carboxylate moiety. These modified molecular tweezers were found to bind the Lysine and Arginine residues of peptides and proteins through fluorescence, ITC and NMR techniques [150].

2.12.6. Polymeric inhibitors

Another class of small molecular protein aggregation inhibitors is the polymeric inhibitors. The use of polymeric inhibitors is very recent, even though it has tremendous potential [19]. Some of its properties, which make it an excellent candidate for inhibition study, can be attributed to its molecular weight, which can be easily modified, its flexibility, surface charge, etc. A few examples of polymeric inhibitors include (polyethylene glycol) PEG compounds, pullulan nanogels, Late embryogenesis abundant (LEA) proteins, glycopolymers, polyelectrolites, etc. PEG has been used in biomedical applications to enhance biocompatibility and solubility, change circulation time, and so on [151, 152]. In various studies, thermal aggregation of HEWL was found to be suppressed by PEG-derived inhibitors such as the monodispersed triangular PEG and by functionalising the Nanochannels of soft nanotubes in combination with PEG [153, 154]. Further, pullulan-based nanogels have been used to protect proteins like chaperones [155]. Also, LEA proteins have been used for protein aggregation inhibition and protection.

They are generally disordered in structure, have low molecular weight and are hydrophilic. In a study, LEA proteins showed anti-aggregation inhibition properties on heat-induced citrate synthase aggregation and lysozyme aggregation [156, 157].

Table 2.4. List of small molecule inhibitors

Type	**Inhibitors molecule**	**Studied protein**	**Mechanism of action**	**Effect on neuronal cells**	**Refs.**
Amino acids	Glycine, Proline, Arginine	B casein, lysozyme, Aβ (1-42)	Hydrophobic prone region masking through hydrophobic interaction	Moderate toxic	[158]
Polyphenol	Quercetin, EGCG, Resveratrol, Ellagic acid	Aβ, HEWL, Lysozyme, α-synuclein	Anti-oxidative stabilisation through Quinone derivative formation	Non-toxic	[159-161]
Peptides	PMet, DRI-SAA1-5	Aβ (1-42), insulin, calcitonin, human serum amyloid	Fibril interaction through hydrophobic and п-п stacking	Non-toxic	[162, 163]
Metal ions chelators	Cyclen macrocycle, Ruthenium(II) polypyridyl complexes, 2-amido-3-hydroxy pyridine-4(1H)-ones	Aβ	Through chelation of metal ions such as Cu2+ and Zn2+, Fe3+	NA	[164-166]
Nanoparticle	C-PVP-Au (curcumin-polyvinyl pyrrolidone gold nanoparticle), Proline-coated gold nanoparticle	Lysozyme, insulin	Interaction with the hydrophobic aggregation-prone region	Non-toxic	[167, 168]
Polymeric inhibitors	N-acetylpyrazoline based, PEGylated Block Copolymer	Aβ	β sheet breaking	Non-toxic	[169, 170]

Molecular tweezer	CLR01, 1a	Aβ, α-synuclein, HEWL, Huntingtin Exon-1	Through binding of positive amino acid residues like K and R	Non-toxic	[171, 172]
Osmolytes	Raffinose, betaine	Insulin	Disintegration of amyloid fibrils	Non-toxic	[19, 173]
Vitamins	Vitamin K3 analogues, Vitamin A, Folic acid, Vitamin B12	Aβ, Tau	Through the binding of monomers as well as fibrils, the formation of non-toxic aggregates	Non-toxic	[174-176]

2.13. Protein aggregation inhibition study through phytochemicals

The prevention of protein aggregation through phytocompounds has recently been investigated extensively [177-180]. This plant-based technique of inhibiting protein aggregation has numerous advantages over other approaches. Naturally occurring chemicals derived from different plants, such as polyphenols, were studied to prevent, heal, and minimise diseases such as cancer, neurological pathologies, diabetes, and cardiovascular diseases [181]. Polyphenols can interact with proteins and peptides and thereby enhance biological activity. Peptide and protein misfolding and aggregation are the root causes of proteopathies, which include Alzheimer's, Parkinson's, and Huntington's illnesses. The initial stages of these conditions result in the development of protein-protein and peptide-peptide interactions. Therapeutic intervention may be possible if tiny phytochemicals interact with proteins and peptides, which can impact these early interactions [182].

A study on preventing hen egg white lysozyme aggregation with curcumin and kaempferol through flourescence quenching experiments and molecular dynamics simulation studies shows that both could prolong the nucleation phase. They have shown that these polyphenols bind to the region responsible for forming the core amyloid fibril [180]. However, the two compounds couldn’t control the aggregation once the nucleus was formed. In another study, Eugenol, a polyphenolic compound, was shown to suppress the spontaneous and seed-induced amyloid formation of insulin and BSA. Through isothermal titration calorimetry (ITC) binding studies, Eugenol was found to interact with insulin in a single binding site [183]. Natural polyphenol Rottlerin was also found to inhibit fibrillation of insulin, lysozyme and Aβ (1-40) peptide at very low concentrations, observed through circular dichroism (CD) spectroscopy, fluorescence and atomic force microscopy studies. In these studies, it was hypothesised that Rottlerin might have interacted with the proteins' amyloidogenic region. Additionally, it was shown that Rottlerin could disassemble pre-formed fibrils [184]. A further study found a hydrophilic fraction of *Centella asiatica* to prevent the fibrillation of transthyretin through TEM analysis and other studies. The presence of phenolics and terpenoids was thought to be the reason behind its property [185].

Plumbagin, a plant-derived compound, effectively attenuated the thermally induced aggregation of insulin and serum albumin. It interacts with the protein structure and stabilises it through strong hydrogen and hydrophobic bonds. Not only does it prevent aggregation, but it was shown to disintegrate the already-formed fibril structure [186]. In another study, α synuclein aggregation was found to be inhibited by extracts of *Ocimum sanctum* through numerous biophysical and biochemical assays. In addition, it was shown to have neuroprotection ability from α synuclein aggregate-induced toxicity of the Neuro2a cell line [178]. Secondary metabolites obtained from *Lawsonia inermis, Punica granatum* and *Pistacia lentiscus* inhibited Aβ (1-42) fibrillogenesis by preventing the transitions of β-sheet amyloid fibrils. *Lawsonia inermis* was found to be the most active extract as it could decrease the toxicity and reactive oxygen species (ROS) generated as a result of the aggregates of Aβ (1-42) [187]. Similar neuroprotection and fibrillogenesis prevention was shown by *Allium roseum* on the aggregation of Aβ (1-42) [188]. *Syzygium aromaticum*, commonly the clove, was also shown to protect neuronal cell line SH-SY5Y from hydrogen peroxide-induced stress. The extract could attenuate the ROS levels and restore the mitochondrial membrane potential. It could also deter lipid peroxidation and has anticholinesterase activity, anti-glycation and anti-fibrillation activity of Aβ fibrillation [189].

Protein aggregation, oxidative stress, and inflammation are the main characteristics of neurodegenerative diseases inside the central nervous system (CNS). Many biological processes and functions are hindered or affected, like insufficient synthesis of neurotransmitters, abnormal protein degradation by ubiquitination, oxidative stress and, among others, deterioration of the blood-brain barrier (BBB), leading to various cognition-related diseases [190, 191]. Many metal ions, including Cu, Zn, Fe, and other transition metals, have been studied regarding protein aggregation inhibition, which has positive and negative impacts. Certain amino acids like glycine and proline have been shown to inhibit the aggregation process and, in some cases, reduce the process. In an attempt to produce therapeutic drugs for treating Alzheimer's disease, various interacting partners of Aβ, like metal ions, receptors like receptors for advanced glycation end products (RAGE), various membrane components like gangliosides, etc., have been studied in vitro. It was found that both Cu and Zn had shown a dual effect on Aβ aggregation. It is, therefore, critical to focus on various metal chelators and compound stabilisers to inhibit or prevent neurodegeneration [192]. Also, in recent times, through numerous researches, various kinds of synthetically prepared drugs have come to the market for treating neurodegenerative diseases like Parkinson's disease, Alzheimer's disease, chronic illnesses, etc. However, these products have heavy side effects that the body must tolerate. Among many other inhibitors, various neuroprotective plants, like *Centella asiatica*, *Bacopa monnieri*, *Withania somnifera*, etc., have been shown to reduce the aggregation of amyloids. However, none of the above-mentioned inhibitors have been studied with shear-induced protein aggregation. Also, in other aggregations induced by other physiological parameters, the mechanism of action has not been properly studied.

Therefore, it has become imperative for researchers to focus on plant extract for its properties against protein aggregation and cognitive enhancement. One more advantage of using phytochemicals or plant-based natural compounds for treating such diseases is that they have potential therapeutic characteristics as they are natural antioxidants and anticholinesterase, have anti-inflammatory properties, and are negligible or have fewer side effects. The myriad properties of plant extracts against protein aggregation are because of the presence of the phytochemicals, mainly polyphenols. Some of the polyphenols which have been used in the inhibition of protein aggregation studies are listed in **Table 2.5.**

In this thesis work, the extracts of a nootropic plant, *Centella asiatica*, will be checked for its ability in shear and thermally induced aggregation of proteins. The next section discusses the literature review regarding *Centella asiatica* in cognitive enhancement and neuroprotection.

Table 2.5. Polyphenols and their action against protein aggregation.

Polyphenols	Plant source	Protein /peptide	Mechanism of action	Ref.
Baicalein	Scutellaria baicalensis, Scutellaria lateriflora	Tau, superoxide dismutase 1 (SOD1)	Inhibits Tau assembly through off-pathway oligomers as well as dissolves Tau PHFs	[193, 194]
Myricetin	Berries, tea, nuts	Aβ (1-42), α-synuclein, superoxide dismutase 1 (SOD1)	Inhibition of oligomerisation, delaying the liquid-to-solid phase transition of α-synuclein, stabilisation of protein	[195-197]

			interface destabilises the fibril	
Ferulic acid	Mostly fruits, oats, pineapple, wheat	Aβ (1-42), Aβ (1-40), β-lactoglobulin	Halting fibril formation, elongation, monomer stabilisation	[198, 199]
EGCG	Tea	Aβ (1-42)	Monomer stabilisation through hydrophobic, hydrogen and π-π stacking interactions	[128]
Quercetin	Wine, berries, citrus fruits, tea, parsley	Islet Amyloid Polypeptide (IAPP), superoxide dismutase 1 (SOD1), prion protein	Disaggregation of preformed IAPP fibrils via shifting of fibrillar-monomeric equilibrium shifting, binding to fibril species of SOD1 and arresting further extension	[194, 200, 201]
Curcumin	Rhizome of curcuma longa	α-synuclein	Halts further extension of the oligomeric state, binds to aggregate species to attenuate further process	[202, 203]
Resveratrol	Apple, peanut, blueberries, plum	Aβ (1-42)	Monomer stabilisation through π-π stacking interactions	[128]
Chlorogenic acid	Plants, green coffee	Aβ (1-40), Aβ (1-42)	Blocking β-sheet formation by caffeoyl group	[204, 205]
Ellagic acid	Cranberries, blackberries, strawberries, pomegranate	Amyloid beta, α-synuclein	Reducing solvent-exposed hydrophobic surface, formation of off-pathway aggregate species, stabilisation of monomer	[133, 206]
Hesperidin	Citrus fruits	Insulin, hen egg white lysozyme (HEWL)	α-helix structure stabilisation, monomer stability	[129, 207]

2.13.1. *Centella asiatica*

Centella asiatica **(Figure 2.10)** is an herbal medicine that has been used mostly in Asian countries for hundreds of years. In the ancient Ayurvedic medical book (Caraka Sumita), *Centella asiatica* has already been specified as herbal medicine for treating dementia [208]. Today, people have used these plants in various forms for cognitive enhancement. This plant contains pentacyclic triterpenes, like Asiatic acid, Asiaticoside, Madecassic acid and Madecassoside. Earlier studies have shown that it has anti-inflammatory, antioxidative (like free radical scavenging, reduction in lipid peroxidation, etc.), anticancer, anxiolytic and memory enhancement properties [209, 210].

Centella asiatica extracts were evaluated for their impact on memory power and learning abilities in rats using different conditions. Here, normal rats were used to provide predictive conclusions related to human patients suffering from Alzheimer's and dementia. It was shown that the aqueous extract of the whole plant has two distinct, profound effects: the capability to enhance learning and memory power. This was because of the antioxidant property of *Centella asiatica*, which decreases lipid peroxidation by boosting the already present antioxidant enzymes in the central nervous system [211].

Figure 2.10. Image depicting *Centella asiatica* herbal plant

2.13.2. *Centella asiatica* as therapeutic agent

Centella asiatica has been known for its memory-boosting ability, neuronal cell regeneration property, prevention and neuroprotective effect **(Figure 2.11)** because of its inhibitory action against toxic neuronal cells in the traditional ayurvedic medicinal system. Its properties protect various biological functions, including peptic ulcers, anti-inflammatory action, anti-mutagenic property, anticancer activity, acetylcholinesterase activity, etc. [212]. These multi-beneficial qualities make it a good candidate for therapeutic medicine, especially in protection and prevention against neuronal cell damage leading to various neurodegenerative diseases.

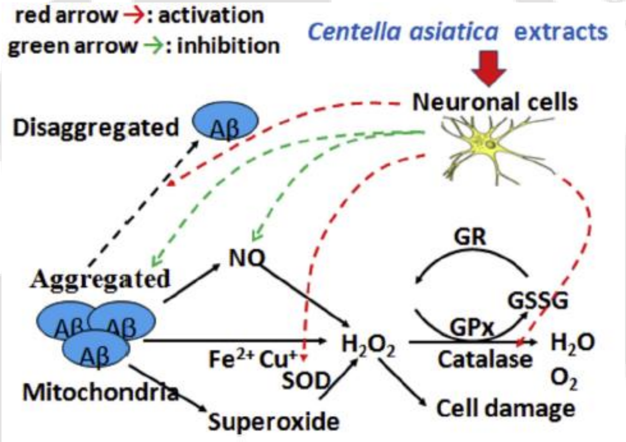

Figure 2.11. Diagrammatic representation of the mechanism of action of *Centella asiatica* plant on neuroprotection [213].

2.13.3. *Centella asiatica* in protein aggregation inhibition

Apart from its various uses in pharmacological applications **(Figure 2.12)**, *Centella asiatica* has been used frequently in Aβ and α synuclein aggregation studies both in vivo and in vitro, but there still remains a great number of amyloid-forming proteins which have not been explored.

Chien-Li Chen et al. investigated the capability of *Centella asiatica* extract using ethanol to prevent two cell lines, i.e., PC12 and IMR32, from reactive oxygen species (ROS) produced due to Aβ (1-40) toxicity. Aβ (1-40) aggregates were treated on the cell line, and it was found that the cell viability was greatly reduced. However, the toxicity was reduced when treated with different concentrations of CAE extract (*Centella asiatica* ethanolic extract) (25, 50, and 100 mg/mL). It was also found that CAE extract could degrade the reactive oxygen species produced due to Aβ (1-40) aggregate toxicity. This shows that *Centella asiatica* extract can support the cell's defence system, especially in anti-oxidation reactions [214]. In another study by Husnul Khotimah et al., rotenone-induced α-synuclein aggregation in zebrafish was studied, and the effect of *Centella asiatica* methanolic extract on the aggregation of α-synuclein aggregation was checked. *Centella asiatica* extracts at 5 and 10 mg/mL were treated, and it was found that the motility of the zebrafish was improved as the dopamine neurotransmitter was stabilised, which was directly correlated with the decrease in the aggregation of α-synuclein [215].

Centella asiatica extract was also tested in a study of the hippocampus of an Alzheimer's disease-infected animal model by Muralikrishnan Dhanasekaran *et al. Centella asiatica* extract (2.5 or 5.0 g/kg/day) was administered before the onset of the disease, i.e. from 2 months old until 8 months, when the disease pathology could be seen properly. A decrease in the deposition level of both Aβ (1-40) and Aβ (1-42) was detected through ELISA assay, and the intensity of congo red dyed fibrils was also observed. It was also shown that *Centella asiatica* extract could scavenge free oxide radicals, protecting against DNA damage and decreasing lipid peroxidation activity [210].

In another in vitro fibrillation inhibition study using fluorescence spectroscopy, different therapeutically important plant extracts were studied, of which *Withania somnifera,* *Convolvulus pluricaulis, Bacopa monnieri* and *Centella asiatica* extracts were found to give maximum inhibition efficiency [216].

In another study by Fredrick Nwude Eze et al., to study the effect of the hydrophobic portion of *Centella asiatica* extract on transthyretin amyloidosis (TTR), a protein misfolding disease caused by transthyretin, acid/urea was used to induce the aggregation or misfolding of transthyretin from human (huTTR). The stabilising effect of the plant extract on the homotetrameric native structure of the protein was investigated since the dissociation of the native conformer into monomer units will induce the formation of oligomers and then further fibrillation. Various high-end techniques like TEM, liquid chromatography, quadruple time-of-flight mass spectrometry (HPLC-QTOF-MS) for determining the chemical components and study the binding of Centella extract and huTTR, nitroblue tetrazolium redox-cycling and 8-anilino-1-naphthalene sulfonic acid displacement assays were employed. The result showed that Centella extract could stabilise the native conformer of huTTR, which could be used for further study to develop drugs against transthyretin amyloidosis [185].

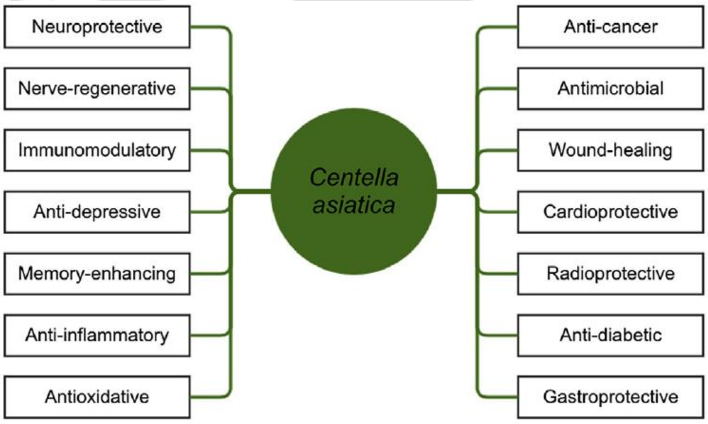

Figure 2.12. Various pharmacological effects of *Centella asiatica* (*adapted with permission from Perera et.al, 2018*) [217].

2.14. Conclusions

Shear-induced protein aggregation is one of the areas that need to be studied and tackled, given its implications in the pharma industry and inside the physiological system. Biopharmaceutical protein-based products are exposed to thermomechanical factors from many processing conditions, from upstream to downstream. Misfolded or distorted proteins, as a result, can lead to aggregation, causing loss of function, loss economically, and even initiating immunologic response once injected inside the body. So, studying the impacts of shear and thermal on different proteins (both amyloidogenic and non-amyloidogenic) is imperative to monitor the biophysical changes and the rheology in the present scenario. Another area of study is the inhibition/prevention of protein aggregation. Although many small molecule inhibitors are on the list for preventing protein aggregation, phytochemical-derived inhibition has many advantages, considering its bioavailability, small size, ability to cross the blood-brain barrier, etc.

CHAPTER-3

Shear and thermal induced aggregation of amyloidogenic proteins Aβ (1-40) (Amyloid beta 1-40) and HEWL (Hen Egg White Lysozyme)

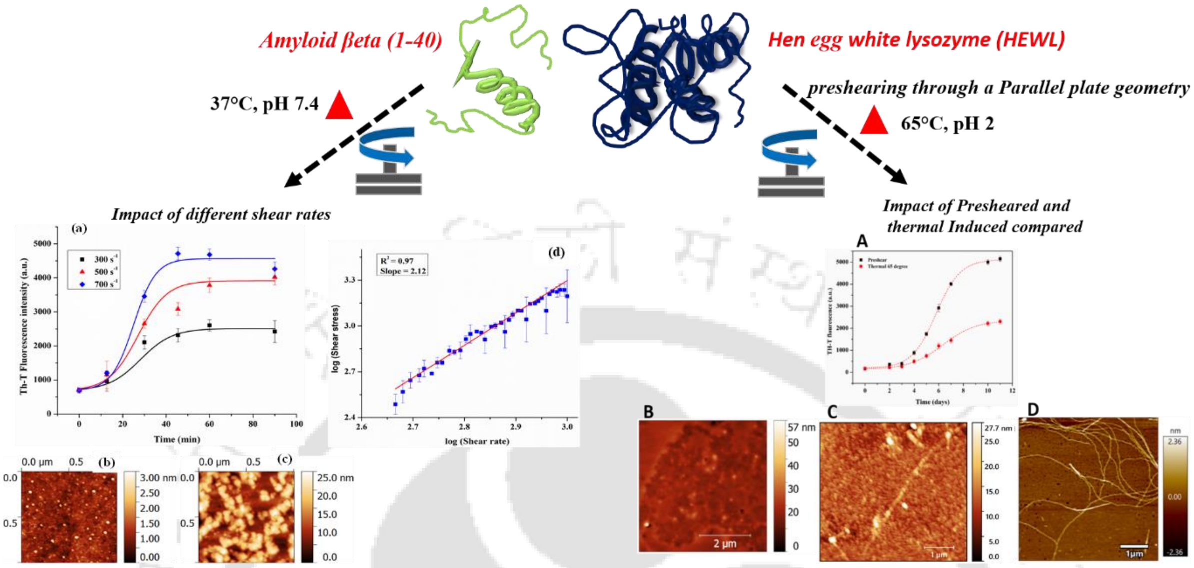

In this chapter, two amyloidogenic proteins, Aβ (1-40) (Amyloid beta 1-40) and HEWL (Hen Egg White Lysozyme), were subjected to shear and thermal induced aggregation. The aggregation kinetics, change in secondary structure, and morphology of the aggregates were then analysed and discussed. This chapter has two subchapters.

3.1. CHAPTER-3A

Shear-induced aggregation of Amyloid beta 1-40 (Aβ (1-40))

This subchapter discusses the shear-induced aggregation of Aβ (1-40). Aβ (1-40) peptide, a derivative of Amyloid precursor protein, was subjected to constant (300 s^{-1}, 500 s^{-1}, 700 s^{-1}) and varying (ramp) shear in a parallel plate geometry to explore the implications of shear in terms of macro (viscosity) and micro (secondary structure, morphology) characteristics.

3.2. Introduction

Shear stress plays an important role in the preparation, storage, handling, transportation and application of proteins [218]. Recently, it has been hypothesized that the shear processes occurring in the Aβ-containing cerebrospinal fluid (CSF) and interstitial fluid (IF) flowing through the brain parenchyma and narrow perivascular pathways might be responsible for accelerating the amyloidogenic cascade. Among all the Aβ isoforms, the Aβ (1-40) peptide is the most abundant in the brains of Alzheimer's disease-infected individuals [219-221]. It is therefore necessary to comprehensively investigate shear-induced Aβ (1-40) aggregation to determine its origins, information which may lead to possible treatments. In this sub-chapter, we have investigated shear-induced aggregation of Aβ (1-40) peptide, which is an abundant derivative of Amyloid precursor protein (APP) [5], using an Anton Paar MCR72 Rheometer in rotational mode equipped with PP50 parallel plate geometry (50 mm diameter). This geometry requires less protein solution and also offers gradient shearing, unlike that provided by a Couette cell. In fact, the physiological shear (10-10^3 s^{-1}) inside the body might not follow a uniform flow pattern [123]. The shear rates chosen for the rotational mode were 300 s^{-1}, 500 s^{-1} and 700 s^{-1}, which are well within the physiological flow range [119]. For the investigation of flow behaviour, a shear ramp range of 400 to 1000 s^{-1} was employed. The aggregation of Aβ (1-40) was monitored using a Thioflavin T (Th-T) assay. The changes in secondary structure were monitored using circular dichroism (CD) and Fourier transform infrared (FTIR) analyses. Further, the morphology of the aggregates was analysed using an atomic force microscope (AFM) and the aggregate molecular weight was determined using gel filtration chromatography.

3.3. Materials and methods

Lyophilised Aβ (1-40) powder was purchased from Dg Peptides, China (T-330, molecular weight 4329 Da, Purity > 95 %). Th-T dye (catalogue no. T3516) was purchased from Sigma-Aldrich, India. Milli Q water (18Ω) was used throughout the experiment.

3.3.1. Aβ (1-40) sample preparation

5 mg of lyophilised Aβ (1-40) powder was dissolved in 10 ml of 10 mM phosphate buffer saline (PBS, pH 7.4) buffer to prepare a stock solution of 0.5 mg/ml. The solution was then filtered through a 0.2 µL syringe filter, and the final O.D was checked at 280 nm to estimate the final concentration using Beer Lambert's law ($\varepsilon_{280} = 1490\ M^{-1}\ cm^{-1}$) [222]. For the working solution, a 0.1 mg/ml of Aβ (1-40) solution was prepared freshly on the requirement.

3.3.2. Shear induction of Aβ (1-40) solution in parallel plate geometry, rotational mode

For this shear-induced aggregation study of Aβ (1-40), an Anton Paar MCR72 series rheometer was employed. About 2 mL of 0.1 mg/ml, Aβ (1-40) solution was carefully loaded between the removable, 50-mm diameter parallel plates (PP50), with a gap of 1 mm between the upper and the lower plates. The temperature throughout the experiment was maintained at 37°C, using a Peltier temperature control system inbuilt within the rheometer. The samples were sheared via varying shear (flow behaviour) and constant shear rates. The flow behaviour of Aβ (1-40) was checked in the range of 400 to 1000 s^{-1} in a logarithmic profile with 30 points per decade, spanning about 960 s in duration. The change in viscosity due to shear-induced aggregation of the peptide solution was also monitored at constant shear rates of 300, 500 and 700 s^{-1} at an ambient temperature of 37°C. The samples were collected at different time intervals for the characterisation of amyloidogenesis through a Th-T assay, the secondary structure evolution using CD spectroscopy, the aggregate molecular weight using gel filtration chromatography and the morphology with AFM.

3.3.3. Th-T fluorescence assay

Th-T fluorescence assay was performed to monitor aggregation kinetics. The assay was performed in a corning 96 well flat black bottom plate (catalogue no. CLS3603). The ratio of protein samples to the Th-T solution (1 mM) was maintained at 1:1 (*v/v*). The fluorescence reading was performed at an excitation-emission wavelength of 450/482 nm and a slit width of 5 nm were used using a microplate reader (TECAN Infinite 200 pro) [223]. All the Th-T fluorescence experiment procedures were conducted in the dark condition to prevent fluorescence decay.

3.3.4. Determination of Secondary structure

The secondary structures of native and sheared samples were analysed using CD and FTIR spectroscopy. For CD, a 0.1 cm path length quartz cuvette was used, and far UV CD spectra in the 260-190 nm range were collected [224-226]. An average of 5 accumulations with a scan speed of 50 nm/min and 0.1 nm bandwidth was set. For baseline correction, the CD spectra of the buffer were first run before the samples were measured. The machine CD signal value θ in millidegree (mdeg) has been converted to mean residue ellipticity value (MRE) in (deg cm^2 $dmol^{-1}$ $residue^{-1}$) to analyse in terms of residues in the protein chain [227]. The percentage content of the secondary structure was analysed through the DICHROWEB web server [228].

FTIR spectroscopy was performed using an FTIR instrument (Shimadzu IR Affinity S1). For this analysis, 2 µL of samples were added on top of the ZnSe crystal. A minimum of 64 scans and a resolution of 4 cm^{-1} were preset for the entire investigation, and the spectra were recorded in the range of 400 to 4000 cm^{-1}. Prior to the FTIR measurements, the buffer was used as the blank and recorded as the background spectra, which were automatically subtracted from the sample spectra. The instrument also performed CO_2 and moisture corrections. The spectrum's amide 1 region (1600-1700 cm-1) was then resolved, deconvoluted, and fitted with Gaussian curves using Origin 8.5 software [229].

3.3.5. Morphology analysis

A 5 µL sample was drop-casted on a clean silicon wafer to analyse the morphology. The protein solution was then left to adsorb for about 15 minutes, and then a thin stream of Milli-Q water was used to wash the drop-casted protein solution to remove salts. The excess water is then adsorbed using lint-free tissue paper, and the samples are left to dry overnight at 37°C. The dried samples were then scanned in non-contact mode using an Oxford Asylum Atomic force microscope (Oxford, Asylum) equipped with a silicon nitride tip [230].

3.3.6. Size and molecular weight analyses

The Dynamic light scattering (DLS) analysis was performed to measure the hydrodynamic diameter of the samples using Litesizer 500 (Anton Paar) at room temperature. The intensity of the light scattered by the particles (aggregates) in the solution was recorded at a fixed angle of 175°. The instrument then calculates the diffusion coefficient, D and the d_H of the particles was then determined from the Stoke-Einstein equation, $d_H = KT/3\pi\eta D$. K implies the Boltzmann constant, T *is* the absolute temperature in K, and η is the viscosity of the solution. The number intensity was used to determine the hydrodynamic diameter. The molecular weights of the samples were analysed using Size Exclusion Chromatography (SEC). SEC was performed for native and sheared samples at all three shear rates, viz. 300 s^{-1}, 500 s^{-1} and 700 s^{-1}. A superdex 75 10/300GL column (25 mL column volume) with a UV detector was employed for this study. Sheared Aβ (1-40) samples were first concentrated using a centricon filter and centrifuged at 13000 rpm for 6 min and 200 µl volume of sample was injected. For all the runs, a 0.3 mg/ml flow rate was maintained. The column was washed properly with Milli Q water and then PBS buffer, using two-column volumes.

3.4. Results and discussion

3.4.1. Effects of shear on Aβ (1-40) solution

3.4.1.1. Flow behaviour

Aβ (1-40) solution (0.1 mg/ml) was sheared in an increasing shear rate range from 400 to 1000 s^{-1} at 37°C to see the flow behaviour of the protein sample. The nature of the flow curve was analysed by fitting the shear stress-shear rate data of the protein solution to the power law rheological model [231]. This model is one of the simplest rheological models, which describes a non-linear flow regime and is expressed as follows:

$$\tau = K\gamma^n \qquad [3.1]$$

$$log\tau = logK + nlog\gamma \qquad [3.2]$$

Here, τ is the shear stress in Pascals, γ is the shear rate in sec^{-1}, K is the consistency coefficient, which describes the texture or flow behaviour of a fluid, and "n" is the performance index. The log plot of experimental data is shown in **Figure 3.1. (a),** to decipher the fluid behaviour. The value of the performance index is used to identify the type of fluid flow [231]. If $n > 1$, the fluid is dilatant or shows shear thickening behaviour, which means its viscosity increases with increasing shear rate; if $n < 1$, it is a pseudoplastic fluid or a shear thinning fluid, where the viscosity decreases with increasing shear rate and if $n = 1$, it is a Newtonian fluid, where the viscosity is independent of the change of shear rate. In the present study, the value of *"n"* was found to be 2.12, which depicted the shear-thickening behaviour of the fluid. The consistency coefficient *"K"* equals the viscosity at 1 s^{-1}. The *"K"* value was found to be 0.0016, which can be used for the crude estimate of the solution. The coefficient of determination "R^2" was approximately 0.97, which validated the fitted model.

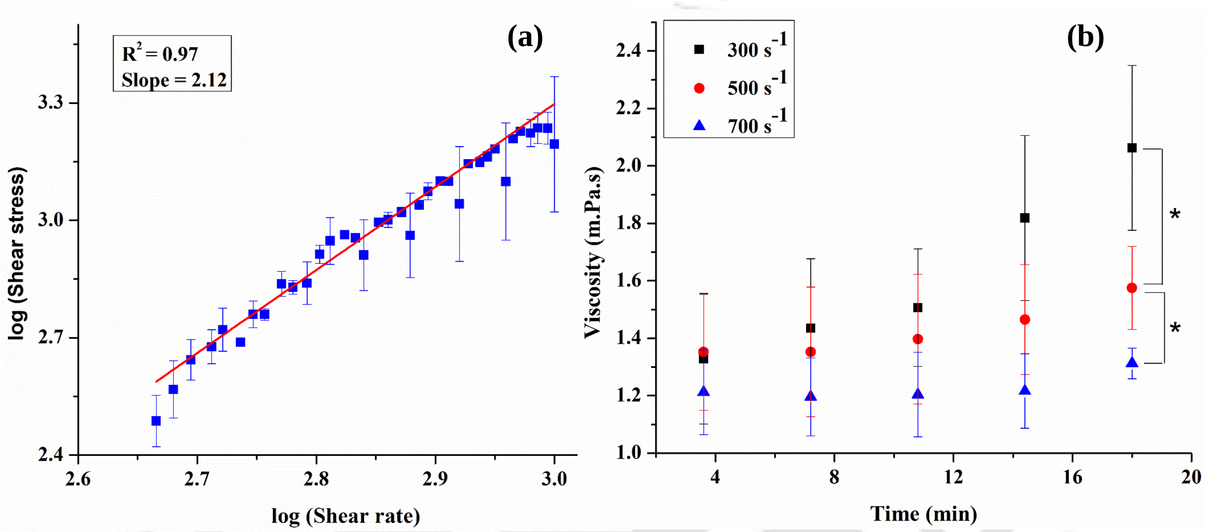

Figure 3.1. (a) Log plot of shear stress and shear rate of 0.1 mg/ml Aβ (1-40) solution sheared in the range of 400 to 1000 s^{-1}. Points represent average experiment data (*n* = 3), and the line indicates fitted data using equation 2; **(b)** Change in viscosity (***η***) of Aβ (1-40) solution at constant shear rates of 300 s^{-1}, 500 s^{-1} and 700 s^{-1}. The experiment was performed using an MCR72 rheometer for 18 minutes. Viscosity data were found to be significantly different at these three shear rates (*p-value < 0.05).

3.4.1.2. Effects of constant shearing on the peptide solution

Aβ (1-40) solution was sheared at three different constant shear rates of 300 s^{-1}, 500 s^{-1} and 700 s^{-1}. It was observed that the viscosity of the Aβ (1-40) solution was gradually increased at all three shear rates with time (**Figure 3.1. (b)**). Interestingly, it was also observed that the magnitude of the rise in viscosity was found to be higher with decreasing shear rate values.

The decreasing trend in the viscosity of the solutions with increasing shear rates indicated that higher shear magnitude, though, resulted in protein aggregation but also broke the micro aggregates clump by virtue of its high shear force [119].

The dissipation energy accompanied by the shearing motion was calculated for the sheared Aβ (1-40) solutions. It was calculated as the product of the shear rate square and the sheared solution's viscosity $(\gamma^2 \times \eta)$ [232]. At 300 s^{-1}, the dissipation energy was gradually increased from 5.2 to 8.1 kJ mol^{-1} (appendix, **Figure 3A.1.**). Similarly, the dissipation energy increased from 14.6 to 17.1 kJ mol^{-1} and 25.7 to 27.8 kJ mol^{-1} at 500 s^{-1} and 700 s^{-1}, respectively. It was observed that the dissipation energy at all three shear rates was higher than the reported free energy of unfolding of Aβ (1-40) peptide (6-8 kJ mol^{-1}) [233]. Therefore, shear imparted additional energy to the shearing fluid, resulting in the peptide structure's deformation or unfolding [13], leading to aggregates (a highly ordered β-sheet structure). The formation of β-sheet structure was validated from Th-T analysis and CD spectroscopy.

3.4.2. Thioflavin-T Assay

The enhanced Th-T fluorescence intensity indicated the formation of β-sheet-aggregates of peptide under applied shear. Th-T profile of Aβ (1-40) sheared at different shear rates followed a typical sigmoidal curve **(Figure 3.2. (a))**, indicating a nucleation-dependent aggregation [223]. The experimental fluorescence intensity (I) data were well fitted to the Boltzmann equation **(equation 3.3)** to estimate the rate of aggregation, k [234]. The experimental Th-T data were fitted to the sigmoidal model with $R^2 \geq 0.98$.

$$I_t = I_{max} + \frac{I_{max} - I_0}{1 + e^{(t_0 - t)/\tau}} \qquad [3.3]$$

Here, $1/\tau$ is the apparent rate constant, k of the aggregation and lag time is calculated as $t_0 - 2\tau$. The lag time was independent of the applied shear rates and calculated as 14 ± 1 min. However, the apparent aggregate rate was found to increase with the increase in share rate and was estimated to be 0.14 ± 0.02 min^{-1}, 0.15 ± 0.02 min^{-1} and 0.21 ± 0.03 min^{-1} in the case of 300 s^{-1}, 500 s^{-1} and 700 s^{-1}, respectively. It has been reported that mechanical stress induces the unfolding of the protein or a fracture of protofibrils to seeds (nuclei), thus escalating the growth of fibrils [235].

The fluorescence intensity was the highest in the Aβ (1-40) sample sheared at 700 s^{-1}, followed by 500 s^{-1} and 300 s^{-1}. These observations complemented the rheological data, as the higher dissipation energy led to the peptide unfolding and subsequent β-sheet formation (aggregation). The highest dissipation energy at 700 s^{-1} resulted in the greater formation of β sheet, which is reflected in terms of the highest Th-T fluorescence intensity. Therefore, the dissipation energy generated by shearing is physical in nature, contributing to the shear-induced aggregation of the Aβ (1-40) peptide. In fact, the rate of aggregation is reported to decrease as the viscosity of the medium increases, i.e. $k \, \alpha \, 1/\eta$ [236]. The least viscosity of the sheared sample at 700 s^{-1} **Figure 3.1. (b)** corresponded to the maximum rate of aggregation at this shear rate.

Aggregation of the peptide was also confirmed by AFM analysis. **Figure 3.2. (b-c)** shows the morphology of the native and the sheared samples. The native Aβ (1-40) resulted in globular structures (10-20 nm) with a z value of 3 nm [237]. Whereas the sheared samples comprised oligomeric and beaded protofibrillar structures **(Figure 3.2. (c))**. The oligomeric species range from 65 to 90 nm, whereas the protofibrils have a diameter range of 30 to 60 nm and length ranges from 100 to 300 nm. The z value for the aggregated (sheared) samples was 25 nm. In fact, the average roughness, R_a of the native sample, was 0.19 nm **(Figure 3.2. (b))**, which enhanced to 4.3 nm for the sheared sample **(Figure 3.2. (c))**. The morphology of the aggregates appears to be amorphous, and a few spherical clumps could also be seen. The size of the native and sheared samples was also monitored using DLS. The hydrodynamic radius of native Aβ (1-40) peptide was 1.23 ± 0.3 nm, while the same for the sheared samples were found to be

169 ± 17, 331 ± 23 and 225 ± 012 nm at 300, 500 and 700 s^{-1}, respectively. The DLS analysis complemented the AFM analysis and confirmed the formation of aggregates.

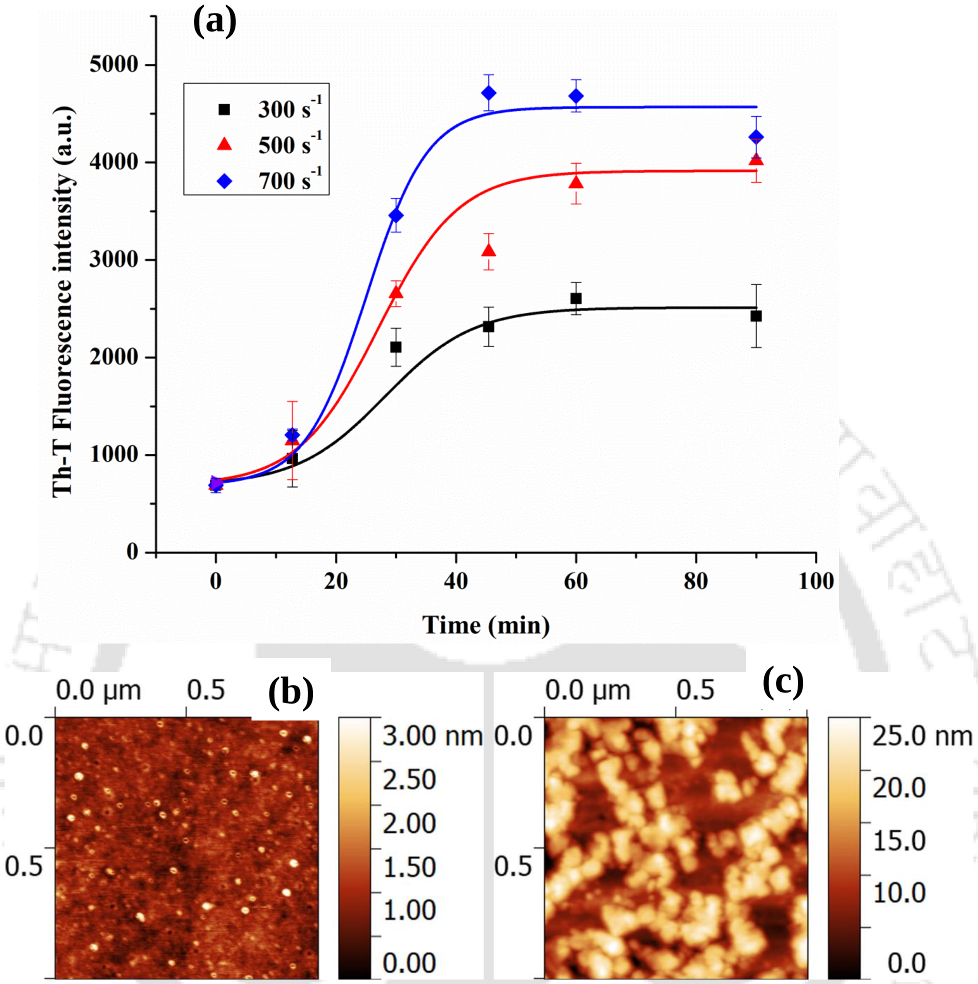

Figure 3.2. (a) Th-T assay for Aβ (1-40) solutions sheared at constant shear rates of 300 s^{-1}, 500 s^{-1} and 700 s^{-1}. The experimental data (symbol) were fitted to a sigmoidal model (equation 3) to estimate the rate of aggregation. Fitted data are depicted as lines and AFM images of (b) native and (c) sheared Aβ (1-40) samples at 700 s^{-1}. Scan size is 1 µm × 1 µm

3.4.3. Monitoring of secondary structures

Figure 3.3. (a) shows the far-UV CD spectra of native Aβ (1-40) and the sheared samples. The native Aβ adopts a random coil conformation, which is depicted by the minima at 200 nm [238]. For the sheared samples, the native random coil conformation gradually changed, as

observed from the disappearance of the minima at 200 nm, which shifted towards a β sheet conformation. This is prominently visible in the case of sample sheared at 700 s^{-1}, which is depicted by a new minimum at 217 nm and a maximum at 196 nm [239]. An interesting observation is made where the sheared samples showed a transitory α helical conformation at 208 nm [240]. This indicated a transition of the random coil to α-helix and finally to a β-sheet rich aggregates [223]. Also, the CD data were converted to the MRE (mean residue ellipticity) value. The MRE at 196 nm, a signature for the β sheet content, was found to increase with the increase in the shear rate, as shown in **Figure 3.3. (b)**.

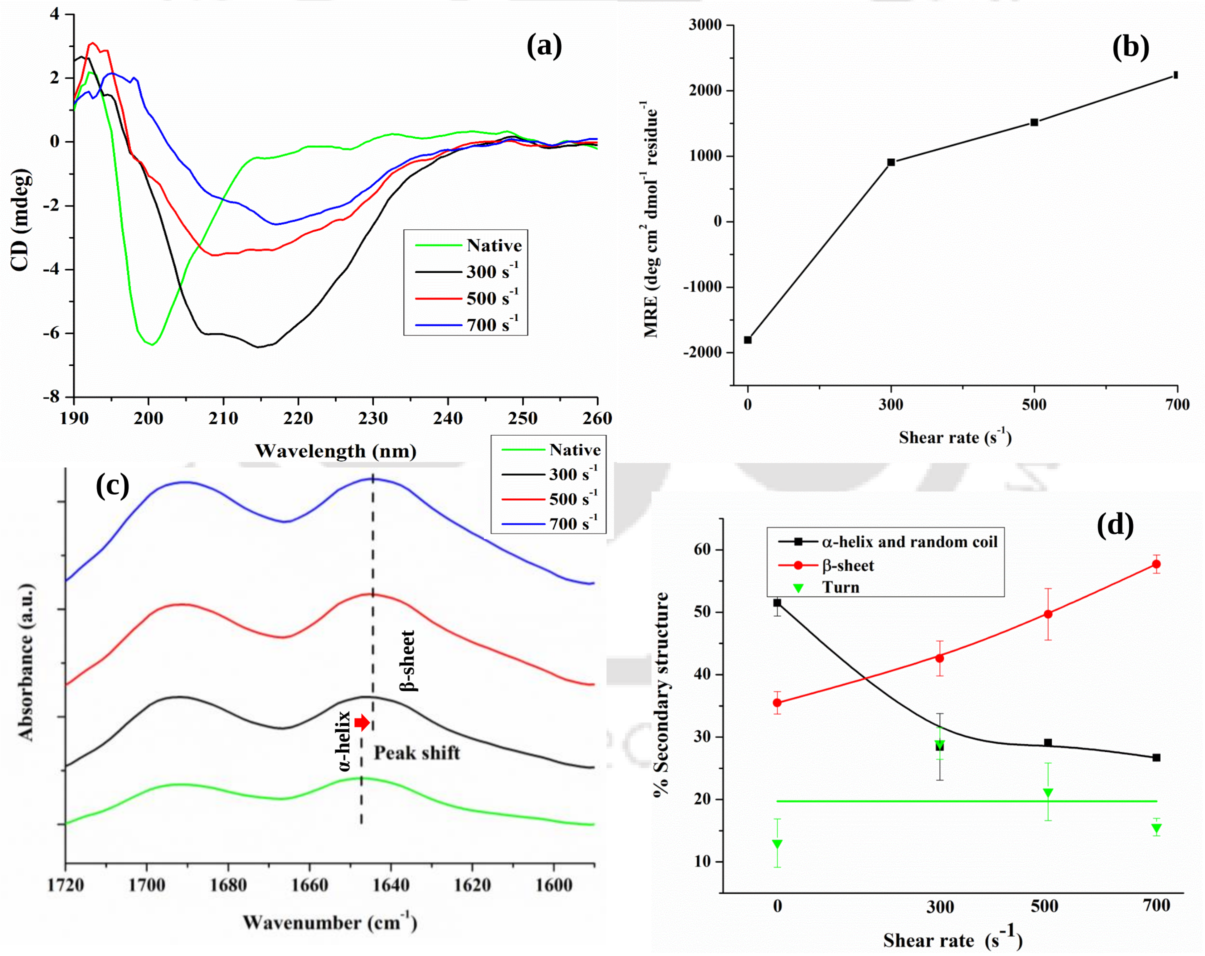

Figure 3.3. (a) CD spectra of native and sheared Aβ (1-40) samples. A transition from random coil-rich conformation of native Aβ to β-sheet rich aggregates is observed. **(b)** MRE values at 196 nm. The increased MRE values designated more contents of the β-sheet. **(c)** FTIR spectra

of native sheared samples in the amide-I region. **(d)** Variations of secondary structure components derived from FTIR data with increased shear rate.

FTIR spectra in the amide I region (1600-1700 cm^{-1}) for the native and sheared samples are shown in **Figure 3.3. (c)**, which were de-convoluted and fitted with Gaussian curves to quantify secondary structures given in the appendix section (**Figure 3A.2.**). The peaks around 1640-1655 cm^{-1} corresponded to α helix and random coils. The peaks between 1615-1635 cm^{-1} and 1685-1695 cm^{-1} were assigned to β-sheet, while peaks around 1665-1680 cm^{-1} were related to β turn [38, 241]. The α helix along with random coil, β sheet and β turn for the native Aβ (1-40) peptide were found to be 52 ± 2 %, 35 ± 2 % and 13 ± 3 %, respectively, which is very close to earlier findings [242, 243]. A gradual decrease in α helix and random coil contents was seen in all the sheared samples collected at the end of the constant shearing experiments, and there was a subsequent increase in β sheet contents **(Figure 3.3. (d))**. These results corresponded to the observations made by CD analysis **(Figure 3.3 (a) and (b))**. Samples sheared at 700 s^{-1} contained 27 ± 1 % of α helix and random coil, 58 ± 2 % of β sheet and 16 ± 2 % of β turn. From these results, it can be inferred that shearing force induced the aggregation of Aβ (1-40) by exposing the aggregation-prone amino acids, which were predicted using Fold-amyloid software [244, 245]. The aggregation-prone sequences were found to be Aβ16-21 and Aβ32-36 (scheme-1), which can easily polymerise into amyloid structures in the fluid environment [245-248]. Also, the amino acids which have a high propensity for forming β sheet structures [30] are situated in these sequences, such as V_{18}, $F_{19,20}$ and $I_{32,33}$. Therefore, the aggregation of Aβ (1-40) peptide resulted in higher contents of β-sheet secondary structure.

NH_2-DAEFRHDSG**Y**EVHHQ**KLVFFA**EDVGSNKGA**IIGLM**VGGVV-**COOH**

Scheme-1. Primary structure of Aβ (1-40) peptide. The aggregation-prone zones (A$\beta_{16\text{-}21}$ and A$\beta_{32\text{-}36}$), as predicted using the Fold-amyloid server [249], are highlighted in red

3.4.4. Determination of approximate aggregate molecular weight using SEC

SEC chromatograms of native and sheared samples are shown in **Figure 3.4.** The approximate molecular weights for the observed peaks were determined by comparing them with the standard elution profile of the superdex75 10/300GL column. The molecular weight of the native peptide was estimated to be 5 kDa, which agreed with its reported molecular weight. The average molecular weights were estimated to be 70 kDa, 62 kDa and 52 kDa for samples sheared at 300 s^{-1}, 500 s^{-1} and 700 s^{-1} shear rates, respectively. This indicated the formation of oligomers containing about 11-14 monomer units of Aβ (1-40) peptide. Oligomeric species of these sizes have also been reported by Pryor *et al.* [237]. An interesting observation was made that the average molecular weight of the oligomeric species was the minimum in the case of the sample sheared at the highest shear rate (700 s^{-1}). This data is in correlation with the work of Hill *et al.* [119], where aggregate species were shortened or cut when a shear field of higher magnitude was applied. This data perfectly resonates with the findings discussed in the earlier sections, that with increasing shear rates, a slight decrease in the solution viscosity was observed **(Figure 3.1. (b)**).

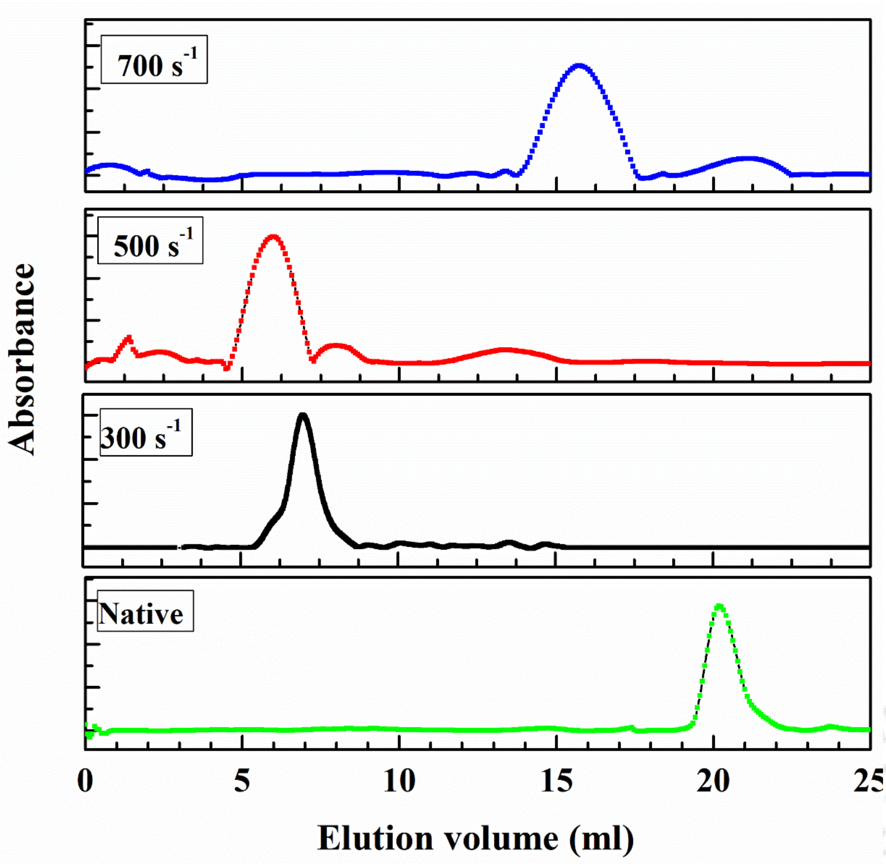

Figure 3.4. Gel elution profile of 0.1 mg/ml native Aβ (1-40) solution and samples sheared at three different constant shear rates of 300 s^{-1}, 500 s^{-1} and 700 s^{-1} using SEC.

3.4.5. Comparison of experimental viscosity data with fitted data

The viscosity dependence on the aggregate molecular weight and concentration was checked by fitting the aggregate molecular weight obtained from the above gel filtration analysis in the viscosity equation **(equation 3.4)** borrowed from the polymer solutions theory [106, 250].

$$\eta = C^a M^b \qquad [3.4]$$

Here, η is the solution viscosity, C is the concentration factor of the protein solution and is defined as the product of concentration and density, and M is the molecular weight factor, which is the ratio of average aggregate molecular weight to the molecular weight of the native. The experimental and fitted viscosity almost coincided when plotted together, as shown in **Figure 3.5**. This justified the correlation between the solution viscosity and the molecular weight of the aggregates. The fitted values of the experimental parameters *a* and *b* were found to be 0.96 and 0.94, respectively. The ratio of *b/a* was found to be 0.97, i.e. greater than 0.5. This indicated that the protein solution is a good solvent and expanded in an energetically favourable manner [63, 250].

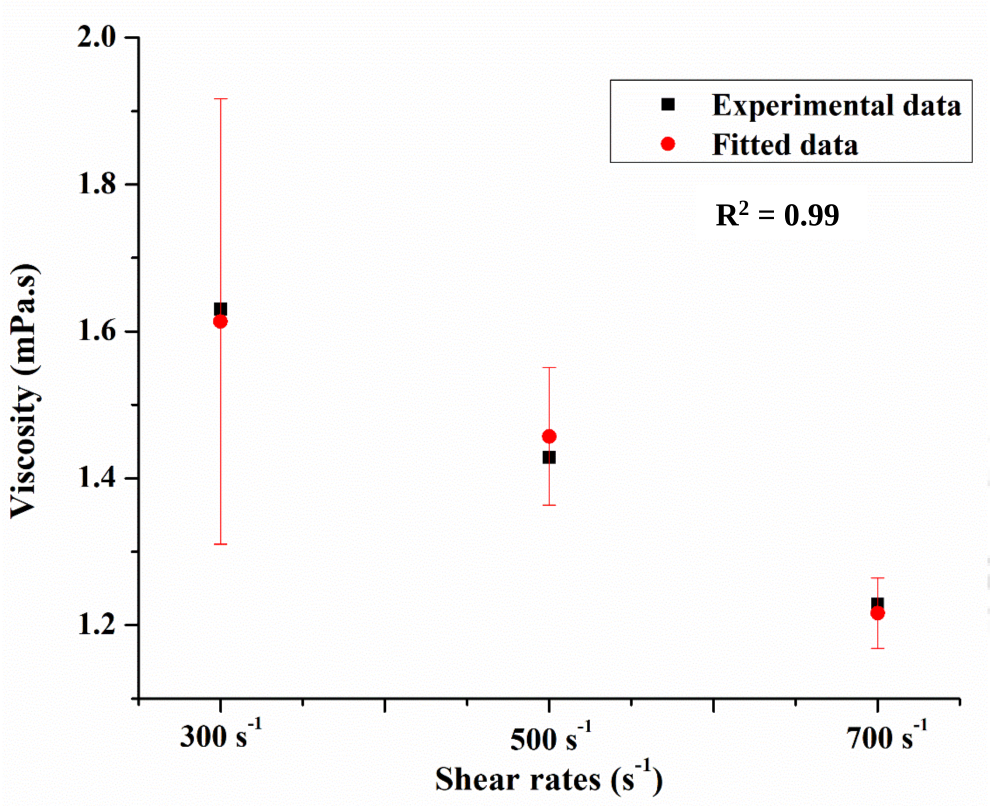

Figure 3.5. Plot of experimental viscosities obtained from constant shearing at three different shear rates (300 s^{-1}, 500 s^{-1} and 700 s^{-1}) and the fitted viscosities derived using equation-3.4.

3.5. Conclusions

In summary, varying and constant shear effects were investigated on Aβ (1-40) solution. Aβ (1-40) solution followed a non-Newtonian (shear-thickening) flow behaviour. Shear forces induced aggregation, which was confirmed by Th-T assay, CD, FTIR and AFM analyses. The apparent rate of aggregation increased with the shear rate and was found to be the maximum (0.21 ± 0.3 min^{-1}) at 700 s^{-1}, which inversely correlated to the solution viscosity of shared samples. The cause of aggregation due to shear was investigated and explained in terms of dissipation energy, which exceeded the free energy of unfolding. The aggregation of Aβ (1-40) exhibited changes in the solution viscosity, which was found to be dependent on the molecular weight of aggregates. The present study highlighted the effect of shear on a protein solution in terms of structural aberration, aggregation, and rheology.

3.6. CHAPTER-3B

Pre Shear and thermal induced aggregation of Hen egg white Lysozyme (HEWL)

In this subchapter, HEWL, another amyloidogenic protein, was subjected to pre-shear and thermal-induced aggregation. HEWL protein was subjected to 65°C thermal induced aggregation at pH2 to induced aggregation. Samples pre-sheared at 300 s^{-1} for an hour at 65°C were used as seeds and incubated at 65°C to compare with the un-sheared, non-seeded sample.

3.7. Introduction

HEWL protein is one of the amyloidogenic proteins frequently studied as a model protein to understand protein folding, misfolding, and aggregation. It is an orthologue of the human lysozyme and is a β glycosidase enzyme that catalyses the hydrolysis reaction of the cell-positive gram-positive bacteria [251]. In humans, lysozyme is present in various body parts, including the GIT, kidney, spleen, liver, lymph nodes, skin, lachrymal gland, and salivary glands. A single-point mutation in the lysozyme gene causes lysozyme amyloidosis, a rare systemic amyloid disease [252]. Two naturally occurring variants of lysozyme cause autosomal hereditary systemic amyloidosis in humans. It is reported to form amyloid depositions in various organs. It may, therefore, cause multiple organ failure, which includes spontaneous liver rupture, renal dysfunction, granulomatosis of bronchi, heart failure, digestive damage, and so on. Lysozyme amyloidosis is linked to the point mutations of the lysozyme gene, which results from the non-conservative substitutions of $_{\text{Ile}}56^{\text{Thr}}$ or $_{\text{Asp}}67^{\text{His}}$, making the protein more prone to aggregation or amyloidogenic [253, 254].

HEWL, a model amyloidogenic protein, was subjected to shear-induced aggregation, and this sheared sample was used as a seed for further aggregation without shear at 65°C and at pH2. The aggregation kinetics was assessed through a Th-T fluorescence assay, and the aggregate size was determined using a dynamic light scattering experiment. The effect of aggregation on the secondary structure of the protein was determined through Circular Dichroism spectroscopy, and the aggregate morphology was analysed using Atomic Force Microscopy.

3.8. Materials and methods

Lyophilised chicken egg white lysozyme (catalogue no. A2153) and Th-T dye (catalogue no. T3516) were purchased from Sigma-Aldrich, India. Sodium azide (NaN_3) (SKU TC704) was obtained from Himedia, India. Milli Q water (18 Ω) was used in all the experiments.

3.8.1. Preparation of protein solution

20 mg/ml of stock chicken egg white lysozyme was prepared in 20 mM Glycine buffer (pH 2) containing 0.02% NaN_3. The protein solution was then filtered using a 0.2 µm syringe filter, and the absorbance was checked at 280 nm in a UV spectrophotometer to check the concentration using Beer Lambert's law. The extinction coefficient was 37646 M^{-1} cm^{-1}. 140 µM (~2 mg/ml) working solution was then prepared for the experiment.

3.8.2. Effect of thermal and shear on the aggregation of HEWL

For thermal-induced aggregation, different solutions containing 140 µM HEWL and increasing extract concentrations were prepared. The thermal-induced aggregation was performed in a 65°C oven. Samples were collected every day till the 10th day. Shear-induced aggregation was performed at 300 s^{-1} and 65°C using a rheometer, which was equipped with parallel plate geometry for 2 hours. As no aggregation was detected through shearing, we used the one-hour sheared sample as a seed and continued the thermal aggregation experiment at 65°C in the oven. An MCR 72 Rheometer from Anton Paar with an inbuilt Peltier temperature control system was used for the pre-shearing. Motor adjustment of the instrument was performed before starting the experiment to avoid errors. Next, a 65°C temperature was set, and a 2 ml sample of HEWL solution (140 µM) was slowly placed on the lower plate of the parallel plate geometry (PP50). Then, the upper plate was descended to a gap of 1 mm standard distance between the two plates. The samples were then sheared at 300 s^{-1} for an hour and used as a seed to check the effect of pre-sheared samples on HEWL aggregation kinetics.

3.8.3. Investigation of the aggregation behaviour

3.8.3.1. Th-T fluorescence assay

To monitor the aggregation kinetics, a Th-T fluorescence assay was performed according to the section 3.3.3.

3.8.3.2. Estimation of hydrodynamic diameter

The DLS experiment was performed to analyse the hydrodynamic diameter (dH) according to section 3.3.5. 70 µM sample solution was used for the experiment.

3.8.3.3. Secondary structure determination

Far UV-CD spectroscopic measurement was performed according to section 3.3.4.

3.8.3.4. Morphological analysis

The morphology analysis was done according to section 3.3.5.

3.9. Results and discussion

3.9.1. Determination of aggregation kinetics and the hydrodynamic diameter

The aggregation kinetics of both the thermal and the pre-sheared induced aggregation of HEWL were analysed through the Th-T fluorescence assay. Thioflavin T is a benzothiazole dye which binds to the cross β-sheet structures of amyloid fibrils (aggregates) [255, 256]. The Th-T fluorescence intensity of the pre-sheared added samples and the thermally induced aggregated samples are shown in **Figure 3.6. (A)**. From the figure, it was observed that there was enhanced aggregation in pre-sheared samples compared to the thermal-only induced samples. Although shearing of HEWL for two hours did not give any significant increase in Th-T fluorescence intensity (data not shown), however, it acts as a seed when incubated with the fresh HEWL for a longer period of time in low pH and high-temperature conditions. The Th-T fluorescence data was then fitted with the Boltzmann equation, a nonlinear sigmoidal equation (1), to determine the aggregation rate k [257]. Here, 1/t denotes k, the apparent rate constant, and the lag time can be calculated as t_0-2τ. It was observed that the apparent rate constant is highest in the case of the pre-sheared induced samples with k value of 1.01 day^{-1}and the k value of the thermal-only induced sample was 0.88 day^{-1}. Adding the pre-sheared sample enhances the rate of aggregation 1.14 fold, but it did not completely reduce the lag time like in the case of various studies where seeds are added to induced aggregation [258, 259]. This could be because the pre-sheared samples do not contain mature fibrils but have become aggregate-prone as their structure was exposed to thermal and shear conditions.

$$I_t = I_{max} + \frac{I_{max} - I_0}{1 + e^{(t0-t)/\tau}} \qquad [3.5]$$

The same trend in the Th-T fluorescence increase was observed in the case of the hydrodynamic diameter, as shown in **Figure 3.6. (B)**. Native lysozyme has a hydrodynamic diameter of about 2 nm [260, 261].

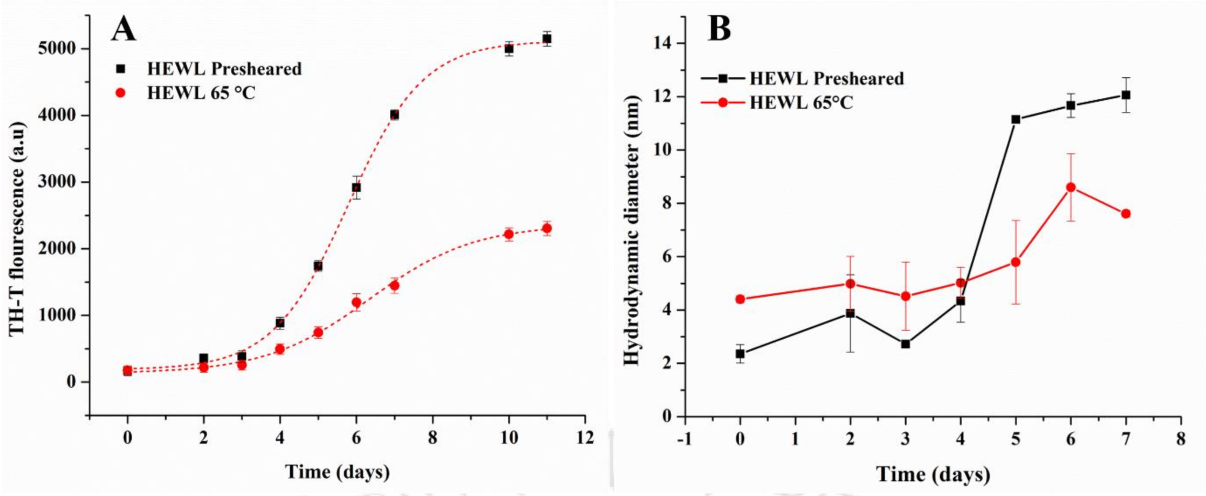

Figure 3.6. Th-T fluorescence assay of HEWL sample pre-sheared at 300 s^{-1} and at temperature 65°C and samples which are thermal incubated at 65°C in the absence and the presence of different concentrations of CWE (A) and the hydrodynamic diameter of pre-sheared and thermally induced HEWL in the presence and in the absence of HEWL (B).

3.9.2. Secondary structure analysis through circular dichroism

The secondary structure of the pre-sheared added samples and the thermally induced samples at 65°C were analysed from the far UV CD from 260-190 nm. **Figure 3.7 (A)** shows the CD spectra of HEWL, which have been pre-sheared and used as a seed for thermally induced aggregation at 65 °C; **(2B)** is the thermal only induced without any extract. The native HEWL CD spectrum has a similar spectrum to that of a model-helix structure with negative dips at 208 and 222 nm. The native HEWL contains 33 % α helix, 13 % β sheet, 17 % turn and 37% unordered structure. Earlier studies have also found similar content of the secondary structure of the native HEWL [262, 263].

Here, analysing the CD spectra, the observed amyloid fibril formed was the type two β proteins (β II). This form of amyloid fibril is generally made up of β sheets structure and unordered structure, with the unordered form slightly higher than the β form [264]. Generally, β-sheet-rich proteins are of two types: the type I β protein and the type II β protein [264-266].

The regular β strand or the type I (β I) protein has a typical CD spectrum, which has a negative band at 218 nm and a positive one at around 195 nm [267], whereas the type II β protein has CD spectra resembling that of an unordered structure with a negative band at around 200 nm, which is thought to adopt more of a polyproline II like conformation [268].

In this study, in all the experimental conditions, the native negative dip at 208 nm gradually shifts towards 200 nm, and additionally, the negative dip at 222 nm slowly diminishes with time. In the case of the pre-sheared added sample, the peak not only shifts towards 200 nm, but the depth of the dip is also greater. The shifts towards 200 nm were visible in the pre-sheared added and the thermal-induced control samples. The observations made in the CD were also beautifully correlated with the morphology data obtained from AFM (section 3.3). The MRE value was calculated from the machine theta value, and the formula is given in equation 3.6.

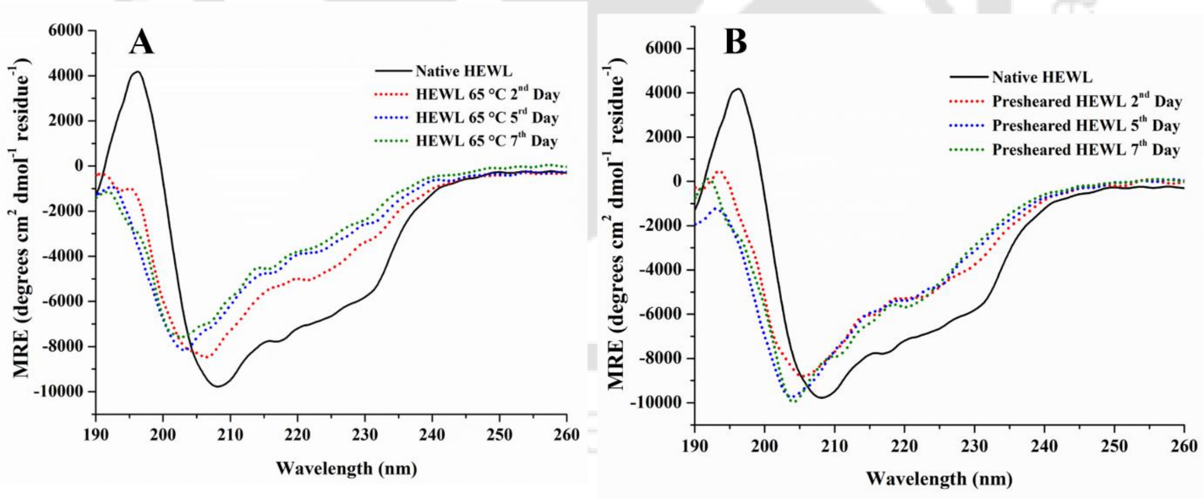

Figure 3.7. CD spectra of HEWL were incubated at thermal only at 65°C (A), and HEWL was pre-sheared at 300 s^{-1} and 65°C (B).

3.9.3. Morphology analysis

The morphology of the samples in different conditions was checked for their morphology through AFM. The images are analysed through Gwydion software. **Figure 3.8. (A)** shows the AFM images of native HEWL, **(B)** thermal induced aggregated HEWL at 65°C and **(C)** pre-sheared HEWL at 300 s^{-1} and continued incubation at 65°C. The native HEWL samples had a diameter in the range of 20 to 42 nm. The apparent increase in monomeric size could be because it is the apparent lateral width distorted by the tip convolution, as the native HEWL monomeric size is around 2nm which is also observed from DLS analysis. The thermal-induced aggregated HEWL has not yet formed fibrils, but we can observe short prefibrillar structure of length in the range 118 to 156 nm. The diameter was in the range of 28 to 45 nm. Surprisingly, proper fibril structure could be observed in the case of pre-sheared samples. The fibrils' length ranges from 1.54 µm to 4.4 µm, with an average diameter of 31 nm.

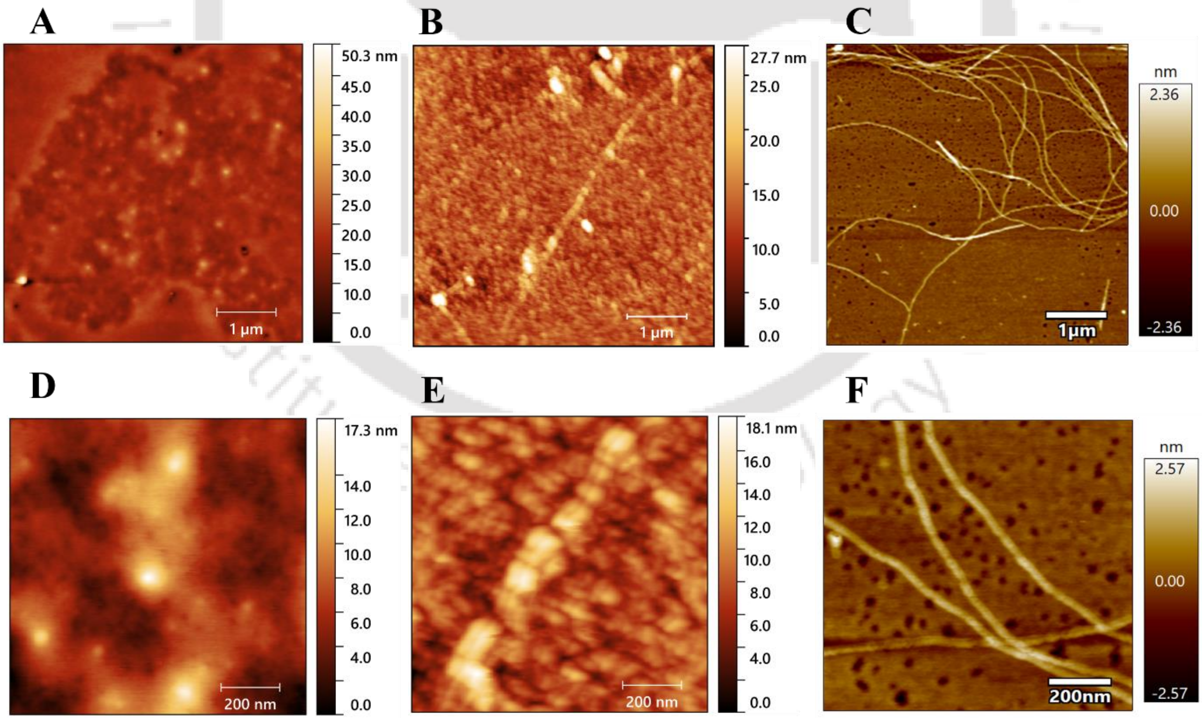

Figure 3.8. Native HEWL (A); thermal induced HEWL at 65°C (B); pre-sheared and thermal induced HEWL at 65°C (D); Figures (A, B and C) were of dimension 5 x5 µm whereas figures

(D, E and F) were that of the corresponding zoomed images of dimension 1 x 1 µm. The scanning was done on a silicon wafer chip.

3.10. Conclusions

In this study, HEWL protein was subjected to 65°C thermal induced aggregation at pH 2 to induced aggregation. Samples pre-sheared at 300 s^{-1} for 1 hour at 65°C were used as seed and incubated at 65°C to compare with the non-seeded sample. Boltzmann fitting of the Th-T fluorescence data revealed that the pre-sheared samples have the maximum aggregation with an apparent rate constant of 1.01 $days^{-1}$ and a short lag period of 3.80 days. In contrast, the non-sheared thermal induced samples had a 4.67 days lag period, and the fluorescence intensity was also lower, with an apparent k of 0.88 $days^{-1}$. With this different kinetics of aggregation, there is also a peculiar behaviour in the change in their secondary structure observed from the far UV-CD data. The fibril formed is found to be a type two β protein, which is made up of β sheets and unordered portions but with a higher constituent of unordered fraction. With the increased fibrillation, the native dip at 208 and 222 nm diminishes and shifts towards a negative dip at 200 nm with more depth, implying more fibril formation.

The morphology of thermal-induced aggregated HEWL has not yet formed fibrils, but short prefibrillar structure of length in the range 118 to 156 nm and diameter in the range of 28 to 45 nm was observed. The pre-shear sample has vividly visible amyloid fibrils of length ranging from 1.54 µm to 4.4 µm.

CHAPTER-4

Shear and thermal induced aggregation of two non-amyloidogenic proteins: BSA (Bovine serum albumin) and BFG (bovine fibrinogen)

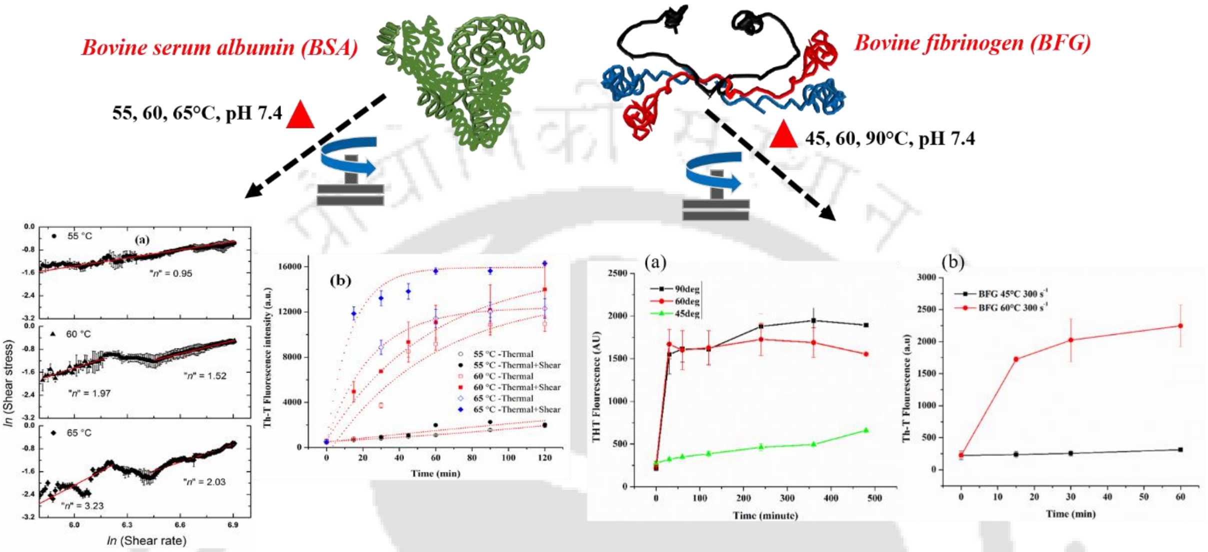

In this chapter, two non-amyloidogenic proteins, bovine serum albumin (BSA) and bovine fibrinogen (BFG), were subjected to shear and thermal-induced aggregation. The aggregation kinetics, the corresponding changes in their secondary structure, and the morphology of the aggregates were then analysed. This chapter covers two sub-chapters.

CHAPTER-4A

Shear and thermal-induced aggregation of Bovine serum albumin (BSA)

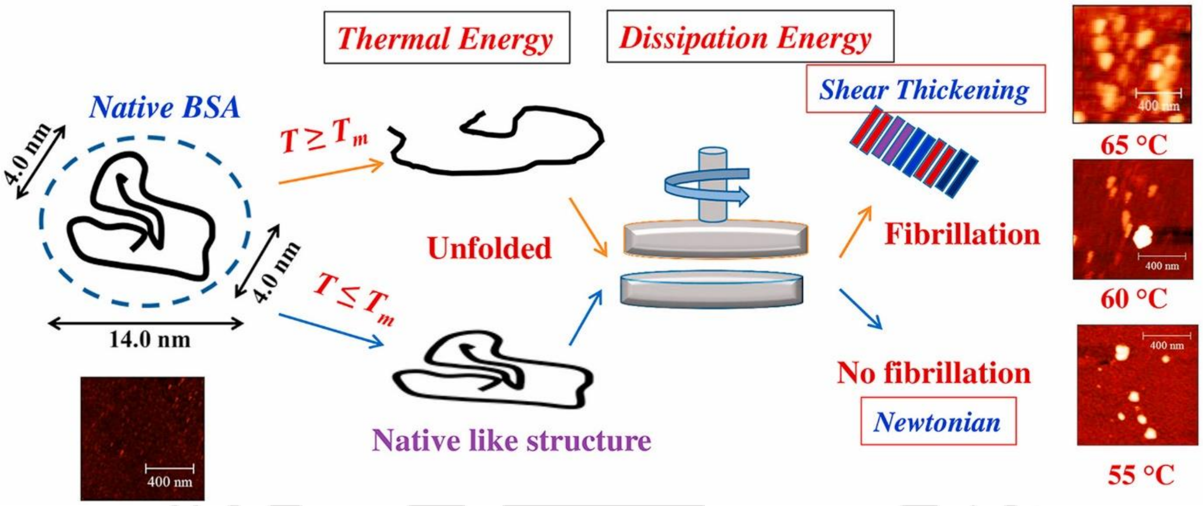

(Food Hydrocolloids 112, 106294, 2020 (Sharma and Pandey, 2020))

In this subchapter, the energetics of the thermomechanical treatment of bovine serum albumin (BSA) and its related impact on the unfolding and aggregation behaviour have been explored to decipher the roles of the thermal and dissipation energy. Shear-induced aggregation of the BSA at a constant shear rate of 300 s^{-1} was performed at the three temperatures (55, 60 and 65 °C) using a Rheometer and the aggregation behaviour was experimentally analysed.

4.1. Introduction

Bovine serum albumin (BSA) is among the most significant serum proteins physiologically and has a multi-diversified function, be it as a carrier molecule or as a stabiliser. Various heat stability studies have been done by researchers in different temperature conditions and found that BSA almost retains its native conformation till the 40-50 °C range, and at around the 52-60 °C range, it undergoes irreversible unfolding after going through some amount of denaturation. As the temperature increased, approximately above 60 °C, prominent unfolding and denaturation were obtained, resulting in aggregation [37, 269]. The melting temperature of BSA is reported to be about 63°C [270]. Mechanical impacts like shearing or extreme pressure also denature proteins' conformation and formulations [42, 271]. Various studies have explored the effect of shear on the aggregation of proteins. Stirring, shaking, mechanical agitation, and ultra-sonication were found to affect the fibril formation [272-276]. However, in most practical applications, such as fluid flow, bioprocessing, formulations, mixing, and transportation, thermal and mechanical stresses are simultaneously experienced [277]. Thus, it is important to explore the thermomechanical behaviour of a protein to gain better insights into the aggregation process.

In this regard, thermodynamic aspects of the thermomechanical treatment of BSA and its related impact on the aggregation behaviour have been explored in the present study. The insights associated with the dissipation energy generated during the shearing process and its implications towards the unfolding and aggregation have also been investigated. To understand the thermal stability, hysteresis temperature loop scans of BSA in solution at physiological pH (7.4) were conducted in the three temperature ranges, i.e. 25-50-25 °C, 25-65-25 °C and 25-75-25 °C at the ramping rate of 1 °C/min. Next, shear-induced aggregation of the BSA solution at a constant shear rate of 300 s^{-1} was conducted at the three temperature conditions (55, 60 and 65 °C) using an MCR 72 Rheometer. To investigate the aggregation behaviour, Thioflavin T (Th-T) fluorescence assay was performed to monitor the aggregation kinetics and hydrodynamic diameter was measured using dynamic light scattering (DLS). Far-UV CD was conducted in the range of 190-260 nm to analyse the structural conformational changes. Morphological analysis was performed using atomic force microscopy (AFM).

This study aims to render some of the mechanistic insights related to the thermomechanical-induced aggregation of globular proteins in terms of its aggregation kinetics, behaviour and morphology. The results could provide information that could be used in manufacturing protein-based therapeutics and in understanding the pathology of diseases related to protein aggregation.

4.2. Materials and methods

Lyophilised BSA, fatty acid-free (catalogue no. A2153) and Thioflavin- T dye (Th-T) (catalogue no. T3516) were purchased from Sigma-Aldrich, India. Milli-Q water (18MΩ) was used throughout the study.

4.2.1. Preparation of BSA solution

Firstly, a 0.5 mM stock solution of lyophilised BSA powder was prepared in 20 mM Tris-HCl buffer (pH 7.4). The solution was filtered through a 0.2 µm syringe filter. The absorbance was recorded at 280 nm using a UV spectrophotometer to estimate the final stock concentration using Beer Lambert's law at an extinction coefficient value of 43,824 M^{-1} cm^{-1} [269]. A 75 µM (5 mg/ml) working concentration was prepared before the experiments.

4.2.2. Thermal stability study of BSA

To determine the stability of BSA, a temperature sweep test was conducted for the three ranges 25-50 °C, 25-65 °C and 25-75 °C at the rate of 1 °C/ min using a UV visible spectrophotometer (Cary 300 bio). Also, a hysteresis loop scan of the above three ranges was performed to see the reversibility of the protein structural changes at respective temperatures. Freshly prepared 1 ml BSA solution (0.5 mg/ml) was added to a quartz cuvette and placed inside the Cary instrument. The samples were collected at three points, including the initial temperature (referred to as "ONE"), the maximum temperature (referred to as "TWO") and back to the initial temperature (referred to as "THREE”). The samples were examined for the aggregation behaviour of BSA.

4.2.3. Effect of shear on the aggregation of BSA

After conducting the stability study, we chose three temperatures (55, 60 and 65 °C) to perform the shear study at a constant shear rate of 300 s^{-1} (thermomechanical set-ups). For this study, an MCR 72 Rheometer from Anton Paar with an inbuilt Peltier temperature control system was used. Before starting the experiment, motor adjustment of the instrument was performed to overcome erroneous data. Next, the required temperature was set, and a 2 ml sample of BSA solution (75 µM) was placed on the lower plate of a parallel plate geometry (PP50). Then, slowly, the upper plate was brought down to a 1 mm standard distance gap between the two plates. Samples were then sheared at 300 s^{-1} for a duration of 120 minutes, and aliquots of samples were collected at different time intervals to monitor the aggregation behaviour.

For analysing the flow behaviour of BSA solution at different temperatures, a linear shear ramp was performed from 1 to 1000 s^{-1} at a rate of 5 points/shift and a constant duration of 6 seconds was maintained at a shear rate.

4.2.4. Investigation of aggregation behaviour

4.2.4.1. Th-T fluorescence assay

Th-T fluorescence assay was performed to monitor aggregation kinetics according to section 3.3.3.

4.2.4.2. Determination of hydrodynamic diameter

The DLS experiment was carried out to analyse the hydrodynamic diameter (d_H) according to section 3.3.5.

4.2.4.3. Analysis of secondary structure

The secondary structure analysis was performed according to section 3.3.4.

4.2.4.4. Morphological analysis

Refer to section 3.3.5.

4.3. Results and discussion

4.3.1. Temperature sweep test to determine the thermal stability of BSA

To determine the thermal stability of BSA, temperature sweep test was conducted for the three temperature ranges, 25-50-25 °C, 25-65-25 °C and 25-75-25 °C at the rate of 1 °C/ min. The sample was analysed at three stages: "ONE", "TWO", and "THREE". The thermal hysteresis data are shown in **Figure 4.1.** In the temperature sweep range of 25-50 °C, the absorbance value clearly indicates that the protein has not lost its original conformation. However, for the other two temperature ranges, significant differences between the absorbance values at "ONE" and "THREE" were observed. This indicated the loss of reversibility of the BSA folding. The absolute error values between stages "ONE" and "THREE" were found to be 0.05±0.001, 0.09±0.002 and 0.15±0.01 for 25-50 °C, 25-65 °C and 25-75 °C ranges, respectively. Similarly, absorbance changes (%) with respect to the initial value of BSA solution were estimated to be 1.6%, 2.9% and 4.8% for the above three conditions, respectively. This highlighted the irreversible unfolding and aggregation of BSA at 65°C and 75°C, above its melting temperature.

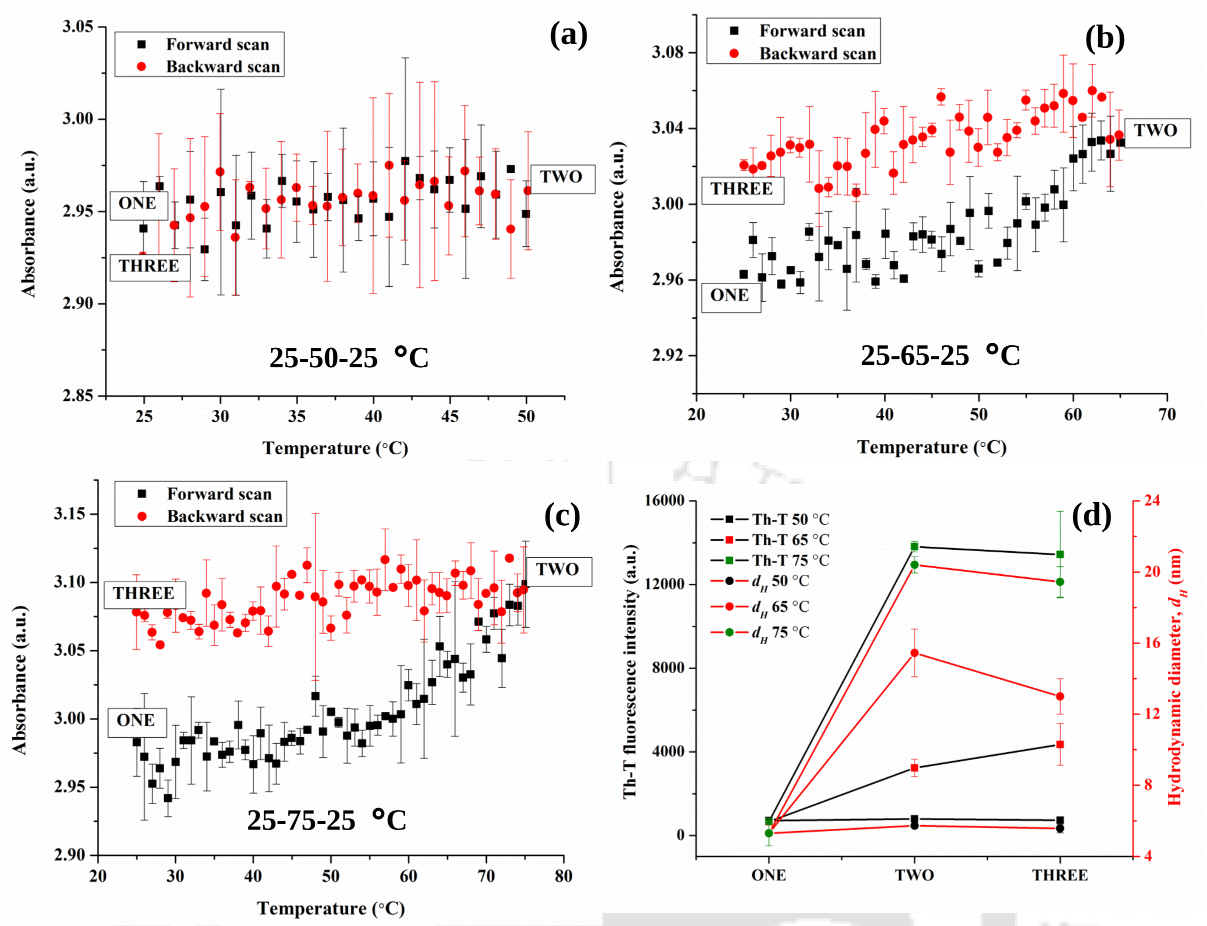

Figure 4.1. Temperature sweep test for determining the thermal stability with respect to the absorbance at 280 nm of BSA solution at three different ranges of (a) 25-50-25 °C, (b) 25-65-25 °C, and (c) 25-75-25 °C at the rate of 1 °C/ min; (d) Th-T fluorescence intensity and the corresponding hydrodynamic radii, d_H, of the samples subjected to the above temperature sweep tests.

Apart from the loss of reversibility, the aggregation behaviour of BSA was also monitored. **Figure 4.1. (d)**, shows the Th-T fluorescence data and corresponding d_H values of the samples subjected to the above three temperature sweep tests. No increase in Th-T fluorescence intensities was observed for the 25-50-25 °C hysteresis loop. Similarly, the corresponding d_H values remained constant (5.5 ± 0.2 nm). This indicated the absence of any significant unfolding and aggregation of BSA up to 50 °C. However, at the other two higher temperature ranges (25-65-25 °C and 25-75-25 °C), the fluorescence intensities were considerably enhanced, which confirmed the formation of aggregates [223]. Thioflavin T is a benzothiazole dye and binds to the amyloid fibrils (aggregates) with the cross β-sheet structures and generates an enhanced flourescence [255, 278]. Congruently, d_H values were increased by two and three folds at 65 °C and 75 °C, respectively. These observations highlighted that the thermal treatment above the melting temperature (63 °C) [270] of BSA caused the unfolding and aggregation.

The thermal energy supplied during the heating process, i.e. enthalpy (ΔH), was calculated as $C_{pmixture}\Delta T$. The heat capacity of the BSA solution was calculated as $C_{pmixture} = y_{BSA}C_{pBSA} + y_{water}C_{pwater}$ [279]. C_{pwater} and C_{pBSA} were taken as 4.18 J/g-K (75.24 J/mol-K) and 1.66 J/g-K (108.6 kJ/mol-K), respectively [280, 281]. Here, we have assumed constant $C_p$values in this study, but it varies with temperature. ΔH values for 25-50°C, 25-65°C and 25-75°C ranges were calculated as 1.9, 3.0, and 3.8 kJ mol^{-1}, respectively. For an open system, heat transfer, Q, is equal to ΔH. Hydrogen bond energy for α-helix in water environment is reported to be 1.93 kJ mol^{-1}[282]. Hence, a higher energy input at 65 and 75 °C broke the intramolecular bonds, resulting in unfolding and intermolecular interactions (aggregation).

To monitor the secondary structure of the samples, the far-UV CD spectra have been recorded from 260-190 nm. **Figure 4.2. (a)** shows the CD spectra of the native BSA and the temperature ramped samples up to 50°C, 65°C and 75°C. CD spectra of native BSA consisted of two characteristics negative band of α-helix at around 208 nm and 222 nm and a positive band near about 195 nm [39, 283]. As the temperature ramp increased, a decrease in the ellipticity value was observed, signifying the loss of the α-helix content. Also, the peak shifts towards 217 nm and 196 nm were observed [239], which signify the formation of β-sheet structures [223, 284]. Also, the MRE values at 222 nm are plotted as a function of temperatures in **Figure 4.2. (b)**. A substantial increase in MRE values for the samples treated at 65°C and 75°C can be observed.

The folded fraction ($\boldsymbol{\alpha}$) for the samples is determined as $\boldsymbol{\alpha} = (\boldsymbol{\theta_t} - \boldsymbol{\theta_u})/(\boldsymbol{\theta_f} - \boldsymbol{\theta_u})$ [285]. Here, θ_t is the MRE value at the desired state of the sample. θ_u and θ_f are the MRE values of the unfolded and folded states, respectively. The loss of helicity was found to be 30 % and 44 % at 65°C and 75°C, respectively. These data correlated with the enhanced Th-T fluorescence intensity and the corresponding changes in hydrodynamic diameter (**Figure 4.1. (d)**.

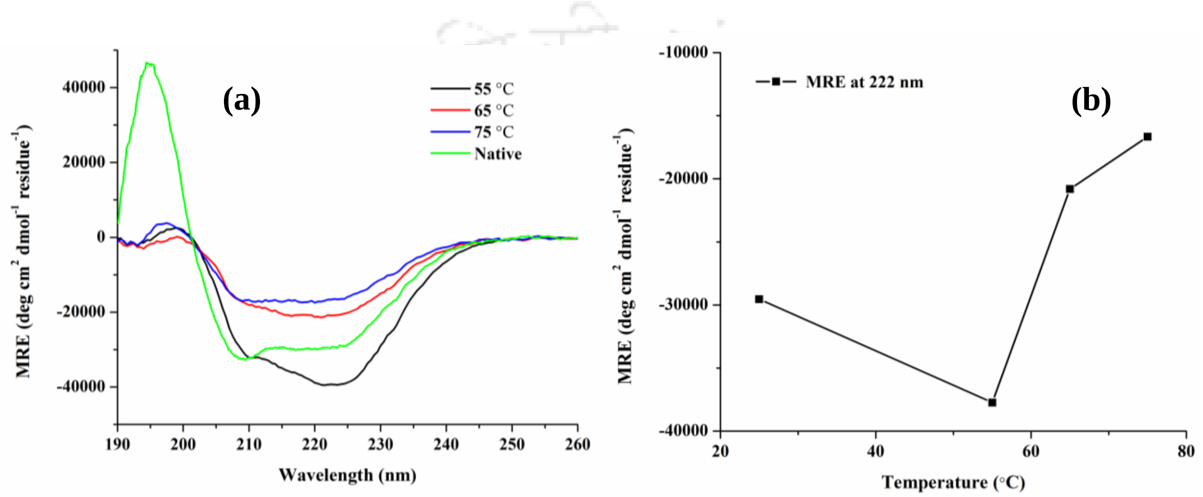

Figure 4.2. (a) Far-UV CD spectra showing the secondary structural conformations of the BSA solution at 55°C (black), 65°C (red) and 75°C (blue) with reference to native (green) BSA. The spectrum of native BSA in Tris-HCl buffer (pH 7.4) was recorded at room temperature without thermal treatment. (b) MRE signals at 222 nm for the above thermal treated samples to monitor the changes in helical content.

4.3.2. Effect of shear on the aggregation of BSA at different temperatures

After conducting the thermal stability study, we chose three temperatures below 65°C (55, 60 and 65°C) to investigate the thermomechanical effects at a constant shear rate of 300 s^{-1}. **Figure 4.3.,** shows the Th-T fluorescence intensity of the samples collected at different time intervals during the shearing. The aggregation was observed for the sheared samples at 60°C and 65°C, although the Th-T intensity and aggregation rate were enhanced at the higher temperature. At these conditions, the BSA solution was exposed to enough energy from both shear and thermal processes, which led to the disruption of intramolecular bonds and the unfolding of the BSA monomer, exposing the free SH group and the hydrophobic core. This ultimately resulted in intermolecular interactions leading to the irreversible hydrophobic aggregates of the protein [225]. While at 55°C, the Th-T intensities were much lower than at the other two temperatures. This indicates that the aggregation of BSA has just begun, and not many aggregates are formed. The hydrodynamic diameter, d_H, values were also correlated with the Th-T fluorescence data **Figure 4.3. (a)**. At 55°C, BSA was present in monomer or dimer forms; however, d_H values were enhanced about 4 and 7 folds when sheared at 60°C and 65°C, respectively. A similar particle size of BSA was reported at 60°C [286]. These observations reflect the vulnerability of a protein towards aggregation after exposing it to shear, even below its melting range (63 °C).

Further, the rate of aggregation (k) was deciphered by fitting the Th-T fluorescence intensity (I_t) with a single exponential expression as $I_t = I_{max}(1 - e^{-kt})$ [281, 287, 288]. The experimental data fitted well to this 1st order kinetic model with R^2 in the range of 0.90 to 0.99. Fitted data are shown as dotted lines in **Figure 4.3 (b)**. The rate constant (k) values were found to be 0.076 ± 0.01 min^{-1}, 0.024 ± 0.005 min^{-1} and 0.021 ± 0.005 min^{-1} for the samples sheared at 55°C, 60°C and 65°C, respectively. The k values were compared with that of only thermal treatment sample at the same temperature. The k values were 1.5 times enhanced for the thermomechanical (sheared) samples compared to thermal treated samples at 55°C, 60°C and 65°C, respectively. These findings indicate the presence of the following steps during the aggregation process as $N(native) \leftrightarrow U(unfolding) \leftrightarrow intermediates(dimer, oligomer\ etc.) \rightarrow A(fibrillation)$ [289-291]. At 55°C temperature (below melting point), the protein did not completely unfold, as only a slight change in d_H was observed. However, aggregation was observed when sheared at 60°C and 65°C, which followed 1st order kinetics (**Figure 4.3 (b)**). This agreed to the second step of the aggregation process.

Furthermore, the activation energy (E_a) were calculated from the slope of Arrhenius plot (lnk vs 1/T) [287] and found to be ~95 and ~81 kJ mol^{-1} for the thermal and thermomechanical treatments, respectively. The Gibbs free energy $\Delta G°$ was estimated as $-RTlnK$. $\Delta G°$ value was increased by 2.5 kJ mol^{-1} and 4.2 kJ mol^{-1} at 65°C compared to 55°C for the thermal and thermomechanical treated samples. This agreed with the decreased stability at higher temperatures and under shearing. The magnitude of energy was found to be comparable with the heat transferred during the thermal treatment at 75°C (see the thermal energy section). This indicated that extra energy during the shearing, even at a lower temperature of 65°C, is compensated by the dissipation energy, which is discussed in the next section.

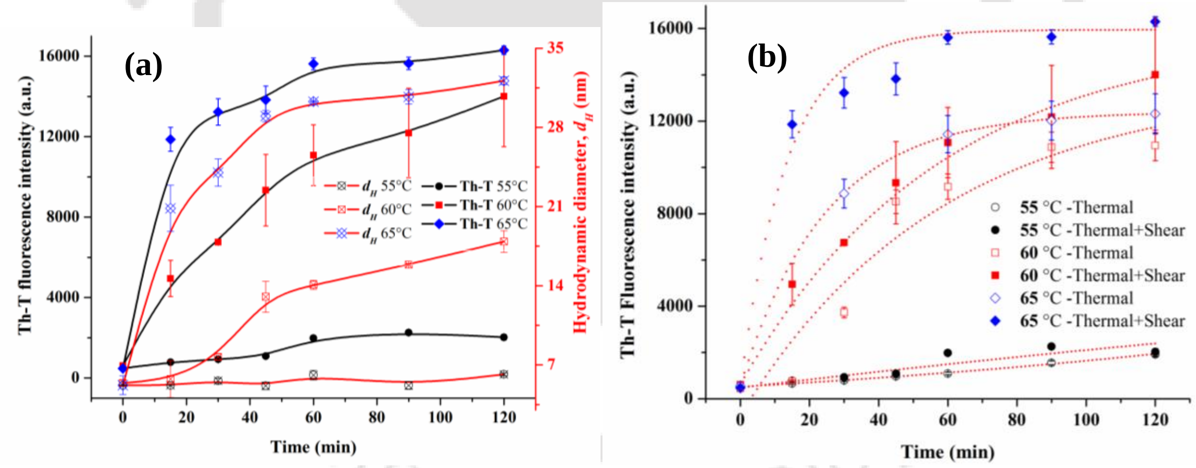

Figure 4.3. (a) Th-T fluorescence intensity and d_H values for the samples sheared at a constant shear rate of 300s^{-1} at 55°C (black circle), 60°C (red square) and 65°C (blue diamond); and **(b)** Th-T fluorescence intensity comparison between thermal and thermomechanical treatments (sheared at 300 s^{-1}) at the above three temperatures. Dotted lines indicate the fitted data using a single exponential expression.

The secondary structural changes in the protein solutions for the shear experiments carried out at 300 s^{-1} and 55°C, 60 °C and 65°C have been recorded for the samples collected at different time intervals. **Figure 4.4.** shows the CD spectra of the sheared samples. It was observed that shearing at 55°C caused no change in secondary structure as compared to the native BSA. However, a slight increase in the helical conformation was seen, presumably due to the formation of new intra and inter-molecular bonds under the influence of dissipation energy below the melting point of the protein. As the temperature increased, the loss of the initial helical conformation was clearly visualised as the negative band at 222 nm gradually shifted towards the positive direction. This increase in ellipticity became more prominent as the temperature and duration of shear increased. These results correlated with the Th-T fluorescence and hydrodynamic data, as shown in **Figure 4.3**.

The change in MRE values at 222 nm is plotted as a function of time for all three temperatures (**Figure 4.4 (d)**). The increase in the MRE signals at 60 and 65 °C correlated with the formation of β-sheet rich aggregates. The rate of increase in MRE data at 65 °C was greater than that at 60 °C. This corresponded to the enhanced aggregation rate at 65 °C (**Figure 4.3 (b)**). The loss of helicity was found to be about 40 % and 90 % at 60°C and 65°C, respectively. This indicated that the thermomechanical treatment at an even lower 60 °C resulted in a similar loss of helicity as thermal treatment at a higher temperature of 75 °C [277].

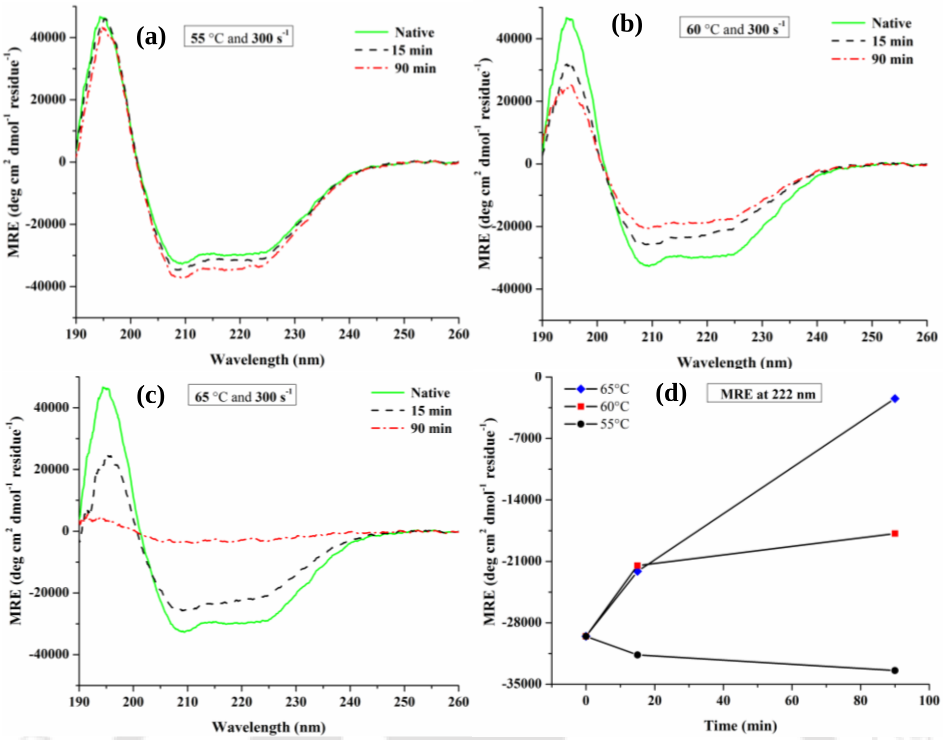

Figure 4.4. Far-UV CD spectra of BSA solutions sheared for different time intervals at 300 s^{-1} at (a) 55°C, (b) 60°C, and (c) 65°C for monitoring the secondary structural changes of 75µM BSA solution; (d) The corresponding change in MRE signals at 222 nm at these temperatures.

4.3.3. Morphology analysis using AFM

To analyse the morphology of the samples, AFM imaging was performed as shown in **Figure 4.5**. The native BSA molecules were in globular shape with an average size of 30-40 nm (**Figure 4.5. (a)**). This size may be overestimated due to the AFM tip's finite radius (~10 nm). For the samples sheared at constant 300 s^{-1} for 15 min, particle sizes were 50 to 70 nm (**Figure 4.5. (b)**), i.e. slightly larger than native BSA. However, at higher temperatures, 60 and 65°C, particle sizes were much increased due to the aggregation observed through enhanced Th-T fluorescence and loss of helicity. The aggregate dimension ranges were 70-100 nm and 100-200 nm for the samples sheared at 60°C and 65°C, respectively (**Figures 4.5. (c) and (d)**).

Here, mixtures of globular and elongated clumps were observed. These sizes and shapes of aggregates agreed with the reported data [292]. The size of aggregates obtained after shearing at 65°C was found to be comparable with thermal-treated BSA at 75 °C (**Figure 4.5. (e)**).

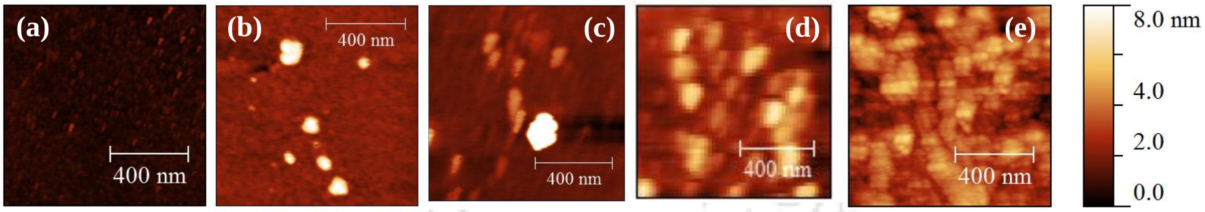

Figure 4.5. AFM images for (a) native BSA solution and sheared at constant 300 s^{-1} for 15 min at (b) 55°C (c) 60°C and (d) 65 °C, and (e) thermal treated (temperature sweep test) BSA sample at 75 °C. The dimensions of all the images are 1μm × 1μm × 8 nm (X × Y × Z).

4.3.4. Flow behaviour and implications of dissipation energy during the thermomechanical process

The BSA solution was subjected to linear shear ramp flow from 1-1000 s^{-1} to determine the flow curves at 55°C, 60°C and 65°C. The flow curves for thermomechanical treatments at three different temperatures (55, 60 and 65 °C) are shown in **Figure 4.6. (a)**. The obtained shear stress ($\tau,\ Pa$) and shear rate ($\gamma,\ s^{-1}$) were fitted to the model power law as $\tau = K\gamma^n$ [231]. Here, *K* is the consistency coefficient, which describes the texture or flow behaviour of a fluid, and "*n*" is the performance index, which describes Newtonian or non-Newtonian fluid [293]. There was only one slope at 55 °C, while two different slopes were observed at higher temperatures. The value of "*n*" at 55 °C was found to be 0.95, indicating the solution's Newtonian behaviour and the absence of aggregates. This agreed with the Th-T fluorescence and CD data (**Figures 4.3 and 4.4**). However, the values of "*n*" at 60 and 65 °C were greater than 1, indicating the solution's shear thickening behaviour due to the aggregation. The "*n*" values were higher at 65 °C than 60 °C, corresponding to the greater aggregation (enhanced rate and larger aggregate sizes) at 65 °C. The values of the first slope were higher than those of the second. This indicated the formation of aggregates during the initial shearing, and a shear thickening ("*n*" =1.97 and 3.23) behaviour was observed. Further, the exposure of greater magnitude of shear force broke the larger aggregates at higher shear rates [54, 55], which resulted in lower values of "*n*" (1.52 and 2.03).

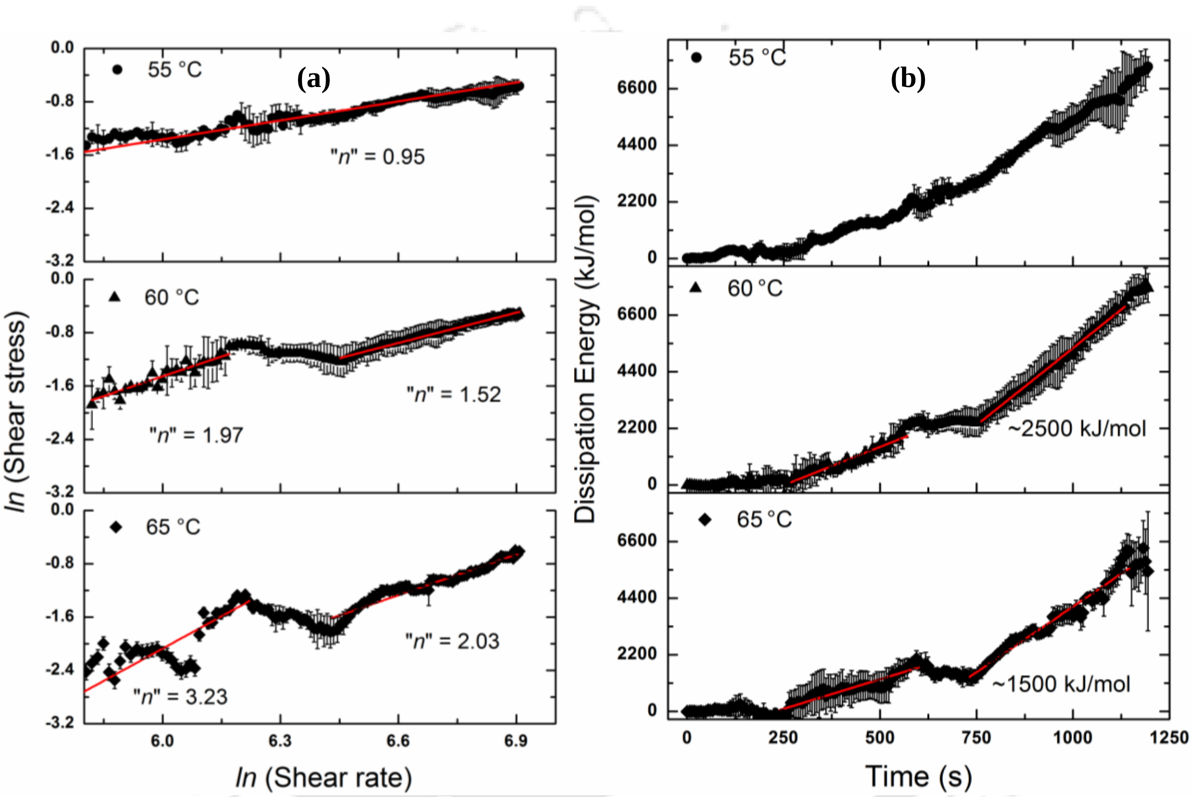

Figure 4.6. (a) Flow curve (Log plot of shear stress and shear rate) of 5 mg/mL BSA solution sheared in the range of 1 to 1000 s^{-1}, and **(b)** Corresponding changes in dissipation energy with time at the respective temperatures. The experiment was performed using an MCR72 rheometer with parallel plate geometry. The dissipation energy is calculated from the respective experimental data as $\boldsymbol{\tau} \times \boldsymbol{\gamma}$.

The energy involved in the shearing process, the dissipation energy, was calculated as the product of shear stress and shear rate or the square of the shear rate and the viscosity ($\tau \times \gamma \; or \; \gamma^2 \times \eta$) [119, 232]. The corresponding generations of dissipation energy with time during the shearing process at the respective temperatures are shown in **Figure 4.6. (b)**. The dissipation energy was found to increase with time or shear rate. Similar to flow curves, there was only one slope at 55 °C and two different slopes at higher temperatures. In fact, transitions between these two slopes were observed at about 1500 and 2500 kJ mol^{-1} at 65 and 60 °C, respectively (**Figure 4.6. (b)**). This indicated that the higher thermal energy at 65°C compensated to achieve the aggregation at lower dissipation energy.

Although the magnitude of the dissipation energy was higher than the energy required to break intramolecular hydrogen bonds, yet the aggregation was not observed at the lower temperature 55 °C. This indicated the loss/transfer of dissipation energy to the neighbouring water molecules and surrounding; hence, the first step (unfolding) of the aggregation process could not be initiated. However, at higher temperatures, 60 and 65 °C, where unfolding was achieved by the thermal energy, dissipation energy has more impact [294] and was found to accelerate the second step (fibrillation) of the aggregation process and the rates of aggregation were enhanced by 1.5 folds (**Figure 4.3.**).

4.4. Conclusions

In this study, the energetics of the thermomechanical treatment of bovine serum albumin (BSA) and its related impact on the unfolding and aggregation behaviour have been explored to decipher the roles of the thermal and dissipation energy. Temperature hysteresis scans of BSA solution at physiological pH (7.4) in the three temperature ranges, i.e. 25-50-25°C, 25-65-25°C and 25-75-25°C show that irreversible unfolding and aggregation occurs at the temperature range above its melting temperature (65 and 75 °C). Heat transfer above 3 kJ mol^{-1} broke the intramolecular bonds, which resulted in unfolding and led to an irreversible aggregation to form a hydrophobic conformation, finally leading to intermolecular hydrophobic aggregation. The loss of helicity was found to be 30% and 44% at 65°C and 75°C, respectively, as observed using CD spectroscopy. Shear-induced aggregation of the BSA at a constant shear rate of 300 s^{-1} was performed at the three temperatures (55, 60 and 65 °C) using an Anton Paar, MCR 72 Rheometer equipped with parallel plate geometry. The rate of aggregation (k) was calculated by fitting the Th-T fluorescence data to a 1st order kinetic equation. The k values were enhanced by 1.5 folds for the thermomechanical (sheared) process as compared to thermal treatment. The loss of helicity was found to be about 40% and 90% at 60°C and 65°C, respectively. This indicated that the thermomechanical treatment at an even lower 60 °C resulted in a similar aggregation effect as thermal treatment at a higher temperature of 75 °C. The flow behaviour of the BSA solution was studied by a shear ramp in the range of 1 to 1000 s^{-1}. BSA solution exhibited a shear thickening behaviour during the aggregation. Dissipation energy generated from the shearing accelerated the aggregation process's second step (fibrillation) at 60 and 65 °C. However, it could not initiate the first step (unfolding) of the aggregation at 55 °C, presumably the heat/energy loss to the neighbouring water molecules and surrounding. The present study highlighted the stability of BSA during the thermal and simultaneous thermomechanical treatment. Thermal energy was found to be effective for unfolding protein, while dissipation energy was influential during the fibrillation process. The present work would provide a mechanistic understanding underlying the thermomechanical induced aggregation of proteins, to be precise, globular proteins. This understanding could help frame process setup and conditions in the therapeutic industry, protein-based food products, and protein science to understand various protein aggregation-related diseases.

CHAPTER-4B

Shear and thermal induced aggregation of Bovine fibrinogen (BFG)

This subchapter discusses the thermal and shear-induced aggregation of another non-amyloidogenic protein, BFG (Bovine fibrinogen). The thermal aggregation was carried out at 45°C, 60°C, and 90°C. The thermal and shear-induced aggregation was carried out at 300 s^{-1} and 60°C using an Anton Paar rheometer with a parallel plate geometry.

4.5. Introduction

Fibrinogen is a multidomain globular protein found in all vertebrates and is the third major protein found in serum. Its concentration in the blood plasma ranges from 1.5 to 4 g/l [35, 295, 296]. It is also known as factor (I), and its main function is to help with blood clotting. Aberrant folding of fibrinogen molecules is a major issue which leads to various diseases due to the blockage of arteries and veins. Also, fibrin deposits have been found in the brain of Alzheimer's disease patients. Fibrin has been found to co-localize with the Aβ plaques, dystrophic neurites, and macrophages and in areas where there is pericyte loss inside the brain in the perivascular region of brain parenchyma [297, 298]. The entry of fibrinogen inside the brain occurs due to the blood-brain barrier disruption, which is an early event in a number of neurological disorders like Alzheimer's disease.

Thus, in this subchapter, we have taken fibrinogen from bovine and exposed it to thermal and shear-induced aggregation. For the shearing, a rheometer with a parallel plate geometry was employed. The impact of both shear and thermal on the fibrinogen molecule in terms of aggregation and change in the protein secondary structure has been assessed and compared. To investigate the aggregation behaviour, a Thioflavin T (Th-T) fluorescence assay was performed to monitor the aggregation kinetics, and hydrodynamic diameter was measured using dynamic light scattering (DLS). Far-UV CD was conducted to analyse the structural conformational changes. Morphological analysis was performed using atomic force microscopy (AFM).

4.6. Materials and methods

Lyophilised bovine fibrinogen powder (F8630-1G) and Th-T dye (catalogue no. T3516) were purchased from Sigma-Aldrich, India. Milli Q water (18Ω) was used in all the experiments.

4.6.1. Preparation of Bovine fibrinogen

A 20 mg/ml stock solution of Lyophilised bovine fibrinogen was prepared in 50 mM Glycine-NaOH buffer (pH 7.4). It was then stirred slowly for about 30 minutes to let the protein dissolve properly. It is then filtered through a 0.2 µm syringe filter, and the absorbance was recorded at 280 nm using a UV spectrophotometer to estimate the final stock concentration using Beer Lambert's law at an extinction coefficient value of 512040 M^{-1} cm^{-1} [269]. A (2 mg/ml) working concentration was prepared before every experiment.

4.6.2. Effect of thermal and shear on the aggregation of Bovine fibrinogen and flow behaviour

For fibrinogen thermal induced aggregation, three sets of 2 mg/ml samples were prepared, and three water baths were ready at three temperatures of 45°C, 60°C, and 90°C for studying in these conditions. Samples were collected every hour till 8 hours. Next, for the thermal and shear study, samples were prepared the same way and were subjected to 300 s^{-1} and at 45 and 60°C. For the shearing experiment, a rheometer (MCR 72, Anton Paar) with an inbuilt Peltier temperature control system was used. Motor adjustment of the instrument was conducted before starting the experiment to avoid errors. The temperature was then set at 60°C, and a 2 ml sample of bovine fibrinogen (2 mg/ml) was placed on the lower plate of the parallel plate geometry (PP50). The upper plate was then descended to a gap of 1 mm standard distance between the upper and the lower plates. The sample was sheared at 300 s^{-1} for a duration of 60 minutes, and at different time points, aliquots of samples were collected. For determining the flow behaviour of BFG, logarithmic shear ramp was performed from 500 to 1000 s^{-1} with 30 points per decade. The flow curve was determined at 0.5 mm gap.

4.6.3. Investigation of the aggregation behaviour of Bovine fibrinogen

4.6.3.1. Th-T fluorescence assay

Th-T fluorescence assay was done according to section 3.3.3.

4.6.3.2. Determination of hydrodynamic diameter

The dynamic light scattering (DLS) experiment was performed according to 3.3.5.

4.6.3.3. Analysis of secondary structure

To study the stability and analyse the secondary structural changes accompanying the thermal and thermomechanical induced aggregation, far UV-CD spectroscopic measurement was performed according to section 3.3.4. For the stability study, a temperature ramp rate of 1°C/min was set.

4.6.3.4. Morphology analysis

Morphology analysis was performed according to section 3.3.5.

4.7. Results and discussion

4.7.1. Stability determination through CD spectroscopy

To determine the stability with the rise in temperature, a CD scan was performed at far UV CD from 260 to 190 nm wavelength, with a temperature ramp from 25 to 105°C. **Figure 4.7 (A)** shows the different CD spectra of the BFG sample as a function of temperature rise. The native sample, at 25°C temperature, has the α-helical CD spectrum with two negative peaks at around 208 nm and 222 nm and a positive peak at 195 nm. As the temperature slowly ramps upwards, a gradual decrease in the above three peaks was observed. From **Figure 4.7 (A)**, three significant phases in the unfolding of BFG were observed, which were at temperatures 25.2 to 44.98°C, 55.06 to 85.02°C and the last phase from 95.09 to 105.03°C. To further analyse the data, the MRE at 222 nm was plotted as shown in **Figure 4.7 (B)**. A gradual decrease in MRE value was detected, signifying the loss in helical structure with an increase in temperature. Three distinct levels of unfolding were observed here. These distinct stages of MRE shift with temperature could be because of the sequential unfolding of the three main domains of the BFG molecule.

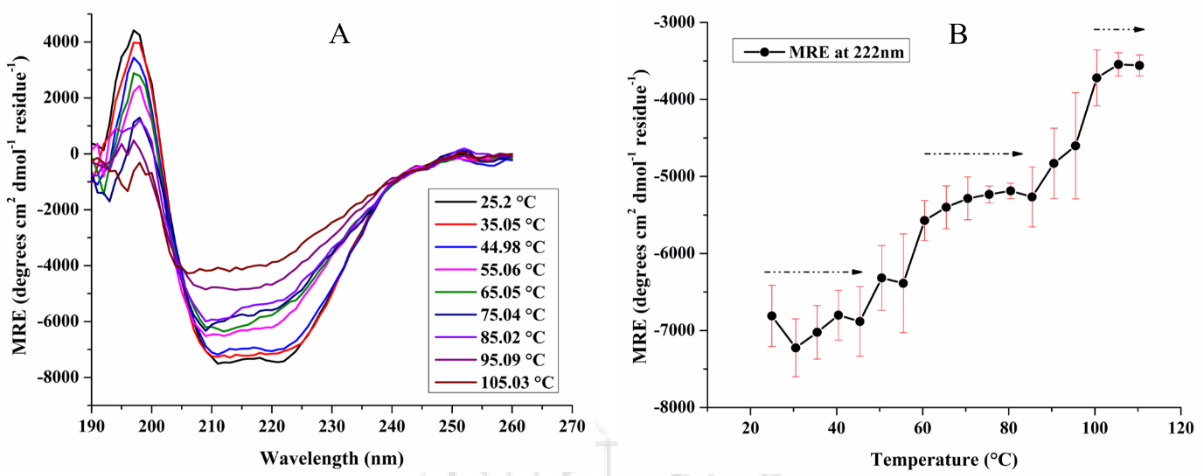

Figure 4.7. Thermal scanning of 0.2 mg/ml BFG from 25°C to 105°C (A) and the corresponding change in MRE (B).

4.7.2. Determination of Inhibition of aggregation and the hydrodynamic diameter

The aggregation kinetics of the BFG (bovine fibrinogen) protein was performed at three different temperatures, 45°C, 60°C and 90°C, which are responsible for the melting of the BFG. The shear effect, along with the thermal at 45°C and 60°C, were also performed. The Th-T fluorescence assay of BFG at the thermal-only incubation at 45°C, 60°C and 90°C are shown in **Figure 4.8. (A)** and the co-effect of both the shear and thermal at 45°C and 60°C in **Figure 4.8. (C**). Thioflavin T is a benzothiazole dye which binds to the cross β-sheet structures of amyloid fibrils (aggregates) [255, 256]. As can be seen from the graph, the Th-T fluorescence intensity did not increase much at 45°C, whereas increased fluorescence intensity was observed for the samples treated at 60 and 90°C. It shows the absence of aggregation in the case of 45°C and the aggregation at higher temperatures of 60 and 90°C. The aggregation intensity was found to be increased abruptly at 60 and 90 °C. This could mean that once the D domain and the C region unfolded, the E region and the αC domain unfold and aggregate readily. Similarly, a corresponding increase in the hydrodynamic diameter was observed in **Figure 4.8. (B**).

Native BFG has around 11 nm hydrodynamic diameter [48]. The turbidity, at 350 nm, was also performed at 45 and 60°C and is shown in **Figure 4.8. (D**). The turbidity was found to increase, corroborating the increase in aggregation as seen in the case of Th-T fluorescence.

For the thermomechanical-induced aggregation, enhanced aggregation was observed at temperatures 60°C, with respect to the thermal-only treated study at just a span of 60 min **Figure 4.8. (C**). However, at 45°C, even with shear, no significant aggregation was observed. Though no significant increase in Th-T was observed at thermal-only induced aggregation at 45°C, a slight increase in the hydrodynamic for the thermomechanical-induced aggregation was observed. At 30 min' treatment, the hydrodynamic diameter for thermal only was around 15.29 nm, whereas, for the shear and thermal aggregation, it was around 18.9 nm. For thermomechanical-induced aggregation at 60°C, the aggregate size increased from 31.68 nm to around 57 nm.

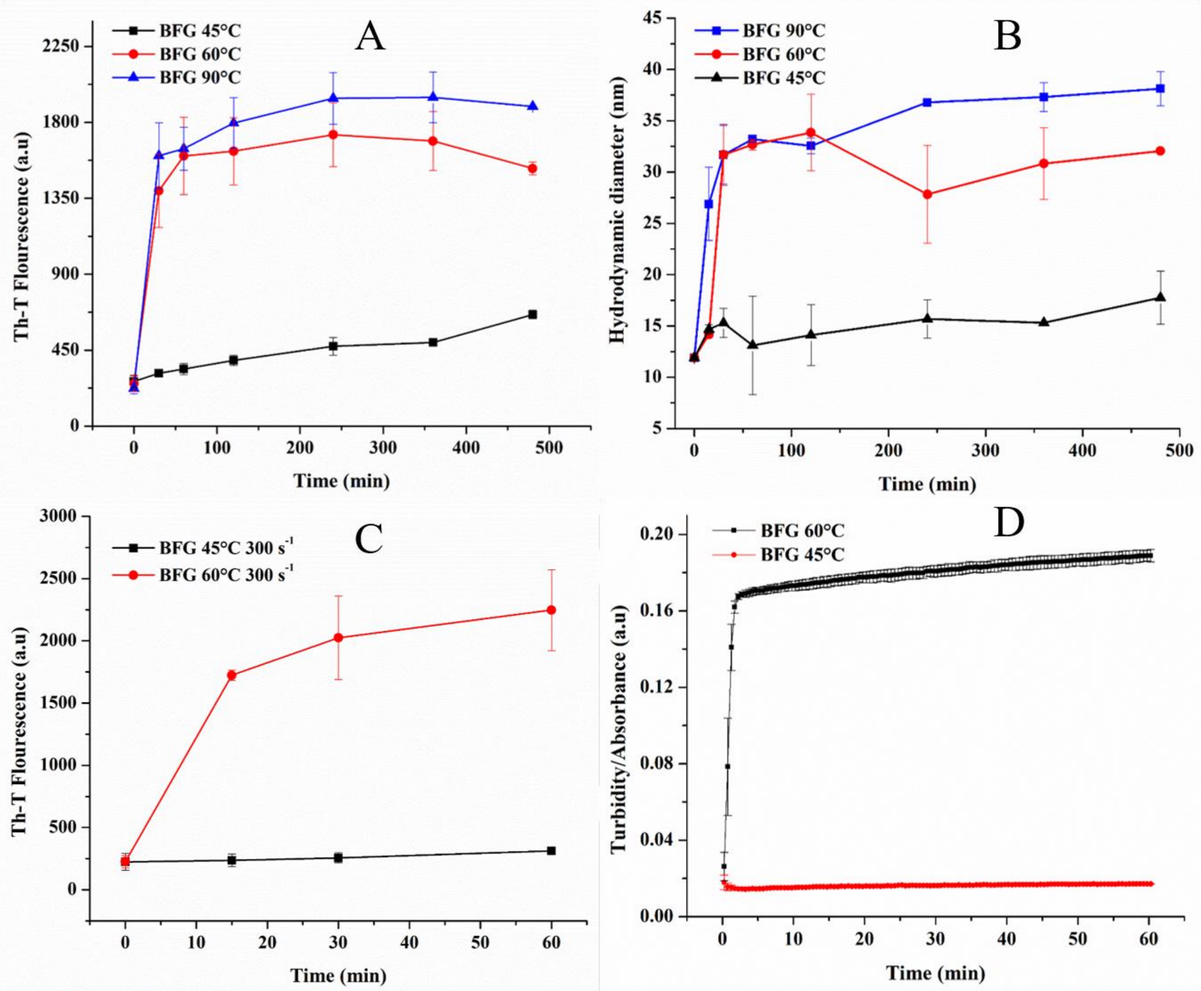

Figure 4.8. Th-T fluorescence assay of thermal induced BFG at 45, 60 and 90 °C (A); the corresponding change in hydrodynamic diameter (B); Th-T fluorescence assay of the shear and thermal induced BFG at 300 s^{-1} and 45 and 60 °C (C); and the turbidity assay of BFG at 350 nm conducted at 45 and 60°C (D).

4.7.3. Effect of constant shearing and flow behaviour

Bovine fibrinogen solution was sheared at constant shear rate of 300 s^{-1} and at 45°C and 60°C temperature to monitor the change in viscosity with the effect of thermomechanical condition. **Figure 4.9. (A)**, shows the increased in viscosity with increasing temperature at constant shear rate of 300 s^{-1}. As observed in the Th-T fluorescence assay, section 4.7.2, the aggregation at

45°C was found to be not much significant in the case of thermal as well as thermomechanical induced aggregation. Similarly, no rise in viscosity was observed in the case of BFG sample sheared at 300 s^{-1} and 40°C where as an increased in viscosity was observed for sample sheared at 60°C and 300 s^{-1} shear rate.

To determine the flow behaviour, BFG solution was sheared from 500 to 1000 s^{-1} at room temperature. The simplest rheological model, power law (equation 4.1) [231, 257] was used to fit the shear rate-shear stress data.

$$\tau = K\Upsilon^{n} \qquad [4.1]$$

$$log\tau = logK + nlog\Upsilon \qquad [4.2]$$

In equation 1, τ is the shear stress in Pascals, γ is the shear rate in s^{-1}, K is the consistency coefficient, and *‘n’* is the performance index. **Figure 4.9. (B**) shows the plot of log shear rate vs log shear stress. As observed from the performance index, *n*, it shows that BFG solution follows a Newtonian like behaviour as it is almost equals to 1 [231].

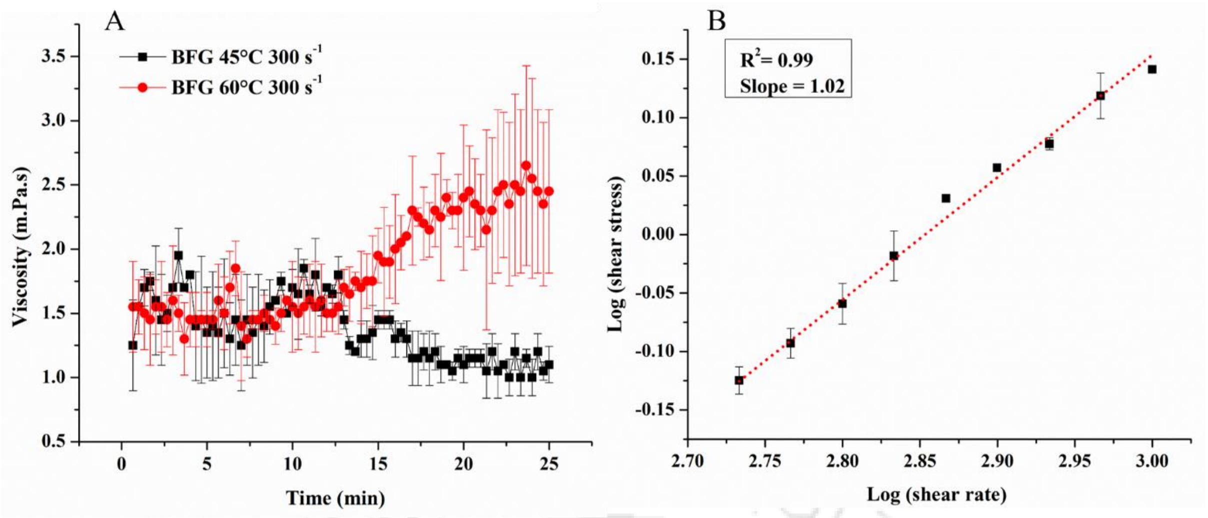

Figure 4.9. Viscosity as a function of time for 2mg/ml BFG sample solution, sheared at 300 s^{-1} and at temperature 45°C and 60°C (A); Flow curve of 2mg/ml BFG solution at room temperature, determined through shearing from 541 to 1000 s^{-1} shear rate (B).

4.7.4. Secondary structure analysis through circular dichroism

The secondary structure of the thermal induced aggregation of BFG at three different temperatures, 45, 60 and 90°C and the thermomechanical induced samples at 45 and 60°C and 300 s^{-1} was analysed through CD spectroscopy in the far UV region from 260-190 nm. **Figure 4.10.** shows the CD spectra of the thermal induced BFG at the mentioned three temperatures at three different times of: 0, 60 and 240 min. **Figure 4.10. (A)** shows the CD spectra at 45°C. Here, from the figure, it was observed that there was not much change in the secondary structure of the samples except that a little increase in α-helix content was observed. In **Figure 4.10. (B)**, the CD spectra of BFG samples treated at 60°C are shown, where the decrease in α-helix content was observed from the reduction in the depth at 208 and 222 nm, respectively. A significant decrease in the α-helix content was observed in the case of the samples incubated at 90°C temperature (**Figure 4.10. (C)**). The decrease in the MRE values of the three sample conditions is shown in **Figure 4.10. (D)**. The MRE value is calculated from the machine theta value given in Equation 4.3. Delta epsilon is the molar circular dichroism, MRW is the mean residue weight, P is the path length in (cm), and C is the concentration of protein in mg/ml. From the MRE at 222 nm, the total helix content was also calculated from Equation 4.5. The value of alpha helix content is shown in Table 4.1 below. The native BFG has around 27.35% α-helix. The percentage reduction in α-helix was 0.33, 11.67 and 17.89 % for samples incubated at 45, 60 and 90 °C, respectively, at 60 min.

In the case of the thermomechanical-induced sample at 45°C and 300 s^{-1} (**Figure 4.11. (A)**), the α-helix was first increased and then decreased with an increase in temperature, as observed from the change in the negative peak at 208 and 222 nm. For the 60°C and 300 s^{-1} (**Figure 4.11. (B)**) samples, the increase in the negative peak at 208 and 222 nm was observed, signifying the decrease in alpha helix with aggregation. **Figure 4.11. (C)** shows the corresponding change in MRE at 222 nm. The α-helix content of the different thermomechanical-induced samples is shown in Table 4.2. The percentage decreased in α-helix was calculated using equation 4.3., and was found to be 1.75 and 12.37 % for samples sheared at 300 s^{-1} and at 60°C, respectively.

$$\alpha - helix\,\% = -\frac{MRE222-4000}{39000} * 100 \tag{4.3}$$

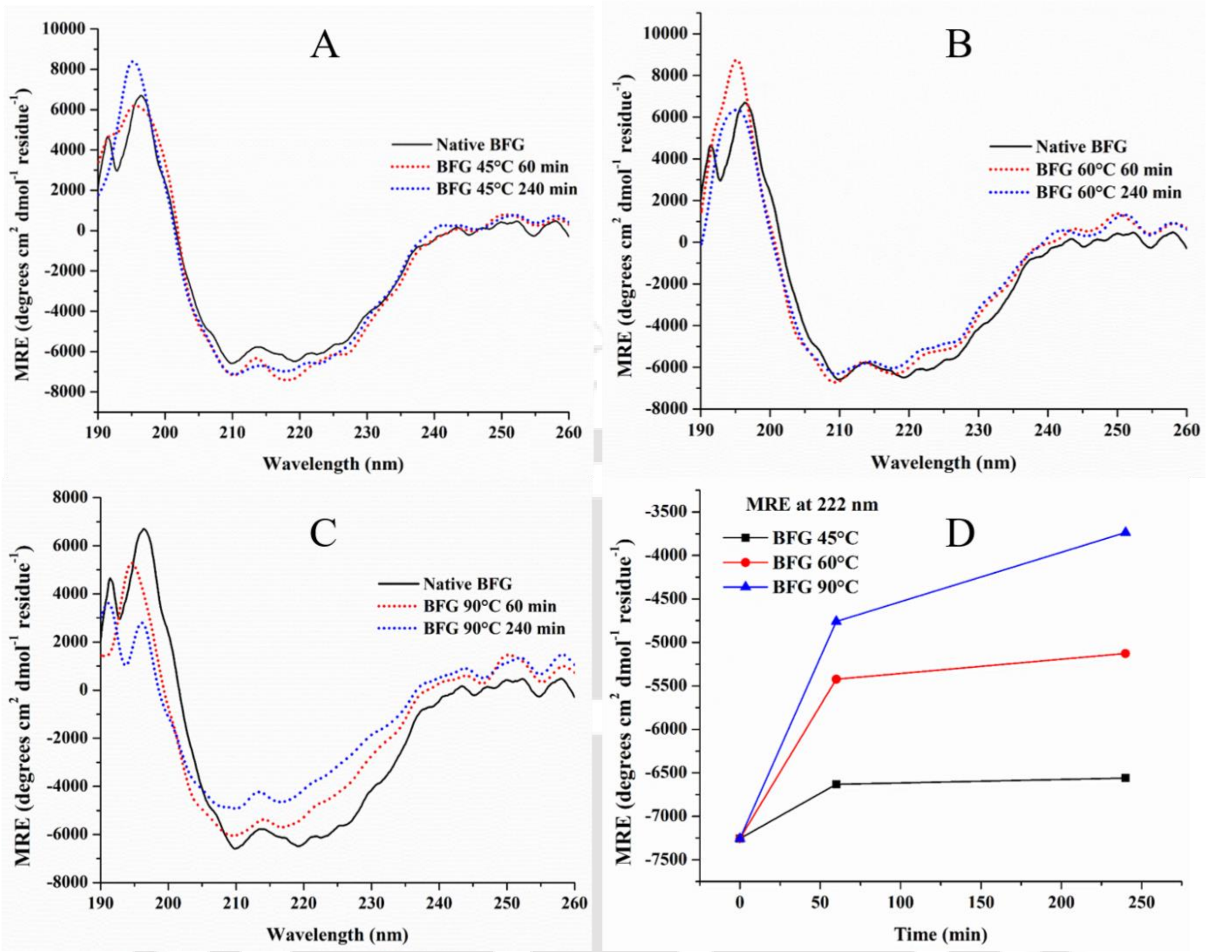

Figure 4.10. The change in the CD spectra for the native, 60 min and 240 min thermal-induced BFG samples at 45°C (A), 60 °C (B), and 90 °C (C); the corresponding change in MRE of the three samples induced at the above three temperatures (D).

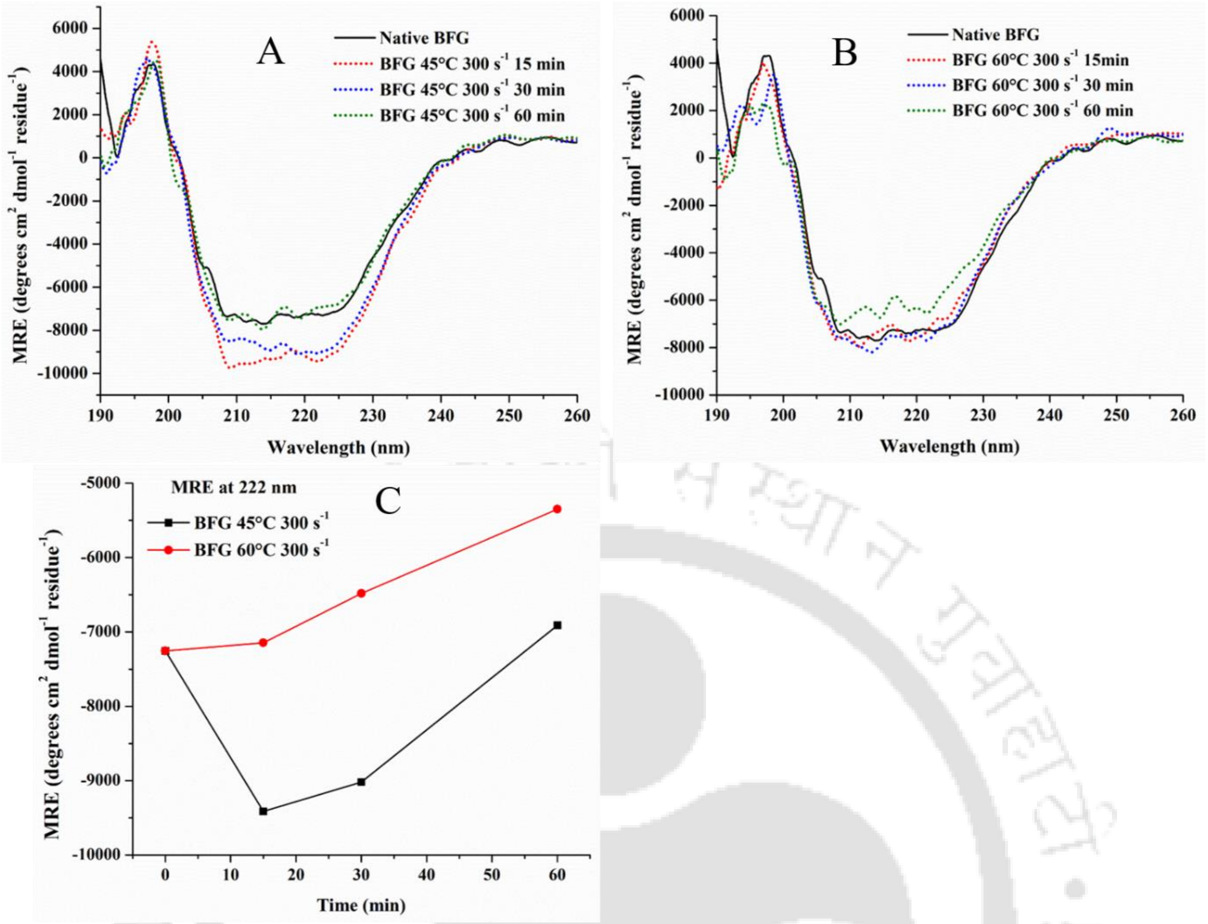

Figure 4.11. The change in the CD spectra for the native, 15 min, 30 min and 60 min, thermos-mechanical induced BFG samples at 45°C (A) and 60 °C (B); the corresponding change in MRE of the above samples induced at the above three temperatures (C).

Table 4.1. α-helix content of the thermal-induced BFG samples at 45, 60 and 90 °C.

Samples	60 min	240 min
45°C	27.3	27.1
60°C	24.2	23.4
90°C	22.5	19.8

Table 4.2. α-helix content of the thermomechanical-induced BFG samples at 45 and 60°C and a shear rate of 300 s^{-1}.

	15 min	30 min	60 min
45°C - 300 s^{-1}	34.4	33.4	28.0
60°C - 300 s^{-1}	28.6	26.9	24.0

4.7.5. Morphology analysis

The morphology of the BFG samples in different conditions is checked through AFM. The images obtained are then analysed through Gwydion software. **Figure 4.12. (A)** shows the AFM images of native BFG, which has an average diameter in the range 24 to 70 nm which is quite high from that obtained from the DLS data (~11 nm). The apparent increase in monomeric size could be because it is the apparent lateral width distorted by the tip convolution. The sample incubated at 60°C is shown in **Figure 4.12. (B)**. Here, the native BFG samples seem to connect to one another to form a distorted native structure with length in the range of 89 to 200 nm. **Figure 4.12. (C)** is the BFG sample sheared at 300 s^{-1} and 60°C. The morphology here seems like amorphous protein aggregates with short dissimilar structures of length varying from 98 to 150 nm, and the diameter is around 30-40 nm.

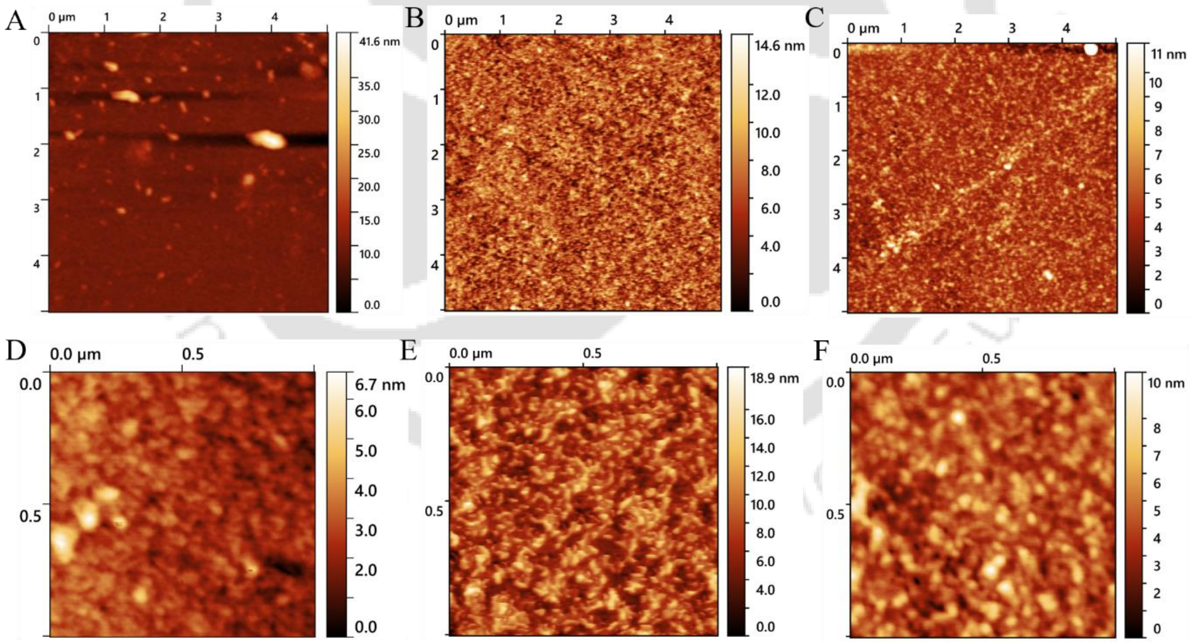

Figure 4.12. Atomic force microscopy of the native BFG sample (A); the thermal induced BFG sample at 60 °C (B); and the shear and thermal induced BFG at 300 s^{-1} and 60 °C (C). Figures (D), (E) and (F) are the corresponding magnified images of the labels in the capital.

4.8. Conclusions

Thermal and shear-induced aggregation of Bovine fibrinogen was performed. The thermal aggregation was carried out at three temperatures which are 45°C, 60°C and 90°C respectively. The thermal and shear-induced aggregation was carried out at 300 s^{-1} and 60°C using an Anton Paar rheometer equipped with a parallel plate geometry. Thermal scanning of BFG was performed through CD spectroscopy from 25°C to 105°C. From the scanning, the three important domains unfolding of BFG were known, which have three transitions in unfolding or aggregation. Three temperatures were chosen from these, and the thermal and shear-induced aggregation was carried out. The aggregation kinetics was determined from the Th-T fluorescence assay, which shows not much aggregation at 45°C and shows enhanced aggregation in the case of 60 and 90 °C. The same trend could also be observed in the case of the turbidity obtained at 350 nm when BFG was monitored for turbidity at 45 and 60°C. In the case of shear-induced aggregation at 60 °C, the intensity of fluorescence was found to be higher at just a span of 60 minutes compared to the thermal induced. Whereas in the case of thermal and shear induced at 45°C and 300 s^{-1}, no significant aggregation was observed. BFG was found to follow a Newtonian like behaviour. The secondary structure shows not much change in the case of the thermal heated BFG at 45°C, though a little increase in the α-helix content was observed. In the case of the sample heated at 90 °C, the α-helix was significantly diminished. The morphology of the samples was also checked through AFM, where it was observed to be more like amorphous aggregates.

CHAPTER-5

Extraction and characterisation of a neuroprotective plant Centella asiatica

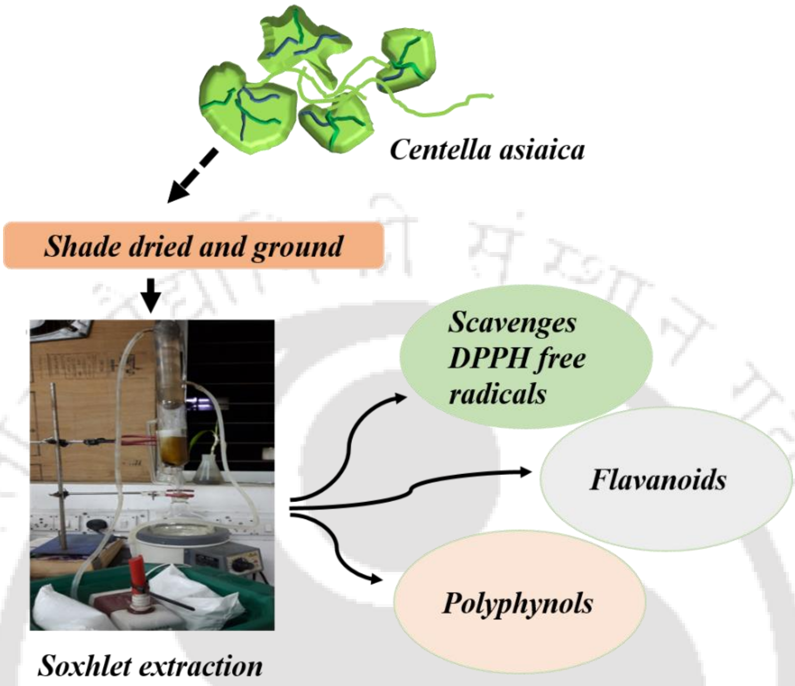

In this chapter, *Centella asiatica*, a neuroprotective herbaceous plant, was extracted through the soxhlet method using three solvents with increasing polarity. These crude extracts were then checked for their antioxidant property, phenolic content, and flavonoid content. The crude extracts were then analysed through HPLC, and two of the crude extracts, which showed maximum inhibition of protein aggregation, were additionally analysed through HRLCMS to identify the bioactive components present in the extract.

5.1. Introduction

Centella asiatica (CA) is an herbal medicine that has been used mostly in Asian countries for hundreds of years. Commonly known as Indian pennywort, Gotu kola in Hindi and Peruk in Manipuri belong to the Apiaceae family. In the ancient Ayurvedic medical book (Caraka Sumita), CA was already specified as an herbal medicine for treating dementia [208]. Today, people have used these plants in various forms in daily life for cognitive enhancement. It contains pentacyclic triterpenes such as Asiatic acid, Asiaticoside, Madecassic acid and Madecassoside. Previous studies have shown that it has anti-inflammatory, antioxidative (like free radical scavenging, reduction in lipid peroxidation, etc.), anticancer, anxiolytic, memory enhancement properties [209, 210], neuroprotection, cardioprotective, hepatoprotective, sedative, antiviral and antifungal property [299-302]. CA has been used to enhance cognitive function and improve intelligence since the ancient period and has been experimentally proved in 28 human samples that it uplifts mood and enhances memory. In a study, CA extracts were evaluated for their impact on memory power and learning abilities in rats using different conditions. Normal rats were used to provide predictive conclusions related to human patients suffering from Alzheimer's and dementia. It was shown that the aqueous extract of the whole plant has two distinct, profound effects: the capability to enhance learning and memory power. This was because of the antioxidant property of CA, which decreases lipid peroxidation and boosts the already present antioxidant enzymes in the central nervous system [211]. In a study conducted in male Spraque–Dawley rats, Asiatic acid has increased memory and learning power [303]. CA also showed improvement in brain function in young mice when administered at 200 mg/kg extract. For drug development against AD, inhibition of acetylcholinesterase (AChE) and its sister enzyme butyrylcholinesterase (BChE) has become a rational target as they are the key enzyme in the pathogenesis of AD [304]. As decreased in the level of acetylcholine (ACh), a neurotransmitter, is hydrolysed by AChE, its level was decreased in the brains of patients diagnosed with AD. At 150 µg/ml CA concentration, 50% AChE was inhibited, which was determined through the Ellman method [305]. Because of its antioxidant properties, CA has been found to increase catalase and glutathione levels and, at the same time, decrease the level of MDA in an in vivo study done in rats [300]. Therefore, for this doctoral work, we have chosen CA to check its effect on the aggregation of shear and thermal-induced aggregation of different proteins.

Dried CA leaves were extracted through the soxhlet method using a solvent system with increasing polarity: ethyl acetate, methanol and water. These crude extracts were then checked for their antioxidant property through the DPPH radical scavenging assay, total phenolic content through the Folin–Ciocalteu method, and total flavonoid content through the Aluminium chloride colorimetric assay. The extracts were then named according to the corresponding solvents from which they were sequentially extracted. The three crude extracts were *Centella asiatica* ethylacetate extract (CEE), *Centella asiatica* methanol extract (CME) and *Centella asiatica* water extract (CWE). The extracts were also analysed through HPLC, and two crude extracts (CEE and CWE), which show maximum inhibition of protein aggregation (discussed in Chapter 6A), were additionally analysed through HRLCMS to identify the bioactive components present in the extract. **Figure 5.1 (A)** shows the soxhlet apparatus setup and **(B)** is the vacuum rotary evaporator.

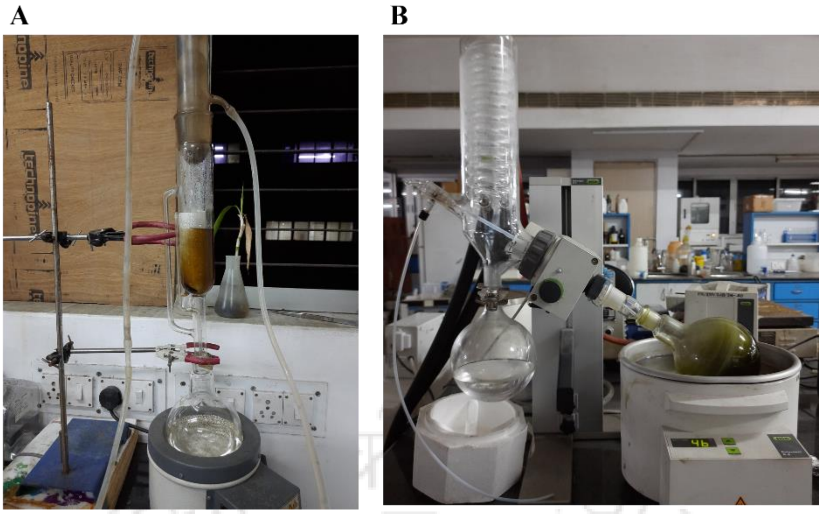

Figure 5.1. (A) Soxhlet setup for *Centella asiatica* extraction and (B) Vacuum rotary evaporator

5.2. Materials and methods

Folin-ciocalteu (F9252-500ML) was purchased from Sigma-Aldrich, India. Acetonitrile, HPLC grade, SAP code (40030LC250) was obtained from FINAR, 1-diphenyl-2 picrylhydrazyl (DPPH) (29128-250MG) was obtained from Alfa Aesar, India, potassium acetate (GRM1091) and quercetin dihydrate (RM6191) was purchased from Himedia, India. Milli Q water (18Ω) was used in all the experiments. All other chemicals used were of analytical grade.

5.2.1. Collection of plant material and extraction

CA (the Indian pennywort), or "Peruk" in Manipur, was plucked from the northeast Indian region of Manipur. Only this perennial medicinal herbs leaves were separated and washed thoroughly in running tap water before it was finally rinsed with Milli Q water. The leaves were then shed-dried in a cool place for about a week. The dried leaves were then ground in a mixture, weighed about 10 g and prepared for solvent extraction through the soxhlet method.

Three solvents, namely ethyl acetate, methanol and water, were used for the extraction. The extraction started from ethyl acetate, a non-polar solvent, and moved towards more polar water. The extracted sample in each solvent step was filtered in a Whatman filter paper, lyophilised and stored at -20°C. The solvent was removed through a vacuum rotary evaporator for ethyl acetate extract and methanol extract.

5.2.2. Characterisation of the crude extracts

5.2.2.1. Determination of phenolic content, flavonoid content and DPPH assay

The total phenolic content of the three different CA extracts (CWE, CME, and CEE) was determined using the Folin–Ciocalteu method. In 25 µl volume of extracts, 100 µl, 10% v/v Folin–Ciocalteu reagent was added, mixed for 60 seconds, and kept for about 5 minutes. Next, 75 µl 7.5 % w/v, $NaCO_3$ was added and incubated for 2 hours in the dark at room temperature [306]. Then, the absorbance was measured at 730 nm using a multi-plate reader (TECAN, Infinite 200 pro). For the calibration curve, Gallic acid at different concentration ranges (10 to 50 µg/ml) was prepared, and the total phenolic content was expressed as µg Gallic acid equivalent/mg extract. Aluminium chloride colorimetric assay was performed to determine the flavonoid content of the three different crude extracts of CA. To a 50 µl extract, 130 µl of methanol was added, and after that, 10 µl 1M potassium acetate was added, followed by the addition of 10 µl 10 % aluminium nitrate [307]. Next, the samples were incubated for 40 minutes at room temperature, and then absorbance was measured at 415 nm in a microplate reader (TECAN, Infinite 200 pro). Quercetin at different concentrations range of (10 to 50 µg/ml) was prepared for determining the calibration curve. The flavonoid content was expressed as µg quercetin equivalent/mg extract. Next, a DPPH antioxidant assay was performed to measure the antioxidants' ability to scavenge free radicals by producing a deep violet colour when a stable free radical is present. When a DPPH solution comes into contact with a free radical scavenging agent, it turns brilliant yellow. The Gallic acid concentrations of 2, 4, 6, and 8 (µg/ml) were added to the DPPH solution. When DPPH reacts with an antioxidant, hydrogen is released, resulting in a lower absorbance value at 515 nm and brilliant yellow colour, indicating a significant DPPH scavenging activity. To determine the antioxidant activity of the produced extract, several diluted quantities of CA extract were combined with DPPH [308].

5.2.3. HR-LCMS (High-resolution liquid chromatography and mass spectrometry) analysis

For HR-LCMS analysis, samples were sent to the Sophisticated Analytical Instrument Facility (SAIF), IIT Bombay, Powai, Mumbai. The CEE and CWE were prepared by Agilent high-resolution liquid chromatography and mass spectrometry model- G6550A with 0.01% mass resolution. For the acquisition of the run, the MS- minimum range was set from 50 (M/Z) and maximum 1000 dalton (M/Z) with scanning of a spectrum per second. The Gas chromatography was maintained at a temperature of 250°C with a gas flow rate of 13 psi/minute.

5.2.4. HPLC (High pressure liquid chromatography) analysis

Crude samples at 5 mg/ml were prepared in methanol for CEE extract, and the CWE extract was prepared in Milli Q water. The samples were then filtered through a 0.2-micron filter. For the stationary phase, a Kinetex 5µ C18 100A column of size 150 x 4.6 mm was used, and the mobile phase was 60 % ACN and 40 % water for running CWE extract and for CEE extract, the ACN to water ratio was 70:30. The bioactive samples were detected through UV at 220 and

206 nm, respectively. The flow rate was set at 0.2 ml/minute. The solvent was properly filtered through a 0.2-micron cellulose filter and was degassed for 30 minutes using a bath sonicator. For CWE eluted fractions (for further analysis), the samples eluted from HPLC were evaporated using a vacuum concentrator (SpeedVac Concentrator, Thermo Fisher, SPD1010) for further analysis.

5.3. Results and discussion

5.3.1. Total phenolic, flavonoids, and antioxidant activity

The total phenolic and flavonoid contents of the three crude extracts, CEE, CME and CWE, were determined by the Folin–Ciocalteu and aluminium nitrate colorimetric assay, respectively. **Table 5.1** shows the analysis results of the three different extracts. The total phenolic content obtained was 224 ± 7 µg GA/mg for CWE, which was the highest among the three extracts, followed by CEE (215 ± 1 µg GA/mg) and CME (208 ± 3 µg GA/mg). The total flavonoid contents obtained were 147 ± 8, 135 ± 5, and 86 ± 1 µg QUE/mg for CWE, CEE and CME, respectively. A comparable range was obtained in a study by Sristisri et al., where CA leaves were extracted through 80% ethanol. The total phenolic content obtained was in the range of (199-277) mg/g catechol equivalent, and the flavonoid content obtained was 144 mg/g quercetin equivalent[309]. In another study, the whole *C. asiatica* plant was extracted using methanol as the solvent and was fractionated in different solvents, including chloroform and ethyl acetate. The phenolic content obtained in the above two solvents was in the range of 116-115 mg/g Gallic acid equivalent, and the flavonoid content was in the range of 193-345 mg/g quercetin equivalent [310]. However, the flavonoid content in their study was higher than the phenolic content.

The free radical scavenging activity of the three crude extracts was determined through the DPPH assay. DPPH is a free radical with nitrogen in its centre and maximum absorption at 517 nm. When the odd electron of DPPH pairs with a radical scavenger to form the reduced DPPH form (DPPH-H), the purple colour of DPPH turns yellow [311]. The IC_{50} values of scavenging activity obtained for CWE, CEE, and CME were 293 ± 15, 345 ± 41, and 792 ± 25 µg/ml, respectively. In another study, the IC_{50} values of different CA samples (fresh sample, freeze-dried, microwave-dried, heat-dried and microwave-assisted-hot air hybrid drying) were reported to be in the range of 130 to 880 µg/ml [312], which shows comparable activity with the present study. The CWE and CEE extracts showed higher phenolic and flavonoid contents than the CME extract. The higher phenolic and flavonoid contents in these two extracts thus have more scavenging power than CME.

Table 5.1. Total phenolic and flavonoid content and the DPPH free radical scavenging activity of the CWE, CEE and CME.

Sample	Total phenolic content (µg GA/mg)	Total flavonoid content (µg QUE/mg)	DPPH radical scavenging activity IC_{50} (µg/ml)
CWE	224 ± 7	147 ± 8	293 ± 15
CEE	215 ± 1	135 ± 5	345 ± 41
CME	208 ± 3	86 ± 1	792 ± 25

5.3.2. Extract analysis from HPLC and HRLCMS

From the aggregation studies discussed in the later section (Chapter 6A), we observed that CWE and CEE showed effective anti-aggregation ability compared to the CME extract; therefore, to further investigate the compound or compounds present in the extract, HPLC and HRLCMS were performed. The HPLC of the three crude samples were performed, the chromatogram of which was shown in **(Figure 5.2.)**. From the HPLC analysis, we observed that compound CWE has less number of peaks as compared to CEE, and later on in chapter 6, we showed that CWE has almost comparable activity with CEE. Therefore, we chose CWE crude extract as the best of the three. Henceforth, the prominent peaks obtained from CWE were eluted separately for further analysis. **Figure 5.2. (B)** shows the HPLC chromatogram of the CWE extract, where we observed four major peaks designated as A, B, C and D, respectively. These peaks were then separately eluted to further analyse the components through ITC and HRLCMS (the detailed study of which is discussed in Chapter 6A). The HRLCMS analysis of the crude CWE and CEE was performed, and the compound has been listed in **(Table 5.2.)**. The major compounds obtained from both positive and negative modes have been listed according to their abundance. In the CEE, three of the significant marker compounds of CA, Asiatic acid, Medecassoside, and Asiaticoside, were present, among which Asiatic acid is the most abundant compound. In the CWE extracts, the marker compound Asiaticoside is present apart from other important polyphenolic compounds like Chlorogenic acid, Quinic acid, Ellagic acid, Kaempferol, etc.

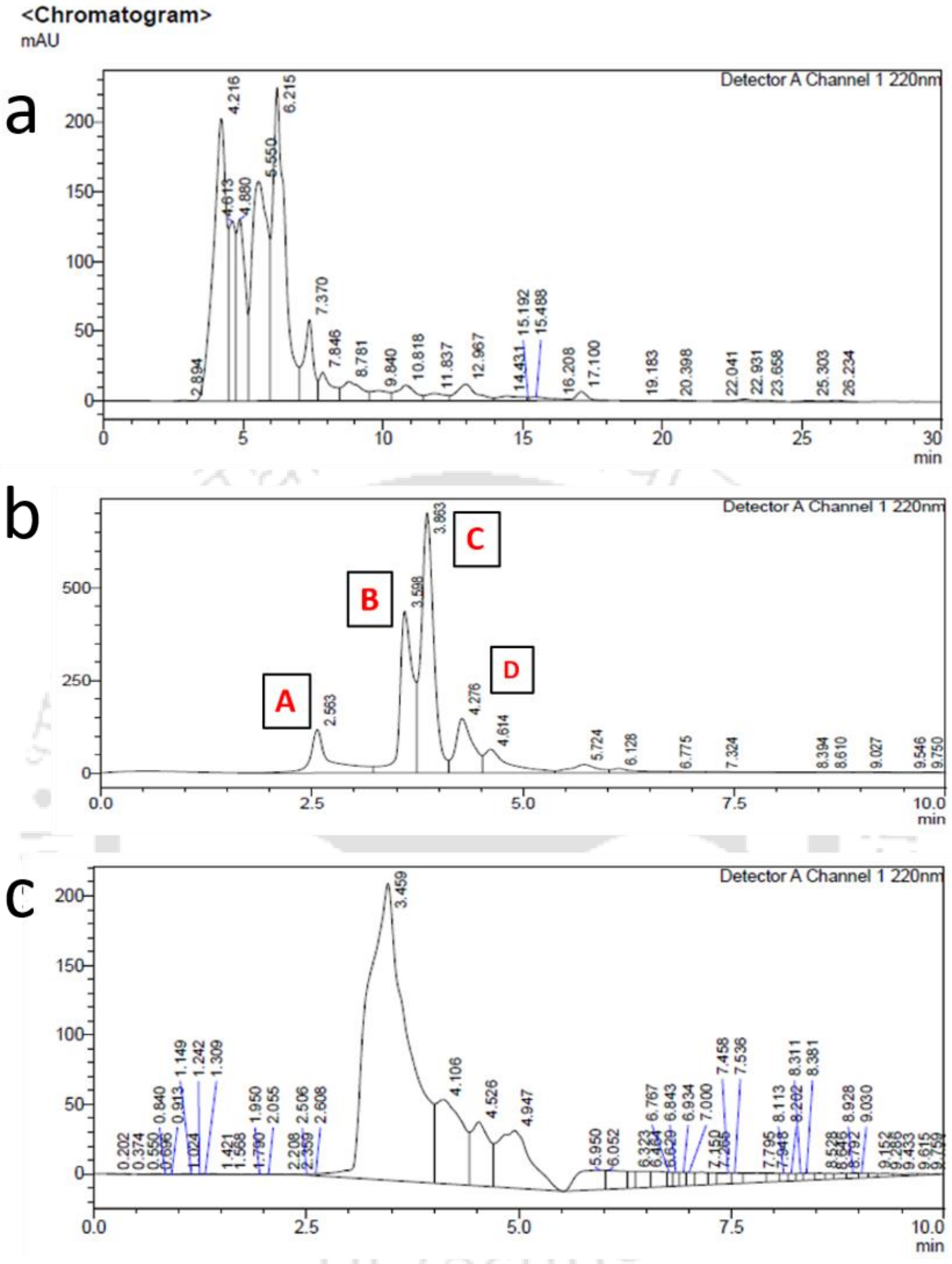

Figure 5.2. HPLC Chromatogram of (a) CEE, (b) CWE crude extract; A, B, C and D denotes the major fraction obtained in this crude extract and (c) CME crude extract.

Table 5.2. Compounds obtained from HRLCMS analysis for the (A) crude CEE extract, (B) crude CWE extract and (C) eluted fraction B of CWE extract

(A) Compounds present in CEE crude extracts

Mass	Abundance	Name	Formula
286.0472	260553	Maritimetin	$C_{15} H_{10} O_6$
488.3495	47687	Asiatic acid	$C_{30} H_{48} O_5$
530.1405	12103	4-O-Caffeoyl-3-Oferuloylquinic acid	$C_{26} H_{26} O_{12}$
354.0933	9340	Trans-Chlorogenic acid	$C_{16} H_{18} O_9$
974.5062	8429	Medecassoside	$C_{48} H_{78} O_{20}$
958.5115	7421	Asiaticoside	$C_{48} H_{78} O_{19}$
516.1222	6203	1,4-Di-O-caffeoylquinic acid	$C_{25} H_{24} O_{12}$

(B) Compounds present in CWE crude extracts

Mass	Abundance	Name	Formula
354.0975	89501	Chlorogenic acid	$C_{16} H_{18} O_9$
192.0637	87853	Quinic acid	$C_7 H_{12} O_6$
110.0371	65432	Resorcinol	$C_6 H_6 O_2$
448.1047	56207	Kaempferol 7-O-glucoside	$C_{21} H_{20} O_{11}$
134.022	28499	Malic acid	$C_4 H_6 O_5$
180.0433	22253	Caffeic acid	$C_9 H_8 O_4$
516.1308	18667	1,4-Di-O-caffeoylquinic acid	$C_{25} H_{24} O_{12}$
958.5154	14973	Asiaticoside	$C_{48} H_{78} O_{19}$
168.042	14347	Vanillic acid	$C_8 H_8 O_4$

(C) Compounds present eluted fraction B of CWE crude extracts

Mass	Abundance	Name	Formula
134.0218	21320	Malic acid	$C_4 H_6 O_5$
354.0964	9164	Chlorogenic acid	$C_{16} H_{18} O_9$
448.1036	8151	Kaempferol 7-O-glucoside	$C_{21} H_{20} O_{11}$
154.0268	7573	2,6-dihydroxybenzoic acid	$C_7 H_6 O_4$
192.0637	7451	Quinic acid	$C_7 H_{12} O_6$
516.1286	4396	1,4-Di-O-caffeoylquinic acid	$C_{25} H_{24} O_{12}$
602.13	2948	Eriodictyol 7-(6-galloylglucoside)	$C_{28} H_{26} O_{15}$
286.0496	2801	Kaempferol	$C_{15} H_{10} O_6$
168.0593	2087	3-Fluoro-1-(4-hydroxyphenyl)-1-propanone	$C_9 H_9 F O_2$
294.2198	2738	10-Oxo-11-octadecen-13-olide	$C_{18} H_{30} O_3$
180.0421	1939	Caffeic acid	$C_9 H_8 O_4$
302.0084	1702	Ellagic acid	$C_{14} H_6 O_8$

170.0226	1497	Gallic acid	$C_7 H_6 O_5$
958.5098	946	Asiaticoside	$C_{48} H_{78} O_{19}$
250.194	878	3-Methyl-alpha-ionyl acetate	$C_{16} H_{26} O_2$
290.08	634	Catechin	$C_{15} H_{14} O_6$
178.0262	499	7,8-Dihydroxycoumarin	$C_9 H_6 O_4$

5.4. Conclusions

The aerial part of CA was collected from the northeast region of India, Manipur. Dried leaves were then extracted through the soxhlet method, using three solvents and thus, in accordance with the solvent from which it was extracted, it was named *Centella asiatica* ethyl acetate extract (CEE), *Centella asiatica* methanol extract (CME) and water extract (CWE). The total phenolic content obtained was 224.01 ± 7.11, 215.50 ± 1.06 and 208.36 ± 3.40 µg GA/mg, respectively, for CWE, CEE and CME, which was determined through FC assay. From the Aluminium nitrate colorimetric assay, the total flavonoid was determined, and the content was 147.11 ± 8.38, 135.88 ± 5.76, and 86.55 ± 0.58 µg QUE/mg for CWE, CEE and CME, respectively. The result showed that CWE and CEE are comparatively more rich in polyphenols and flavonoids. The DPPH radical scavenging data shows that CME has a higher IC_{50} value for scavenging the DPPH, which is 792.14 ± 25.65 µg/ml, whereas CWE and CME have lesser IC_{50} values, which were 293.97 ± 15.51 and 345.56 ± 41.63 µg/ml. We observed from the HPLC results that many compounds are present in CEE compared to CWE and CME. However, since CEE and CWE showed almost comparable results and CWE has less compound than CEE, CWE has been selected for further analysis. CWE has four peaks, which we have eluted separately and designated as A, B, and D. HRLCMS analysis of the crude CEE shows that Meritimetin is the most abundant compound, followed by Asiatic acid. Many other important terpenes like Medecassoside and Asiaticoside were also found in CEE extracts. In the case of CWE extract, malic acid was abundant, followed by Chlorogenic acid.

CHAPTER-6

Effect of Centella asiatica (CA) on the non-amyloidogenic and amyloidogenic proteins (BSA and HEWL) and in-vitro study of the cytotoxicity of the aggregates formed due to shearing of the above proteins on neuroblast cell line (IMR32)

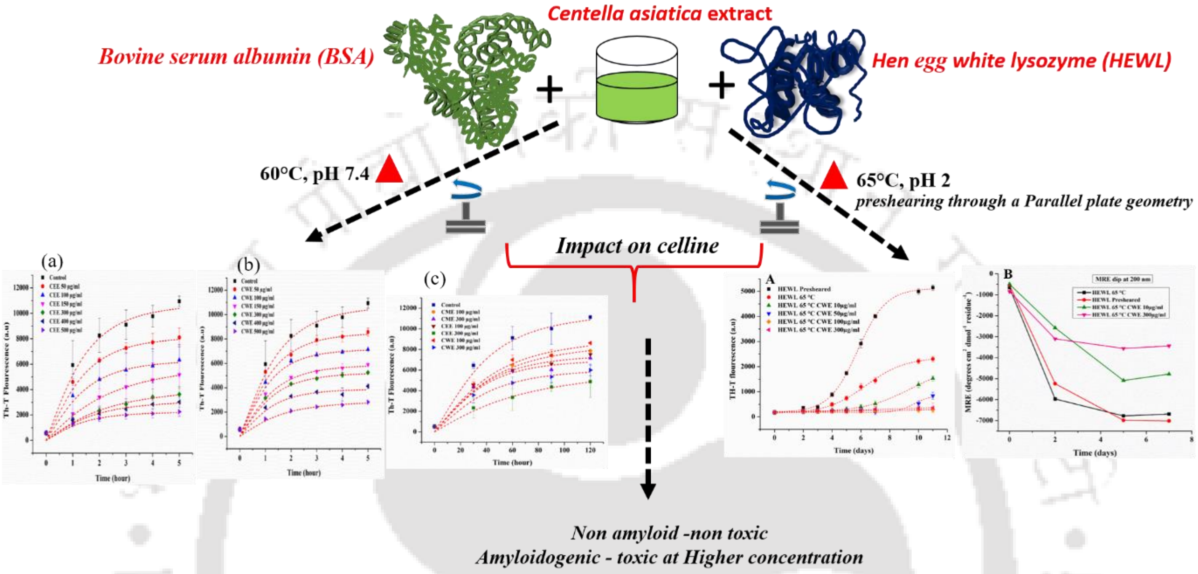

In this chapter, the effect of CA on the aggregation of a non-amyloidogenic protein (BSA) and an amyloidogenic protein (HEWL) was studied. Consequently, the toxicity of the shear-induced protein aggregates of the non-amyloidogenic BSA and the amyloidogenic HEWL was tested on a neuroblast cell line IMR32. This chapter has three subchapters, which completes chapter six as a whole.

6.1. CHAPTER-6A

Attenuation of thermal and thermomechanical induced aggregation of Bovine serum albumin by three different extracts of Centella asiatica, a neuroprotective plant

The inhibition action of *Centella asiatica* (CA) extract against thermal and shear-induced aggregation of BSA at 60°C and a shear rate of 300 s^{-1} was studied. Three types of extract were tested, namely, CA ethyl acetate extract (CEE), CA methanolic extract (CME), and CA water extract (CWE), which were extracted sequentially with increasing polarity of the solvent. The combined analysis of HPLC, HRLCMS, docking and ITC was employed to narrow down the probable compound responsible for the anti-aggregation ability.

6.2. Introduction

Protein aggregation inhibition and prevention through phytocompounds have been investigated extensively recently [177-180]. Polyphenols can interact with proteins and peptides and thereby enhance biological activity. Protein misfolding and aggregation are one of the root causes and hallmarks of neurodegenerative diseases, which include Alzheimer's, Parkinson's, and Huntington's illnesses. Therapeutic intervention can be made if small molecule inhibitors such as phytochemicals can interact with these proteins and peptides, by modulating the native protein structure or by degrading or preventing already formed toxic aggregates which can impact the early interactions of proteins with one another in such disease conditions [182]. CA is a perennial herbaceous plant known for its neuroprotection and nootropic effect. It has been used in Ayurveda and ancient traditional medicines in many parts of the world [215].

In the present study, BSA was subjected to thermal and thermomechanical-induced aggregation and the impact of different CA extracts on BSA aggregation was determined. The aggregation induced by thermal conditions were conducted within an oven, while for both thermal and shear-induced aggregation, the MCR72 rheometer was employed. Different fractions of CA [*Centella asiatica* ethyl acetate (CEE), *Centella asiatica* methanol extract (CME) and *Centella asiatica* water extract (CWE)] extracted through different solvents with increasing polarity were used. The extraction was carried out so that the extract would consist of compounds with different polarities. The aggregation kinetics was assessed through Thioflavin T (Th-T) fluorescence assay, the change in the secondary structure of the protein was analysed through Circular dichroism (CD) and the aggregate size was analysed through Dynamic light scattering (DLS) analysis. To narrow down the probable compound responsible for the inhibition of aggregation, High-resolution liquid chromatography-mass spectrometry (HR-LCMS) in combination with High-performance liquid chromatography (HPLC) and ITC was performed (Chapter 5). Docking was also performed for the probable compound, which gave the highest aggregation inhibition, and the binding mechanism was analysed through Stern-Volmer (SV) quenching studies.

6.3. Materials and Methods

Lyophilised BSA powder fatty acid-free (A2153), Th-T dye (catalogue no. T3516) was purchased from Sigma-Aldrich, India. Milli Q water (18Ω) was used in all the experiments. All other chemicals used were of analytical grade.

6.3.1. Preparation of BSA solution

1mM stock solution of lyophilised BSA was prepared in 20 mM Tris-HCl buffer (pH 7.4). It was then filtered through a 0.2 µm syringe filter, and the absorbance was recorded at 280 nm using a UV spectrophotometer to estimate the final stock concentration using Beer Lambert's law at an extinction coefficient value of 43,824 M^{-1} cm^{-1} [269]. A 75 µM (~5 mg/ml) working concentration was prepared before every experiment.

6.3.2. Collection of plant material and extraction

The collection of plant material and extraction has been discussed in Chapter 5.

6.3.3. Preparation of *Centella asiatica* extract

50 mg/ml stock solutions of all three extracts (CEE, CME and CWE) were prepared. For CWE, it was dissolved in Tris-HCl buffer itself, whereas the other two extracts were dissolved in dimethyl sulfoxide (DMSO). The maximum percentage of DMSO used was 1%. For the experimental studies, different concentrations of the extracts (50 µg/ml, 100 µg/ml, 150 µg/ml, 300 µg/ml, 400 µg/ml, and 500 µg/ml) were tested with the native BSA solution (75 µM) for thermally induced aggregation study at 60°C, and for thermomechanical study at 300 s^{-1} and 60 °C. The extract concentrations studied were 100 µg/ml and 300 µg/ml for the thermomechanical-induced aggregation.

6.3.4. Effect of thermal and shear on the aggregation of BSA in the presence and absence of *Centella asiatica* extract

For thermal-induced aggregation, different solutions containing the same amount of BSA and increasing extract concentrations were prepared for all three different crude CA extracts. The thermal aggregation was performed in an oven set at 60°C. Samples were collected every hour till the 5th hour. For the thermal and shear study, samples were prepared similarly and subjected to 300 s^{-1} and 60°C. For this experiment, a Rheometer (MCR 72, Anton Paar) with an inbuilt Peltier temperature control system was employed. Before starting the experiment, the instrument motor adjustment was performed to overcome the error. Then, the required temperature was set, and a 2 ml sample of BSA solution (75µM) was gently placed on the lower plate of the parallel plate geometry (PP50). Then, gradually, the upper plate descended to a 1 mm standard distance gap between the two plates. The samples were then sheared at 300 s^{-1} separately for 30, 60, 90, and 120 minutes and collected for further analysis.

6.3.5. Investigation of the aggregation behaviour

6.3.5.1. Th-T fluorescence assay

Th-T fluorescence assay was performed according to section 3.3.3.

6.3.5.2. Determination of hydrodynamic diameter

The DLS experiment was performed according to section 3.3.5.

6.3.5.3. Secondary structure analysis through CD spectroscopy

To analyse the secondary structure changes CD was performed according to section 3.3.4. From the MRE value at 222 nm, the percentage alpha helix was also calculated using (equation 4.3).

6.3.6. Binding studies

6.3.6.1. ITC for binding study

Isothermal titration calorimetry was performed using ITC 200 pro (GE Healthcare) to check the interaction between the protein sample and the extract. For the eluted samples from HPLC, the samples were first dried using the vacuum concentrator (SpeedVac Concentrator, Thermo Fisher, SPD1010) and were dissolved in the buffer in which the protein BSA solution is made; here, we have used Tris-HCl, pH 7.4. Before starting the experiment, the syringe and the cell compartment were thoroughly washed with methanol and then rinsed properly with Milli Q water. A 280 µl volume of protein solution was carefully loaded into the cell using a Hamilton syringe, avoiding bubble formation inside the cell. In a PCR tube, around 70 µl titrant was loaded and placed in a titrant loading station, of which only 40 µl will be used. The cell temperature was set at 37°C, the number of injections was kept at 35, and the speed of the stirring syringe was at 180 rpm. Except for the first one, 1.0 µl titrant volume was added for every injection, and 120 seconds was kept between two injections. To correct the heat of dilution, a control experiment was performed where the extract was titrated to the buffer alone, which was then subtracted later from the main titration experiment between the protein and the extract. The result analysis was performed using Microcal's origin software [313]. For performing unknown compounds present in CWE eluted fraction, the same amount of dried fraction was weighed (0.3 mg/ml) from each fraction and interacted with 50 µM BSA solution in Tris-HCl buffer, pH 7.4.

6.3.6.2. Docking study

The CB-Dock online server (http://cao.labshare.cn/cb-dock) was employed for the docking study to perform the blind docking of the compounds and BSA. Here, molecular docking is performed through AutoDock Vina (version 1.1.2), which is guided by the protein surface curvature-based detection of the cavity (the Curpocket) [314]. The crystal structure of BSA with PDB ID 3V03 was downloaded from the Protein Data Bank database. Since it is in dimer conformation, chain B was deleted, and only chain A was selected for docking using the chain splitting tool of the CB dock. The protein and ligand in pdb and sdf file format were then used for the docking. The abundant bioactive compounds in the CEE and CWE were downloaded from the PubChem database. Blind docking was performed, and the analysis and visualisation were done using Discovery Studio Visualizer tools [315].

6.3.6.3. Fluorescence quenching

The BSA intrinsic fluorescence experiment was carried out at an excitation wavelength of 280 nm and emission in the 310-450 nm range to study the quenching mechanism through the Stern-Volmer plot. BSA concentration was kept constant at 1 µM, and increasing concentrations of 2, 4, 6, 8, and 10 µM of CWE eluted fraction B, calculated in terms of Chlorogenic acid, were prepared. The experiment was performed at three temperatures, i.e., 298, 310 and 318 K. Samples were first incubated for about half an hour at these temperatures and then the measurement was performed immediately. A 1cm quartz cuvette was employed, and spectral correction was made before giving the final average spectra. The fluorescence measurement was performed in a spectrofluorimeter (Floromax 4, Horiba).

6.4. Results and discussion

6.4.1. Monitoring aggregation in the presence and absence of extracts

The aggregation kinetics of both the thermal and the thermomechanical-induced aggregation of BSA in the presence of the three types of extract were monitored through the Th-T fluorescence assay. Th-T is a benzothiazole dye which binds to the amyloid fibrils (aggregates) with the cross β-sheet structures [255, 256]. The Th-T fluorescence intensity of BSA in the presence of the three crude extracts, namely CME, CWE and CEE, in the thermal induced aggregation at 60 °C is shown in **Figure 6.1. (A, C, and E)**. It was observed that Th-T fluorescence intensity decreased with respect to the control, where no extracts were added. A decrease in intensity was observed in all three extracts, with the maximum inhibition depicted by CEE followed by CWE and CME. The corresponding change in hydrodynamic diameter is shown in **Figure 6.1. (B, D, and F)**. Similarly, a decrease in the Th-T fluorescence intensity and hydrodynamic diameter were also observed in the case of thermomechanical induced aggregation of BSA in the presence of the extract at 60 °C and 300 s^{-1}, however, with lesser intensity as shown in **Figure 6.1. (G)**, and **Figure 6.1. (H)** respectively.

To understand the kinetics further, Th-T fluorescence data were fitted by a single exponential function, $I_t = I_{max}(1 - e^{-kt})$, where I_t, represents the Th-T fluorescence intensity at time t, I_{max} is the maximum intensity and k is the rate of aggregation [256, 287].

In thermal-induced aggregation, the rate decreased from 0.89 h^{-1} to 0.39 h^{-1}, 0.58 h^{-1} and 0.69 h^{-1} in the case of CEE, CWE and CME, respectively, at 500 µg/ml. It was observed that after 300 µg/ml, the aggregation rate did not vary significantly, mostly in the case of CEE and CWE, which were 0.41 h^{-1} and 0.59 h^{-1}, respectively, at 400 µg/ml. Therefore, for the study of thermomechanical-induced aggregation of BSA in the presence of extract, the concentration of extract studied was 300 µg/ml.

In the thermomechanical treatment, the rate of aggregation increases to 1.64 h^{-1} from 0.89 h^{-1} in the absence of shear. When both shear and thermal were applied to induce the aggregation, the BSA protein got enough energy from both the thermal and the shear-induced process, disrupting the intramolecular bonds. This disruption results in unfolding the BSA monomer, which exposes the free SH group and the protein's hydrophobic core, finally leading to aggregation through intermolecular hydrophobic interactions [256, 257]. The dissipation energy, which is the energy generated from the shearing process, which is the product of the shear rate and the shear stress or the product of the square of shear rate and viscosity, along with the thermal energy, leads to the enhancement in aggregation as compared to thermal alone. It is increased when there is an increase in shear rate and also with time. The k value was around 1.8 fold increase in the thermomechanical treated sample compared to the thermal-only induced sample at 60°C, which was comparable to the data (~ 1.5 fold increase) that we performed in our previous study [256]. When in the presence of extracts, the rate of aggregation decreased from 1.64 h^{-1} in the absence of extract to 0.96 h^{-1}, 1.35 h^{-1} and 1.60 h^{-1} at 300 µg/ml CEE, CWE and CME, respectively. Samples collected at different intervals were also tested for the change in secondary structure using far-UV CD, which is discussed in the next section, **section (6.4.2.)**.

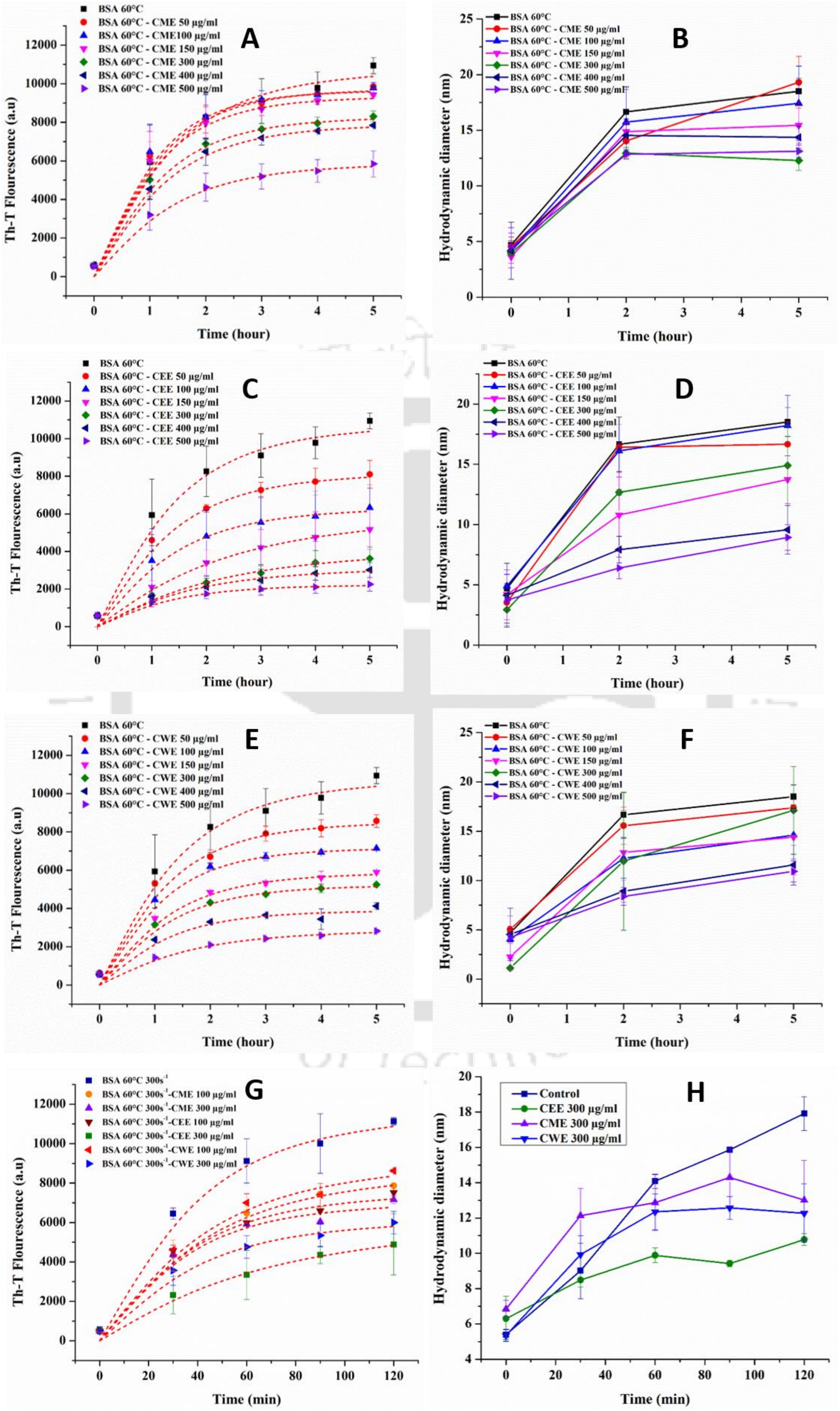
A
BSA 60°C
BSA 60°C - CME 50 µg/ml
BSA 60°C - CME100 µg/ml
BSA 60°C - CME 150 µg/ml
BSA 60°C - CME 300 µg/ml
BSA 60°C - CME 400 µg/ml
BSA 60°C - CME 500 µg/ml
Th-T Flourescence (a.u)
Time (hour)
B
BSA 60°C
BSA 60°C - CME 50 µg/ml
BSA 60°C - CME 100 µg/ml
BSA 60°C - CME 150 µg/ml
BSA 60°C - CME 300 µg/ml
BSA 60°C - CME 400 µg/ml
BSA 60°C - CME 500 µg/ml
Hydrodynamic diameter (nm)
Time (hour)
C
BSA 60°C
BSA 60°C - CEE 50 µg/ml
BSA 60°C - CEE 100 µg/ml
BSA 60°C - CEE 150 µg/ml
BSA 60°C - CEE 300 µg/ml
BSA 60°C - CEE 400 µg/ml
BSA 60°C - CEE 500 µg/ml
Th-T Flourescence (a.u)
Time (hour)
D
BSA 60°C
BSA 60°C - CEE 50 µg/ml
BSA 60°C - CEE 100 µg/ml
BSA 60°C - CEE 150 µg/ml
BSA 60°C - CEE 300 µg/ml
BSA 60°C - CEE 400 µg/ml
BSA 60°C - CEE 500 µg/ml
Hydrodynamic diameter (nm)
Time (hour)
E
BSA 60°C
BSA 60°C - CWE 50 µg/ml
BSA 60°C - CWE 100 µg/ml
BSA 60°C - CWE 150 µg/ml
BSA 60°C - CWE 300 µg/ml
BSA 60°C - CWE 400 µg/ml
BSA 60°C - CWE 500 µg/ml
Th-T Flourescence (a.u)
Time (hour)
F
BSA 60°C
BSA 60°C - CWE 50 µg/ml
BSA 60°C - CWE 100 µg/ml
BSA 60°C - CWE 150 µg/ml
BSA 60°C - CWE 300 µg/ml
BSA 60°C - CWE 400 µg/ml
BSA 60°C - CWE 500 µg/ml
Hydrodynamic diameter (nm)
Time (hour)
G
BSA 60°C 300s⁻¹
BSA 60°C 300s⁻¹-CME 100 µg/ml
BSA 60°C 300s⁻¹-CME 300 µg/ml
BSA 60°C 300s⁻¹-CEE 100 µg/ml
BSA 60°C 300s⁻¹-CEE 300 µg/ml
BSA 60°C 300s⁻¹-CWE 100 µg/ml
BSA 60°C 300s⁻¹-CWE 300 µg/ml
Th-T Flourescence (a.u)
Time (min)
H
Control
CEE 300 µg/ml
CME 300 µg/ml
CWE 300 µg/ml
Hydrodynamic diameter (nm)
Time (min)

Figure 6.1. Thioflavin T fluorescence assay of thermal treated BSA with different concentrations of the three extracts. A) Th-T fluorescence of BSA with different concentrations of CME, C) CEE and E) CWE. The hydrodynamic diameter of BSA in the presence and absence of B) CME, D) CEE and F) CWE extracts, respectively; (G) Th-T assay of shear and thermal induced aggregation of BSA at 60°C and 300 s^{-1} in the presence of the three extracts at 300 µg/ml and 100 µg/ml concentrations of CME, CEE and CWE respectively and (H) the corresponding change in hydrodynamic diameter.

6.4.2. Secondary structure analysis through CD spectroscopy

To analyse the change in secondary structure in the absence and the presence of the three extracts (CME, CWE and CEE), far-UV CD spectroscopy was performed in the wavelength range 260-190 nm. **Figure 6.2. (A, C, and E)** shows the CD spectrum of the BSA solutions in the presence of the three different extracts at increasing concentrations of 50, 100, 150, 300, 400 and 500 µg/ml at 0 hours.

With the addition of extracts, visible changes in the spectra could be seen in the case of CME and CEE, mostly at the positive band around 195 nm, whereas in the case of CWE extracts, there were no visible changes. In the CD spectra of CME and CEE extracts at 0 hours, the positive band at around 195 nm redshifts slightly, and the intensity decreases, meaning the helix conformation becomes more hydrophilic. Generally, the sum of the backbone dihedral angles ϕ (phi) and ψ (psi) remains constant, and a change in any of these angles will lead to the change of the other angle to maintain the sum. So, with the interaction of the compound, the carbonyl group might have tilted outwards, making it more exposed to solvent [316]. Though no drastic change is observed in the CWE after the addition of extract, a minute increase in the helix content could be observed, as seen from the decrease in intensity at the two negative bands 208 and 222 nm. The α helix content of native BSA was 68.36 %, and with the addition of 500 µg/ml CWE, it increased to 68.7%. Earlier reports have shown that increased α helix content increases the stability of the native conformation [317].

Figure 6.2. (B, D and F) shows the CD spectra of the BSA in the presence of the three extracts after 2 hours of incubation at 60° C at the different concentrations studied. From the CD spectra, the signature alpha-helical dip decreased, which is more prominent in CME and less in the case of CWE and CEE. This is supported by their corresponding mean residue ellipticity values (MRE) at 222 nm, where the increase in MRE 222 nm is the highest in the case of CME and lesser for CWE and CEE with increasing extract concentration **Figure 6.2. (G, H, and I)**. The mean residue ellipticity (MRE) at 208 and 222 nm is generally used to determine the total α helix content of protein.

The alpha helix content in the native BSA was around 68.36 %, comparable to the reported value [256]. After 2 hours of incubation, α helix content of the native BSA decreased to 54% in the absence of extract, i.e. a 21% reduction compared to the native protein. However, in the presence of the extract, the α helix content of BSA was 63.12 %, 60.0% and 56.0 % in the presence of CEE, CWE and CME, respectively, after 2 hours of incubation. So, we observed that with the addition of extract, the decrease in α helix content was slowed with respect to the control (without extract).

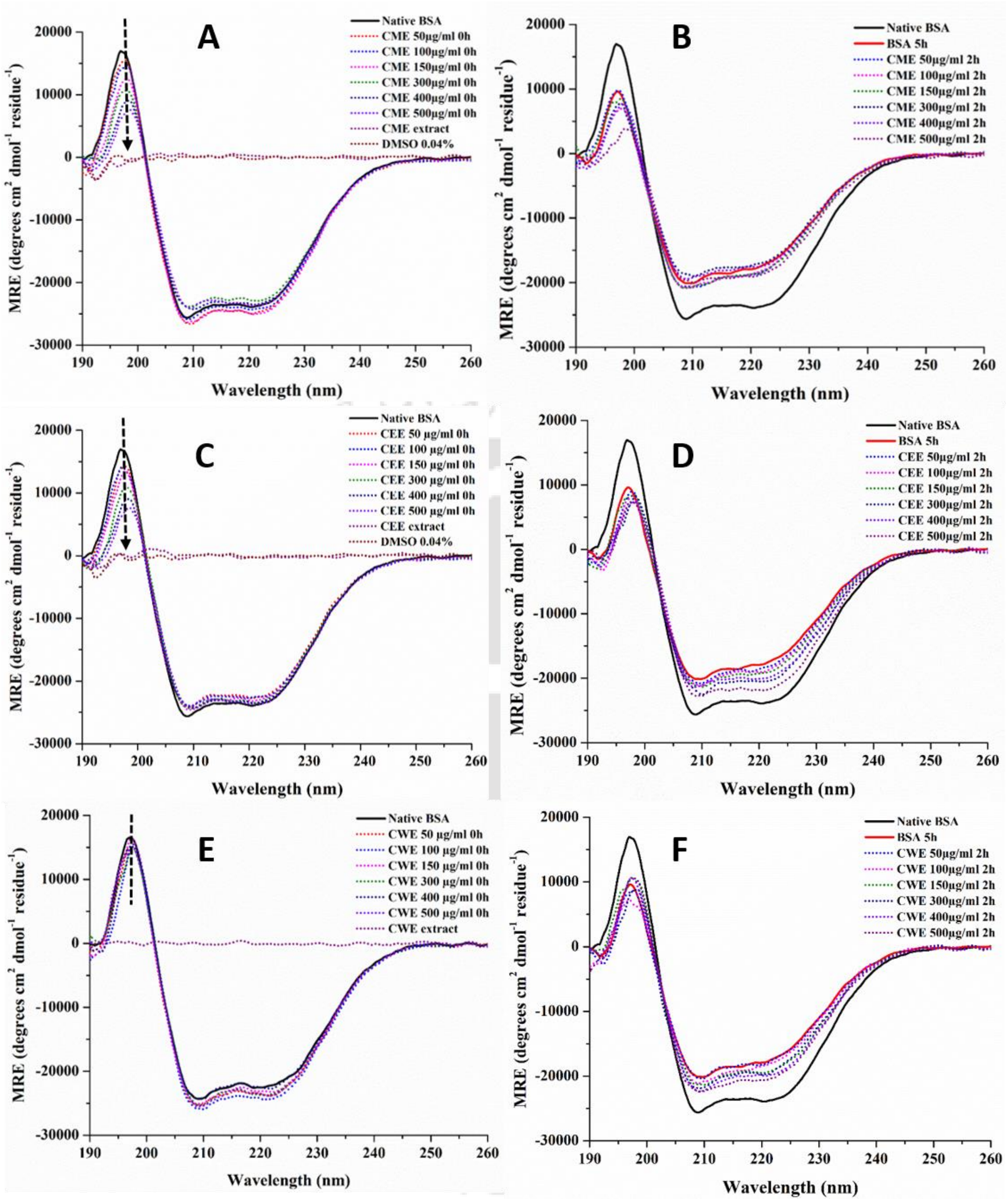
A
Native BSA
CME 50µg/ml 0h
CME 100µg/ml 0h
CME 150µg/ml 0h
CME 300µg/ml 0h
CME 400µg/ml 0h
CME 500µg/ml 0h
CME extract
DMSO 0.04%
B
Native BSA
BSA 5h
CME 50µg/ml 2h
CME 100µg/ml 2h
CME 150µg/ml 2h
CME 300µg/ml 2h
CME 400µg/ml 2h
CME 500µg/ml 2h
C
Native BSA
CEE 50 µg/ml 0h
CEE 100 µg/ml 0h
CEE 150 µg/ml 0h
CEE 300 µg/ml 0h
CEE 400 µg/ml 0h
CEE 500 µg/ml 0h
CEE extract
DMSO 0.04%
D
Native BSA
BSA 5h
CEE 50µg/ml 2h
CEE 100µg/ml 2h
CEE 150µg/ml 2h
CEE 300µg/ml 2h
CEE 400µg/ml 2h
CEE 500µg/ml 2h
E
Native BSA
CWE 50 µg/ml 0h
CWE 100 µg/ml 0h
CWE 150 µg/ml 0h
CWE 300 µg/ml 0h
CWE 400 µg/ml 0h
CWE 500 µg/ml 0h
CWE extract
F
Native BSA
BSA 5h
CWE 50µg/ml 2h
CWE 100µg/ml 2h
CWE 150µg/ml 2h
CWE 300µg/ml 2h
CWE 400µg/ml 2h
CWE 500µg/ml 2h
MRE (degrees cm^2 dmol^{-1} residue^{-1})
Wavelength (nm)
20000
10000
0
-10000
-20000
-30000
190
200
210
220
230
240
250
260

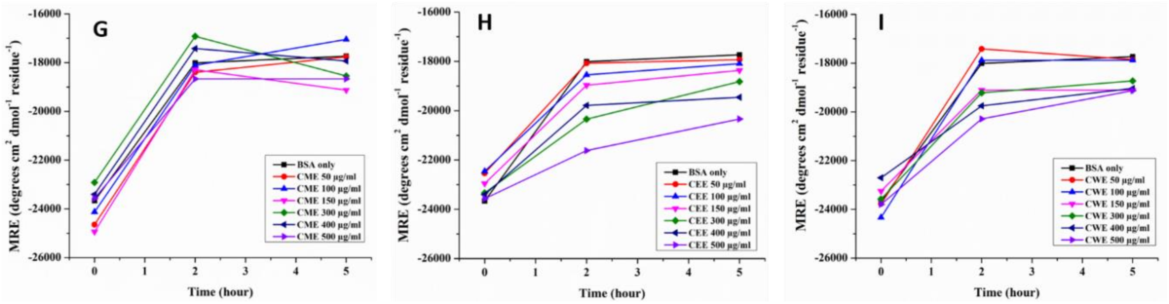

Figure 6.2. CD fluorescence spectrum of thermal induced BSA in the presence of different concentrations of (A) CME extract, (C) CWE extract and (E) CEE extract at 0 hours and (B, D and F) at 2 hours, respectively and MRE values of all the concentrations of (G) CME extract (H) CWE extract and (I) CEE extract respectively.

6.4.3. Extract analysis from HPLC and HR-LCMS

From the aggregation studies discussed in the earlier section, we observed that CWE and CEE showed promising protein aggregation inhibition ability compared to the CME extract. Therefore, HPLC and HR-LCMS analyses were performed to investigate the compounds present in CEE and CWE (details in Chapter 5). From the HPLC analyses of the crude sample CEE **(Figure 5.2. (A), chapter 5)** and CWE **(Figure 5.2. (B))**, it was observed that more compounds were present in CEE than in CWE, which is also evident as the first solvent used for the sequential extraction was CEE. We observed four significant peaks in the CWE chromatogram: A, B, C, and D, respectively. With few compounds, the activity of CWE in slowing down the aggregation is intriguing, and from **section 6.4.2.**, we observed from the CD spectra that the addition of CWE to BSA did not lead to much change in the secondary structure of BSA compared to both the CEE and CME **(Figure 6.2. (A), (C) and (E))**. These peaks were then separately eluted to analyse the components using HRLCMS and further binding assays through ITC and fluorescence studies.

From the ITC study (discussed in **section 6.4.4.**), it was observed that peak fraction B showed the maximum affinity with the BSA molecule among the remaining fractions. Therefore, we performed an HRLCMS analysis **((chapter 5, Table 5.2. (C))**. The compounds present in CWE eluted fraction B are almost the same as those of the crude CWE. The compound chlorogenic acid was again found to be present in this fraction in abundance, implying that it could be the major compound conferring the protein aggregation inhibition property.

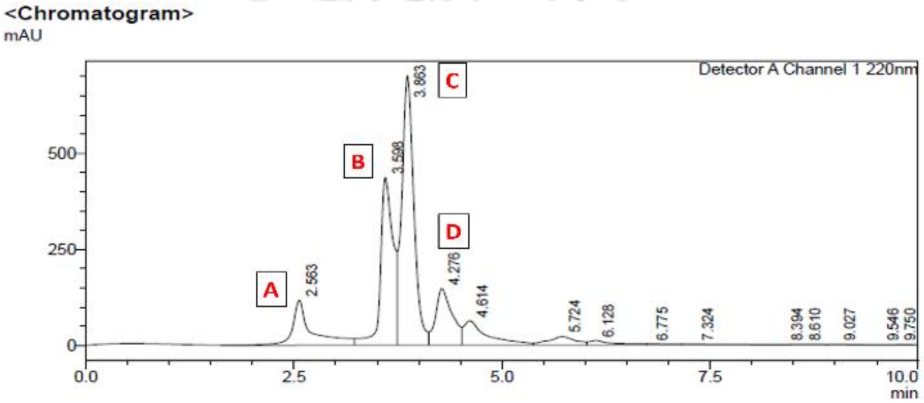

Figure 6.3. HPLC Chromatogram of CWE crude extract. A, B, C and D denote the major fraction obtained in this crude extract.

6.4.4. Isothermal titration calorimetry (ITC) for binding analysis

To further narrow down the compound responsible for the protein aggregation inhibition property, binding analysis between the BSA molecules and the four eluted fractions A, B, C and D collected from CWE crude extracts through HPLC were checked through ITC. It is a sensitive calorimetric technique that can determine the binding energetics of biological interactions. The thermodynamic parameter obtained from the interaction provides valuable information regarding the forces involved in the binding [318]. **(Figure 6.4. (A, B, C, and D))** shows the heat change with time for the four fractions when interacted with BSA.

From the thermograms, we observed that peak fraction A has a poor interaction with BSA, and peak fraction B showed maximum affinity with BSA molecule among remaining fractions B, C and D. Since the exact compounds were unknown, the thermodynamic properties could not be determined [319]. However, by examining the graph, it was observed that fraction B showed the best interaction with BSA. So, a more optimised ITC study was carried out with peak fraction B and BSA, as shown in **Figure 6.5. (A)**. Here, the most abundant compound present in CWE, i.e. Chlorogenic acid (**Chapter 5, Table 5.2. (B)**), was considered for calculating thermodynamic parameters.

The data was fitted with sequential binding site models using the microcal origin software. The best-fitted graph was obtained by fitting the three sites' sequential model with the lowest chi-square value. The K values obtained were 8.14×10^4, 5.16×10^4, and 8.82×10^4 M^{-1} for K_1, K_2 and K_3, respectively. The binding at the first and third sites was exothermic in nature, while the binding at the second site was endothermic.

The binding at the third site has the highest affinity, as seen from the K_3 value. However, considering the change in enthalpy, $\Delta H°$ and the Gibbs free energy, $\Delta G°$ values, the binding site one, with a K value of 8.14×10^4 M^{-1}, was found to be the most favourable among the three sites. The $\Delta H°$ value at site one was -1.69 kcal mol^{-1} (7.32 kJ mol^{-1}), and the change in entropy, $\Delta S°$, was 16.8 cal/mol/deg (72.47 J/mol/deg). The change in Gibbs free energy, $\Delta G°$ obtained was -2.32 kcal mol^{-1} (-10.0 kJ mol^{-1}), and the ($-T\Delta S$) was - 0.62 kcal mol^{-1} (-2.68 kJ mol^{-1}). From the thermodynamic parameter, it can be concluded that the reaction was both enthalpically and entropically driven **(Figure 6.5. (B))**. The negative $\Delta H°$ and positive $\Delta S°$ values show the exothermic and the favourability of the binding reaction, respectively [48], and additionally, it indicates that the binding involves mostly hydrogen bonds and hydrophobic interaction. The $\Delta G°$ value obtained indicates that the binding process was spontaneous in nature [320].

Further, components present in fraction B were explored for molecular docking study with BSA. The detailed docking results are discussed in the next section **(section 6.4.5.)**.

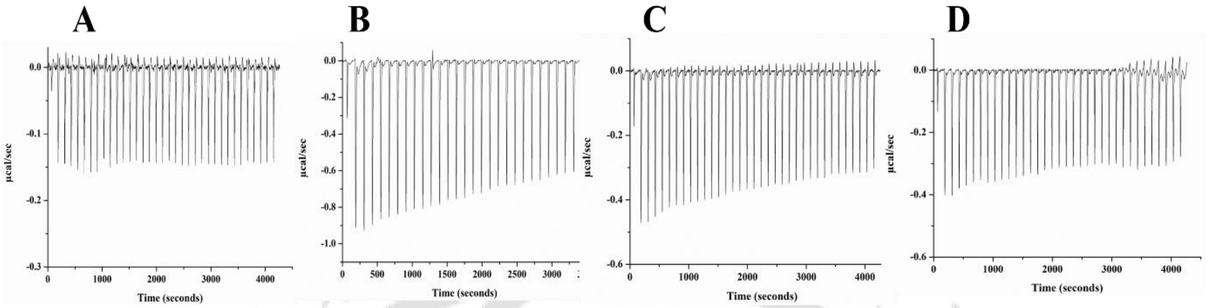

Figure 6.4. The crude fractions of CWE titrated with 50 μM BSA and (0.3 mg/ml) dried fractions dissolved in the same buffer in which BSA was prepared (Tris-HCl pH 7.4). Figures (A), (B), (C), and (D) are the eluted fractions A, B, C, and D from crude CWE.

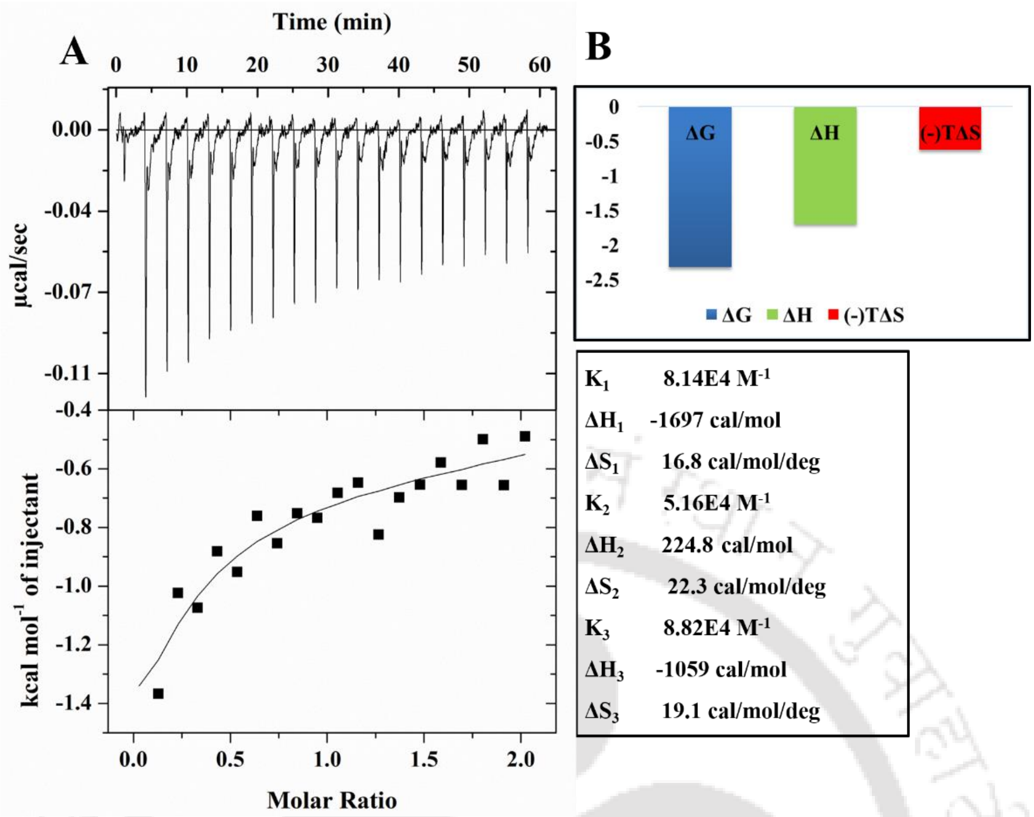

K_1	8.14E4 M^{-1}
ΔH_1	-1697 cal/mol
ΔS_1	16.8 cal/mol/deg
K_2	5.16E4 M^{-1}
ΔH_2	224.8 cal/mol
ΔS_2	22.3 cal/mol/deg
K_3	8.82E4 M^{-1}
ΔH_3	-1059 cal/mol
ΔS_3	19.1 cal/mol/deg

Figure 6.5. ITC thermogram of 50 µM BSA titrated with the CWE eluted fraction B (0.45 mg/ml) dried fractions dissolved in the same buffer in which BSA was prepared (Tris-HCl, pH 7.4) (A); the thermodynamic parameters of the best fit at site one (B).

6.4.5. Docking results

Compounds obtained from HRLCMS data for CEE, CWE, and CWE eluted fraction B were chosen based on their abundance for docking. These compounds were then docked with BSA, and the best-interacting compounds were selected based on the binding score obtained. The docking score and the contact residues of each compound docked with BSA are shown in **Table 6.1.** The docked diagram of these compounds was given in the annexure section **(Table 6A.1.)**. The details of the best-scored compounds for CEE, CWE, and CWE eluted fraction B are discussed here in this section.

From the CEE extract, Asiatic acid was the best-fit compound to interact with BSA with a binding score of -8.4 kcal/mol. The docked diagram is shown in **Figure 6.6.**, along with its contact residues, which can be seen from the 2D diagram (**Figure 6.6. (C)**). It was observed that Asiatic acid binds to BSA in the drug-binding site of subdomain IB. The active binding residues were Tyr$_{137}$, Leu$_{122}$, Leu$_{115}$, Pro$_{117}$, Tyr$_{160}$, and Ile$_{181}$, where the Ile$_{181}$ residue formed a conventional hydrogen bond with the ligand molecule, and the remaining others formed alkyl and pi alkyl bonds. The contact residues also consisted of Tyr$_{137}$ and Tyr$_{160}$, among the critical residues involved in the ligand binding site of subdomain IB [321]. Two other compounds that showed more binding affinity than Asiatic acid were Asiaticoside and Medecassoside, with a binding score of -9.3 kcal/mol. However, considering the high abundance of Asiatic acid in the CEE extract, the main compound probably has to be Asiatic acid. Asiatic acid, Medecassoside and Asiaticoside are among the marker compounds of *Centella asiatica* [322]. Therefore, we could decipher that the protein aggregation inhibition property shown by CEE extracts could be majorly contributed because of the presence of Asiatic acid.

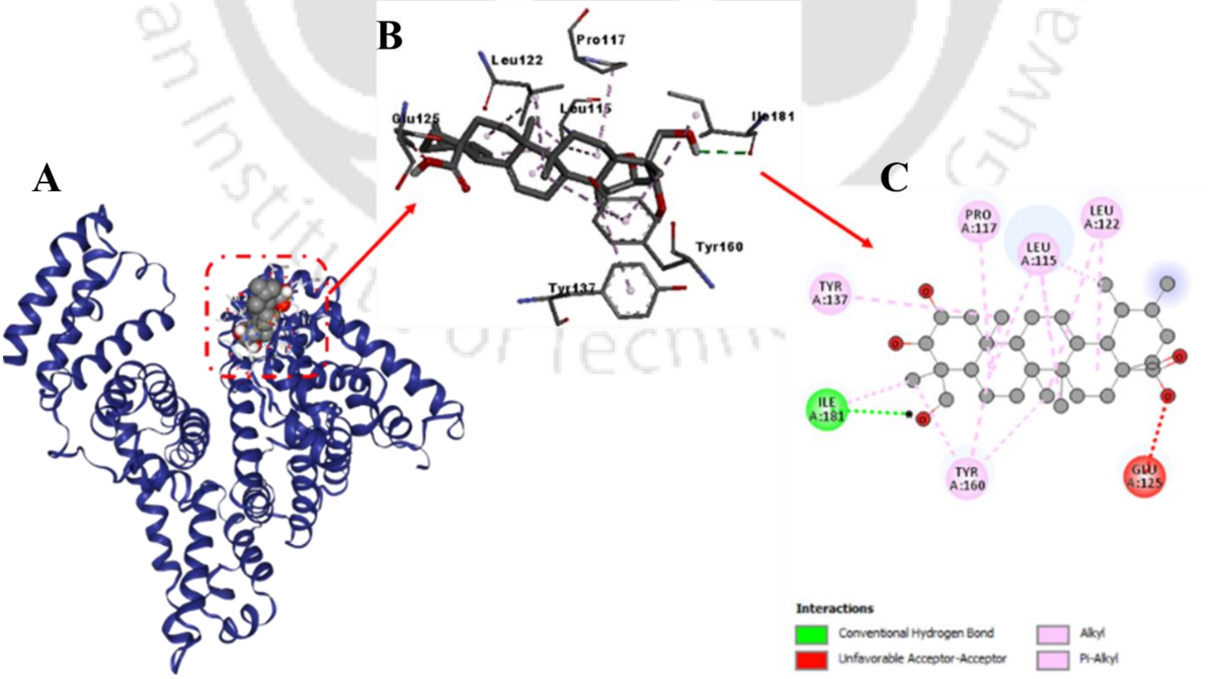

Figure 6.6. Docking of Asiatic acid and BSA (A); 3D diagram (B) and 2D diagram (C).

In the case of CWE and CWE eluted fraction B, Chlorogenic acid, also known as 3 O Caffeoylquinic acid, interacted with BSA with the highest negative binding score of -9.0 kcal/mol. **Figure 6.7.**, shows the docked pose of BSA with Chlorogenic acid along with its 2D and 3D diagrams. The residues which interacted with Chlorogenic acid were Y_{149}, E_{152}, Y_{156}, S_{191}, R_{194}, R_{198}, R_{217}, L_{237}, H_{241}, R_{256}, L_{259}, A_{260}, I_{263}, S_{286}, H_{287}, I_{289}, A_{290}, and E_{291}. From the binding residues and the region, it was observed that Chlorogenic acid bound with BSA in the region of site I and site III sudlows binding sites, which are located in the subdomain IIA and IB, respectively of BSA [323].

The interaction between the ligand and the protein was mostly the conventional hydrogen bonds and few hydrophobic bonds were contributed to by the alkyl and the pi alkyl interactions. Therefore, the protein aggregation inhibition property shown by CWE could be majorly attributed to the presence of compound Chlorogenic acid. An interaction study between BSA and three types of Caffeoylquinic acids (Chlorogenic acid, Neochlorogenic acid, and Cryptochlorogenic acid) also shows that all three types bind to the Sudlow's site I, which is located in the subdomain IIA of BSA [324]. Moreover, the residues in red were part of the amyloidogenic sequences determined through the fold amyloid online server. This shows that the binding of the components of CWE covers the aggregation-prone region.

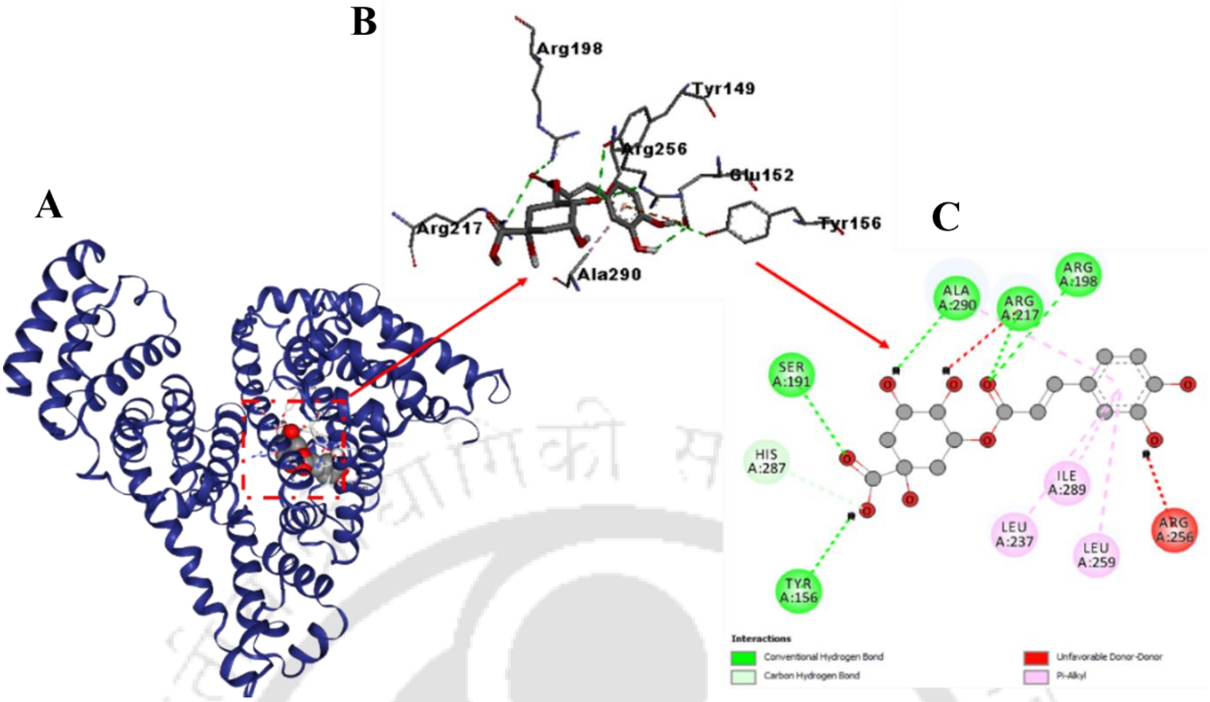

Figure 6.7. Docking of Chlorogenic acid (3, O, Caffeoylquinic acid) with BSA (A), 3D diagram (B) and 2D diagram (C).

Table 6.1. Docking parameters for CWE and CEE extract

(A) Compounds present in CEE extract		
Compound	Energy score (kcal/mol)	Contact amino acid residues in the active pocket
Maritimetin	-8.1	K$_{204}$, F$_{205}$, G$_{206}$, E$_{207}$, R$_{208}$, A$_{209}$, K$_{211}$, A$_{212}$, V$_{215}$, F$_{227}$, T$_{231}$, V$_{234}$, T$_{235}$, K$_{322}$, D$_{323}$, A$_{324}$, L$_{326}$, G$_{327}$, L$_{330}$, L$_{346}$, A$_{349}$, L$_{350}$, E$_{353}$, T$_{477}$, E$_{478}$, S$_{479}$, L$_{480}$ and V$_{481}$
Asiatic acid	-8.4	L$_{115}$, K$_{116}$, P$_{117}$,T$_{121}$, L$_{122}$, E$_{125}$, K$_{136}$, Y$_{137}$, E$_{140}$, I$_{141}$, R$_{144}$, Y$_{160}$, I$_{181}$ and R$_{185}$
4-O-Caffeoyl-3-O-feruloylquinic acid	-8.2	S$_{201}$, F$_{205}$, G$_{206}$, E$_{207}$, R$_{208}$, A$_{209}$, L$_{210}$, K$_{211}$, A$_{212}$, W$_{213}$, V$_{215}$, F$_{227}$, V$_{228}$, V$_{230}$, T$_{231}$, K$_{232}$, V$_{234}$, T$_{235}$, K$_{322}$, D$_{323}$, A$_{324}$, F$_{325}$, L$_{326}$, G$_{327}$, S$_{328}$, F$_{329}$, L$_{330}$, L$_{346}$, R$_{347}$, A$_{349}$, K$_{350}$, E$_{353}$, A$_{354}$, E$_{357}$, E$_{478}$, S$_{479}$, L$_{480}$, V$_{481}$ and N$_{482}$
Medeccasoside	-9.3	D$_{108}$, S$_{109}$, P$_{110}$, D$_{111}$, L$_{112}$, P$_{113}$, K$_{114}$, L$_{115}$, K$_{116}$, P$_{117}$, D$_{118}$, T$_{121}$, L$_{122}$, E$_{125}$, K$_{136}$, Y$_{137}$, E$_{140}$, I$_{141}$, R$_{143}$, R$_{144}$, H$_{145}$, P$_{146}$, Y$_{160}$, I$_{181}$, E$_{182}$, R$_{185}$, E$_{186}$, L$_{189}$, T$_{190}$, S$_{192}$, A$_{193}$, R$_{196}$, E$_{399}$, Q$_{403}$, P$_{420}$, T$_{421}$, V$_{423}$, Q$_{424}$, R$_{427}$, S$_{428}$, K$_{431}$, V$_{432}$, Y$_{451}$, L$_{454}$, I$_{455}$, R$_{458}$, L$_{462}$, T$_{518}$, E$_{519}$ and I$_{522}$
Asiaticoside	-9.3	D$_{107}$, D$_{108}$, S$_{109}$, P$_{110}$, D$_{111}$, L$_{112}$, P$_{113}$, K$_{114}$, L$_{115}$, K$_{116}$, P$_{117}$, E$_{140}$ I$_{141}$, R$_{144}$, H$_{145}$, P$_{146}$, Y$_{147}$, E$_{182}$, R$_{185}$, E$_{186}$,

		V188, L189, T190, S192, A193, R196, P420, V423, E424, V425, R427, S428, K431, V432, Y451, L454, I455, R458, P516, D517, T518, E519 and I522
1,4 Di-O-Caffeoylquinicacid	-8.5	D108, S109, P110, R144, H145, P146, Y147, F148, T183, E186,K187, L189, T190, S192, A193, R196, E424, S428, K431, V432, R435, Y451, L454, I455 and R458
(B) Compounds present in CWE extract		
Compound	Energy score (kcal/mol)	Contact amino acid residues in the active pocket
Chlorogenic acid	-9.0	Y149, E152, Y156, L187, S191, R194, R198, R217, L237, H241, R256, L259, A260, I263, S286, H287, I289, A290 and E291
Quinic acid	-6.0	R208, K211, A212, V215, F227, V230, T231, V234, T235, D323, L326, G327, L330, L346, A349, K350, and Q353
Resorcinol	-4.9	Y149, R217, L218, L237, R256, L259, A260, I263, S286, H287, I289 and A290
Kaempferol 7-O-glucoside	-8.3	F205, G206, R208, A209, K211, A212, V215, T231, V234, K322, D323, A324, L326, G327, L346, A349, K350, Q353, Q478, S479, L480 and V481
Malic acid	-4.9	Y149, Q152, R217, L237, R256, L259, A260, I263, K285, S286, H287, I289, A290 and Q291
Caffeic acid	-6.6	R347, L348, K350, E351, L379, D381, E382, P383, Q384, N385, L386, I387, Q389, N390, C391, Q393, F402, L406, R409, Y410, K413, L429, G430, K431, V432, G433, T434, C436, C437, M445, T448, E449, L452, L456, N482, R484, P485, F487, S488, A489, L490, T491 and P492
1,4 Di-O-Caffeoylquinicacid	-8.5	D108, S109, P110, D111, L112, P113, K114, L115, K116, P117, L122, E125, F133, K136, Y137, E140, I141, R144, H145, Y160, I181, R185, L189 and R458
Kaempferol	-7.5	F148, Y149, Q152, Y156, K187, T190, S191, S192, R194, Q195, R198, R217, H241, R256, H287, A290 and Q291
Asiaticoside	-9.3	D107, D108, S109, P110, D111, L112, P113, K114, L115, K116, P117, E140 I141, R144, H145, P146, Y147, E182, R185, E186, V188, L189, T190, S192, A193, R196, P420, V423, E424, V425, R427, S428, K431, V432, Y451, L454, I455, R458, P516, D517, T518, E519 and I522
Vanillic acid	-6.2	R347, L379, E382, P383, Q384, N385, L386, I387, Q389, N390, C391, Q393, F402, L406, R409, Y410, K413, L429, G430, K431, V432, G433, C437, T448, E449,, L452, N482, R484, P485, F487, S488, A489,

6.4.6. Fluorescence quenching studies of the eluted CWE fraction

An intrinsic fluorescence experiment was performed to understand the binding mechanism of the CWE eluted fraction B and BSA solution. Similar to the ITC experiment, the calculation was done in terms of Chlorogenic acid as it is the most abundant compound in CWE **(Chapter**

5, Table 5.2. (B)). The fluorescence experiment is a highly sensitive experiment frequently used to determine the binding dynamics of proteins and ligands [325]. Fluorescence quenching occurs when the small molecule ligands bind with the protein, and due to the binding, the microenvironment of the fluorophore molecule of proteins is changed [317]. The intrinsic fluorescence property of protein is primarily because of the tryptophan and the tyrosine moieties and, to a lesser extent, by the phenylalanine amino acid. BSA has two tryptophan residues at positions 134 and 213, which are responsible for the intrinsic fluorescence of BSA and give a maximum fluorescence at around 340 nm when excited at 280 nm [326]. The fluorescence emission of BSA at 340 nm was analysed with increasing concentrations of the eluted CWE fraction B, given in the annexure section (**Figure 6A.2.**). The concentration of BSA was kept at 1µM. The quenching mechanism was determined by using the Stern-Volmer (SV) equation given in equation (6.4) [27].

$$\frac{F_0}{F} = 1 + K_{sv}[Q] = 1 + K_q\ \tau_0[\mathrm{Q}] \tag{6.4}$$

Here, F_0 and F are the fluorescence intensity without and with the ligand, respectively, K_{sv} is the SV constant, $[Q]$ is the quencher or the ligand concentration, τ_0 is the lifetime of the fluorophore without the ligands, which equals to (~10^{-8} s) for BSA and K_q is the bimolecular constant [24, 28]. K_{sv} was determined from the slope of the plot $F0/F$ vs $[Q]$, and K_q was calculated as $K_{sv}/\ \tau_0$.

The SV plot was performed at three temperatures, i.e., 298 K, 310 K, and 318 K. **Figure 6.8. (A)** shows the (F_0/F) versus the quencher concentration $[Q]$ to determine the bimolecular quenching constant (K_{sv}) and the quenching constant (K_q).

For determining the binding stoichiometry (n) and the binding constant (K_a), the double log plot of ((F_0/F)-1) and $[Q]$ was performed using equation (6.5) and is shown in **Figure 6.8. (B)**.

$$log\frac{F0-F}{F} = logK_a + nlog[Q] \quad [6.5]$$

The binding force involved between the small molecule ligand and the macromolecule can be contributed by electrostatic, van der Waals forces, hydrogen bonding and hydrophobic interactions. To determine the binding force, the thermodynamic parameters of the binding need to be evaluated. If the change in heat or enthalpy does not vary drastically over a range of temperatures studied, then $\Delta H°$ and $\Delta S°$, the enthalpic and the entropic changes accompanied by the binding of the protein and the ligand can be determined from the Van't Hoff plot of (lnK_a) versus ($1/T$) [327] **Figure 6.8. (C)** using equations (6.6) and (6.7).

$$lnK_a = \frac{\Delta H°}{RT} + \frac{\Delta S°}{R} \quad [6.6]$$

$$\Delta G° = \Delta H° - T\Delta S° \quad [6.7]$$

Tables (6.2.) and **(6.3.)** summarise the quenching and the thermodynamic parameters at the three different temperatures. The K_{sv} value obtained at 298 K, 310 K and 318 K were 2.79 × 10^4 M^{-1}, 3.92 × 10^4 $M^{-1}$and 4.56 × 10^4 M^{-1}respectively and the K_a values were 3.33 × 10^4 M^{-1}, 1.08 × 10^5 $M^{-1}$and 2.12 × 10^5 M^{-1}respectively.

Since the K_{sv} and the K_a values increase with an increase in temperature, the binding mechanism follows a dynamic mechanism, which implies that the quenching is initiated by the collision of the quencher and the excited state fluorescent molecule. The increase in temperature increases the diffusivity of the fluorophore, increasing the collision and, therefore, increasing the value of the K_{sv} [328].

However, if we look into the value of the quenching constant, it lies in the range of ~$10^{12,}$ which is higher than (~10^{10}), which is the maximum scattering collision constant. It indicates that the binding mechanism is static, where the complex formation of the BSA and the ligand is initiated in the ground state. These findings suggested that the fluorescence quenching mechanism observed here was hybrid quenching, where static and dynamic quenching occur [325, 329].

The K_a value obtained here is 1.08 × 10^5 M^{-1} at 310 K, which is almost close to the highest K value, which is the K_3 value obtained through ITC 8.82 × 10^4 M^{-1} at 37°C. The number of binding sites in all three temperatures, 298 K, 310 K and 318 K, were almost close to one from the fluorescence studies, whereas, from the ITC, the data could be best fitted through three binding sites in sequential mode, implicating the presence of more than one site which is true as we know for BSA. Also, the $\Delta H°$ and $\Delta S°$ values obtained are 73.06 kJ $mol^{-1}$and 331.82 J mol^{-1} respectively, implying that the binding is through hydrophobic interaction.

The difference in result from the ITC and fluorescence quenching may be because of the fact that the fluorescence technique depends solely on the fluorophore molecule of the protein, and therefore, the outcome is focussed on the region where the tryptophan residue is present. Whereas, ITC is a direct method that measures the overall system where the reaction occurs. The negative $\Delta G°$ value obtained at all three temperatures indicates that the binding process is spontaneous [330].

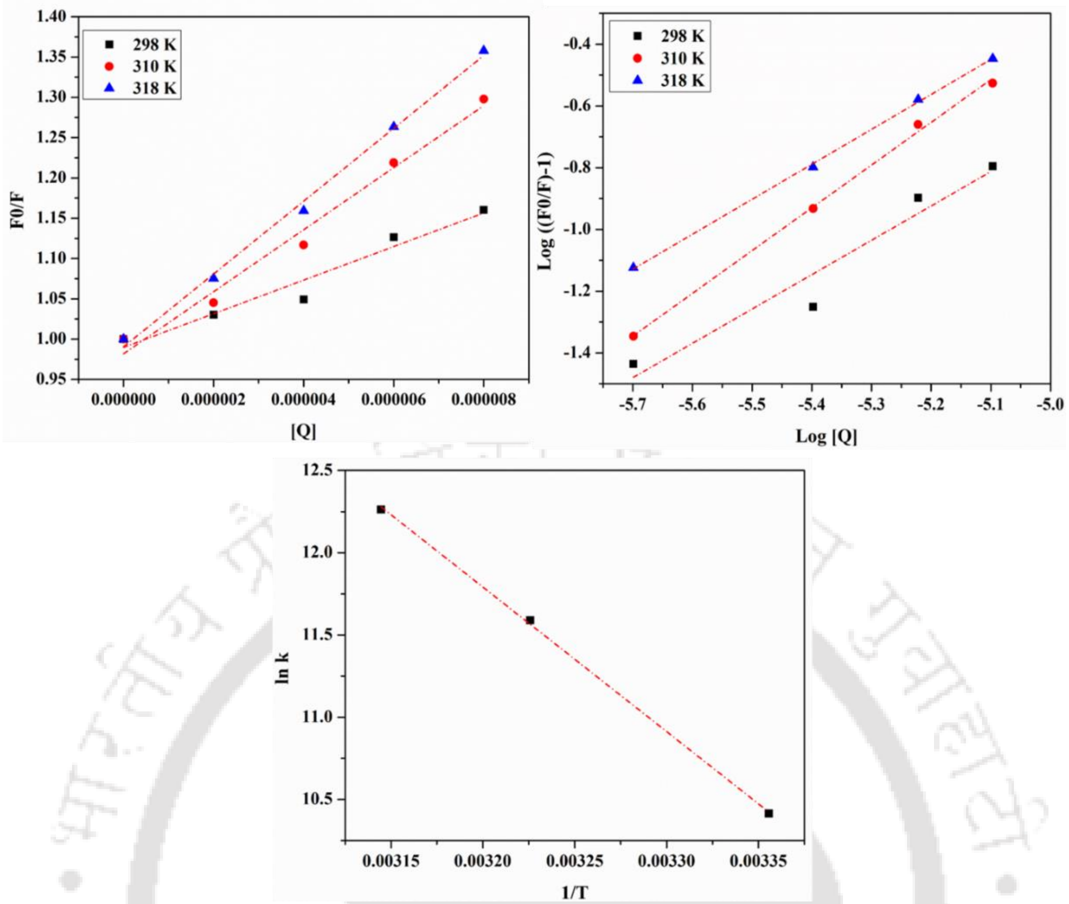

Figure 6.8. (A) Stern-Volmer plot F_0/F versus the quencher concentration $[Q]$ for determining the bimolecular quenching constant K_{sv} and the quenching constant K_q (B) double log plot of $((F_0/F)-1)$ and $[Q]$, for determination of the binding constant K_a and the number of binding sites "n" and (C) Van't Hoff plot of ln K_a versus the reciprocal of temperature ($1/T$) to determine the thermodynamic parameters.

Table 6.2. Binding and quenching parameters of CWE elute in interaction with BSA at 298, 310 and 318 K

Temperature	K_{sv} (M^{-1})	K_q ($M^{-1}s^{-1}$)	R^2
298 K	2.79×10^4	2.79×10^{12}	0.99
310 K	3.92×10^4	3.92×10^{12}	0.97
318 K	4.56×10^4	4.56×10^{12}	0.97

Table 6.3. Binding constant and thermodynamic parameters of CWE elute and BSA

Temperature	Log K_a	K_a (M^{-1})	*n*	R^2	$\Delta G°$ (kJ mol^{-1})	$\Delta H°$ (kJ mol^{-1})	$\Delta S°$ (J mol^{-1} K^{-1})
298 K	4.52	3.33×10^4	1.03	0.99	-25.80	73.06	331.84
310 K	5.03	1.08×10^5	1.11	0.98	-29.86		
318 K	5.32	2.12×10^5	1.13	0.96	-32.42		

6.5. Conclusions

BSA, a major serum protein, was subjected to thermal and thermomechanical-induced aggregation in the presence and absence of a perennial herb, CA, known for its neuroprotection activity. Among the three crude extracts studied, CEE showed maximum inhibition property followed by CWE and CME, which was reflected both in the Th-T fluorescence intensity and the k value obtained by fitting the Th-T fluorescence intensity curve.

The aggregation rate obtained at thermal-only induced aggregation was 0.89 h^{-1}, and in the presence of extract, the aggregation rate obtained was 0.39 h^{-1}, 0.58 h^{-1} and 0.69 h^{-1}in the case of CEE, CWE and CME, respectively, at 500 µg/ml extract concentration. With the reduction in aggregation, a corresponding reduction in the increased in the hydrodynamic diameter was also observed with respect to the control. In the case of the thermomechanical induced aggregation, the rate was enhanced by around 1.83 fold (1.64 h^{-1}) with respect to the thermal alone aggregation. In the presence of extract, the rate of aggregation was 0.96 h-1, 1.35 h^{-1} and 1.60 h^{-1} at 300 µg/ml CEE, CWE and CME, respectively.

Secondary structure analysis through CD showed that with the interaction of extract, there is a notable change in the structure of CEE and CME, whereas, in the case of CWE, no significant change was observed except the minute increase in α helix content. For further analysis of the extracts (CEE and CWE) with promising inhibition properties, HR-LCMS and HPLC were performed. It was observed that CWE has less prominent major peak as compared to CEE and has aggregation inhibition properties almost comparable to that of CEE, and therefore, CWE was selected for further binding study. Another perspective for selecting CWE was that BSA, after interacting with CWE, does not show a prominent change in their secondary structure, but instead, a minute increase in the α helix content was observed, which supposedly enhances the stability. The peaks obtained in the HPLC for CWE were separately eluted, and their binding interaction with BSA was further studied through ITC. Peak B from the crude CWE extract showed a maximum change in heat. Therefore, it was further analysed through HR-LCMS, molecular docking and fluorescence study. Chlorogenic acid, also called the 3-O-Caffeoylquinic acid, was found to be the most abundant and has the highest binding affinity with BSA, with a binding score of -9.0 kcal/mol. Optimising the ITC experiment and finding the thermodynamic data in terms of Chlorogenic acid showed that the interaction was spontaneous with a negative $\Delta G°$ value of -2.32 kcal/mol (-10.0 kJ mol^{-1}), and the $\Delta H°$ and $\Delta S°$ values were -1.69 kcal mol^{-1} (7.32 kJ mol^{-1}) and 16.8 cal/mol/deg (72.47 J/mol/deg) respectively showing both enthalpic and entropic contribution. From the docking analysis of all the compounds analysed from CEE, CWE and CWE eluted fraction, Asiatic acid, a major marker compound of *Centella asiatica*, was found to be the best-interacting compound with BSA with a binding score of -8.4 kcal mol^{-1} for CEE, and for CWE extract, Chlorogenic acid was found to be the best-fit compound with a negative binding score of -9.0 kcal mol^{-1}. The compound Asiatic acid interacted in the drug binding site of subdomain IB, and Chlorogenic acid binds in the region of site I and site III sudlows binding sites, which are located in the subdomain IIA and IB, respectively of BSA. The crude eluted fraction of CWE showing the best interaction with BSA was then checked for the SV fluorescence quenching to determine the binding mechanism. From the quenching experiment, the binding mechanism determined was hybrid quenching with an increased K_a value were 3.33×10^4 M^{-1}, 1.08×10^5 $M^{-1}$and 2.12 $\times$ 10^5 M^{-1}, respectively and bimolecular quenching constant K_q in the range of 10^{12} $M^{-1}s^{-1}$.

6.6. CHAPTER 6B

Inhibition of thermal induced aggregation of hen egg white lysozyme by Centella asiatica water extract

This subchapter discusses the impact of the *C.asiatica* water extract (CWE) on the aggregation of the amyloidogenic protein HEWL. In the earlier section, we observed that CWE has many advantages over CEE in terms of interaction with protein and showed almost comparable properties with fewer compounds than CEE. Therefore, in this study, the CWE was checked for its impact on the aggregation of HEWL. The impact of CWE was tested with the thermal-induced aggregation of HEWL at 65 °C and pH2.

6.7. Introduction

The use of plant-derived extract, which is rich in polyphenols, is one of the increasingly sought-after strategies for addressing protein aggregation issues because of its high efficacy and compatibility. These small molecules inhibitors are mostly aimed at attenuating the toxic aggregate through stabilisation of the native structure from aggregation, and the other approach is by degrading already formed aggregates, which can be fibrils or oligomers [331, 332]. CA is a perennial herbaceous plant mostly found and eaten in the southeast Asian countries of India, Srilanka and Bangladesh [333]. It has been used in traditional Ayurvedic medicine preparation and has also been used in ancient Chinese medicine [334, 335]. It is known for its excellent cognitive enhancement properties and various other properties such as anti-inflammatory, antioxidative, anticancer, antimicrobial, wound healing, etc.

Here, in this study, HEWL, a model amyloidogenic protein, was subjected to thermal alone and thermomechanical induced aggregation at acidic pH ((which was also discussed in Chapter 3B); for the sake of comparison, we will be showing the previous HEWL results here in this section again). Along with the aggregation study, the water extract fraction of a known memory enhancer plant, CA, was checked for its protein aggregation inhibition property.

The aggregation kinetics was assessed through a Th-T fluorescence assay, and the aggregate size was determined using a Dynamic Light Scattering (DLS) experiment. The effect of aggregation on the secondary structure of the protein was determined through Circular dichroism spectroscopy, and the aggregate morphology was analysed using atomic force microscopy. The binding mechanism and binding dynamics of the extract and the protein were then assessed through the Stern-Volmer (SV) quenching experiment of HEWL in the presence of the CWE. The compounds present in the crude extract, identified from High-resolution-liquid chromatography coupled with mass spectrometry (HR-LCMS) analysis (Chapter 5), were docked to determine the probable compounds which interact with the protein.

6.8. Materials and methods

Lyophilised chicken egg white lysozyme (catalogue no. A2153) and Th-T dye (catalogue no. T3516) were purchased from Sigma-Aldrich, India. Sodium azide (NaN_3) (SKU TC704) was obtained from Himedia, India. Milli Q water (18 Ω) was used in all the experiments.

6.8.1. Preparation of protein solution

20 mg/ml of stock chicken egg white lysozyme was prepared in 20 mM Glycine buffer (pH 2) containing 0.02% NaN_3. The protein solution was then filtered using a 0.2 µm syringe filter, and the absorbance was checked at 280 nm in a UV spectrophotometer to check the concentration using Beer Lambert's law. The extinction coefficient was 37646 M^{-1} cm^{-1}. 140 µM (~2 mg/ml) working solution was prepared in the presence and absence of *Centella asiatica* water extract (CWE).

6.8.2. Preparation of *Centella asiatica* water extract

The last extract of the final sequential extraction, i.e., the CWE, which was extracted in water, was used in this study as it was the most efficient among the three, considering various perspectives. The crude powder extract was dissolved in the same buffer where the protein is dissolved. Stock solution was prepared, and from that, 10 µg/ml, 50 µg/ml, 100 µg/ml and 300 µg/ml working solutions were prepared with the protein solution.

6.8.3. Effect of thermal and shear on the aggregation of HEWL in the presence and absence of *Centella asiatica* water extract

For thermal-induced aggregation, different solutions containing 140 µM HEWL and increasing extract concentrations were prepared. The thermal-induced aggregation was performed in a 65°C oven. Samples were collected every day till the 10th day.

6.8.4. Investigation of the aggregation behaviour

6.8.4.1. Th-T fluorescence assay

To monitor the aggregation kinetics, Th-T fluorescence assay was performed according to section 3.3.3.

6.8.4.2. Estimation of hydrodynamic diameter

The DLS experiment was performed according to section 3.3.5.

6.8.4.3. Secondary structure determination

Far UV-CD spectroscopic measurement was performed according to section 3.3.4. The percentage content of the secondary structure was analysed through the DICHROWEB web server [228].

6.8.4.4. Morphological analysis

Morphology analysis was performed according to section 3.3.5.

6.8.5. Interaction studies

6.8.5.1. Fluorescence quenching study

To study the interaction of the extract and HEWL, the quenching mechanism was determined through a Stern-Volmer (SV) quenching plot at three different temperatures, i.e., 298 and 310 K. The excitation wavelength was set as 280 nm, and the emission spectra were collected from 300 to 450 nm. The excitation and the emission slit width were set at 5 and 3 nm, respectively, and an average of 5 accumulations was run to give the final averaged spectra. 1 µM HEWL sample was used, and an increasing extract concentration of 2, 4, 6, 8 and 10 µg/ml was added. Samples were first incubated at the respective temperatures for around 30 minutes, and the fluorescence measurement was performed instantly afterwards. The measurement was made in a 10 mm fluorescence quartz cuvette, and the spectra were corrected before the final average spectra were given. The fluorescence measurement was performed using a spectrofluorimeter (Floromax 4, Horiba).

6.8.5.2. Docking analysis

Through the CB-Dock online server (http://cao.labshare.cn/cb-dock), the blind docking of the compounds and HEWL were performed. The docking was performed through AutoDock Vina (version 1.1.2) after the surface curvature had been detected by the software (the Curpocket) [314]. HEWL crystal structure, with PDB ID, 6LYZ was downloaded from the Protein Data Bank database, and the compounds present in the CWE extract were obtained from the PubChem database in SDF file format. Blind docking was performed, and the docked poses were visualised through the Discovery Studio Visualizer tools [315].

6.9. Results and discussion

6.9.1. Determination of Inhibition of aggregation and the hydrodynamic diameter

The aggregation kinetics of both the thermal and the pre-sheared induced aggregation of HEWL in the presence of (*Centella asiatica* water extract) CWE at 10, 50, 100 and 300 µg/ml were analysed through Th-T fluorescence assay. Thioflavin T is a benzothiazole dye which binds to the cross β-sheet structures of amyloid fibrils (aggregates) [255, 256]. The Th-T fluorescence intensity of the pre-sheared added samples and the thermally induced aggregated samples are shown in **Figure 6.9. (A)**. From the figure, it was observed that CWE significantly reduces the aggregation, as can be seen from the decrease in Th-T fluorescence intensity. The extract concentration at 100 and 300 µg/ml almost gives the same amount of inhibition of aggregation. Another observation is the enhanced aggregation in pre-sheared samples compared to the only thermal-induced samples. Although shearing of HEWL for two hours did not give any significant increase in Th-T fluorescence intensity (data not shown), it acts as a seed when incubated with the fresh HEWL for a longer period in low pH and high-temperature conditions. The Th-T fluorescence data was then fitted with the Boltzmann equation, which is a nonlinear sigmoidal equation (6.8), to determine the aggregation rate k [257]. Here, 1/t denotes k, which is the apparent rate constant, and the lag time can be calculated as $t_0-2\tau$. The fitting parameters of all the samples studied are given in **Table 6.4**. It was observed that the apparent rate constant is highest in the case of the pre-sheared induced samples with k value of 1.01 day^{-1}and the k value of the thermal only induced sample was 0.88 day^{-1}.

Then, it was observed that the apparent rate of HEWL aggregation decreases with the addition of CWE and the increase of CWE concentration. The thermally induced HEWL samples in the presence of 10, 50, 100 and 300 μg/ml of CWE showed k values of 0.60, 0.32, 0.04 and 0.04 day^{-1}, respectively. The pre-sheared samples have the shortest lag time of 3.80 days, and the samples with the highest CWE concentration have the longest lag time of 54.76 days.

$$I_t = I_{max} + \frac{I_{max} - I_0}{1 + e^{(t0 - t)/\tau}} \qquad [6.8]$$

The same trend in the Th-T fluorescence increase can be seen in the case of the hydrodynamic diameter, as shown in **Figure 6.9. (B)**. Native lysozyme has a hydrodynamic diameter of about 2 nm [260, 261]. The samples incubated with CWE extract don't show much increase in the hydrodynamic diameter compared to the pre-sheared and thermal control sample at 65°C over time.

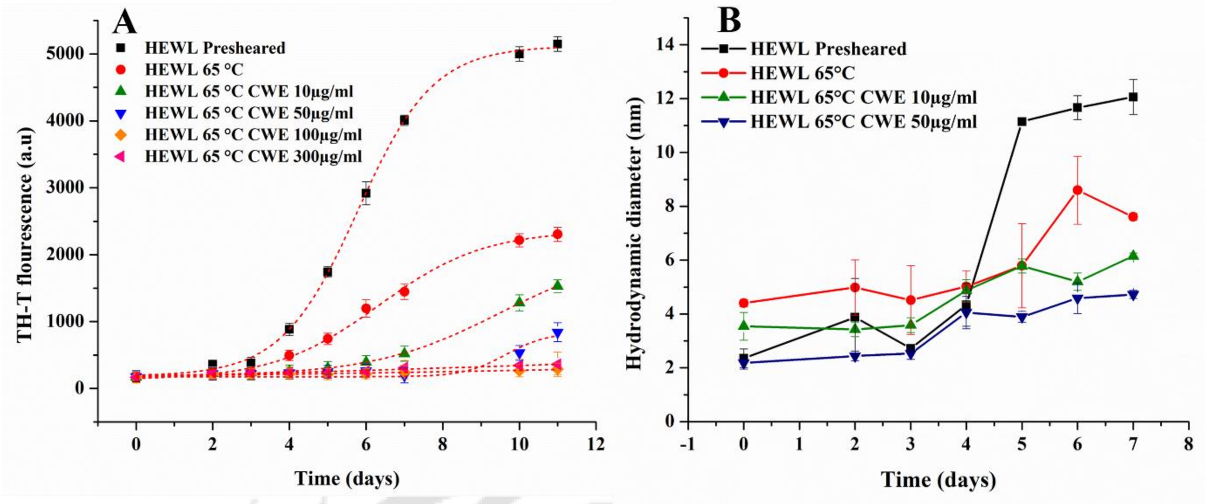

Figure 6.9. Th-T fluorescence assay of HEWL sample pre-sheared at 300 s^{-1} and at temperature 65°C and samples which are thermal incubated at 65°C in the absence and presence of different concentrations of CWE (A) and the hydrodynamic diameter of pre-sheared and thermal induced HEWL in presence and absence of HEWL (B).

Table 6.4. Boltzmann fitting parameters for the aggregation kinetics of 140 µM HEWL in the presence and absence of CWE and the presence of seeds.

Sample	t_0	τ	$1/t_0$ (days^{-1})	2τ	$t_0 - 2\tau$ (days)
Preshear	5.78	0.99	1.01	1.97	3.80
Thermal 65°C	6.95	1.14	0.88	2.28	4.67
Thermal 65°C 10 µg/ml CWE	9.51	1.65	0.60	3.31	6.20
Thermal 65°C 50 µg/ml CWE	13.68	3.09	0.32	6.17	7.51
Thermal 65°C 100 µg/ml CWE	79.42	22.92	0.04	45.83	33.59
Thermal 65°C 300 µg/ml CWE	99.32	22.28	0.04	44.56	54.76

6.9.2. Secondary structure analysis through circular dichroism

The secondary structure of the pre-sheared added samples, the thermally induced samples at 65°C and the samples incubated with different extract concentrations of CWE were analysed from the far UV CD from 260-190 nm. **Figure 6.10 (A)** shows the CD spectra of HEWL, which is thermal only induced without any extract; **Figure 6.10 (B)** is the HEWL sample which has been pre-sheared and used as a seed for thermal induced aggregation at 65 °C; **Figure 6.10 (C)** and **Figure 6.10 (D)** shows the HEWL containing 10 and 300 µg/ml CWE extract and **Figure 6.10 (E)** is the MRE values at 200 nm for all the different experimental conditions. As already discussed in **Chapter 3, section 3.9.2.,** native HEWL CD spectrum has a spectrum like that of a model α- helix structure with negative dips at 208 and 222 nm.

Also, as discussed earlier **(chapter 3, section 3.9.2.),** the amyloid fibril observed here is mainly constituted by type two β proteins (β II). Hence, for analysing the extent of aggregation, the negative dip at MRE 200 nm and a shift towards 200 nm peak were used.

In all the experimental conditions, the native negative dip at 208 nm gradually shifts towards 200 nm, and the negative dip at 222 nm slowly disappears with time. The shifts towards 200 nm were vividly observed in the pre-sheared added and the thermal-induced control samples. In the case of samples containing 10 µg/ml and 300 µg/ml CWE, the shifts were first upwards, which could mean a gradual decrease in alpha helix content before shifting to 200 nm, which denotes the formation of amyloid fibrils. The CD results also corroborated well with the AFM data **(section 6.9.3)**. **Figure 6.10. (E),** shows the intensity of the amyloid fibril formed, as detected through the shift in the negative band at 200 nm. The MRE value is calculated from the machine theta value, using the formula, given in equation (3.6) [336].

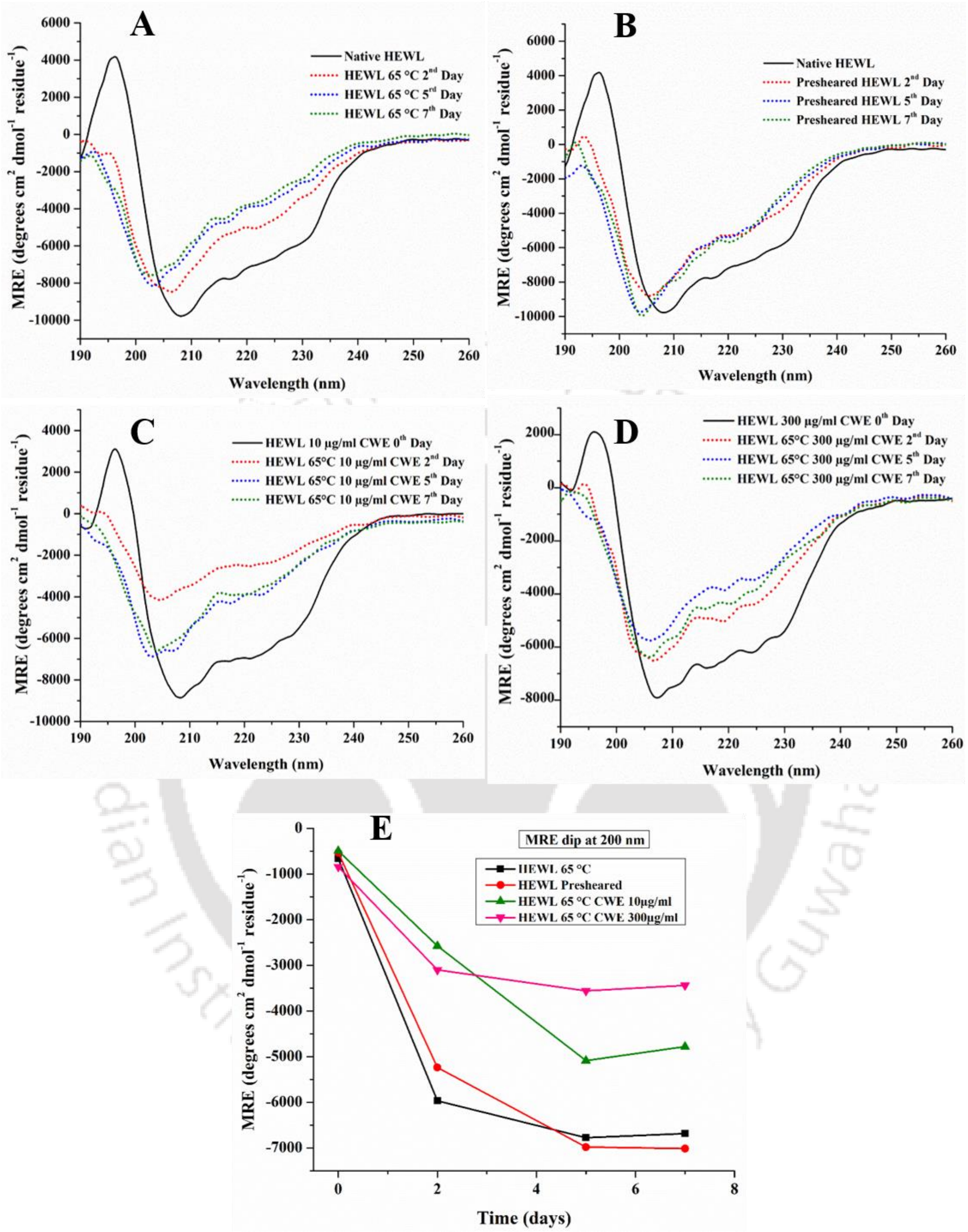

Figure 6.10. CD spectra of HEWL pre-sheared at 300 s^{-1} and 65°C (A); HEWL incubated at thermal only at 65°C (B); HEWL treated with 10 µg/ml CWE at 65°C (C); HEWL treated with

300 µg/ml CWE at 65°C (D) and the shift towards 200 nm with increasing fibrillation determined through MRE at 200 nm (E).

6.9.3. Morphology analysis

The morphology of different HEWL samples is shown in **Figure 6.11**. **Figure 6.11. (A)** shows the AFM images of native HEWL, **Figure 6.11. (B)** is the thermal induced aggregated HEWL at 65°C, **Figure 6.11. (C)** thermal induced HEWL in the presence of 300 µg/ml CWE extract and **Figure 6.11. (D)** pre-sheared HEWL at 300 s^{-1} and continued incubation at 65°C. As the morphology of the pre-shared added, the thermally induced samples have already been discussed in Chapter 3, section 3.9.3, and the CWE-treated sample was discussed here. In the HEWL sample treated with 300 µg/ml of extract, few prefibrillar aggregates of length as short as 117 nm and longer length of 429 nm were observed. This observation fully flagged supports the inhibition of fibril formation in the presence of *Centella asiatica* water extract (CWE). Spherical diameter oligomers in the 41 to 102 nm range were also present. Therefore, comparing the results from a previous study, it was observed that in the presence of CWE, the formation of prefibrillar structure has been attenuated.

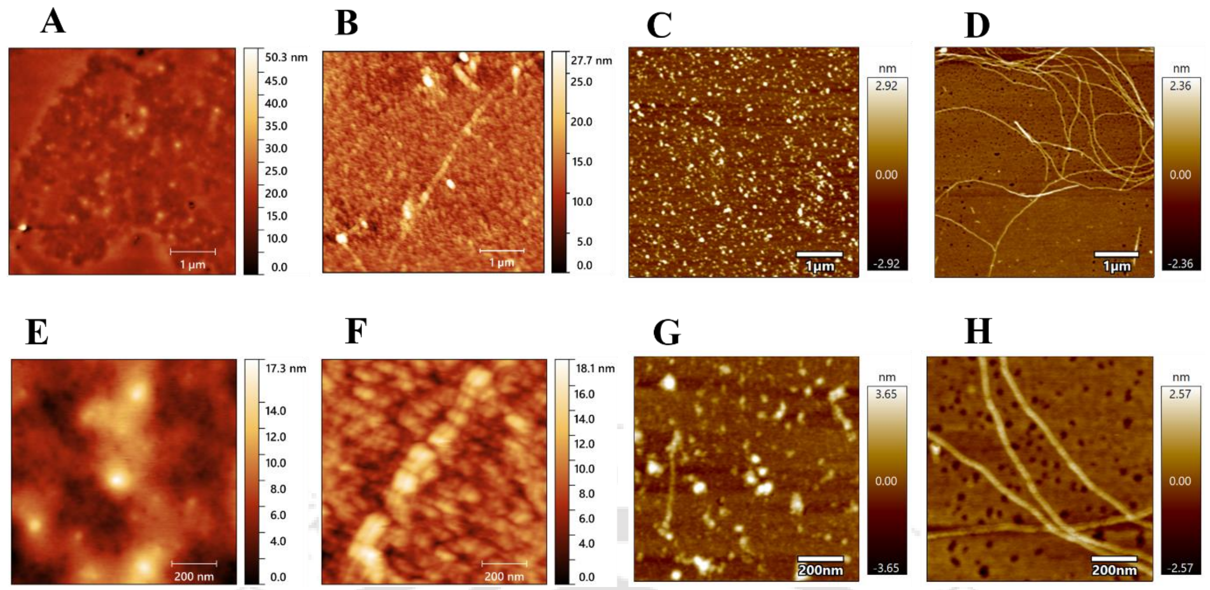

Figure 6.11. Native HEWL (A); thermal induced HEWL at 65°C (B); thermal induced HEWL in the presence of 300 µg/ml CWE at 65°C (C); pre-sheared and thermal induced HEWL at 65°C (D); Figures A, B, C and D are of dimension 5 x5 µm whereas figures E, F, G and H are that of the corresponding zoomed images of dimension 1 x 1 µm.

6.9.4. Fluorescence quenching study with crude CWE

To determine the behaviour of interaction between the ligand, which is the extract here, and the macromolecule, tryptophan intrinsic fluorescence of HEWL was analysed in the presence of the CWE crude extract, which quenches the fluorescence with increasing concentrations [337, 338]. Fluorescence quenching occurs when there is a decrease in the fluorescence quantum yield of the fluorophore molecule due to various interactions with the quencher molecule [339]. HEWL has six tryptophan residues at positions 28, 62, 63, 108, 111 and 123. The majority of the fluorescence is given by the residues at 62 and 108 positions. The intrinsic fluorescence at 1µM HEWL and increasing extract concentration was measured at 298 K and 310 K. **Figure 6A.3** (annexure section) shows the fluorescence spectrum of HEWL with increasing concentrations of CWE (2, 4, 6, 8, 10 and 20) µg/ml at 298 K and 310 K. Native HEWL has a fluorescence maximum at 332 nm. The fluorescence intensity was gradually quenched with increasing concentration of the extract [337]. This indicates that CWE could interact with HEWL and showed the quenching effect. The quenching mechanism was then determined using the Stern-Volmer equation in equation (6.9)[340].

$$\frac{F_0}{F} = 1 + K_{SV}[Q] = 1 + K_q\tau_0[Q] \tag{6.9}$$

F_0 and F are the fluorescence intensity without and with the ligand, respectively, K_{sv} is the Stern-Volmer constant, $[Q]$ is the quencher concentration, τ_0 is the lifetime of the fluorophore without the quencher, which equals to (~10^{-8} s) for HEWL and K_q is the bimolecular constant [337, 341]. K_{sv} was determine from the slope of the plot F_0/F vs $[Q]$ **(Figure 6.12. (A))** and K_q was calculated as $K_{sv}/\ \tau_0$. The different quenching parameters are given at **Table 6.5**. As the value of K_q comes in the order of 10^{12}, the mechanism of quenching is static, as it is found to be higher than the maximal scatter collision quenching constant (2.0×10^{10} L/mol·s). Also, the value of K_{sv} decreases with increased in temperature, implying that the complex become unstable at higher temperature. Therefore, HEWL and the CWE extract interacts and form a stable complex in the ground state [342]. Next, the binding constant and the number of binding sites were determined by plotting log $F_0/F\text{-}1$ vs $[Q]$ **(Figure 6.12. (B))**. The linear regression curve was then expressed as y=mx + c, where the slope m denotes the number of binding sites and from the c, which is the Log K_a, the binding constant was calculated.

If the enthalpy change of the system does not change significantly, the thermodynamics parameters ($\Delta H°$ and $\Delta S°$) can be calculated from the plot of lnK_a vs $1/T$ (**Figure 6.12. (C))** using Van't Hoffs equation (equation 6.10) [327], and then the change in Gibbs free energy can be calculated from (equation 6.11).

$$lnK_a = \frac{-\Delta H°}{RT} + \frac{\Delta S°}{R} \tag{6.10}$$

$$\Delta G^\circ = \Delta H^\circ - T\Delta S^\circ \tag{6.11}$$

The binding and quenching parameters at the two temperatures are given in **Table 6.6.** The number of binding sites, n, obtained was almost close to 1 at both 298 and 310 K. The binding constant K_a was found to be 4.23 × 10^4 and 2.85 × 10^4 ml $g^{-1,}$ respectively, at 298 and 310 K. The change in enthalpy ΔH° and entropy ΔS° were -25.38 kJ ml g^{-1} and -15.73 J ml g^{-1}, respectively. Since both ΔH° and ΔS° are negative, the binding force involved in the interaction between the ligand and the protein is mostly hydrogen bonds and van der Waals interaction. The Gibbs free energy was found to be -20.69 kJ ml g^{-1} and -20.50 kJ ml g^{-1} at 298 and 310 K, respectively, depicting the exothermic nature of the interaction.

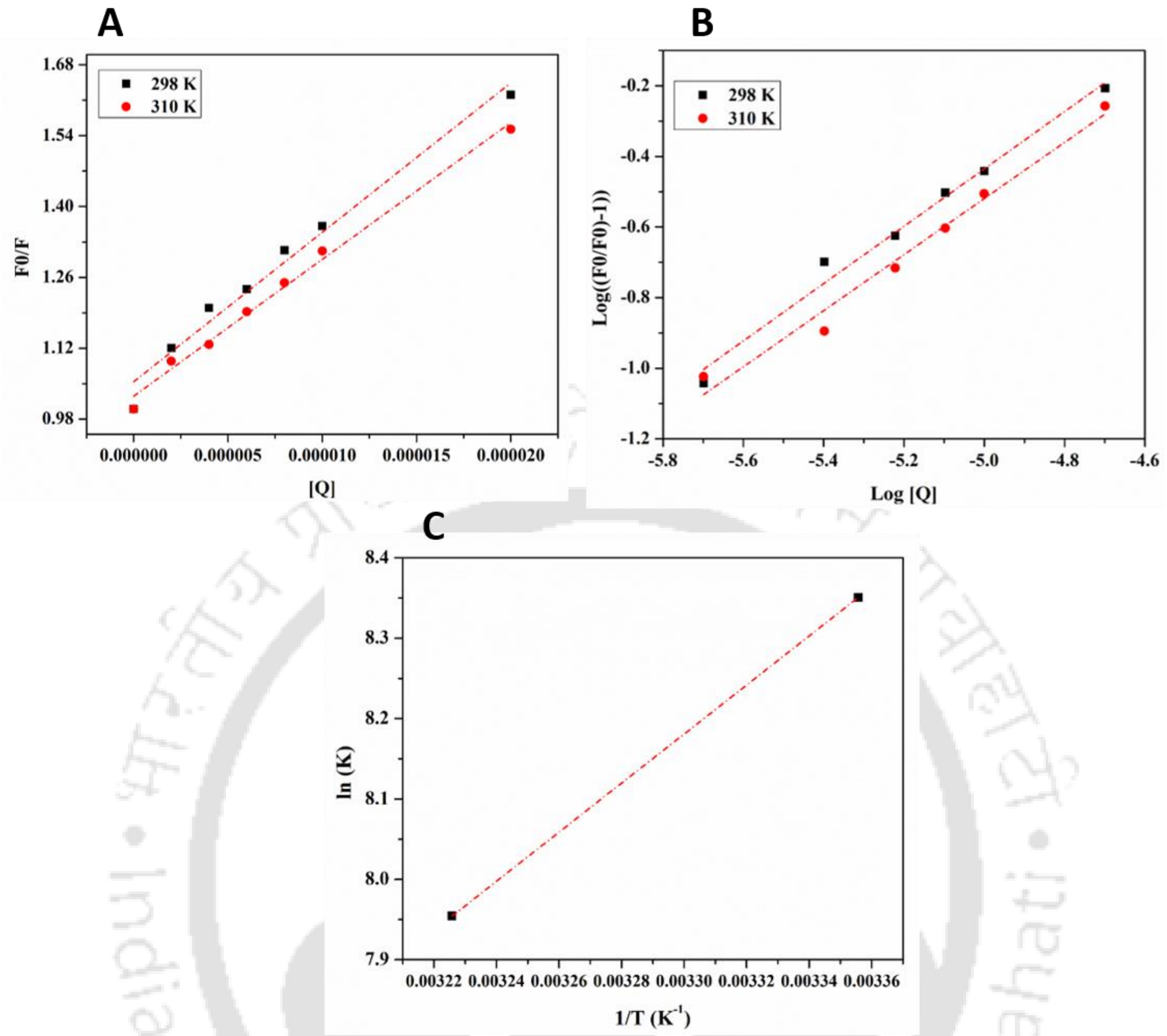

Figure 6.12. (A) Stern-Volmer plot F_0/F versus the quencher concentration $[Q]$ for determining the bimolecular quenching constant K_{sv} and the quenching constant K_q (B) double log plot of $((F_0/F)-1)$ and $[Q]$, for determination of the binding constant K_a and the number of binding sites "n" and (C) Van't Hoff plot of lnK_a versus the reciprocal of temperature to determine the thermodynamic parameters.

Table 6.5. Binding and quenching parameters of CWE in interaction with HEWL at 298 and 310 K.

Temperature	K_{sv} (ml g^{-1})	K_q (ml g^{-1} s^{-1})	R^2
298 K	2.80×10^4	2.80×10^{12}	0.98
310 K	2.64×10^4	2.64×10^{12}	0.99

Table 6.6. Binding and quenching parameters of CWE in interaction with HEWL at 298 and 310 K.

Temperature	**Log K_a**	**K_a (ml g^{-1})**	***n***	**R^2**	**ΔG° (kJ ml g^{-1})**	**ΔH° (kJ ml g^{-1})**	**ΔS° (J ml g^{-1})**
298 K	3.62	4.23×10^4	0.81	0.99	-20.69	-25.38	-15.73
310 K	3.45	2.85×10^4	0.79	0.98	-20.50		

6.9.5. Docking analysis

HEWL is a multi-tryptophan containing protein with 6 tryptophan residues at positions 28, 62, 63, 108, 111 and 123. Approximately 80 % of the native's intrinsic fluorescence comes from residues 62 and 108. The compounds detected from HRLCMS for the CWE were docked with hen egg white lysozyme through the CB dock server, and the list of compounds with their binding score and contact residue details is given in **Table 6.7. (A)** and **(B)**. The docking details of the best-fitted compound with HEWL are discussed, and the docking poses of all other compounds are given in the appendix, **Table 6A.2. Figure 6.13.** shows the docking of HEWL with 1,4 di O Caffeoylquinic acid, which has the highest binding affinity with a docking score of -8.6 kcal/mol. The residues which are in contact with the ligand are Q_{35}, N_{46}, T_{47}, D_{48}, S_{50}, D_{52}, N_{57}, I_{58}, N_{59}, R_{61}, W_{62}, W_{63}, I_{98}, A_{107}, W_{108} and V_{109}. Three important tryptophan residues, W_{62}, W_{63}, and W_{108}, can be seen in contact with the ligand. It was observed that the binding force involved was mainly due to the conventional hydrogen bond, where we observed important binding residues of HEWL, Q_{35}, D_{52}, W_{62}, W_{63} and W_{108} [343] were involved in hydrogen bonding. These results correlate well with the overall thermodynamic parameter obtained from the fluorescence quenching by CWE. Also, through the fold analysis server, the amyloidogenic region was determined, depicted in red. This region was found to interact with the ligand, which explains the attenuation of aggregation. The next two compounds with the highest binding affinity with HEWL were Kaempferol 7 O glucoside and chlorogenic acid, which have a binding score of -7.6 kcal mol^{-1} and -7.4 kcal mol^{-1}, respectively.

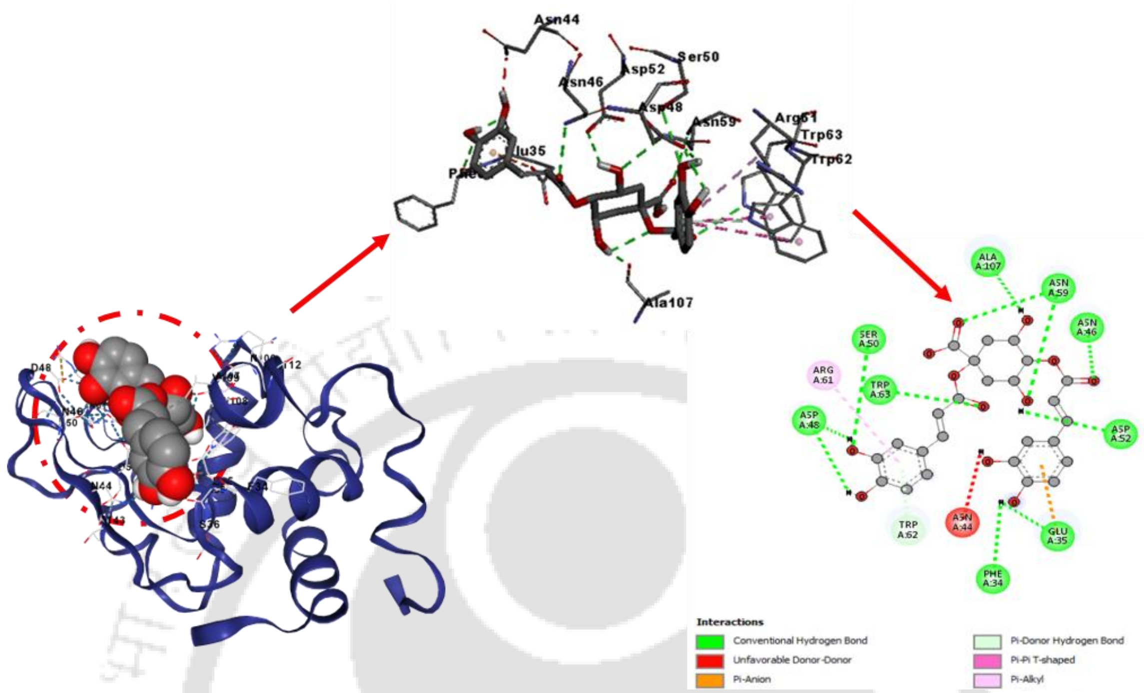

Figure 6.13. Docking pose of HEWL with 1,4-Di-O Caffeoylquinic acid.

Table 6.7. Compounds present in crude CWE and their docking score with HEWL.

(A) Compounds present in crude CWE

Mass	Abundance	Name	Formula
354.0975	89501	Chlorogenic acid	$C_{16}H_{18}O_9$
192.0637	87853	Quinic acid	$C_7H_{12}O_6$
110.0371	65432	Resorcinol	$C_6H_6O_2$
448.1047	56207	Kaempferol 7-O-glucoside	$C_{21}H_{20}O_{11}$
134.022	28499	Malic acid	$C_4H_6O_5$
180.0433	22253	Caffeic acid	$C_9H_8O_4$
516.1308	18667	1,4-Di-O-caffeoylquinic acid	$C_{25}H_{24}O_{12}$
958.5154	14973	Asiaticoside	$C_{48}H_{78}O_{19}$
168.042	14347	Vanillic acid	$C_8H_8O_4$

(B): Docking score and the contact residues details

Compound	Energy score (kcal/mol)	Contact amino acid residues
Chlorogenic acid	-7.4	Q_{35}, N_{46}, D_{52}, L_{56}, Q_{57}, I_{58}, N_{59}, W_{62}, W_{63}, K_{97}, I_{98}, D_{101}, G_{102}, N_{103}, A_{107}, W_{108} and V_{109}
Quinic acid	-5.8	N_{46}, D_{52}, L_{56}, Q_{57}, I_{58}, N_{59}, W_{62}, W_{63}, I_{98}, D_{101}, N_{103}, A_{107} and W_{108}
Malic acid	-4.6	Q_{35}, N_{46}, S_{50}, D_{52}, L_{56}, Q_{57}, I_{58}, N_{59}, A_{107}, W_{108}, V_{109} and A_{110}
Resorcinol	-4.5	D_{52}, L_{56}, Q_{57}, I_{58}, N_{59}, W_{63}, I_{98}, A_{107} and W_{108}
Kaempferol 7-O- glucoside	-7.6	N_{46}, S_{50}, D_{52}, L_{56}, Q_{57}, I_{58}, N_{59}, W_{62}, W_{63}, L_{75}, I_{98}, D_{101}, A_{107} and W_{108}
1,4 Di-O-Caffeoylquinicacid	-8.6	**Q_{35}**, N_{46}, T_{47}, D_{48}, S_{50}, **D_{52}**, N_{57}, I_{58}, N_{59}, R_{61}, **W_{62}**, **W_{63}**, I_{98}, A_{107}, **W_{108}** and V_{109}

6.10. Conclusions

In this study, C. asiatica, a nootropic plant, was employed for the anti-aggregation properties of HEWL fibrillation. HEWL protein was subjected to 65°C thermal induced aggregation at pH2 to induced aggregation. Samples pre-sheared at 300 s^{-1} for 1 hour at 65°C were used as seed and incubated at 65°C to compare with the non-seeded sample. The HEWL sample was also incubated with CWE at increasing concentrations of 10, 50, 100 and 300 µg/ml to check whether the extract could confer inhibition of fibrillation and or aggregation. Boltzmann fitting of the Th-T fluorescence data revealed that the pre-sheared samples have the maximum aggregation with an apparent rate constant of 1.01 days^{-1} and a short lag period of 3.80 days, whereas the non-sheared thermal induced samples have 4.67 days' lag period and the intensity of fluorescence was also lesser, with an apparent k of 0.88 days^{-1}. For samples treated with CWE, the lag phase is significantly longer, which is 6.20, 7.51, 33.59 and 54.76 days, respectively, for samples incubated with 10, 50, 100 and 300 µg/ml extract, respectively. The samples with higher concentrations of extracts were in the lag phase when the pre-sheared samples had already reached the plateau phase. With this different kinetics of aggregation, there is also a peculiar behaviour in the change in their secondary structure observed from the far UV-CD data. The fibril formed is a type two β protein made up of β sheets and unordered portions but with a higher constituent of unordered fraction. With the increase of fibrillation, the native dip at 208 and 222 nm diminishes and shifts towards a negative dip at 200 nm with more depth, implying more fibril formation. Therefore, in the case of HEWL treated with CWE extract, no significant shift towards 200 nm was observed, but there seems to be a decrease in alpha helix secondary structure content. The different courses of aggregation, the inhibition and the effect of pre-shearing were also distinctly observed in the morphology obtained through AFM. From the morphology of the CWE-treated HEWL aggregates, the attenuation of fibrillation was observed. Here, only a few short fibrils and mostly oligomeric species were distributed, which were of diameters in the range of 41 to 102 nm and lengths in the range of 117 nm to 429 nm, respectively. From the binding parameters and the energetics determined through fluorescence quenching of the extract and HEWL, the quenching was found to be static, and the binding force involved between the ligand and protein was hydrogen and van der Waals forces. Compounds obtained from the HRLCMS analysis were docked with HEWL, and the compound with the highest binding affinity was 1, 4-Di-O-Caffeoylquinic acid, with a binding score of – 8.6 kcal mol^{-1}.

6.11. CHAPTER 6C

In-vitro study of the cytotoxicity of the aggregates formed due to shearing of amyloidogenic protein (HEWL) and non-amyloidogenic protein (BSA) on neuroblast cells (IMR32)

In this subchapter, we studied the effect of non-amyloidogenic and amyloidogenic protein aggregates on a neuroblast cell line IMR32. The shear and thermal-induced aggregates of a non-amyloidogenic protein, the BSA, and one amyloidogenic protein, the HEWL, were studied. Protein samples treated with the CWE extract were also tested.

6.12. Introduction

Shear-induced aggregation of protein is one of the important fields of study where protein aggregation occurs directly or indirectly because of the effects of shear of various kinds. Shear exposure of protein can occur mainly in the biopharmaceutical industry, the physiological circulatory system, and the cerebrospinal fluid inside the brain, though the third hypothesis is made from the observation of many laboratory experiments. In the biopharmaceutical industry, protein formulations such as enzymes, hormones, cytokines, etc., are subjected to various extensional flows from processes like pumping, filtering filling, etc., [105, 344, 345]. In the circulatory system, the blood flow generates shear stress, which is non-uniform in the circulatory system. In clogged coronary arteries, the shear rate flows at 1640 s^{-1} and can reach an enormous 400 s^{-1}. The stress generated through the blood flow, mainly impacted by a small diameter arterial wall, results in the formation of arterial amyloid-like aggregates, which stimulate the inflammatory system and alter the biochemical process, for example, lipid metabolism [346]. When an injury or cut of the vascular system occurs, platelets in the bloodstream are targeted at this site and activated to form haemostatic thrombi, which helps in the coagulation of blood, thus stopping the bleeding. However, in the case of thrombosis, the platelets are activated pathologically, which leads to the abnormal growth of thrombi. This can lead to various cardiovascular diseases like myocardial infarction, ischemic stroke, and so on. The abnormal thrombotic event is mainly caused by biochemical factors and biomechanical factors. Biochemical factors include adhesive molecules, soluble agonists, and extracellular matrix proteins. The biomechanical factor arises due to the hemodynamic shear stress [117, 347, 348].

The shear force inside the cerebrospinal fluid has also been hypothesised to initiate aggregation of the Aβ peptides, which then leads to the formation of amyloid plaques in between the neuronal region and the neurofibrillary tangles within the neurons, which is the hallmark neurodegenerative diseases like Alzheimer's disease and Parkinson's disease.

As these protein aggregates finally have to do with the physiological system, we have also checked the impact of sheared-induced aggregate species in the presence and absence of CWE extract. The cell line used in our study was a neuroblast cell line IMR 32.

Here, the impact of the shear and thermal aggregate of amyloidogenic and non-amyloidogenic proteins was checked for toxicity. To compare the shear-induced aggregate toxicity level of HEWL, an amyloidogenic protein, with that of a non-amyloidogenic protein, we have also checked the impact of BSA shear-induced aggregates on the IMR32 cell line.

6.13. Materials and method

MTT (Cat No.: TC191, Himedia laboratories, Mumbai, MH, India), IMR-32 neuroblastoma cells were purchased from the National Centre for Cell Science (Pune, MH, India),

6.13.1. Effect of different HEWL aggregates in the absence and presence of CWE

6.13.1.1. Cytotoxicity assessment

Cytotoxicity of IMR-32 neuroblastoma cells in the presence of extract was assessed by the 3-(4,5-dimethylthiazol-2-yl)-2,5-diphenyltetrazolium bromide, MTT assay. Cellular enzymes of live cells reduce the tetrazolium dye MTT to an insoluble purple-coloured formazan product [8]. IMR-32 neuroblastoma cells were maintained at 37 °C and 5% CO_2 condition in DMEM/high glucose medium supplemented with 10% FBS and 1% antibiotic. Cells were seeded in a 96-well plate at a seeding density of 10^4 cells/well 24 h prior to the experiment. Further, cells were stimulated with HEWL aggregates (10 µM and 50 µM) with or without CWE (10 and 50 µM) for 24 h. For the BSA, both sheared and non-sheared aggregates at 15 µM were treated on the neuronal cells for 24 h before checking the viability. The absorbance was recorded at λ_{abs} = 570 nm using the FLUOstar® Omega microplate reader, and the percentage viability was evaluated.

6.14. Result and discussion

6.14.1. Effects of HEWL and BSA aggregates on IMR32 neuroblastoma cells

The cytotoxic effect of HEWL and BSA aggregates in the presence and absence of CWE was assessed on the IMR32 neuroblastoma cells. To evaluate the concentration-dependent cytotoxicity, two concentrations of HEWL (10 µM and 50 µM) aggregated over the period of 4 and 7 days were used. As indicated by the Th-T fluorescence intensity graph in **Figure 6.9. (A)**, the 4th day corresponds to the log phase, whereas the 7th day corresponds to the plateau phase of the HEWL aggregation. To further examine the positive effect of the CWE, three different concentrations of the CWE (10, 50, and 100 µg/ml) were considered. **Figure 6.14. (A),** indicates about 79 ± 9% and 83 ± 13% cell viability with 10 µM HEWL samples aggregated over 4 and 7 days, respectively. A similar observation for the aggregated HEWL was reported earlier [179]. With the gradual increase in the concentration of the CWE, a significant increase in the cell viability was observed, with the cell viability increasing up to 101 ± 2% and 100 ± 3% for 10 µM HEWL samples supplemented with 100 µg/ml of CWE and aggregated over 4 and 7 days, respectively. A decrease in the cell viability was evident for 50 µM aggregated HEWL samples, as compared to the 10 µM concentration, with viability value remaining at 55 ± 3% and 65 ± 13% for HEWL samples aggregated over 4 and 7 days, respectively (**Figure 6.14. (B))**. A concentration-dependent rescuing effect of the CWE was also similarly observed, with viability increasing up to 67 ± 2% and 76 ± 2% for 50 µM HEWL samples supplemented with 100 µg/ml of CWE and aggregated over 4 and 7 days, respectively. The regained cell viability could be due to the anti-amyloidogenic behaviour of CWE and its ability to inhibit the toxic β-sheet conformation, as indicated by Th-T and CD assays. From our observations, HEWL samples aggregated over 4 days may be inferred as more toxic than those for 7 days, considering the aggregation phase to be mostly populated by membrane-permeable toxic oligomers, contributing towards more pronounced toxicity [349].

Next, the shear-induced aggregates and the thermal-induced aggregates of non-amyloidogenic protein, BSA, at 15 µM concentrations, were treated on the neuronal cells. **Figure 6.15. (A)** shows the MTT assay of the different BSA aggregates on IMR32 cells. BSA aggregates, both shear and temperature-induced aggregates, were not toxic to the neuronal cells and showed viability at 80 % and above in all the aggregate species. Moreover, in both the HEWL and BSA-treated cells in the presence of the extract, viability seems to be enhanced compared to cells without extract. **Figure 6.15. (B),** shows the impact of different concentrations of only extract. It was observed that the viability of the neuronal cell was all well above 80 %.

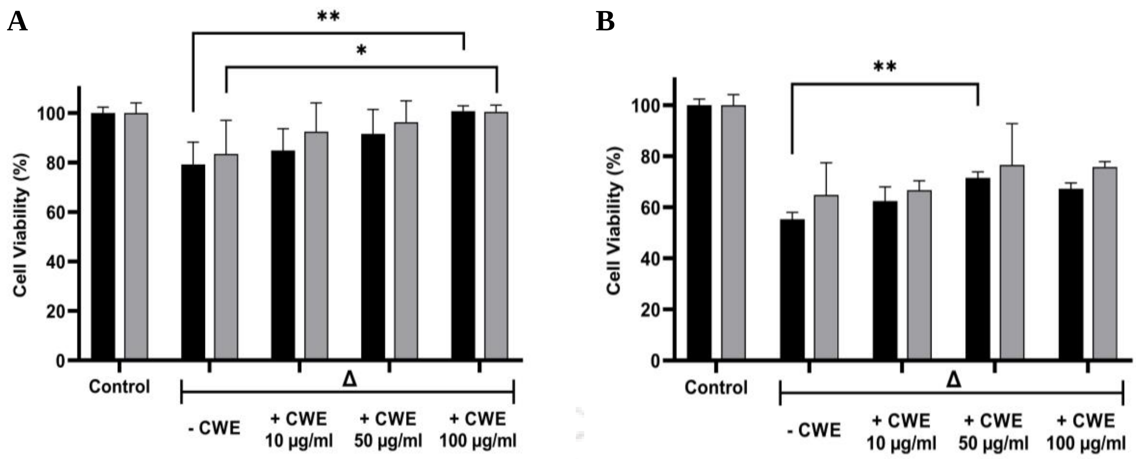

Figure 6.14. The cytotoxic effect of two different concentrations (A) 10 µM and (B) 50 µM of HEWL samples aggregated over 4 days (black) and 7 days (grey) in the absence and in the presence of different concentrations of CWE on IMR32 neuroblastoma cells. The p-values < 0.033, and <0.002 are labelled with *, and **, respectively.

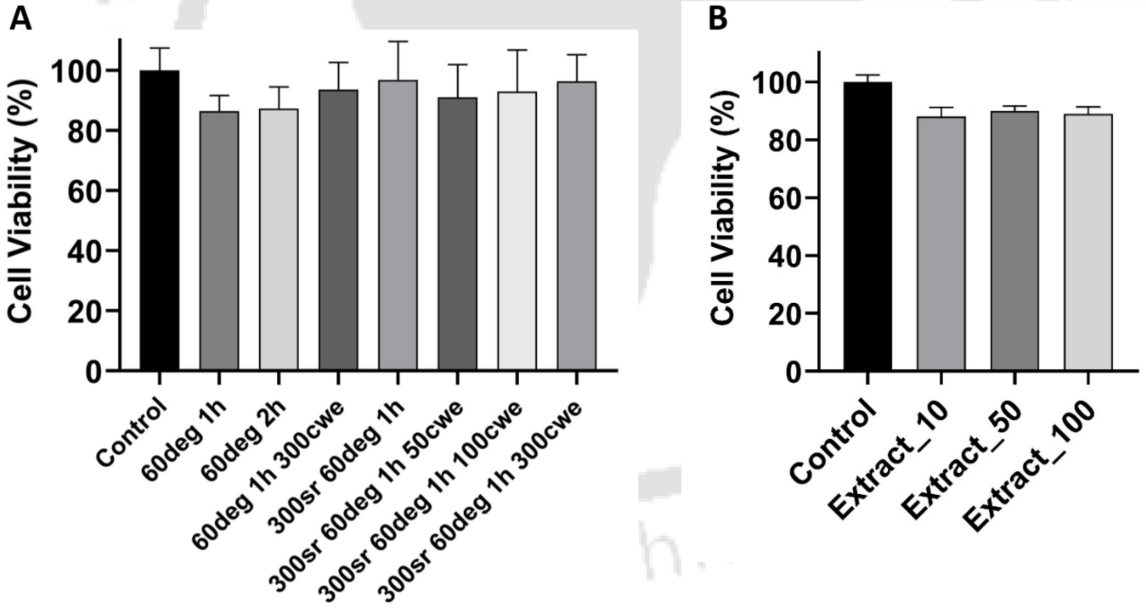

Figure 6.15. The cytotoxic effect of 15 µM concentration of BSA samples, both thermal induced and thermomechanical induced and in the presence of CWE on IMR32 neuroblastoma cells (A); the impact of different extract (CWE) concentration on cell viability (B).

6.15. Conclusions

The impact of sheared and non-sheared aggregates of HEWL in the presence and absence of CWE extract were tested for their toxicity on the IMR32 cell line, which is a neuroblast cell line. The aggregates show toxicity at higher concentrations among the two concentrations studied (10 and 50 µM). Comparatively, the pre-shared and the aggregates collected on day 4 were more toxic than the other. CWE extracts attenuate the aggregation of HEWL, which is reflected in the viability of cells. Sheared and non-sheared BSA aggregates with and without CWE were also assessed for their impact on the IMR32 cell line, and no significant toxicity was observed for all the aggregates studied. The aggregates showed toxicity at higher concentrations among the two concentrations studied (10 and 50 µM) and the 4th day sample, respectively. CWE attenuates the aggregation of HEWL, and the same is reflected in the viability of cells.

CHAPTER-7

Conclusions and future scope

This chapter summarises the crucial inclusive inferences of studies performed in the present dissertation. Furthermore, the chapter also confers future research ideas related to the present study.

7.1. The overall conclusions of the thesis

Shear and thermal-induced aggregation studies of amyloidogenic and non-amyloidogenic proteins were carried out. The amyloidogenic proteins studied were Aβ (1-40) and HEWL; the non-amyloidogenic proteins were BSA and BFG. Through a rheometer, the effects of varying and constant shear were investigated on Aβ (1-40) solution. Aβ (1-40) solution followed a non-Newtonian (shear-thickening) flow behaviour. Shear forces induced aggregation, which was confirmed by Th-T assay, CD, FTIR and AFM analyses. The apparent rate of aggregation increased with the shear rate and was found to be inversely correlated to the solution viscosity of shared samples. The cause of aggregation due to shear was investigated and explained in terms of dissipation energy, which exceeded the free energy of unfolding.

Then, another amyloidogenic protein, HEWL, was subjected to 65°C thermal induced aggregation at pH 2 to induced aggregation. The pre-sheared sample under the above conditions was then compared with the non-sheared samples. Th-T fluorescence data revealed that the pre-sheared samples had a higher aggregation rate than the non-sheared thermal-induced samples. With this different kinetics of aggregation, there is also a peculiar behaviour in the change in their secondary structure observed from the far UV-CD data.

Further, the energetics of the thermomechanical treatment of BSA and its related impact on the unfolding and aggregation behaviour were explored to decipher the roles of the thermal and dissipation energy. Temperature hysteresis scans of BSA at three temperature ranges show the irreversible unfolding and aggregation above its melting temperature (65 and 75 °C). Shear-induced aggregation of the BSA was performed at a constant shear rate and three temperatures. The rate of aggregation (*k*) was enhanced by 1.5 folds for the thermomechanical (sheared) process compared to thermal treatment, and a corresponding loss in the α-helix content was observed. Dissipation energy generated from the shearing accelerated the aggregation process's second step (fibrillation) at 60 and 65 °C. However, it could not initiate the first step (unfolding) of the aggregation at 55 °C, presumably the heat/energy loss to the neighbouring water molecules and surrounding.

Thermal and shear-induced aggregation of Bovine fibrinogen was also performed. From the thermal scanning study of BFG through CD spectroscopy, the unfolding of the three important transitions could be observed, which could be attributed to the three important domains unfolding of BFG. Three temperatures were chosen, and the thermal and shear-induced aggregation was carried out. Similar to the above case, enhanced aggregation was observed for the thermomechanical treated sample compared to the thermal alone treated sample.

Centella asiatica, a neuroprotective plant, was extracted using three solvents sequentially with increasing polarity to study protein aggregation inhibition further. The extracts were *Centella asiatica* ethyl acetate extract (CEE), *Centella asiatica* methanol extract (CME) and *Centella asiatica* water extract (CWE). The phenolic and flavonoid content was found to be highest in the case of CWE, followed by CEE and CME. In the same way, the IC50 value for scavenging the DPPH was lowest in the case of the CWE, followed by CEE and CME.

HRLCMS analysis revealed the presence of important compounds of *Centella asiatica*, like Asiatic acid, Medeccassic acid and Asiaticoside. From HPLC, it was found that more compounds are present in CEE than in CME and CWE. HRLCMS analysis of the crude CEE shows that Meritimetin is the most abundant compound, followed by Asiatic acid. Many other important terpenes like Medecassoside and Asiaticoside were also found in CEE extracts. In the case of CWE extract, malic acid was abundant, followed by Chlorogenic acid.

The extract was then checked with one non-amyloidogenic protein, BSA, and another amyloidogenic protein, HEWL. BSA was subjected to thermal and thermomechanical-induced aggregation in the presence and absence of CA extracts. CEE showed the maximum inhibition property of the three crude extracts studied, followed by CWE and CME. With the increase in extract concentration, the inhibition rate also increases, which attains saturation at around 300 μg/ml. For further analysis, CWE was chosen as it showed no significant changes after interaction with BSA, except a minute increase in α helix content and has comparable inhibition properties with CEE.

The combined study of HR-LCMS, HPLC, ITC and docking studies showed that Chlorogenic acid could be one of the major compounds present in CWE, which is involved in inhibiting aggregation. The interaction of BSA and the CWE in chlorogenic acid determined through ITC shows entropic and enthalpic contribution and spontaneous process. From Stern-Volmer quenching studies, the binding mechanism was determined to be hybrid quenching.

Further, CWE was also checked for its protein aggregation inhibition ability with HEWL treated with thermal-induced aggregation. The aggregation rate decreased, and the inhibition enhanced with increasing extract concentration. A corresponding increase in the lag phase was also observed. As observed from the far UV CD data, the formation of the type two β protein aggregates was prevented in the presence of CWE. The result was then further confirmed by the AFM analysis. HRLCMS and docking analysis showed that the probable major compound present in CWE, involved in the prevention of aggregation, could be 1,4-Di-O-Caffeoylquinic acid. From the SV quenching analysis, the binding mechanism involved was static, and the binding force between the ligand and protein was mainly hydrogen and van der Waals forces. Further, from the viability studies, HEWL aggregates showed toxicity at higher concentrations, whereas BSA aggregates showed negligible toxicity towards the IMR32 neuroblast cell line. CWE attenuates the aggregation of HEWL, and the same is reflected in the viability of cells.

Table 7.1: Summary of the shear induced aggregation of different proteins.

Studied proteins	Experimental condition	Rate of aggregation	Native	After aggregation	Rate of aggregation in presence of CWE	Lag time
Aβ (1−40)	300 s^{-1}, 500 s^{-1}, 700s^{-1} At 37°C	0.14 ± 0.02 min^{-1}, 0.15 ± 0.02 min^{-1} and 0.21 ± 0.03 min-^{1}	α-helix and RC:52 ± 2 %, , β sheet :35 ± 2 % and β turn :13 ± 3 %,	α-helix and RC:27 ± 1 %, , β sheet :58 ± 2% and β turn :16 ± 2 %,sheared at 700 s-^{1}	NA	14 ± 1 min (found independent of shear)
HEWL	300 s^{-1}, 65°C and at pH2,	Pre-sheared HEWL:1.01 day^{-1} Thermal HEWL: 0.88 day-1	α helix: 33 %, β sheet :13 %, β turn :17 % and unordered structure : 37%	conformation towards a type II beta protein secondary structure		3.80 days 4.67 days
BSA	55°C, 60°C and 65°C, At 300 s^{-1}	0.076 ± 0.01 min^{-1}, 0.024 ± 0.005 min^{-1} and 0.021 ± 0.005 min^{-1}		40% and 90% at 60°C and 65°C 55°C caused no change in secondary structure		No lag time
	300 s^{-1} , 60°C				BSA alone :1.64 h^{-1} BSA+ 300 µg/ml CEE :0.96 h^{-1}, BSA+ 300 µg/ml CWE: 1.35 h^{-1} and BSA+ 300 µg/ml CME: 1.60 h^{-1}	
BFG	45°C 60°C and At 300 s^{-1}	0.093± 0.01 min^{-1} 0.096± 0.02 min^{-1}	27.35% α-helix	1.75 and 12.37 % decrease in α-helix	NA	No lag time

7.2. Future scope

1. **Further binding studies of the five best-scored compounds with the proteins can be carried out**

   To further determine the compound responsible for the aggregation inhibition study we covered earlier in the thesis work, an interaction study of the five individual compounds that scored highest in the docking can be performed. Isothermal titration calorimetry and intrinsic fluorescence quenching studies can be performed for these five compounds with BSA and HEWL. This study will further support the results obtained in the thesis work more qualitatively.

2. **Shear-induced aggregation study of intrinsically disordered proteins (IDPs), such as Aβ and α-synuclein, using surface modified surface.**

   We know the implications of shear in the physiological system, particularly the brain parenchyma. However, in many cases, the shear-induced studies of protein involve the protein being subjected to shear in a suitable apparatus/machine, such as the rheometer. However, to perform the shear studies in a more realistic approach, mimicking the natural conditions of the brain parenchyma is an obvious option. To perform this, coverslips or suitable surfaces can be surface-modified by **adsorbing proteins such as collagen, laminin, and HSPG to mimic the parenchymal environment,** and then after the successful adsorption of the proteins, shear-induced aggregation of proteins such as Amyloid beta, α synuclein and other protein related to neurodegeneration can be performed.

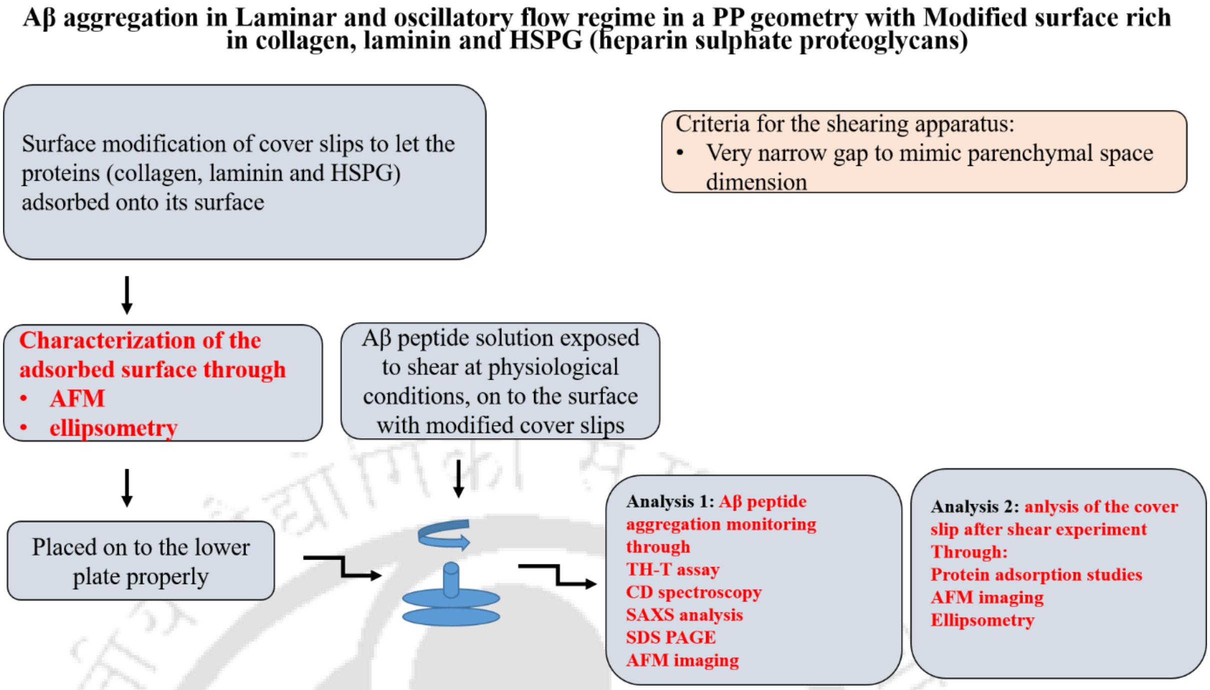

Figure 7.1. Flow diagram depicting the steps of shear-induced aggregation of IDPs on surface-modified surface

3. Shear-induced aggregation study with the same molecular mass

Next, shear-induced aggregation of different proteins with the same molecular mass or almost similar mass, for example (alpha2 globulin and beta globulin and lysozyme and ribonuclease A), can be checked. Here, both laminar and oscillatory flow modes can be tested, as such types of flow have been found to prevail inside our system.

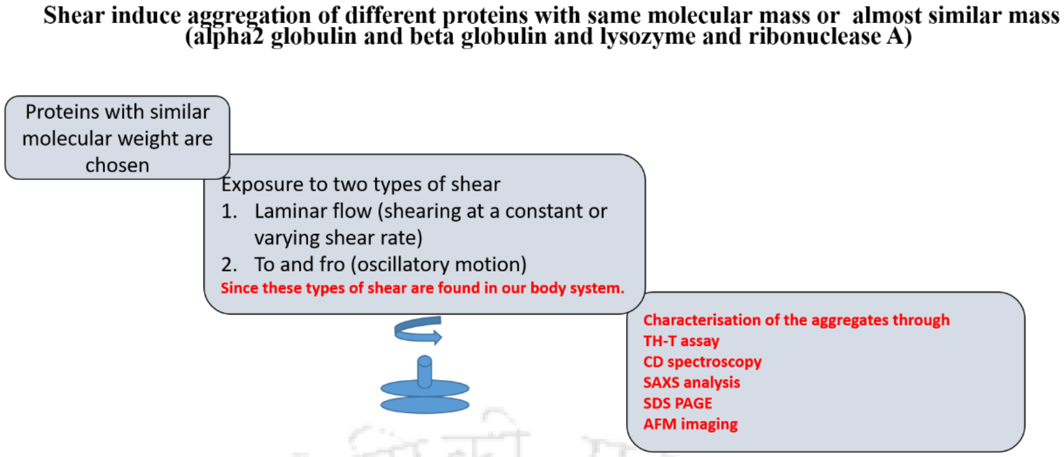

Figure 7.2. Flow diagram depicting the steps of shear-induced aggregation of similar molecular mass proteins in laminar and oscillatory flow.

APPENDICES

Appendix 3A

Shear and thermal induced aggregation of amyloidogenic proteins Aβ (1-40) (Amyloid beta 1-40) and HEWL (Hen Egg White Lysozyme)

3A.1. Dissipation energy

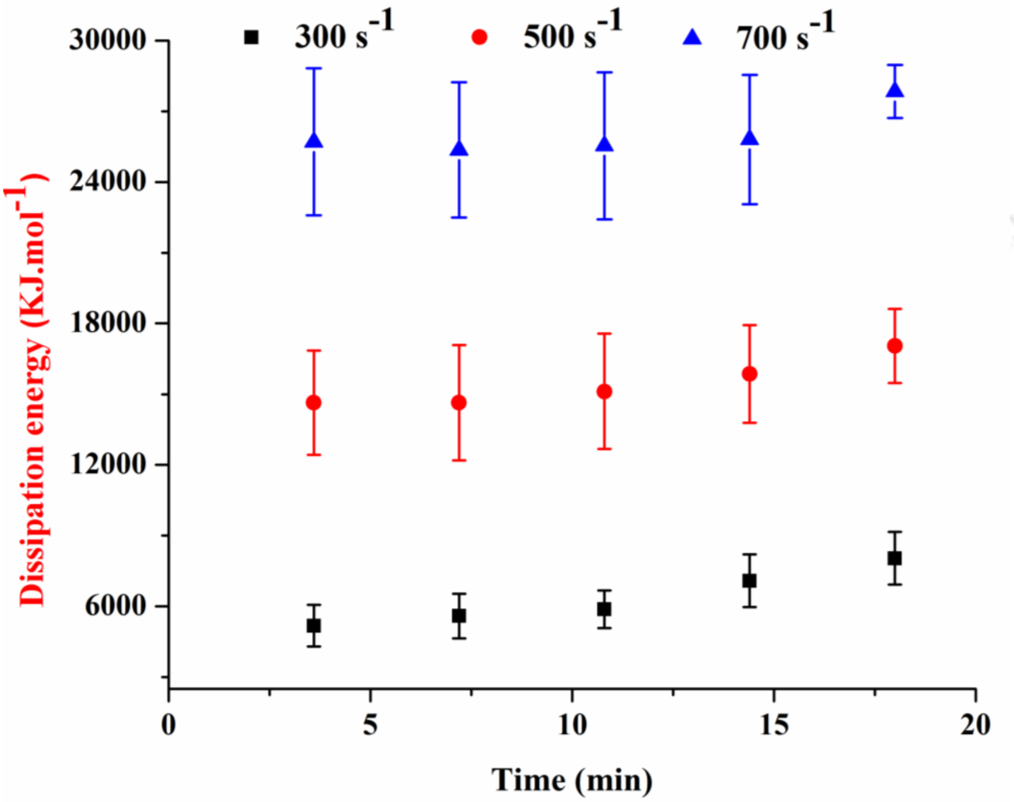

Figure 3A.1. The change in dissipation energy ($\gamma^2 \times \eta$) of Aβ (1-40) solution at constant shear rates of 300 s^{-1}, 500 s^{-1} and 700 s^{-1}. The experiment was performed using an MCR72 rheometer for 18 minutes.

3A.2. Secondary structure determination through FTIR analysis

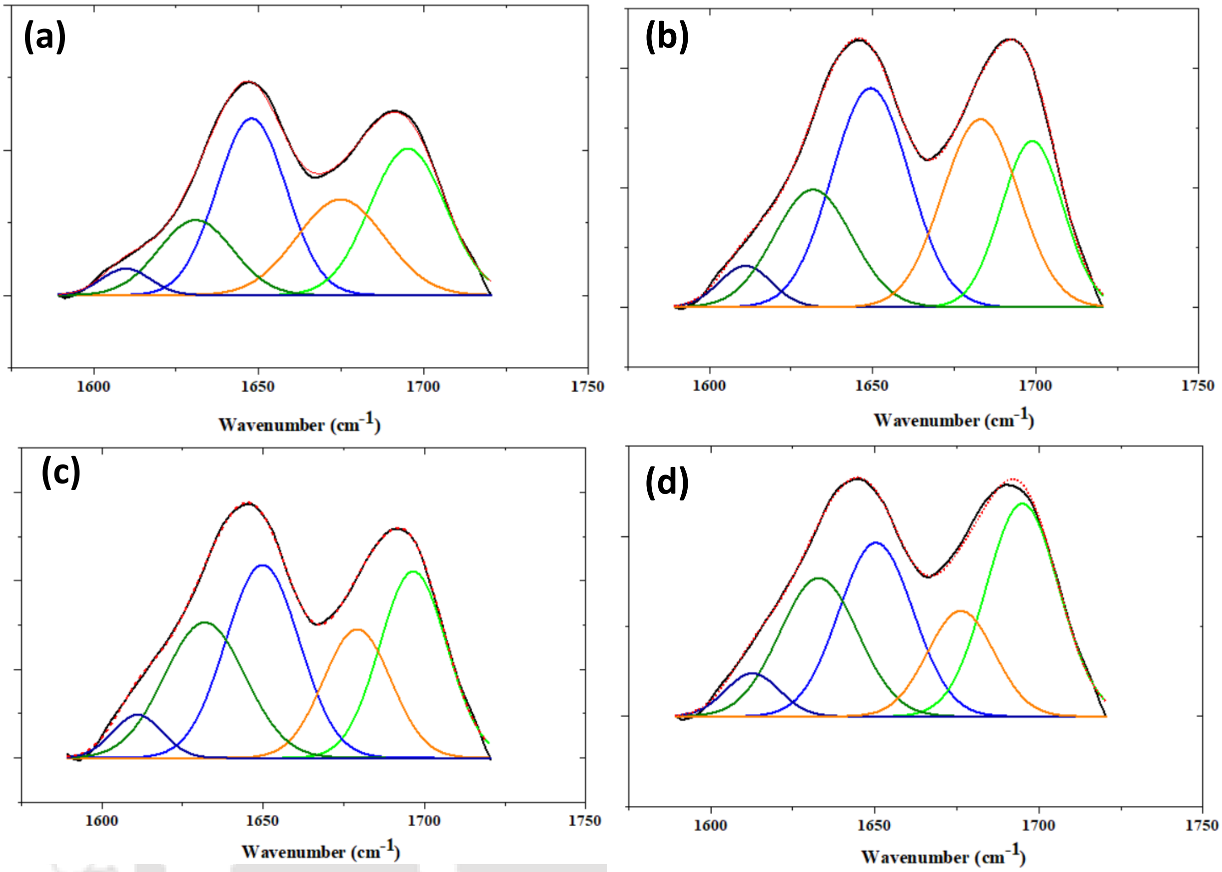

Figure 3A.2. FTIR spectra of native (a) and sheared samples 300 s^{-1}(b), 500 s^{-1} (c) and 700 s^{-1} (d) in the Amide-I region. The spectra were deconvoluted and fitted using the origin 8.5 version to extract the components of the secondary structure.

Appendix 6A

Effect of *Centella asiatica* (CA) on the non-amyloidogenic and amyloidogenic proteins (BSA and HEWL) and in-vitro study of the cytotoxicity of the aggregates formed due to shearing of the above proteins on neuroblast cell line (IMR32)

6A.1. Docking results of compounds obtained from HRLCMS

Table 6A.1. Docking of compounds obtained from CEE and CWE extract

Sl.no.	Compound	2D pose of BSA and ligand interaction	CB dock score
A	1,4 di caffeoylquinic acid	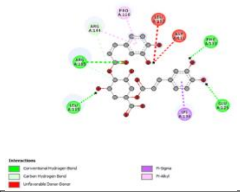	-8.5
B	Malic acid	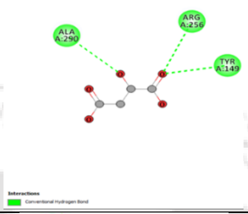	-4.9
C	Quinic acid	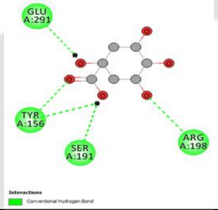	-6.0
D	Resorcinol	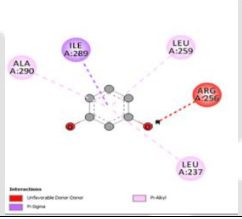	-4.9
E	Kaempferol	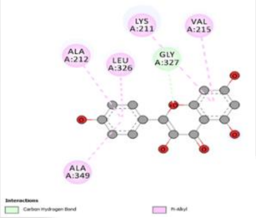	-7.5
F	4-O-Caffeoyl-3-Oferuloylquinic acid	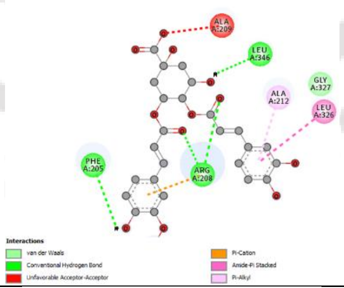	-8.2
G	Asiaticoside	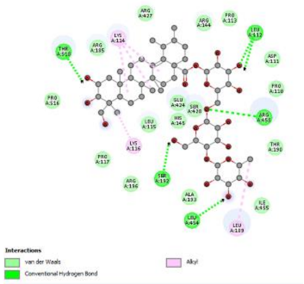	-9.3

H	Caffeic acid	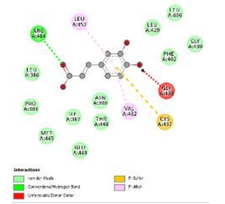	-6.6
I	Kaempferol 7-O-glucoside	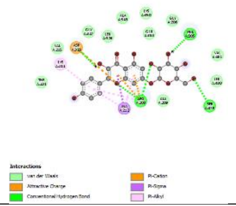	-8.3
J	Maritimetin	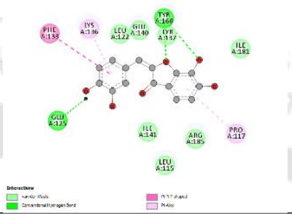	-8.1
K	Medecassoside	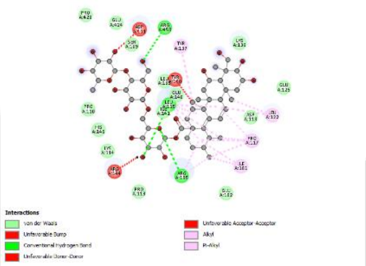	-9.3
L	Vanillic acid	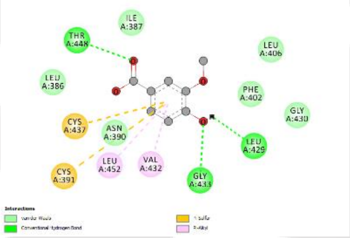	-6.2

6A.2. Fluorescence spectra of BSA with CWE eluted fraction B.

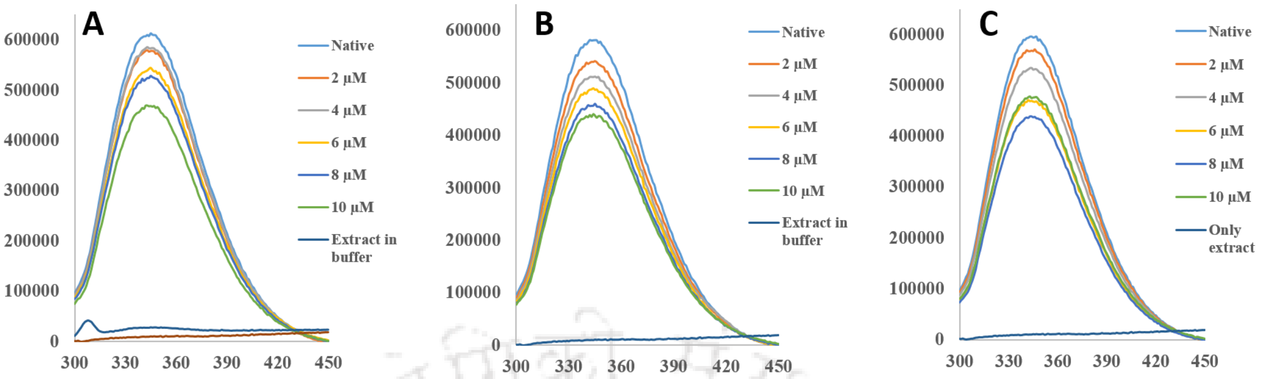

Figure 6A.2. BSA quenching by eluted CWE B fraction at (A)298 K, (B)310 K, and (C)318 K, respectively. The concentration of BSA was 2 µM, and the extract concentrations were 2 µg.ml^{-1}, 4 µg.ml^{-1}, 6 µg.ml^{-1}, 8 µg.ml^{-1} and 10 µg.ml^{-1}.

6A.3. Fluorescence quenching study with crude CWE with HEWL.

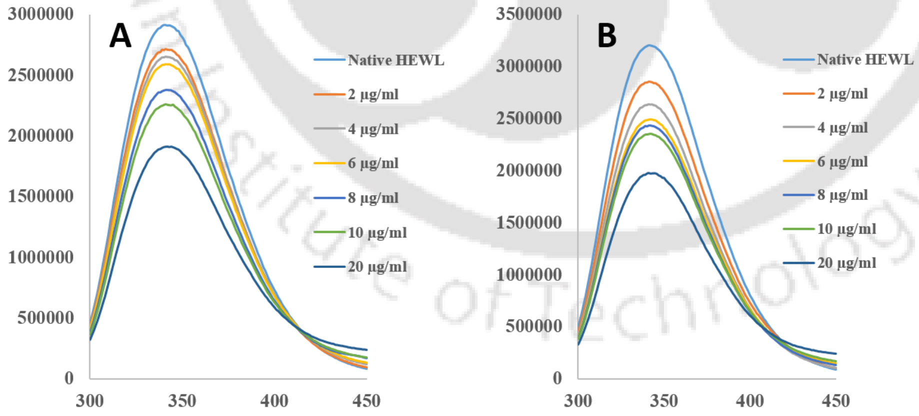

Figure 6A.3. Fluorescence quenching of HEWL by CWE at (A) 298 K and (B) 310 K

Table 6A.2. Docking of compounds obtained from CWE extract with HEWL

Sl.no.	Compound	2D pose of HEWL and ligand interaction	CB dock score
A	Chlorogenic acid	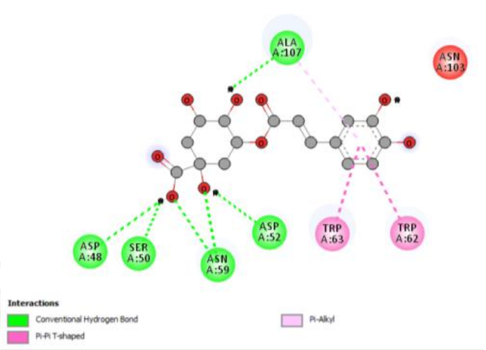	-7.4
C	Malic acid	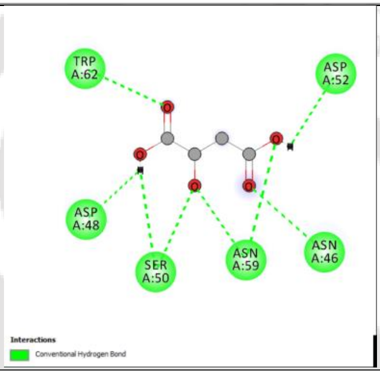	-4.6
D	Quinic acid	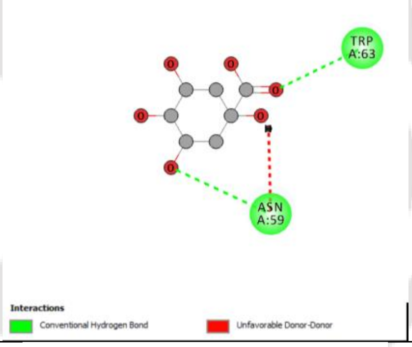	-4.5
E	Resorcinol	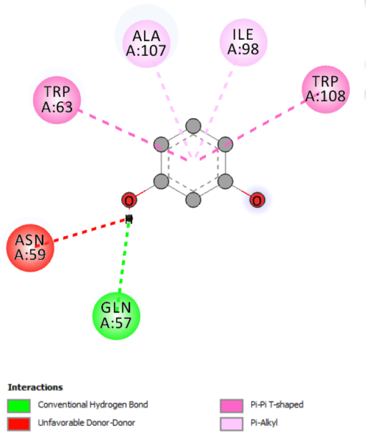	-7.6

References

1. Chaturvedi, S.K., et al., *Protein misfolding and aggregation: mechanism, factors and detection.* Process Biochemistry, 2016. **51**(9): p. 1183-1192.
2. Yoon, M.-K., et al., *Cell cycle regulation by the intrinsically disordered proteins p21 and p27.* Biochemical Society Transactions, 2012. **40**(5): p. 981-988.
3. Kocaturk, N.M. and D. Gozuacik, *Crosstalk between mammalian autophagy and the ubiquitin-proteasome system.* Frontiers in cell and developmental biology, 2018. **6**: p. 128.
4. Li, Y., S. Li, and H. Wu, *Ubiquitination-proteasome system (UPS) and autophagy two main protein degradation machineries in response to cell stress.* Cells, 2022. **11**(5): p. 851.
5. Buell, A.K., *The nucleation of protein aggregates-from crystals to amyloid fibrils.* International review of cell and molecular biology, 2017. **329**: p. 187-226.
6. Lomont, J.P., et al., *Spectroscopic signature for stable β-amyloid fibrils versus β-sheet-rich oligomers.* The Journal of Physical Chemistry B, 2017. **122**(1): p. 144-153.
7. Gomes, C.M., W. Hoyer, and J. Luo, *The Biochemistry of Amyloids in Neurodegenerative Diseases, Volume I*. 2021, Frontiers Media SA. p. 819481.
8. Gomes, C.M., W. Hoyer, and J. Luo, *The biochemistry of amyloids in neurodegenerative diseases, volume II*. 2023, Frontiers Media SA. p. 1236518.
9. Buchanan, L.E., et al., *Structural polymorphs suggest competing pathways for the formation of amyloid fibrils that diverge from a common intermediate species.* Biochemistry, 2018. **57**(46): p. 6470-6478.
10. Wang, W., S. Nema, and D. Teagarden, *Protein aggregation—Pathways and influencing factors.* International journal of pharmaceutics, 2010. **390**(2): p. 89-99.
11. Trumbore, C.N., *Shear-induced amyloid formation in the brain: I. Potential vascular and parenchymal processes.* Journal of Alzheimer's Disease, 2016. **54**(2): p. 457-470.
12. Lichota, A., E.M. Szewczyk, and K. Gwozdzinski, *Factors affecting the formation and treatment of thrombosis by natural and synthetic compounds.* International journal of molecular sciences, 2020. **21**(21): p. 7975.
13. Schenk, S. and V. Quaranta, *Tales from the crypt [ic] sites of the extracellular matrix.* Trends in cell biology, 2003. **13**(7): p. 366-375.
14. Hocking, D.C., et al., *Extracellular matrix fibronectin mechanically couples skeletal muscle contraction with local vasodilation.* Circulation research, 2008. **102**(3): p. 372-379.
15. Bayer, T.A., *Proteinopathies, a core concept for understanding and ultimately treating degenerative disorders?* European Neuropsychopharmacology, 2015. **25**(5): p. 713-724.
16. Kwan, T.O., et al., *Measuring Protein Aggregation and Stability Using High-Throughput Biophysical Approaches.* Frontiers in Molecular Biosciences, 2022. **9**: p. 890862.
17. Fang, W.-J., et al., *Freeze-Dried Monoclonal Antibody Formulations are Unexpectedly More Prone to Degradation Than Liquid Formulations Under Shaking Stress.* Journal of Pharmaceutical Sciences, 2022. **111**(7): p. 2134-2138.
18. Wöll, A.K., et al., *Analysis of phase behavior and morphology during freeze-thaw applications of lysozyme.* International Journal of Pharmaceutics, 2019. **555**: p. 153-164.
19. Rajan, R., et al., *Review of the current state of protein aggregation inhibition from a materials chemistry perspective: Special focus on polymeric materials.* Materials Advances, 2021. **2**(4): p. 1139-1176.
20. Brown, M.R., S.E. Radford, and E.W. Hewitt, *Modulation of β-amyloid fibril formation in Alzheimer's disease by microglia and infection.* Frontiers in molecular neuroscience, 2020. **13**: p. 609073.
21. Yang, H., et al., *Based on molecular structures: Amyloid-β generation, clearance, toxicity and therapeutic strategies.* Frontiers in Molecular Neuroscience, 2022. **15**: p. 927530.

22. Rodríguez-Rodríguez, C., et al., *Crystal structure of thioflavin-T and its binding to amyloid fibrils: insights at the molecular level.* Chemical Communications, 2010. **46**(7): p. 1156-1158.
23. Shehabeldin, A., et al., *Increased Diagnostic Specificity of Congo Red Stain for Amyloid: The Potential Role of Texas Red–Filtered Fluorescence Microscopy.* Archives of Pathology & Laboratory Medicine, 2023. **147**(8): p. 907-915.
24. Lee, S., et al., *Aggregation and cellular toxicity of pathogenic or non-pathogenic proteins.* Scientific reports, 2020. **10**(1): p. 5120.
25. Ganguly, G., et al., *Proteinopathy, oxidative stress and mitochondrial dysfunction: cross talk in Alzheimer's disease and Parkinson's disease.* Drug design, development and therapy, 2017: p. 797-810.
26. Castillo, V. and S. Ventura, *Amyloidogenic regions and interaction surfaces overlap in globular proteins related to conformational diseases.* PLoS computational biology, 2009. **5**(8): p. e1000476.
27. Fändrich, M., M.A. Fletcher, and C.M. Dobson, *Amyloid fibrils from muscle myoglobin.* Nature, 2001. **410**(6825): p. 165-166.
28. Lehmann, S., et al., *Cerebrospinal fluid A beta 1–40 peptides increase in Alzheimer's disease and are highly correlated with phospho-tau in control individuals.* Alzheimer's research & therapy, 2020. **12**: p. 1-12.
29. Qiu, T., et al., *Aβ42 and Aβ40: similarities and differences.* Journal of peptide science, 2015. **21**(7): p. 522-529.
30. Coles, M., et al., *Solution structure of amyloid β-peptide (1− 40) in a water− micelle environment. Is the membrane-spanning domain where we think it is?* Biochemistry, 1998. **37**(31): p. 11064-11077.
31. Chen, G.-f., et al., *Amyloid beta: structure, biology and structure-based therapeutic development.* Acta pharmacologica sinica, 2017. **38**(9): p. 1205-1235.
32. Olubiyi, O.O. and B. Strodel, *Structures of the amyloid β-peptides Aβ1–40 and Aβ1–42 as influenced by pH and a D-peptide.* The Journal of Physical Chemistry B, 2012. **116**(10): p. 3280-3291.
33. Janek, T., et al., *Synergistic effect of hen egg white lysozyme and lysosomotropic surfactants on cell viability and membrane permeability.* Colloids and Surfaces B: Biointerfaces, 2020. **185**: p. 110598.
34. Pleyer, C., J. Flesche, and F. Saeed, *Lysozyme amyloidosis–a case report and review of the literature.* Clinical nephrology. Case studies, 2015. **3**: p. 42.
35. Chapman, J. and A. Dogan, *Fibrinogen alpha amyloidosis: insights from proteomics.* Expert review of proteomics, 2019. **16**(9): p. 783-793.
36. Otzen, D.E., O. Kristensen, and M. Oliveberg, *Designed protein tetramer zipped together with a hydrophobic Alzheimer homology: a structural clue to amyloid assembly.* Proceedings of the National Academy of Sciences, 2000. **97**(18): p. 9907-9912.
37. Murayama, K. and M. Tomida, *Heat-induced secondary structure and conformation change of bovine serum albumin investigated by Fourier transform infrared spectroscopy.* Biochemistry, 2004. **43**(36): p. 11526-11532.
38. Pandey, L.M., S.K. Pattanayek, and D. Delabouglise, *Properties of adsorbed bovine serum albumin and fibrinogen on self-assembled monolayers.* The Journal of Physical Chemistry C, 2013. **117**(12): p. 6151-6160.
39. Chen, M., et al., *The secondary and aggregation structural changes of BSA induced by trivalent chromium: A biophysical study.* Journal of Luminescence, 2015. **158**: p. 116-124.
40. Valim, M.D., A.L. Cavallieri, and R.L. Cunha, *Whey protein/arabic gum gels formed by chemical or physical gelation process.* Food Biophysics, 2009. **4**(1): p. 23-31.
41. Sharif, H.R., et al., *Current progress in the utilization of native and modified legume proteins as emulsifiers and encapsulants–A review.* Food Hydrocolloids, 2018. **76**: p. 2-16.

42. Quevedo, M., et al., *Kinetics of denaturation and aggregation of highly concentrated β-Lactoglobulin under defined thermomechanical treatment.* Journal of Food Engineering, 2020. **274**: p. 109825.
43. Rondeau, P., et al., *Thermal aggregation of glycated bovine serum albumin.* Biochimica et Biophysica Acta (BBA)-Proteins and Proteomics, 2010. **1804**(4): p. 789-798.
44. Arakawa, T. and Y. Kita, *Protection of bovine serum albumin from aggregation by Tween 80.* Journal of pharmaceutical sciences, 2000. **89**(5): p. 646-651.
45. Deeth, H.C. and N. Bansal, *Whey proteins: from milk to medicine*. 2018: Academic Press.
46. Clark, A., G. Kavanagh, and S. Ross-Murphy, *Globular protein gelation—theory and experiment.* Food Hydrocolloids, 2001. **15**(4-6): p. 383-400.
47. Zhmurov, A., et al., *Mechanical transition from α-helical coiled coils to β-sheets in fibrin (ogen).* Journal of the American Chemical Society, 2012. **134**(50): p. 20396-20402.
48. Bratek-Skicki, A., P. Żeliszewska, and J.M. Ruso, *Fibrinogen: a journey into biotechnology.* Soft Matter, 2016. **12**(42): p. 8639-8653.
49. Hassan, N., et al., *Fibrinogen stability under surfactant interaction.* Journal of colloid and interface science, 2011. **362**(1): p. 118-126.
50. Soria, J., et al., *Fibrinogen αC domain: its importance in physiopathology.* Research and Practice in Thrombosis and Haemostasis, 2019. **3**(2): p. e12183.
51. Page, M.J., et al., *Serum amyloid A binds to fibrin (ogen), promoting fibrin amyloid formation.* Scientific reports, 2019. **9**(1): p. 3102.
52. Stangou, A.J., et al., *Hereditary fibrinogen A α-chain amyloidosis: phenotypic characterization of a systemic disease and the role of liver transplantation.* Blood, The Journal of the American Society of Hematology, 2010. **115**(15): p. 2998-3007.
53. Herrick, S., et al., *Fibrinogen.* The international journal of biochemistry & cell biology, 1999. **31**(7): p. 741-746.
54. Lee, C.F., *Self-assembly of protein amyloids: A competition between amorphous and ordered aggregation.* Physical Review E, 2009. **80**(3): p. 031922.
55. Hamley, I.W., *Peptide fibrillization.* Angewandte Chemie International Edition, 2007. **46**(43): p. 8128-8147.
56. Lambert, M.P., et al., *Diffusible, nonfibrillar ligands derived from Aβ1–42 are potent central nervous system neurotoxins.* Proceedings of the National Academy of Sciences, 1998. **95**(11): p. 6448-6453.
57. Dahlgren, K.N., et al., *Oligomeric and fibrillar species of amyloid-β peptides differentially affect neuronal viability.* Journal of Biological Chemistry, 2002. **277**(35): p. 32046-32053.
58. Hartley, D.M., et al., *Protofibrillar intermediates of amyloid β-protein induce acute electrophysiological changes and progressive neurotoxicity in cortical neurons.* Journal of Neuroscience, 1999. **19**(20): p. 8876-8884.
59. Wang, S.S.S., et al., *Diseases of protein aggregation and the hunt for potential pharmacological agents.* Biotechnology Journal: Healthcare Nutrition Technology, 2008. **3**(2): p. 165-192.
60. Glabe, C.G., *Common mechanisms of amyloid oligomer pathogenesis in degenerative disease.* Neurobiology of aging, 2006. **27**(4): p. 570-575.
61. Lashuel, H.A., et al., *Neurodegenerative disease: amyloid pores from pathogenic mutations.* Nature, 2002. **418**(6895): p. 291.
62. Kourie, J.I. and C.L. Henry, *Ion channel formation and membrane-linked pathologies of misfolded hydrophobic proteins: the role of dangerous unchaperoned molecules.* Clinical and experimental pharmacology and physiology, 2002. **29**(9): p. 741-753.
63. Nagel-Steger, L., M.C. Owen, and B. Strodel, *An account of amyloid oligomers: facts and figures obtained from experiments and simulations.* ChemBioChem, 2016. **17**(8): p. 657-676.

64. Masson, P. and S. Lushchekina, *Conformational stability and denaturation processes of proteins investigated by electrophoresis under extreme conditions.* Molecules, 2022. **27**(20): p. 6861.
65. Nelson, D.L., A.L. Lehninger, and M.M. Cox, *Lehninger principles of biochemistry*. 2008: Macmillan.
66. Zhang, L., D. Lu, and Z. Liu, *How native proteins aggregate in solution: A dynamic Monte Carlo simulation.* Biophysical chemistry, 2008. **133**(1-3): p. 71-80.
67. Weiss IV, W.F., T.M. Young, and C.J. Roberts, *Principles, approaches, and challenges for predicting protein aggregation rates and shelf life.* Journal of pharmaceutical sciences, 2009. **98**(4): p. 1246-1277.
68. Cabra, V., et al., *The effect of sulfhydryl groups and disulphide linkage in the thermal aggregation of Z19 α-zein.* Biochimica et Biophysica Acta (BBA)-Proteins and Proteomics, 2008. **1784**(7-8): p. 1028-1036.
69. Rosenfeld, M., et al., *Self-assembly of fibrin monomers and fibrinogen aggregation during ozone oxidation.* Biochemistry (Moscow), 2009. **74**(1): p. 41-46.
70. Buchner, J. and T. Kiefhaber, *Protein folding handbook*. Vol. 3. 2005: Wiley-VCH Weinheim.
71. Barz, B. and B. Urbanc, *Minimal model of self-assembly: Emergence of diversity and complexity.* The Journal of Physical Chemistry B, 2014. **118**(14): p. 3761-3770.
72. Kumar, S., et al., *Relationship between potential aggregation-prone regions and HLA-DR-binding T-cell immune epitopes: implications for rational design of novel and follow-on therapeutic antibodies.* Journal of pharmaceutical sciences, 2012. **101**(8): p. 2686-2701.
73. Brubaker, W.D., et al., *Separating instability from aggregation propensity in γS-crystallin variants.* Biophysical journal, 2011. **100**(2): p. 498-506.
74. Wang, W. and C.J. Roberts, *Protein aggregation–Mechanisms, detection, and control.* International journal of pharmaceutics, 2018. **550**(1-2): p. 251-268.
75. Wang, W. and C.J. Roberts, *Non-Arrhenius protein aggregation.* The AAPS journal, 2013. **15**(3): p. 840-851.
76. Oliva, A., J.B. Fariña, and M. Llabrés, *Pre-study and in-study validation of a size-exclusion chromatography method with different detection modes for the analysis of monoclonal antibody aggregates.* Journal of Chromatography B, 2016. **1022**: p. 206-212.
77. Ramakrishna, D., M.D. Prasad, and A.K. Bhuyan, *Hydrophobic collapse overrides Coulombic repulsion in ferricytochrome c fibrillation under extremely alkaline condition.* Archives of biochemistry and biophysics, 2012. **528**(1): p. 67-71.
78. Andrews, J.M. and C.J. Roberts, *Non-native aggregation of α-chymotrypsinogen occurs through nucleation and growth with competing nucleus sizes and negative activation energies.* Biochemistry, 2007. **46**(25): p. 7558-7571.
79. Luan, B., et al., *Cooperative cold denaturation: the case of the C-terminal domain of ribosomal protein L9.* Biochemistry, 2013. **52**(14): p. 2402-2409.
80. Esfandiary, R., et al., *Mechanism of reversible self-association of a monoclonal antibody: role of electrostatic and hydrophobic interactions.* Journal of pharmaceutical sciences, 2015. **104**(2): p. 577-586.
81. Nishi, H., et al., *Phase separation of an IgG1 antibody solution under a low ionic strength condition.* Pharmaceutical research, 2010. **27**(7): p. 1348-1360.
82. Casaz, P., et al. *Resolving self-association of a therapeutic antibody by formulation optimization and molecular approaches*. in *MAbs*. 2014. Taylor & Francis.
83. Trnková, L., J. Dršata, and I. Boušová, *Oxidation as an important factor of protein damage: Implications for Maillard reaction.* Journal of biosciences, 2015. **40**(2): p. 419-439.
84. Torosantucci, R., C. Schöneich, and W. Jiskoot, *Oxidation of therapeutic proteins and peptides: structural and biological consequences.* Pharmaceutical research, 2014. **31**(3): p. 541-553.

85. Fazeli, A., et al., *Effect of arginine on pre-nucleus Stage of interferon beta-1b aggregation.* AAPS PharmSciTech, 2014. **15**(6): p. 1619-1629.
86. Jana, A.K., et al., *Glycation induces conformational changes in the amyloid-β peptide and enhances its aggregation propensity: molecular insights.* Physical Chemistry Chemical Physics, 2016. **18**(46): p. 31446-31458.
87. Shi, Y., et al., *Deamidation of asparagine to aspartate destabilizes Cu, Zn superoxide dismutase, accelerates fibrillization, and mirrors ALS-linked mutations.* Journal of the American Chemical Society, 2013. **135**(42): p. 15897-15908.
88. Joshi, V., et al., *Avoiding antibody aggregation during processing: establishing hold times.* Biotechnology journal, 2014. **9**(9): p. 1195-1205.
89. Filipe, V., et al., *Transient molten globules and metastable aggregates induced by brief exposure of a monoclonal IgG to low pH.* Journal of pharmaceutical sciences, 2012. **101**(7): p. 2327-2339.
90. Brummitt, R.K., et al., *Nonnative aggregation of an IgG1 antibody in acidic conditions: part 1. Unfolding, colloidal interactions, and formation of high-molecular-weight aggregates.* Journal of pharmaceutical sciences, 2011. **100**(6): p. 2087-2103.
91. Buell, A.K., et al., *Solution conditions determine the relative importance of nucleation and growth processes in α-synuclein aggregation.* Proceedings of the National Academy of Sciences, 2014. **111**(21): p. 7671-7676.
92. Bhattacharya, M., N. Jain, and S. Mukhopadhyay, *Insights into the mechanism of aggregation and fibril formation from bovine serum albumin.* The Journal of Physical Chemistry B, 2011. **115**(14): p. 4195-4205.
93. Buell, A.K., et al., *Electrostatic effects in filamentous protein aggregation.* Biophysical journal, 2013. **104**(5): p. 1116-1126.
94. Bis, R.L., et al., *Role of benzyl alcohol in the unfolding and aggregation of interferon α-2a.* Journal of pharmaceutical sciences, 2015. **104**(2): p. 407-415.
95. Liu, L., et al., *The effects of excipients on protein aggregation during agitation: an interfacial shear rheology study.* Journal of pharmaceutical sciences, 2013. **102**(8): p. 2460-2470.
96. Kishore, R.S., et al., *The degradation of polysorbates 20 and 80 and its potential impact on the stability of biotherapeutics.* Pharmaceutical research, 2011. **28**(5): p. 1194-1210.
97. Bis, R.L. and K.M. Mallela, *Antimicrobial preservatives induce aggregation of interferon alpha-2a: The order in which preservatives induce protein aggregation is independent of the protein.* International journal of pharmaceutics, 2014. **472**(1-2): p. 356-361.
98. Luo, X.-D., et al., *Macromolecular crowding favors the fibrillization of β2-microglobulin by accelerating the nucleation step and inhibiting fibril disassembly.* Biochimica et Biophysica Acta (BBA)-Proteins and Proteomics, 2016. **1864**(11): p. 1609-1619.
99. Barnard, J.G., et al., *Subvisible particle counting provides a sensitive method of detecting and quantifying aggregation of monoclonal antibody caused by freeze-thawing: Insights into the roles of particles in the protein aggregation pathway.* Journal of pharmaceutical sciences, 2011. **100**(2): p. 492-503.
100. Dengl, S., et al., *Aggregation and chemical modification of monoclonal antibodies under upstream processing conditions.* Pharmaceutical research, 2013. **30**(5): p. 1380-1399.
101. Brückl, L., et al., *The effect of shear on the structural conformation of rhGH and IgG1 in free solution.* Journal of pharmaceutical sciences, 2016. **105**(6): p. 1810-1818.
102. Mozziconacci, O. and C. Schoeneich, *Chemical degradation of proteins in the solid state with a focus on photochemical reactions.* Advanced drug delivery reviews, 2015. **93**: p. 2-13.
103. Jaspe, J. and S.J. Hagen, *Do protein molecules unfold in a simple shear flow?* Biophysical journal, 2006. **91**(9): p. 3415-3424.
104. Thomas, C. and D. Geer, *Effects of shear on proteins in solution.* Biotechnology letters, 2011. **33**(3): p. 443-456.

105. Bekard, I.B., et al., *The effects of shear flow on protein structure and function.* Biopolymers, 2011. **95**(11): p. 733-745.
106. Barnett, G.V., et al., *Aggregate structure, morphology and the effect of aggregation mechanisms on viscosity at elevated protein concentrations.* Biophysical chemistry, 2015. **207**: p. 21-29.
107. Trumbore, C.N., *Shear-induced amyloid formation in the brain: II. An experimental system for monitoring amyloid shear processes and investigating potential spinal tap problems.* Journal of Alzheimer's Disease, 2017. **59**(2): p. 543-557.
108. Niazi, S.K. and M. Magoola, *mRNA and Synthesis-Based Therapeutic Proteins: A Non-Recombinant Affordable Option.* Biologics, 2023. **3**(4): p. 355-379.
109. Niazi, S.K., *The FDA's New Guideline "Generally Accepted Scientific Knowledge"(GASK): An Opportunity to Expedite the Approval of Biosimilars.* Pharmaceuticals, 2023. **16**(11): p. 1517.
110. Murphy, R.M. and C.J. Roberts, *Protein misfolding and aggregation research: some thoughts on improving quality and utility.* Biotechnology Progress, 2013. **29**(5): p. 1109-1115.
111. Li, J., et al., *Interfacial stress in the development of biologics: fundamental understanding, current practice, and future perspective.* The AAPS journal, 2019. **21**: p. 1-17.
112. Desai, K.G., et al., *Transportation of mAb Dosing Solution in Intravenous Bag: Impact of Manual, Vehicle, and Pneumatic Tube System Transportation Methods on Product Quality.* Molecular Pharmaceutics, 2023.
113. Drago, J.Z., S. Modi, and S. Chandarlapaty, *Unlocking the potential of antibody–drug conjugates for cancer therapy.* Nature Reviews Clinical Oncology, 2021. **18**(6): p. 327-344.
114. Dunstan, D.E., et al., *Shear flow promotes amyloid-β fibrilization.* Protein Engineering, Design & Selection, 2009. **22**(12): p. 741-746.
115. Ashton, L., et al., *Susceptibility of different proteins to flow-induced conformational changes monitored with Raman spectroscopy.* Biophysical journal, 2010. **98**(4): p. 707-714.
116. Dopheide, S.M., M.J. Maxwell, and S.P. Jackson, *Shear-dependent tether formation during platelet translocation on von Willebrand factor.* Blood, The Journal of the American Society of Hematology, 2002. **99**(1): p. 159-167.
117. Rana, A., et al., *Shear-dependent platelet aggregation: mechanisms and therapeutic opportunities.* Frontiers in cardiovascular medicine, 2019. **6**: p. 141.
118. Teoh, C.L., et al., *Shear flow induced changes in apolipoprotein C-II conformation and amyloid fibril formation.* Biochemistry, 2011. **50**(19): p. 4046-4057.
119. Hill, E.K., et al., *Shear flow induces amyloid fibril formation.* Biomacromolecules, 2006. **7**(1): p. 10-13.
120. Sharma, V., et al., *Rheology of globular proteins: apparent yield stress, high shear rate viscosity and interfacial viscoelasticity of bovine serum albumin solutions.* Soft Matter, 2011. **7**(11): p. 5150-5160.
121. Phillips, M., et al., *Structure and properties of protein films adsorbed at the air-water interface.* Colloid and Polymer Science, 1975. **253**: p. 424-427.
122. Castellanos, M.M., J.A. Pathak, and R.H. Colby, *Both protein adsorption and aggregation contribute to shear yielding and viscosity increase in protein solutions.* Soft Matter, 2014. **10**(1): p. 122-131.
123. Grigolato, F. and P. Arosio, *Synergistic effects of flow and interfaces on antibody aggregation.* Biotechnology and bioengineering, 2020. **117**(2): p. 417-428.
124. Giusteri, G.G. and R. Seto, *A theoretical framework for steady-state rheometry in generic flow conditions.* Journal of Rheology, 2018. **62**(3): p. 713-723.
125. Arakawa, T., et al., *Suppression of protein interactions by arginine: a proposed mechanism of the arginine effects.* Biophysical chemistry, 2007. **127**(1-2): p. 1-8.
126. Wang, J., et al., *The effect of arginine on inhibiting amyloid fibril derived from β-casein and the binding studies with multi-spectroscopic techniques.* Spectrochimica Acta Part A: Molecular and Biomolecular Spectroscopy, 2022. **282**: p. 121681.

127. Ito, L., et al., *Glycine amide shielding on the aromatic surfaces of lysozyme: Implication for suppression of protein aggregation.* FEBS letters, 2011. **585**(3): p. 555-560.
128. Li, F., et al., *Molecular mechanisms of resveratrol and EGCG in the inhibition of Aβ 42 aggregation and disruption of Aβ 42 protofibril: Similarities and differences.* Physical Chemistry Chemical Physics, 2021. **23**(34): p. 18843-18854.
129. Khan, M.S., et al., *Hesperidin attenuate fibrillation and cytotoxicity of human insulin: Role of secondary structure and its hydrophobicity in protein aggregation.* Journal of Molecular Structure, 2024. **1295**: p. 136713.
130. Ali, S.M., et al., *Evaluating the inhibitory potential of natural compound luteolin on human lysozyme fibrillation.* International Journal of Biological Macromolecules, 2023. **233**: p. 123623.
131. Lü, M.-H., et al., *Hybrids of polyphenolic/quinone acids, the potential preventive and therapeutic drugs for PD: Disaggregate α-Syn fibrils, inhibit inclusions, and repair damaged neurons in mice.* European Journal of Medicinal Chemistry, 2023. **249**: p. 115122.
132. Kolaj, I., et al., *Ferulic acid amide derivatives with varying inhibition of amyloid-β oligomerization and fibrillization.* Bioorganic & Medicinal Chemistry, 2021. **43**: p. 116247.
133. Kumar, S., et al., *Ellagic acid inhibits α-synuclein aggregation at multiple stages and reduces its cytotoxicity.* ACS Chemical Neuroscience, 2021. **12**(11): p. 1919-1930.
134. Li, X., et al., *Molecular Insights into the Inhibition and Disaggregation Effects of EGCG on Aβ40 and Aβ42 Cofibrillation.* The Journal of Physical Chemistry B, 2024.
135. Cabaleiro-Lago, C., et al., *Inhibition of amyloid β protein fibrillation by polymeric nanoparticles.* Journal of the American Chemical Society, 2008. **130**(46): p. 15437-15443.
136. Sonawane, S.K., A. Ahmad, and S. Chinnathambi, *Protein-capped metal nanoparticles inhibit tau aggregation in Alzheimer's disease.* ACS omega, 2019. **4**(7): p. 12833-12840.
137. Mirzaei-Behbahani, B., et al., *Efficient inhibition of amyloid fibrillation and cytotoxicity of α-synuclein and human insulin using biosynthesized silver nanoparticles decorated by green tea polyphenols.* Scientific Reports, 2024. **14**(1): p. 3907.
138. Andrikopoulos, N., et al., *Zinc–Epigallocatechin-3-gallate Network-Coated Nanocomposites against the Pathogenesis of Amyloid-Beta.* ACS Applied Materials & Interfaces, 2023. **15**(6): p. 7777-7792.
139. Brahmkhatri, V.P., et al., *Curcumin nanoconjugate inhibits aggregation of N-terminal region (Aβ-16) of an amyloid beta peptide.* New Journal of Chemistry, 2018. **42**(24): p. 19881-19892.
140. Shelke, T., et al., *Quercetin Nanoconjugates for Anti-Alzheimer's Activity: An Investigation on Drosophila melanogaster Model.* BioNanoScience, 2024: p. 1-11.
141. Suman, M. and D. Koushik, *Trehalose-Functionalized Gold Nanoparticle for Inhibiting Intracellular Protein Aggregation.* 2017.
142. Ghosh, N. and L.M. Kundu, *Cyclic di-peptide in situ inhibited protein-aggregation.* Bioorganic & Medicinal Chemistry Letters, 2023. **91**: p. 129379.
143. Ratha, B.N., et al., *Inhibition of insulin amyloid fibrillation by a novel amphipathic heptapeptide.* Journal of biological chemistry, 2016. **291**(45): p. 23545-23556.
144. Sehra, N., et al., *Synthesis and mechanistic study of ultrashort peptides that inhibits Alzheimer's Aβ-aggregation-induced neurotoxicity.* Bioorganic Chemistry, 2024. **144**: p. 107159.
145. Kapadia, A., et al., *Effect of C-terminus amidation of Ab39–42 fragment derived peptides as potential inhibitors of Ab aggregation.*
146. Mitra, A. and N. Sarkar, *Elucidating the inhibitory effects of rationally designed novel hexapeptide against hen egg white lysozyme fibrillation at acidic and physiological pH.* Biochimica et Biophysica Acta (BBA)-Proteins and Proteomics, 2023. **1871**(3): p. 140899.
147. Acharya, S., et al., *Molecular basis for preventing α-synuclein aggregation by a molecular tweezer.* Journal of Biological Chemistry, 2014. **289**(15): p. 10727-10737.

148. Lantz, C., et al., *Characterization of Molecular Tweezer Binding on α-Synuclein with Native Top-Down Mass Spectrometry and Ion Mobility-Mass Spectrometry Reveals a Mechanism for Aggregation Inhibition.* Journal of the American Society for Mass Spectrometry, 2023. **34**(12): p. 2739-2747.
149. Lopes, D.H., et al., *Molecular tweezers inhibit islet amyloid polypeptide assembly and toxicity by a new mechanism.* ACS chemical biology, 2015. **10**(6): p. 1555-1569.
150. Dutt, S., et al., *Molecular tweezers with varying anions: a comparative study.* The Journal of organic chemistry, 2013. **78**(13): p. 6721-6734.
151. Katre, N.V., *The conjugation of proteins with polyethylene glycol and other polymers: altering properties of proteins to enhance their therapeutic potential.* Advanced Drug Delivery Reviews, 1993. **10**(1): p. 91-114.
152. Veronese, F.M. and G. Pasut, *PEGylation, successful approach to drug delivery.* Drug discovery today, 2005. **10**(21): p. 1451-1458.
153. Muraoka, T., et al., *A structured monodisperse PEG for the effective suppression of protein aggregation.* Angewandte Chemie, 2013. **125**(9): p. 2490-2494.
154. Kameta, N., et al., *Short polyethylene glycol chains densely bound to soft nanotube channels for inhibition of protein aggregation.* RSC advances, 2016. **6**(43): p. 36744-36750.
155. Akiyoshi, K., et al., *Self-aggregates of hydrophobized polysaccharides in water. Formation and characteristics of nanoparticles.* Macromolecules, 1993. **26**(12): p. 3062-3068.
156. Goyal, K., L.J. Walton, and A. Tunnacliffe, *LEA proteins prevent protein aggregation due to water stress.* Biochemical journal, 2005. **388**(1): p. 151-157.
157. Furuki, T., et al., *Group 3 LEA protein model peptides suppress heat-induced lysozyme aggregation. Elucidation of the underlying mechanism using coarse-grained molecular simulations.* The Journal of Physical Chemistry B, 2020. **124**(14): p. 2747-2759.
158. Das, U., et al., *Inhibition of protein aggregation: supramolecular assemblies of arginine hold the key.* PloS one, 2007. **2**(11): p. e1176.
159. Sternke-Hoffmann, R., et al., *The aggregation conditions define whether EGCG is an inhibitor or enhancer of α-synuclein amyloid fibril formation.* International Journal of Molecular Sciences, 2020. **21**(6): p. 1995.
160. Zaidi, F.K. and R. Bhat, *Two polyphenols with diverse mechanisms towards amyloidosis: differential modulation of the fibrillation pathway of human lysozyme by curcumin and EGCG.* Journal of Biomolecular Structure and Dynamics, 2022. **40**(10): p. 4593-4611.
161. Álvarez-Berbel, I., et al., *Three to Tango: Inhibitory effect of quercetin and apigenin on acetylcholinesterase, amyloid-β aggregation and acetylcholinesterase-amyloid interaction.* Pharmaceutics, 2022. **14**(11): p. 2342.
162. Clauss, Z.S., et al., *Supramolecular protein stabilization with zwitterionic polypeptide–cucurbit [7] uril conjugates.* Biomacromolecules, 2022. **24**(1): p. 481-488.
163. Jana, A.K., A.B. Greenwood, and U.H. Hansmann, *Small peptides for inhibiting serum amyloid A aggregation.* ACS Medicinal Chemistry Letters, 2021. **12**(10): p. 1613-1621.
164. El Safadi, M., et al., *Cyclen-based chelators for the inhibition of Aβ aggregation: Synthesis, anti-oxidant and aggregation evaluation.* Inorganica Chimica Acta, 2017. **467**: p. 343-350.
165. Peng, Y.-B., et al., *Inhibition of Aβ peptide aggregation by ruthenium (II) polypyridyl complexes through copper chelation.* Journal of Inorganic Biochemistry, 2021. **224**: p. 111591.
166. Gaeta, A., et al., *Synthesis, physical–chemical characterisation and biological evaluation of novel 2-amido-3-hydroxypyridin-4 (1H)-ones: Iron chelators with the potential for treating Alzheimer's disease.* Bioorganic & medicinal chemistry, 2011. **19**(3): p. 1285-1297.
167. Rananaware, P., et al., *Polymeric curcumin nanospheres for lysozyme aggregation inhibition, antibacterial, and wound healing applications.* Environmental Science and Pollution Research, 2023: p. 1-16.

168. Prajapati, K.P., et al., *Osmoprotectant coated thermostable gold nanoparticles efficiently restrict temperature-induced amyloid aggregation of insulin.* The Journal of Physical Chemistry Letters, 2021. **12**(7): p. 1803-1813.
169. Khambete, M.P., et al., *Exploring the potential of pyrazoline containing molecules as Aβ aggregation inhibitors in Alzheimer's disease.* Drug Metabolism and Personalized Therapy, 2020. **35**(3): p. 20190031.
170. Som Chaudhury, S., et al., *A novel PEGylated block copolymer in new age therapeutics for Alzheimer's disease.* Molecular Neurobiology, 2019. **56**: p. 6551-6565.
171. Tobias, V.p., et al., *Inhibition of Huntingtin Exon-1 Aggregation by the Molecular Tweezer CLR01.* 2017.
172. Mittal, S., K. Bravo-Rodriguez, and E. Sanchez-Garcia, *Mechanism of inhibition of beta amyloid toxicity by supramolecular tweezers.* The Journal of Physical Chemistry B, 2018. **122**(15): p. 4196-4205.
173. Choudhary, S., N. Kishore, and R.V. Hosur, *Inhibition of insulin fibrillation by osmolytes: Mechanistic Insights.* Scientific reports, 2015. **5**(1): p. 17599.
174. Huy, P.D.Q., et al., *In silico and in vitro characterization of anti-amyloidogenic activity of vitamin K3 analogues for Alzheimer's disease.* Biochimica et Biophysica Acta (BBA)-General Subjects, 2013. **1830**(4): p. 2960-2969.
175. Alam, P., et al., *Elucidating the inhibitory potential of Vitamin A against fibrillation and amyloid associated cytotoxicity.* International journal of biological macromolecules, 2019. **129**: p. 333-338.
176. Ghasemzadeh, S. and G.H. Riazi, *Inhibition of Tau amyloid fibril formation by folic acid: In-vitro and theoretical studies.* International journal of biological macromolecules, 2020. **154**: p. 1505-1516.
177. Dong, X., et al., *Green tea extract EGCG plays a dual role in Aβ42 protofibril disruption and membrane protection: A molecular dynamic study.* Chemistry and Physics of Lipids, 2021. **234**: p. 105024.
178. Meena, V.K., V. Kumar, and S. Karalia, *Inhibitory effect of naturally occurring Ocimum sanctum extract on α-Synuclein aggregation in aqueous solution.* Journal of Molecular Liquids, 2021. **336**: p. 116176.
179. Khan, M.S., et al., *Rutin attenuates negatively charged surfactant (SDS)-induced lysozyme aggregation/amyloid formation and its cytotoxicity.* International journal of biological macromolecules, 2018. **120**: p. 45-58.
180. Borana, M.S., et al., *Curcumin and kaempferol prevent lysozyme fibril formation by modulating aggregation kinetic parameters.* Biochimica et Biophysica Acta (BBA)-Proteins and Proteomics, 2014. **1844**(3): p. 670-680.
181. Sgarbossa, A., *Natural biomolecules and protein aggregation: emerging strategies against amyloidogenesis.* International journal of molecular sciences, 2012. **13**(12): p. 17121-17137.
182. Berg, T., *Modulation of protein–protein interactions with small organic molecules.* Angewandte Chemie International Edition, 2003. **42**(22): p. 2462-2481.
183. Dubey, K., et al., *Eugenol prevents amyloid formation of proteins and inhibits amyloid-induced hemolysis.* Scientific reports, 2017. **7**(1): p. 40744.
184. Siposova, K., et al., *Inhibition of amyloid fibril formation and disassembly of pre-formed fibrils by natural polyphenol rottlerin.* Biochimica et Biophysica Acta (BBA)-Proteins and Proteomics, 2019. **1867**(3): p. 259-274.
185. Eze, F.N., L. Leelawatwattana, and P. Prapunpoj, *Structural Stabilization of Human Transthyretin by Centella asiatica (L.) Urban Extract: Implications for TTR Amyloidosis.* Biomolecules, 2019. **9**(4): p. 128.
186. Anand, B.G., et al., *Evidence of anti-amyloid characteristics of plumbagin via inhibition of protein aggregation and disassembly of protein fibrils.* Biomacromolecules, 2021. **22**(9): p. 3692-3703.

187. Dhouafli, Z., et al., *Screening for amyloid-β aggregation inhibitor and neuronal toxicity of eight Tunisian medicinal plants.* Industrial Crops and Products, 2018. **111**: p. 823-833.
188. Boubakri, A., et al., *Allium roseum L. extract inhibits amyloid beta aggregation and toxicity involved in Alzheimer's disease.* PLoS One, 2020. **15**(9): p. e0223815.
189. Sharma, H., et al., *Multi-Targeting Neuroprotective Effects of Syzygium aromaticum Bud Extracts and Their Key Phytocompounds against Neurodegenerative Diseases.* International Journal of Molecular Sciences, 2023. **24**(9): p. 8148.
190. Rasool, M., et al., *Recent updates in the treatment of neurodegenerative disorders using natural compounds.* Evidence-Based Complementary and Alternative Medicine, 2014. **2014**.
191. Akagi, M., et al., *Nonpeptide neurotrophic agents useful in the treatment of neurodegenerative diseases such as Alzheimer's disease.* Journal of pharmacological sciences, 2015. **127**(2): p. 155-163.
192. Han, S.-H., J.-C. Park, and I. Mook-Jung, *Amyloid β-interacting partners in Alzheimer's disease: From accomplices to possible therapeutic targets.* Progress in neurobiology, 2016. **137**: p. 17-38.
193. Sonawane, S.K., V.N. Uversky, and S. Chinnathambi, *Baicalein inhibits heparin-induced Tau aggregation by initializing non-toxic Tau oligomer formation.* Cell Communication and Signaling, 2021. **19**: p. 1-16.
194. Bhatia, N.K., et al., *Quercetin and baicalein act as potent antiamyloidogenic and fibril destabilizing agents for SOD1 fibrils.* ACS Chemical Neuroscience, 2020. **11**(8): p. 1129-1138.
195. Kimura, A.M., et al., *Myricetin prevents high molecular weight Aβ1-42 oligomer-induced neurotoxicity through antioxidant effects in cell membranes and mitochondria.* Free Radical Biology and Medicine, 2021. **171**: p. 232-244.
196. Xu, B., et al., *Myricetin inhibits α-synuclein amyloid aggregation by delaying the liquid-to-solid phase transition.* Chembiochem, 2022. **23**(16): p. e202200216.
197. Sharma, S., V.R. Tomar, and S. Deep, *Myricetin: A potent anti-amyloidogenic polyphenol against superoxide dismutase 1 aggregation.* ACS Chemical Neuroscience, 2023. **14**(13): p. 2461-2475.
198. Ono, K., M. Hirohata, and M. Yamada, *Ferulic acid destabilizes preformed β-amyloid fibrils in vitro.* Biochemical and biophysical research communications, 2005. **336**(2): p. 444-449.
199. PALa, S., et al., *Antioxidant ferulic acid prevents the aggregation of bovine b-lactoglobulin in vitro.*
200. Abioye, R.O., O.D. Okagu, and C.C. Udenigwe, *Inhibition of islet amyloid polypeptide fibrillation by structurally diverse phenolic compounds and fibril disaggregation potential of rutin and quercetin.* Journal of Agricultural and Food Chemistry, 2021. **70**(1): p. 392-402.
201. Yu, K.-H. and C.-I. Lee, *Quercetin disaggregates prion fibrils and decreases fibril-induced cytotoxicity and oxidative stress.* Pharmaceutics, 2020. **12**(11): p. 1081.
202. Pandey, N., et al., *Curcumin inhibits aggregation of α-synuclein.* Acta neuropathologica, 2008. **115**: p. 479-489.
203. Singh, P.K., et al., *Curcumin modulates α-synuclein aggregation and toxicity.* ACS chemical neuroscience, 2013. **4**(3): p. 393-407.
204. Majid, A. and S. Garg, *Modeling Inhibitory Effects of Chlorogenic Acid on Amyloid Beta Aggregation.* Industrial & Engineering Chemistry Research, 2024.
205. Miyamae, Y., et al., *Protective effects of caffeoylquinic acids on the aggregation and neurotoxicity of the 42-residue amyloid β-protein.* Bioorganic & medicinal chemistry, 2012. **20**(19): p. 5844-5849.
206. Meena, V.K., et al., *Ellagic Acid Modulates Uninduced as well as Mutation and Metal-Induced Aggregation of α-Synuclein: Implications for Parkinson's Disease.* ACS Chemical Neuroscience, 2021. **12**(19): p. 3598-3614.
207. Ratnaparkhi, A., et al., *Effects of hesperidin, a flavanone glycoside interaction on the conformation, stability, and aggregation of lysozyme: multispectroscopic and molecular

dynamic simulation studies? Journal of Biomolecular Structure and Dynamics, 2015. **33**(9): p. 1866-1879.

208. Azerad, R., *Chemical structures, production and enzymatic transformations of sapogenins and saponins from Centella asiatica (L.) Urban.* Fitoterapia, 2016. **114**: p. 168-187.
209. Jia, G. and X. Lu, *Enrichment and purification of madecassoside and asiaticoside from Centella asiatica extracts with macroporous resins.* Journal of Chromatography A, 2008. **1193**(1-2): p. 136-141.
210. Dhanasekaran, M., et al., *Centella asiatica extract selectively decreases amyloid β levels in hippocampus of Alzheimer's disease animal model.* Phytotherapy Research: An International Journal Devoted to Pharmacological and Toxicological Evaluation of Natural Product Derivatives, 2009. **23**(1): p. 14-19.
211. Kumar, M.V. and Y. Gupta, *Effect of different extracts of Centella asiatica on cognition and markers of oxidative stress in rats.* Journal of ethnopharmacology, 2002. **79**(2): p. 253-260.
212. Huang, S.-S., et al., *Antioxidant and antiproliferative activities of the four Hydrocotyle species from Taiwan.* Botanical Studies, 2008. **49**(4): p. 311-322.
213. Chen, C.-L., et al., *Centella asiatica extract protects against amyloid β1–40-induced neurotoxicity in neuronal cells by activating the antioxidative defence system.* Journal of traditional and complementary medicine, 2016. **6**(4): p. 362-369.
214. Roy, S. and H. Awasthi, *Herbal medicines as neuroprotective agent: A mechanistic approach.* Int J Pharm Pharm Sci, 2017. **9**: p. 1-7.
215. Khotimah, H., et al., *Decreasing α-synuclein aggregation by methanolic extract of Centella asiatica in zebrafish Parkinson's model.* Asian Pacific Journal of Tropical Biomedicine, 2015. **5**(11): p. 948-954.
216. Witter, S., et al., *Medical Plants and Nutraceuticals for Amyloid-β Fibrillation Inhibition.* Journal of Alzheimer's Disease Reports, 2018(Preprint): p. 1-14.
217. Sabaragamuwa, R., C.O. Perera, and B. Fedrizzi, *Centella asiatica (Gotu kola) as a neuroprotectant and its potential role in healthy ageing.* Trends in food science & technology, 2018. **79**: p. 88-97.
218. Nicoud, L., et al., *Impact of aggregate formation on the viscosity of protein solutions.* Soft matter, 2015. **11**(27): p. 5513-5522.
219. Mori, H., et al., *Mass spectrometry of purified amyloid beta protein in Alzheimer's disease.* J Biol Chem, 1992. **267**(24): p. 17082-6.
220. Singh, A., et al., *Therapeutic Advancement in Alzheimer Disease: New Hopes on the Horizon?* CNS & Neurological Disorders-Drug Targets (Formerly Current Drug Targets-CNS & Neurological Disorders), 2018. **17**(8): p. 571-589.
221. Schmidt, A.M., et al., *The role of RAGE in amyloid-beta peptide-mediated pathology in Alzheimer's disease.* Current opinion in investigational drugs (London, England: 2000), 2009. **10**(7): p. 672-680.
222. Zhang-Haagen, B., et al., *Monomeric amyloid beta peptide in hexafluoroisopropanol detected by small angle neutron scattering.* PloS one, 2016. **11**(2): p. e0150267.
223. Pandey, L.M., et al., *Surface chemistry at the nanometer scale influences insulin aggregation.* Colloids and Surfaces B: Biointerfaces, 2012. **100**: p. 69-76.
224. Iannazzo, D., et al., *Graphene-based materials for application in pharmaceutical nanotechnology*, in *Fullerens, Graphenes and Nanotubes*. 2018, Elsevier. p. 297-329.
225. Militello, V., V. Vetri, and M. Leone, *Conformational changes involved in thermal aggregation processes of bovine serum albumin.* Biophysical chemistry, 2003. **105**(1): p. 133-141.
226. Liu, X., et al., *Mg2+ inhibits heat-induced aggregation of BSA: The mechanism and its binding site.* Food Hydrocolloids, 2020. **101**: p. 105450.
227. Johnson Jr, W.C., *Secondary structure of proteins through circular dichroism spectroscopy.* Annual review of biophysics and biophysical chemistry, 1988. **17**(1): p. 145-166.

228. Whitmore, L. and B.A. Wallace, *Protein secondary structure analyses from circular dichroism spectroscopy: methods and reference databases.* Biopolymers: Original Research on Biomolecules, 2008. **89**(5): p. 392-400.
229. Saxena, V., et al., *Edible oil nanoemulsion: An organic nanoantibiotic as a potential biomolecule delivery vehicle.* International Journal of Polymeric Materials and Polymeric Biomaterials, 2018. **67**(7): p. 410-419.
230. Elofsson, C., et al., *Atomic force microscopy studies on whey proteins.* International dairy journal, 1997. **7**(12): p. 813-819.
231. Manoi, K. and S.S. Rizvi, *Rheological characterizations of texturized whey protein concentrate-based powders produced by reactive supercritical fluid extrusion.* Food Research International, 2008. **41**(8): p. 786-796.
232. Barnes, H.A., J.F. Hutton, and K. Walters, *An introduction to rheology*. 1989: Elsevier.
233. Granata, D., et al., *The inverted free energy landscape of an intrinsically disordered peptide by simulations and experiments.* Scientific reports, 2015. **5**(1): p. 1-15.
234. Ratha, B.N., et al., *Inhibition of insulin amyloid fibrillation by a novel amphipathic heptapeptide mechanistic details studied by spectroscopy in combination with microscopy.* Journal of Biological Chemistry, 2016. **291**(45): p. 23545-23556.
235. Heyn, T.R., et al., *The threshold of amyloid aggregation of beta-lactoglobulin: Relevant factor combinations.* Journal of Food Engineering, 2020. **283**: p. 110005.
236. Norde, W., *Colloids and interfaces in life sciences and bionanotechnology*. 2011: CRC Press.
237. Pryor, N.E., M.A. Moss, and C.N. Hestekin, *Unraveling the early events of amyloid-β protein (Aβ) aggregation: techniques for the determination of Aβ aggregate size.* International journal of molecular sciences, 2012. **13**(3): p. 3038-3072.
238. Lim, K.H., et al., *Characterizations of distinct amyloidogenic conformations of the Aβ (1–40) and (1–42) peptides.* Biochemical and biophysical research communications, 2007. **353**(2): p. 443-449.
239. Jayamani, J. and G. Shanmugam, *Diameter of the vial plays a crucial role in the amyloid fibril formation: Role of interface area between hydrophilic-hydrophobic surfaces.* International journal of biological macromolecules, 2017. **101**: p. 290-298.
240. Divsalar, A., et al., *Biological Evaluation and Interaction of a Newly Designed Anti-cancer Pd(II) Complex and Human Serum Albumin.* Journal of Biomolecular Structure and Dynamics, 2011. **29**(2): p. 283-296.
241. Hasan, A., V. Saxena, and L.M. Pandey, *Surface Functionalization of Ti6Al4V via Self-assembled Monolayers for Improved Protein Adsorption and Fibroblast Adhesion.* Langmuir, 2018. **34**(11): p. 3494-3506.
242. Sarroukh, R., et al., *Transformation of amyloid β (1–40) oligomers into fibrils is characterized by a major change in secondary structure.* Cellular and molecular life sciences, 2011. **68**(8): p. 1429-1438.
243. Lin, S.-Y., H.-L. Chu, and Y.-S. Wei, *Secondary Conformations and Temperature Effect on Structural Transformation of Amyloid β(1–28),(1–40) and (1–42) Peptides.* Journal of Biomolecular Structure and Dynamics, 2003. **20**(4): p. 595-601.
244. Karmakar, S., et al., *Neuronal SNARE complex: A protein folding system with intricate protein-protein interactions, and its common neuropathological hallmark, SNAP25.* Neurochemistry international, 2018.
245. Garbuzynskiy, S.O., M.Y. Lobanov, and O.V. Galzitskaya, *FoldAmyloid: a method of prediction of amyloidogenic regions from protein sequence.* Bioinformatics, 2009. **26**(3): p. 326-332.
246. Tjernberg, L.O., et al., *Arrest of-amyloid fibril formation by a pentapeptide ligand.* Journal of Biological Chemistry, 1996. **271**(15): p. 8545-8548.
247. Petkova, A.T., et al., *A structural model for Alzheimer's β-amyloid fibrils based on experimental constraints from solid state NMR.* Proceedings of the National Academy of Sciences, 2002. **99**(26): p. 16742-16747.

248. Wang, C.-C., et al., *Characterization of Aβ aggregation mechanism probed by congo red.* Journal of Biomolecular Structure and Dynamics, 2012. **30**(2): p. 160-169.
249. Garbuzynskiy, S.O., M.Y. Lobanov, and O.V. Galzitskaya, *FoldAmyloid: a method of prediction of amyloidogenic regions from protein sequence.* Bioinformatics, 2010. **26**(3): p. 326-332.
250. Onogi, S., et al., *Dependence of viscosity of concentrated polymer solutions upon molecular weight and concentration.* Journal of Polymer Science Part A-2: Polymer Physics, 1967. **5**(5): p. 899-913.
251. Ow, S.-Y. and D.E. Dunstan, *The effect of concentration, temperature and stirring on hen egg white lysozyme amyloid formation.* Soft Matter, 2013. **9**(40): p. 9692-9701.
252. Pepys, M., et al., *Human lysozyme gene mutations cause hereditary systemic amyloidosis.* Nature, 1993. **362**(6420): p. 553-557.
253. Chen, X., et al., *Inhibition of lysozyme amyloid fibrillation by silybin diastereoisomers: The effects of stereochemistry.* ACS omega, 2021. **6**(4): p. 3307-3318.
254. Ganz, T., *Antimicrobial polypeptides in host defense of the respiratory tract.* The Journal of clinical investigation, 2002. **109**(6): p. 693-697.
255. Wolfe, L.S., et al., *Protein-induced photophysical changes to the amyloid indicator dye thioflavin T.* Proceedings of the National Academy of Sciences, 2010. **107**(39): p. 16863-16868.
256. Sharma, L.G. and L.M. Pandey, *Thermomechanical process induces unfolding and fibrillation of bovine serum albumin.* Food Hydrocolloids, 2021. **112**: p. 106294.
257. Sharma, L.G. and L.M. Pandey, *Shear-induced aggregation of amyloid β (1–40) in a parallel plate geometry.* Journal of Biomolecular Structure and Dynamics, 2021. **39**(17): p. 6415-6423.
258. Morozova-Roche, L.A., et al., *Amyloid fibril formation and seeding by wild-type human lysozyme and its disease-related mutational variants.* Journal of structural biology, 2000. **130**(2-3): p. 339-351.
259. Kong, L.-X. and C.-M. Zeng, *Effects of seeding on lysozyme amyloid fibrillation in the presence of epigallocatechin and polyethylene glycol.* Biochemistry (Moscow), 2017. **82**: p. 156-167.
260. Khan, J.M., et al., *Sodium louroyl sarcosinate (sarkosyl) modulate amyloid fibril formation in hen egg white lysozyme (HEWL) at alkaline pH: a molecular insight study.* Journal of Biomolecular Structure and Dynamics, 2018. **36**(6): p. 1550-1565.
261. Sivalingam, V., et al., *Wild-type hen egg white lysozyme aggregation in vitro can form self-seeding amyloid conformational variants.* Biophysical chemistry, 2016. **219**: p. 28-37.
262. Zeng, H.j., et al., *Investigation on the effect of three isoflavones on the fibrillation of hen egg-white lysozyme.* Journal of Molecular Recognition, 2021. **34**(6): p. e2889.
263. Zeng, H.j., et al., *Effect of silybin on the fibrillation of hen egg-white lysozyme.* Journal of Molecular Recognition, 2017. **30**(1): p. e2566.
264. Sreerama, N. and R.W. Woody, *Structural composition of βI-and βII-proteins.* Protein Science, 2003. **12**(2): p. 384-388.
265. Manavalan, P. and W.C. Johnson Jr, *Sensitivity of circular dichroism to protein tertiary structure class.* Nature, 1983. **305**(5937): p. 831-832.
266. Hirst, J.D., S. Bhattacharjee, and A.V. Onufriev, *Theoretical studies of time-resolved spectroscopy of protein folding.* Faraday discussions, 2003. **122**: p. 253-267.
267. Wu, J., J.T. Yang, and C.-S.C. Wu, *β-II conformation of all-β proteins can be distinguished from unordered form by circular dichroism.* Analytical biochemistry, 1992. **200**(2): p. 359-364.
268. Rogers, D.M., H. Do, and J.D. Hirst, *Electronic circular dichroism of proteins computed using a diabatisation scheme.* Molecular Physics, 2023. **121**(7-8): p. e2133748.
269. Bekard, I.B., et al., *Bovine serum albumin unfolds in Couette flow.* Soft Matter, 2012. **8**(2): p. 385-389.

270. Pal, S., et al., *Thermal stability modulation of the native and chemically-unfolded state of bovine serum albumin by amino acids.* Physical Chemistry Chemical Physics, 2020. **22**(1): p. 179-188.
271. Belitz, H.-D. and W. Grosch, *Lehrbuch der lebensmittelchemie*. 2013: Springer-Verlag.
272. Collins, S.R., et al., *Mechanism of prion propagation: amyloid growth occurs by monomer addition.* PLoS Biol, 2004. **2**(10): p. e321.
273. Liu, J.-J. and S. Lindquist, *Oligopeptide-repeat expansions modulate 'protein-only'inheritance in yeast.* Nature, 1999. **400**(6744): p. 573-576.
274. Serio, T.R., et al., *Nucleated conformational conversion and the replication of conformational information by a prion determinant.* Science, 2000. **289**(5483): p. 1317-1321.
275. Maruyama, T., et al., *Mechanism of bovine serum albumin aggregation during ultrafiltration.* Biotechnology and bioengineering, 2001. **75**(2): p. 233-238.
276. Zhang, Z., et al., *Effects of ultrasound on the kinetics and thermodynamics properties of papain entrapped in modified gelatin.* Food Hydrocolloids, 2020. **105**: p. 105757.
277. Bogahawaththa, D. and T. Vasiljevic, *Shearing accelerates denaturation of β-lactoglobulin and α-lactalbumin in skim milk during heating.* International Dairy Journal, 2020. **105**: p. 104674.
278. Khurana, R., et al., *Mechanism of thioflavin T binding to amyloid fibrils.* Journal of structural biology, 2005. **151**(3): p. 229-238.
279. Smith, J.M., *Introduction to chemical engineering thermodynamics*. 1950, ACS Publications.
280. Kong, J.-Y., et al., *The "intrinsic" thermal conductivity of some wet proteins in relation to their average hydrophobicity: analyses on gels of egg-albumin, wheat gluten and milk casein.* Agricultural and Biological Chemistry, 1982. **46**(3): p. 789-794.
281. Solá, R.J., W. Al-Azzam, and K. Griebenow, *Engineering of protein thermodynamic, kinetic, and colloidal stability: Chemical glycosylation with monofunctionally activated glycans.* Biotechnology and bioengineering, 2006. **94**(6): p. 1072-1079.
282. Sheu, S.-Y., et al., *Energetics of hydrogen bonds in peptides.* Proceedings of the National Academy of Sciences, 2003. **100**(22): p. 12683-12687.
283. Paul, B.K., D. Ray, and N. Guchhait, *Unraveling the binding interaction and kinetics of a prospective anti-HIV drug with a model transport protein: results and challenges.* Physical Chemistry Chemical Physics, 2013. **15**(4): p. 1275-1287.
284. Kamada, A., et al., *Flow-assisted assembly of nanostructured protein microfibers.* Proceedings of the National Academy of Sciences, 2017. **114**(6): p. 1232-1237.
285. Greenfield, N.J., *Using circular dichroism collected as a function of temperature to determine the thermodynamics of protein unfolding and binding interactions.* Nature protocols, 2006. **1**(6): p. 2527.
286. Povey, M.J., et al., *Investigation of bovine serum albumin denaturation using ultrasonic spectroscopy.* Food hydrocolloids, 2011. **25**(5): p. 1233-1241.
287. Singh, A., P. Datta, and L.M. Pandey, *Deciphering the mechanistic insight into the stoichiometric ratio dependent behavior of Cu (II) on BSA fibrillation.* International journal of biological macromolecules, 2017. **97**: p. 662-670.
288. Holm, N.K., et al., *Aggregation and fibrillation of bovine serum albumin.* Biochimica et Biophysica Acta (BBA)-Proteins and Proteomics, 2007. **1774**(9): p. 1128-1138.
289. Danielsson, J., et al., *Thermodynamics of protein destabilization in live cells.* Proceedings of the National Academy of Sciences, 2015. **112**(40): p. 12402-12407.
290. Haynes, C.A. and W. Norde, *Structures and stabilities of adsorbed proteins.* Journal of colloid and interface science, 1995. **169**(2): p. 313-328.
291. Liu, X., et al., *Effect of the degree of glycation on the stability and aggregation of bovine serum albumin.* Food Hydrocolloids, 2020: p. 105892.
292. Dubey, K., et al., *Eugenol prevents amyloid formation of proteins and inhibits amyloid-induced hemolysis.* Scientific reports, 2017. **7**: p. 40744.

293. Kontogiorgos, V., S. Tosh, and P. Wood, *Phase behaviour of high molecular weight oat β-glucan/whey protein isolate binary mixtures.* Food hydrocolloids, 2009. **23**(3): p. 949-956.

294. Dobson, J., et al., *Inducing protein aggregation by extensional flow.* Proceedings of the National Academy of Sciences, 2017. **114**(18): p. 4673-4678.

295. Straub, P.W., *A study of fibrinogen production by human liver slices in vitro by an immunoprecipitin method.* The Journal of Clinical Investigation, 1963. **42**(1): p. 130-136.

296. Vilar, R., et al., *Fibrin (ogen) in human disease: both friend and foe.* Haematologica, 2020. **105**(2): p. 284.

297. Miners, J.S., I. Schulz, and S. Love, *Differing associations between Aβ accumulation, hypoperfusion, blood–brain barrier dysfunction and loss of PDGFRB pericyte marker in the precuneus and parietal white matter in Alzheimer's disease.* Journal of Cerebral Blood Flow & Metabolism, 2018. **38**(1): p. 103-115.

298. Cortes-Canteli, M., et al., *Fibrin deposited in the Alzheimer's disease brain promotes neuronal degeneration.* Neurobiology of aging, 2015. **36**(2): p. 608-617.

299. Gnanapragasam, A., et al., *Protective effect of Centella asiatica on antioxidant tissue defense system against adriamycin induced cardiomyopathy in rats.* Life Sciences, 2004. **76**(5): p. 585-597.

300. Phukan, P., M. Bawari, and M. Sengupta, *Promising neuroprotective plants from north-east India.* Int J Pharm Pharm Sci, 2015. **7**(3): p. 28-39.

301. Pingale, S.S., *Evaluation of effect of Centella asiatica on CCL4 induced rat liver damage.* Pharmacologyonline, 2008. **3**: p. 537-43.

302. Naz, E. and M. Ahmad, *Evaluation of Five Indigenous Medicinal Plants of Sindh, Pakistan for their Antifungal Potential: Antifungal Potential of Some Medicinal Plants.* Biological Sciences-PJSIR, 2009. **52**(6): p. 328-333.

303. Nasir, M., et al., *Inhibitory effect of asiatic acid on acetylcholinesterase, excitatory post synapticpotential and locomotor activity.* Phytomedicine, 2012. **19**(3-4): p. 311-316.

304. Orhan, G., I. Orhan, and B. Sener, *Recent developments in natural and synthetic drug research for Alzheimer's disease.* Letters in Drug Design & Discovery, 2006. **3**(4): p. 268-274.

305. Mukherjee, P.K., V. Kumar, and P.J. Houghton, *Screening of Indian medicinal plants for acetylcholinesterase inhibitory activity.* Phytotherapy Research: An International Journal Devoted to Pharmacological and Toxicological Evaluation of Natural Product Derivatives, 2007. **21**(12): p. 1142-1145.

306. Dehimat, A., et al., *Cytotoxicity and antioxidant activities of leaf extracts of Varthemia sericea (Batt. et Trab.) Diels.* European Journal of Integrative Medicine, 2021. **44**: p. 101338.

307. Sembiring, E.N., B. Elya, and R. Sauriasari, *Phytochemical screening, total flavonoid and total phenolic content and antioxidant activity of different parts of Caesalpinia bonduc (L.) Roxb.* Pharmacognosy journal, 2018. **10**(1).

308. Jawed, A., A.K. Golder, and L.M. Pandey, *Synthesis of iron oxide nanoparticles mediated by Camellia sinensis var. Assamica for Cr (VI) adsorption and detoxification.* Bioresource Technology, 2023. **376**: p. 128816.

309. Upadhyaya, S. and L. Saikia, *Evaluation of phytochemicals, antioxidant activity and nutrient content of Centella asiatica (L.) urban leaves from different localities of Assam.* International Journal of Pharma and Bio Sciences, 2012. **3**(4): p. 656-663.

310. Rashid, M.H.-O.-., et al., *Antioxidant, cytotoxic, antibacterial and thrombolytic activities of Centella asiatica L.: possible role of phenolics and flavonoids.* Clinical Phytoscience, 2023. **9**(1): p. 1.

311. Iqbal, E., K.A. Salim, and L.B. Lim, *Phytochemical screening, total phenolics and antioxidant activities of bark and leaf extracts of Goniothalamus velutinus (Airy Shaw) from Brunei Darussalam.* Journal of King Saud University-Science, 2015. **27**(3): p. 224-232.

312. Ng, Z.X., P.H. Yong, and S.Y. Lim, *Customized drying treatments increased the extraction of phytochemicals and antioxidant activity from economically viable medicinal plants.* Industrial Crops and Products, 2020. **155**: p. 112815.
313. Chatziathanasiadou, M.V., et al., *Amplifying and broadening the cytotoxic profile of quercetin in cancer cell lines through bioconjugation.* Amino Acids, 2018. **50**: p. 279-291.
314. Liu, Y., et al., *CB-Dock2: Improved protein–ligand blind docking by integrating cavity detection, docking and homologous template fitting.* Nucleic acids research, 2022. **50**(W1): p. W159-W164.
315. Yadav, R.P., et al., *Exploring the mechanism of andrographolide in the treatment of gastric cancer through network pharmacology and molecular docking.* Scientific Reports, 2022. **12**(1): p. 18413.
316. Manning, M.C., M. Illangasekare, and R.W. Woody, *Circular dichroism studies of distorted α-helices, twisted β-sheets, and β-turns.* Biophysical chemistry, 1988. **31**(1-2): p. 77-86.
317. Qureshi, M.A. and S. Javed, *Investigating binding dynamics of trans resveratrol to HSA for an efficient displacement of aflatoxin B1 using spectroscopy and molecular simulation.* Scientific Reports, 2022. **12**(1): p. 2400.
318. Su, H. and Y. Xu, *Application of ITC-based characterization of thermodynamic and kinetic association of ligands with proteins in drug design.* Frontiers in pharmacology, 2018: p. 1133.
319. Zhou, X., R.M. Kini, and J. Sivaraman, *Application of isothermal titration calorimetry and column chromatography for identification of biomolecular targets.* Nature protocols, 2011. **6**(2): p. 158-165.
320. Ross, P.D. and S. Subramanian, *Thermodynamics of protein association reactions: forces contributing to stability.* Biochemistry, 1981. **20**(11): p. 3096-3102.
321. Mishra, V. and R.J. Heath, *Structural and biochemical features of human serum albumin essential for eukaryotic cell culture.* International journal of molecular sciences, 2021. **22**(16): p. 8411.
322. Masi, F., et al., *Phytochemical profile of Centevita®, a Centella asiatica leaves extract, and isolation of a new oleanane-type saponin.* Fitoterapia, 2022. **158**: p. 105163.
323. Vinod, S.M., et al., *Complexity of the Role of Various Site-Specific and Selective Sudlow Binding Site Drugs in the Energetics and Stability of the Acridinedione Dye–Bovine Serum Albumin Complex: A Molecular Docking Approach.* ACS omega, 2023. **8**(6): p. 5634-5654.
324. Jiao, Q., et al., *Study on the interactions between caffeoylquinic acids with bovine serum albumin: Spectroscopy, antioxidant activity, LC-MSn, and molecular docking approach.* Frontiers in chemistry, 2019. **7**: p. 840.
325. Qureshi, M.A. and S. Javed, *Aflatoxin B1 induced structural and conformational changes in bovine serum albumin: A multispectroscopic and circular dichroism-based study.* ACS omega, 2021. **6**(28): p. 18054-18064.
326. Yao, C., et al., *Effects of chlorogenic acid on the binding process of cadmium with bovine serum albumin: A multi-spectroscopic and docking study.* Journal of Molecular Structure, 2020. **1204**: p. 127531.
327. Zhang, G., et al., *Spectroscopic investigation of the interaction between chrysin and bovine serum albumin.* Journal of Molecular Structure, 2009. **921**(1-3): p. 346-351.
328. Jiao, Q., et al., *Study on the interaction between active components from traditional Chinese medicine and plasma proteins.* Chemistry Central Journal, 2018. **12**: p. 1-20.
329. Javaheri-Ghezeldizaj, F., et al., *Binding process evaluation of bovine serum albumin and Lawsonia inermis (henna) through spectroscopic and molecular docking approaches.* Journal of Molecular Liquids, 2021. **331**: p. 115792.
330. Joshi, R., et al., *Is the Sudlow site I of human serum albumin more generous to adopt prospective anti-cancer bioorganic compound than that of bovine: A combined spectroscopic and docking simulation approach.* Bioorganic Chemistry, 2017. **75**: p. 332-346.

331. Velander, P., et al., *Natural product-based amyloid inhibitors.* Biochemical pharmacology, 2017. **139**: p. 40-55.
332. Arosio, P., et al., *Chemical kinetics for drug discovery to combat protein aggregation diseases.* Trends in pharmacological sciences, 2014. **35**(3): p. 127-135.
333. Hossain, S., R. Parul, and M. Zuberi, *Potential health dangers of new invasive species similar to indigenous plants that are used as food or medicine--an example from Bangladesh.* World Nutrition, 2018. **9**(3): p. 163-175.
334. Orhan, I.E., *Centella asiatica (L.) Urban: From traditional medicine to modern medicine with neuroprotective potential.* Evidence-based complementary and alternative medicine, 2012. **2012**.
335. Sun, B., et al., *Therapeutic potential of Centella asiatica and its triterpenes: A review.* Frontiers in pharmacology, 2020. **11**: p. 568032.
336. Panda, C., L.G. Sharma, and L.M. Pandey, *Experimental procedures to investigate fibrillation of proteins.* MethodsX, 2023. **11**: p. 102445.
337. Pangeni, D., et al., *Inter-domain helix h10 DOMI–h1 DOMII is important in the molecular interaction of bovine serum albumin with curcumin: spectroscopic and computational analysis.* European Biophysics Journal, 2015. **44**(3): p. 139-148.
338. Wani, T.A., et al., *Study of interactions of an anticancer drug neratinib with bovine serum albumin: spectroscopic and molecular docking approach.* Frontiers in chemistry, 2018. **6**: p. 47.
339. Hao, S.-Z., et al., *Study of the interaction of Na9 [SbW9O33]· 19.5 H2O with bovine serum albumin: Spectroscopic and voltammetric methods.* Journal of luminescence, 2009. **129**(11): p. 1320-1325.
340. Tang, H., et al., *Interaction mechanism of flavonoids on bovine serum albumin: Insights from molecular property-binding affinity relationship.* Spectrochimica Acta Part A: Molecular and Biomolecular Spectroscopy, 2020. **239**: p. 118519.
341. Togashi, D.M. and A.G. Ryder, *A fluorescence analysis of ANS bound to bovine serum albumin: binding properties revisited by using energy transfer.* Journal of fluorescence, 2008. **18**(2): p. 519-526.
342. Yan, J., et al., *Effect of luteolin on xanthine oxidase: Inhibition kinetics and interaction mechanism merging with docking simulation.* Food Chemistry, 2013. **141**(4): p. 3766-3773.
343. Singh, K., et al., *pH Effect on Ligand Binding to an Enzyme Active Site.* bioRxiv, 2022: p. 2022.07. 01.498456.
344. Thomas, C. and M. Winkler, *Chemical engineering problems in biotechnology.* Critical reports in applied chemistry. London: Elsevier Applied Science, 1990: p. 23-93.
345. Yim, S. and P. Shamlou, *The engineering effects of fluids flow on freely suspended biological macro-materials and macromolecules.* Influence of stress on cell growth and product formation, 2000: p. 83-122.
346. Kroll, M.H., et al., *Platelets and shear stress.* 1996.
347. Maxwell, M.J., et al., *Identification of a 2-stage platelet aggregation process mediating shear-dependent thrombus formation.* Blood, 2007. **109**(2): p. 566-576.
348. Jackson, S., W.S. Nesbitt, and E. Westein, *Dynamics of platelet thrombus formation.* Journal of thrombosis and Haemostasis, 2009. **7**: p. 17-20.
349. Harte, N.P., et al., *Amyloid oligomers and mature fibrils prepared from an innocuous protein cause diverging cellular death mechanisms.* Journal of Biological Chemistry, 2015. **290**(47): p. 28343-28352.

List of publications

From thesis

1. **Sharma, L.G.** and Pandey, L.M., 2021. Shear-induced aggregation of amyloid β (1–40) in a parallel plate geometry. *Journal of Biomolecular Structure and Dynamics*, *39*(17), pp.6415-6423.
2. **Sharma, L.G.** and Pandey, L.M., 2021. Thermomechanical process induces unfolding and fibrillation of bovine serum albumin. *Food Hydrocolloids*, *112*, p.106294.
3. **Sharma, L.G.,** S Senthikumar, L Rangan and Pandey, L.M., Attenuation of thermal and thermomechanical induced aggregation of Bovine serum albumin by three different extracts of *Centella asiatica*, a neuroprotective plant **(submitted)**
4. **Sharma, L.G.,** C. Panda and Pandey, L.M., Thermal and presheared-induced aggregation of hen egg white lysozyme and the effect of *Centella asiatica* water extract on the aggregation **(submission awaited)**

Other publications:

1. Karmakar, S., **Sharma, L.G**., Roy, A., Patel, A. and Pandey, L.M., 2019. Neuronal SNARE complex: A protein folding system with intricate protein-protein interactions and its common neuropathological hallmark, SNAP25. *Neurochemistry International*, *122*, pp.196-207.
2. Mahanta, N., Sharma, S., **Sharma, L.G**., Pandey, L.M. and Dixit, U.S., 2022. Unfolding of the SARS-CoV-2 spike protein through infrared and Ultraviolet-C radiation based disinfection. *International Journal of Biological Macromolecules*, *221*, pp.71-82.
3. Panda, C., **Sharma, L.G**. and Pandey, L.M., 2023. Experimental procedures to investigate fibrillation of proteins. *MethodsX*, *11*, p.102445.

4. Pandey, S., Das, A., **Sharma, L.G.**, Pandey, L.M. and Dobbidi, P., 2023. Exploring Multifunctional Response of Ca10 (PO4) 6 (OH) 2–K0. 5Na0. 5NbO3 Ceramic Composite for Biomedical Applications. *ACS Biomaterials Science & Engineering*, *9*(10), pp.5687-5699.
5. Mahanta, N., **Sharma, L.G.**, Pandey, L.M. and Dixit, U.S., 2024. Artificial aging of rice using a sterilization box equipped with infrared heating and Ultraviolet-C radiation. *Journal of Food Process Engineering*, *47*(2), p. e14544.

Conferences and seminars attended:

1. **Laipubam Gayatri Sharma**, Abhishek Roy and Lalit M. Pandey, Rheological properties of BSA due to formation of nano size agglomerate, International Conference on Advanced Nanomaterials and Nanotechnology, ICANN-2017 at Indian Institute of Technology Guwahati, December 18-21, 2017
2. **Laipubam Gayatri Sharma** and Lalit M. Pandey, Fibrillation of Aβ (1-40) under variable shear fields in parallel plate geometry, International Conference on Frontiers in Chemical Sciences (FICS - 2018), IIT Guwahati, India, 2018
3. **Laipubam Gayatri Sharma**, “Recent Advances on Bio-inspired Nanomaterials for Environmental Applications”, UK-India Education and Research Initiative (UKIERI), IIT Guwahati, India, 2018
4. **Laipubam Gayatri Sharma,** “Thermal and shear induced aggregationstudy of BSA”, 1st Departmental Retreat, IIT Guwahati, India, 2019 (Oral presentation)
5. **Laipubam Gayatri Sharma**, workshop cum symposium on “Bio- Nanomaterials For Environmental Applications”, UK-India Education and Research Initiative (UKIERI), IIT Guwahati, India, 2020

6. **Laipubam Gayatri Sharma**, Lalit M. Pandey, Inhibition of Thermal and Shear Induced Aggregation of Albumin (Bovine Serum Albumin) by *Centella asiatica* extract, *Latin American Conferences on Natural and Applied Sciences Universided Juarez Autonoma de Tabasco, Villahermosa, Mexico,* November 5-6, 2021 (Oral presentation)
7. **Laipubam Gayatri Sharma**, Lalit M. Pandey, Thermomechanical induced aggregation of BSA, CHEMCON, December 26-30, 2021 (Oral presentation)
8. **Laipubam Gayatri Sharma**, Lalit M. Pandey, North-East Research Conclave: Sustainable Science and Technology (NERC-2022). poster presentation on "*Inhibition of thermal and shear induced aggregation of Albumin (Bovine serum albumin) by Centella asiatica extract"*, May 20-22, 2022
9. **Laipubam Gayatri Sharma**, Chinmay Panda and Lalit M. Pandey, ACS Publications Symposium: Biological and Medicinal Chemistry "Inhibition of Thermal and shear-induced aggregation of Albumin by *C.asiatica* extract: A mechanistic insight" for the poster sessions at the symposium, Bonn, Germany, Monday, March 6 - Wednesday, March 8, 2023
10. **Laipubam Gayatri Sharma**, Chinmay Panda and Lalit M. Pandey, Indian Peptide Symposium "Inhibition of Thermal and shear-induced aggregation of Albumin by *Centella asiatica*" February 23-24, 2024